Developing Raman Microspectroscopy as a Technique to Analyse Single Caco-2 Cells

By

Rachael Smith, MSci

Thesis submitted in partial fulfilment of the requirements for the degree of Doctor of Philosophy

July 2019

Department of Chemistry, Lancaster University

Abstract

Raman spectroscopy is rapidly advancing as a cell imaging technique due to its advantages over existing techniques: it requires little sample preparation, is label-free and can be carried out in aqueous environments to image both fixed and live cells. However, Raman spectroscopy is not commonly used in clinical practice due to perceived long acquisition times and complex data analysis. The aim of this work is to develop Raman spectroscopy as a technique to image cells, specifically Caco-2 cells, and to use Raman spectroscopy to measure the response of these cells to abiotic perturbations.

We have developed methodologies for mapping both fixed and live Caco-2 cells, as well as robust shading parameters to allow for direct comparisons. Using a metal rhenium complex to identify the mitochondria of these cells, we have demonstrated the difficulties in shading Raman maps to specific peaks of interest, and how the shading range needs to be carefully considered to avoid over or under interpretation of the data.

Raman spectroscopy was also used to evaluate the effect of the cannabinoids cannabidiol (CBD) and anandamide (AEA) on Caco-2 cells. CBD affects Caco-2 cells differently at different concentrations; at low concentrations it may induce proliferation, but at high concentrations it causes cell death characterised by DNA breakdown. Investigating the mechanism of CBD induced cell death in Caco-2 cells suggested that it is not apoptosis or necrosis, but is mediated by caspases 3/7 with the broken down DNA being exported from the cell, which is more consistent with autophagy-dependent cell death or lysosomal-dependent cell death. At low concentrations, AEA may also induce proliferation, but at high concentrations it affects Caco-2 cells differently and does not cause cell death; instead, we hypothesise that the drug has an anti-proliferative effect on these cells. Overall, we have demonstrated how Raman spectroscopy can be used to gain valuable visual and biochemical information about cells.

Contents

List of Figures

List of Tables:

Acknowledgements

Firstly, I'd like to thank both of my supervisors, Dr Lorna Ashton and Dr Karen Wright. None of this would have been possible without all of your help, guidance and support over the last four years. I would like to express my gratitude to Michelle Bates for getting me up and running in the cell culture lab, to Dr Mike Coogan, for your help with the complex study and to Dr Elisabeth Shaw for all the help around the lab. Thanks to Nikoletta for answering all my questions along the way, and thanks to Jess, for being the best lab partner, and for proofreading this for me – I will return the favour for you!

Thanks to Helen and Laura, for keeping me sane along the way – I don't know what I'd do without you. Finally, I'd like to thank my parents for everything – I wouldn't have been able to do this without your support.

Declaration

I declare that this thesis is my own work and has not been submitted in part, or as a whole, for the award of a higher degree or qualification elsewhere. Sections of this thesis which have been published have been clearly identified in the figure legends.

Rachael Smith, MSci

Abbreviations List

A	Adenine
ADCD	Autophagy dependent cell death
AEA	Anandamide
AIF	Apoptosis-inducing factor
C	Cytosine
CAD	Caspase-activated DNase
CARS	Coherent anti-Stokes Raman spectroscopy
CB_1	Cannabinoid receptor type 1
CB_2	Cannabinoid receptor type 2
CBD	Cannabidiol
CCD	Charged coupled device
DMEM	Dulbecco's modified eagle medium
DMSO	Dimethyl sulfoxide
DNA	Deoxyribonucleic acid
DPBS	Dulbecco's phosphate buffered saline
ECACC	European collection of cell cultures
EDTA	Ethylenediaminetetraacetic acid
G	Guanine
HEPES	4-(2-hydroxyethyl)-1-piperazineethanesulfonic acid
ICD	Immunogenic cell death
IR	Infrared
LC3	Microtubule-associated protein 1A/1B-light chain 3
LDCD	Lysosome-dependent cell death
MEM	Minimal essential medium eagle
MOMP	Mitochondrial outer membrane potential
MPT	Mitochondrial permeability transition
MVB	Multivesicular body
NA	Numerical aperture

PAR	Poly adenosine diphosphate ribose
PBS	Phosphate buffered saline
PCA	Principal component analysis
PFA	Paraformaldehyde
Phe	Phenylalanine
ROS	Reactive oxygen species
SERS	Surface-enhanced Raman spectroscopy
SNV	Standard normal variate
T	Thymine
TAE	Tris-acetate-EDTA
Tyr	Tyrosine
UV	Ultraviolet
UVRR	Ultraviolet resonance Raman spectroscopy

Chapter 1: Background and Literature Review

1.1 Introduction

Cells are the basic biological unit of all living organisms, and it is necessary to study cells to gain insights into both normal and abnormal cellular behaviour. Traditionally, cells have been studied using optical light microscopy, which allows for the observation of living cells but has a limited resolution (Wilson and Bacic, 2012). The development of electron microscopy led to improvements in resolution, however this can only be carried out on fixed cells which undergo extensive sample preparation (e.g. cryofixation, dehydration and sectioning). As cells are fixed, this technique can only give a 'snapshot' of the cells current state, and the preparation procedures have the potential to introduce artefacts in addition to interfering with the cells intracellular physiology (Koster and Klumperman, 2003).

Imaging live cells is therefore vital to observe normal cellular behaviour and processes in real time, and over time. The development of fluorescence microscopy allowed for living cells to be imaged. However, as this technique usually involves the expression of exogenous fluorescent molecules intracellularly via the introduction of external genes, it may not reflect the normal physiology of the cell (Stephens and Allan, 2003). Several studies have reported that the introduction of fluorescent markers affected cell behaviour, by inhibiting the migration of macrophages (Denholm and Stankus, 1995), and leukocytes (Abbitt, Rainger and Nash, 2000). As a result, novel imaging techniques are required that can overcome the issues associated with current methods, and Raman spectroscopy has emerged as a potential alternative to fluorescence microscopy for cell studies.

Raman spectroscopy is a valuable biochemical technique that combines microscopy and vibrational spectroscopy in order to analyse samples according to the chemical information contained within their unique Raman spectra. It is particularly useful as an imaging technique, as these Raman spectra can be used to construct a Raman map of a sample to give spatially resolved biochemical information (Smith and Dent, 2005). As Raman spectroscopy does not require as much sample preparation prior to analysis in comparison to other techniques, is label-free and can be carried out in aqueous conditions, it is a viable technique for imaging both fixed and live cells.

Raman imaging of cells is a relatively new and emerging field that has vast potential, including in the diagnosis of disease (Kong *et al.*, 2013) and in cytological research (Palonpon, Sodeoka and Fujita, 2013). In addition, it could prove to be an invaluable technique in the pharmaceutical industry, providing viable models of living human cells that can be monitored over an extended period of time for any biochemical and physiological changes in response to different drugs. It has the potential to enhance the knowledge of how different compounds interact with different cell types, and to be used in early phases of drug development in order to assess toxicity, delivery or uptake, and to visualise the intracellular distribution of a drug, all of which may reduce the high cost associated with drug development and testing, as well as potentially reduce the need for testing on animals (Kann *et al.*, 2015). Overall, Raman spectroscopy is an important research tool with far-reaching applications that is at the forefront of cell-based imaging techniques.

1.2 Vibrational Spectroscopy

Vibrational spectroscopy is a technique used to detect vibrations in molecules. It has a wide range of uses, from providing structural information or determining chemical structure, to identifying substances from the specific spectra they produce, or to determining the amount of a specific substance within a sample. Vibrational spectroscopy can be used on samples in

gas, liquid or solid phases, and to examine single cells or surface layers, meaning that there are a wide range of applications for this type of spectroscopy.

Molecular vibrations can be measured in two ways: via the inelastic scattering of photons, or the absorption of light. Vibrational spectroscopy based on the direct absorption of light is known as infrared (or IR) spectroscopy, while the inelastic scattering of photons is associated with Raman spectroscopy.

1.2.1 Raman Scattering

A molecule can either absorb or scatter photons when it interacts with light, and it is this scattering that is measured in Raman spectroscopy. Scattering involves the excitation of a molecule to a short-lived virtual state due to the distortion of electrons surrounding the functional group bonds within it, and there are three outcomes of this process (represented in figure 1.1). If the molecule relaxes back down to the ground state, it emits a photon that has the same energy as the incident photon; there is no change in energy. This is known as elastic, or Rayleigh scattering, and the majority of photons are scattered in this manner (Smith and Dent, 2005).

Inelastic scattering occurs when there is a change in energy between the incident photon and the scattered, or emitted, photon. If the molecule relaxes into an excited vibrational state from the virtual state, then it emits a photon with less energy than the incident photon in a process known as Stokes scattering. If the molecule is already in an excited vibrational state and relaxes back down to the ground state after interacting with the photon, the scattered photon will have more energy than the incident photon. Here, the photon gains energy from the molecule, and this is known as anti-Stokes scattering (Smith and Dent, 2005; Amer., 2010). As most molecules are in the ground state at room temperature, anti-Stokes scattering is weaker than Stokes scattering, and is less commonly measured in traditional Raman spectroscopy.

However, coherent anti-Stokes Raman spectroscopy (CARS) is a method that measures anti-Stokes scattering and is being used increasingly in biological studies (El-Diasty, 2011).

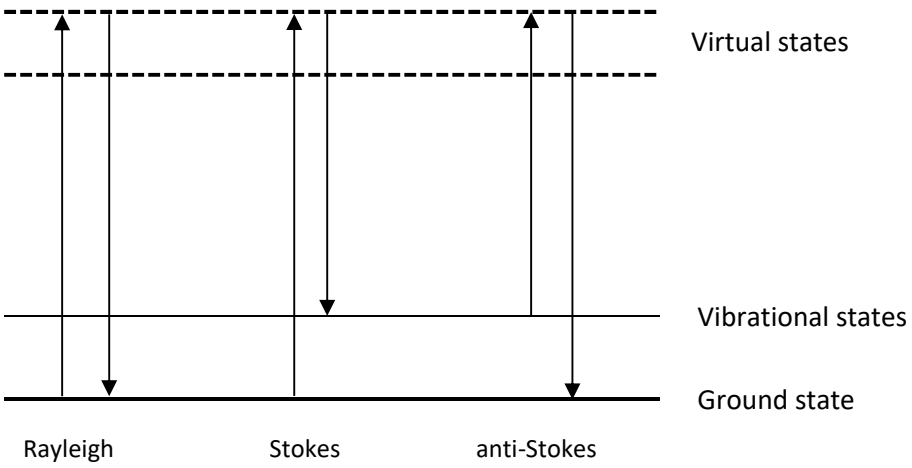

Figure 1.1: Diagrammatic representation of the three types of Raman scattering. Adapted from (Smith and Dent, 2005).

1.2.2 Theoretical Aspects of Raman spectroscopy:

The key property that determines whether a molecule is able to scatter a photon is the molecule's polarisability. Polarisability, α, is the ability of an applied electrical field, *E*, to induce a dipole moment, p, in an atom or molecule:

$$p = \alpha E$$

Equation 1.1 (Schrader, 1995)

For a molecule to be Raman active there must be a change in polarisability. The rate of change in the polarisability must therefore not be equal to zero. This is known as a selection rule; a molecular motion will be Raman-active only if the motion occurs with a changing polarisability (Schrader, 1995).

1.2.3 Molecular Vibrations:

Molecules comprise of atoms with a specific mass connected by elastic bonds. Due to this elasticity, they are able to perform periodic motions, or vibrations (Schrader, 1995)**.** The number of possible vibrations (or vibrational degrees of freedom) for any particular molecule is 3N – 6 (3N – 5 for linear molecules), where N is the number of atoms the molecule contains. There are many different modes of vibration, depending on whether it is the bond length or angle that is changing. Stretching (symmetrical or asymmetrical) occurs when the bond length changes, and bending or deformation (scissoring, rocking, wagging, twisting) when the bond angle is altered (Wilson *et al.*, 1955; Smith and Dent, 2005). These vibrational modes are demonstrated for a linear molecule in figure 1.2 below.

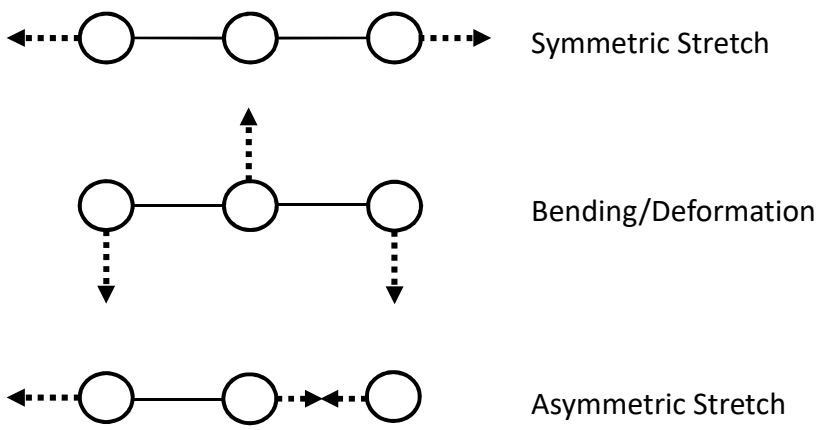

Figure 1.2: Diagram representing the three different types of vibrations for a linear molecule.

Vibrational spectra, such as those measured in Raman spectroscopy, are representative of these different modes of vibration, although due to the selection rule only some vibrational modes will be Raman-active.

As previously mentioned, Raman scattering depends on a change in polarisation within the molecule, distorting the electron cloud around the nucleus.

Highly polar bonds, such as the O-H bond, have a low polarisability and produce only a weak Raman peak as little scattering occurs. This makes Raman spectroscopy ideal for studying samples in aqueous environments (Smith and Dent, 2005).

Raman spectra depend not only on the geometrical arrangement of atoms within a molecule, but also on the masses of the atoms in the molecule and the strength of the chemical bonds between them. The relationship between these three factors that influence the position of Raman peaks in a sample is represented by the equation below, with *f* the force constant of the bonds between atoms, and *m* the mass of the atoms (Schrader, 1995).

$$\nu = \frac{1}{2\pi}\sqrt{\frac{f}{m}}$$

Equation 1.2

Lighter atoms will have a higher frequency when compared to heavier atoms (e.g. C-H vibrations lie at 3000 cm^{-1} while C-I vibrations lie at 500 cm^{-1}). As the force constant is a measure of bond strength, the stronger the bond the higher the frequency will be (Smith and Dent, 2005; Baia, Astilean and Iliescu, 2008; Siebert and Hildebrandt, 2008). As a result of this, the vibrational spectra will be different for different molecules containing different atoms and bonds, providing a unique spectral fingerprint.

1.2.4 Fluorescence and Raman spectroscopy:

Raman scattering and fluorescence emission have a similar origin. In Raman scattering, the molecule is excited into a short-lived virtual state when a photon of light is scattered from it. In fluorescence, the molecule absorbs a photon and is excited into a higher electronic state, and fluorescent light is emitted while molecules relax back to the lower energy level. However, as the Raman effect is a relatively weak process, any fluorescent signal can overwhelm the Raman signal and make it difficult to analyse the resulting Raman spectrum (Cebeci-Maltaş *et al.*, 2017). This is one of the main disadvantages of Raman spectroscopy, however, it is possible

to reduce the amount of fluorescent signal generated by carefully selecting the wavelength of laser used, as well as by reducing the amount of fluorescent species in a sample e.g. by using phenol-red free cell culture media.

1.3 Cells and Raman spectroscopy

1.3.1 Cells

The Raman fingerprint of a cell is shown in figure 1.3. The cell is the basic biological unit of all living organisms. They are the smallest units of life, able to replicate independently, and are invaluable in terms of biological research as most diseases arise from intracellular biochemical changes resulting in cellular abnormalities. Most eukaryotic cells have a similar structure, enclosed within a cell membrane consisting of a phospholipid bilayer. Membrane-bound organelles such as the nucleus (containing DNA), mitochondria and ribosomes exist within the cytoplasm, along with many other biomolecules including proteins and nucleic acids (Lodish *et al.*, 2012).

There are a number of different cell types and cell lines, but the ones we have focused on are Caco-2 cells. These are a human colon epithelial cancer cell line that are frequently used as a model of the intestinal barrier. After long-term culture (14-21 days), Caco-2 cells undergo spontaneous differentiation to express several characteristics of intestinal enterocytes, including tight junctions, a brush border, and the expression of several enzymes (Pinto *et al.*, 1983; Hidalgo, Raub and Borchardt, 1989). These properties make them an ideal model for studying drug absorption (Artursson, 1990) and uptake (Derakhshandeh, Hochhaus and Dadashzadeh, 2011), as well as drug toxicity (Shappell, 2003) (Meunier *et al.*, 1995). In contrast, undifferentiated Caco-2 cells, as they are derived from a colon carcinoma, are more similar in morphology to cancer cells (Macpherson *et al.*, 2014), and are therefore a good model for studying the toxicity of potential anti-cancer compounds.

Studying and understanding the way cells work, from their replication to the process of cell death, is vital not just in the field of cell biology, but for a number of scientific research areas, particularly in the study of disease and in the development of drugs targeted towards those diseases. The visualisation of cells is an important part of this research, allowing for physical changes to be observed. There are a number of existing imaging techniques, including optical light microscopy, electron microscopy and fluorescence microscopy, but each of these have issues associated with them (limited resolution (Wilson and Bacic, 2012), introduction of artefacts (Koster and Klumperman, 2003), introduction of fluorescent markers that may affect cell behaviour (Stephens and Allan, 2003)). As a result, novel imaging techniques are required that can overcome the issues associated with current methods, and Raman spectroscopy has emerged as a potential alternative to these techniques to image both fixed and live cells.

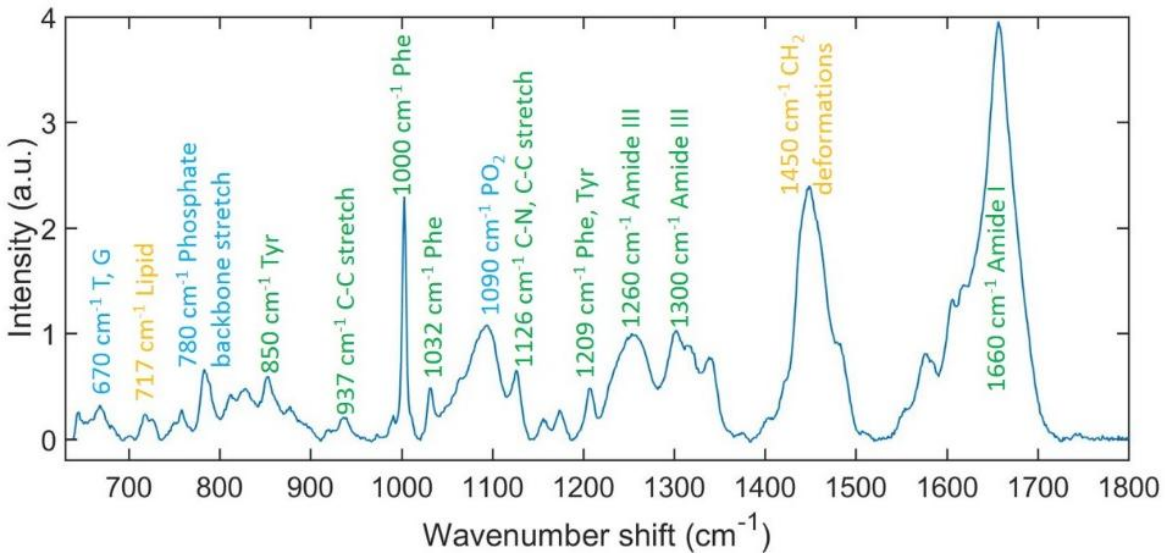

Figure 1.3: Typical labelled cell spectrum.

A typical cell spectrum is shown in figure 1.3, with specific peaks labelled. Blue labels represent DNA peaks, green labels represent protein peaks and yellow labels represent lipid peaks. The assignments for each of these peaks is listed in table 1.1. A Raman spectrum therefore gives information from across the whole cell, and has a number of different uses. For example, Raman spectroscopy has been used to determine cell cycle stage by observing changes in

Raman spectra corresponding to lipid and DNA levels (Short *et al.*, 2005; Swain, Jell and Stevens, 2008). Raman spectroscopy has also been used to identify cell phenotype or bacterial species by identifying key peaks (Sun *et al.*, 2015), and has been used to distinguish between tumour and non-tumour cells by examining differences between their Raman spectra (Neugebauer *et al.*, 2010; Dochow *et al.*, 2011).

Table 1.1 Peak assignments for a typical cell spectrum.

Wavenumber:	**Assignment:**	**Reference:**
670 cm^{-1}	Nucleic acids T and G	(Puppels, Garritsen, *et al.*, 1991; Overman *et al.*, 1998)
717 cm^{-1}	C-N stretches in phospholipid head ends	(Overman *et al.*, 1998; Kunapareddy, Freyer and Mourant, 2008)
780 cm^{-1}	O-P-O diester symmetric stretch of the DNA backbone	(Puppels, Garritsen, *et al.*, 1991; Yiming *et al.*, 1999; Stone *et al.*, 2004)
850 cm^{-1}	Ring breathing in the amino acid tyrosine	(Naumann *et al.*, 2001; Stone *et al.*, 2004)
937 cm^{-1}	C-C backbone stretching	(Omberg *et al.*, 2002)
1000 cm^{-1}	Symmetric ring breathing in the amino acid phenylalanine	(Overman *et al.*, 1998; Wolthuis *et al.*, 1999; Yiming *et al.*, 1999)
1032 cm^{-1}	C-H in-plane phenylalanine bending	(Omberg *et al.*, 2002; Stone *et al.*, 2004)
1090 cm^{-1}	PO_2^- stretch	(Overman *et al.*, 1998; Omberg *et al.*, 2002)
1126 cm^{-1}	C-N and C-C stretches	(Borchman, Tang and Yappert, 1999; Naumann *et al.*, 2001; Omberg *et al.*, 2002; Stone *et al.*, 2004)
1209 cm^{-1}	$C\text{-}C_6H_5$ stretches in phenylalanine and tryptophan	(Omberg *et al.*, 2002; Stone *et al.*, 2004)
1260 cm^{-1}	Amide III β-sheet	(Gremlich, 2018)
1300 cm^{-1}	Amide III α-helix	(Gremlich, 2018)
1450 cm^{-1}	C-H deformations	(Borchman, Tang and Yappert, 1999; Naumann *et al.*, 2001; Omberg *et al.*, 2002; Stone *et al.*, 2004)
1660 cm^{-1}	Amide I α-helix)	(Puppels, Garritsen, *et al.*, 1991; Naumann *et al.*, 2001; Omberg *et al.*, 2002; Gremlich, 2018

1.3.2 Raman Spectroscopy and Microscopy

In addition to giving qualitative chemical information, Raman spectroscopy can also be combined with optical light microscopy, first described in the literature in 1975 (Delhaye and Dhamelincourt, 1975), with the first self-built Raman microspectrometer being described in 1990 (Puppels *et al.*, 1990). This development enabled Raman mapping to become a possibility, however, because only one in every 10^6-10^8 of scattered photons have a different energy than the incident photon, Raman scattering is an inherently weak process, resulting in long acquisition times. This meant that Raman spectroscopy was not a feasible option for imaging biological samples until relatively recently, where advances in technology and methodology have resulted in a decrease in these acquisition times, making Raman spectroscopy a novel and attractive choice for the imaging of biological samples (Adar, Delhaye and DaSilva, 2007; Zoladek *et al.*, 2010; Kong *et al.*, 2013).

In this technique, a microscope lens is used to focus the laser beam onto a sample, resulting in a better resolution than can be achieved with Raman spectroscopy alone (Puppels *et al.*, 1990). If the spectrometer is coupled to a camera, usually a charged-coupled device (CCD), confocal Raman spectroscopy can be used to image or map samples in order to visualise their underlying chemical components according to their Raman spectra (Zoladek *et al.*, 2010). In Raman imaging, the entire sample is globally illuminated and Raman spectra at a specific wavenumber are collected in a single measurement, whereas Raman mapping involves collecting full Raman spectra from across the entire sample (Delhaye and Dhamelincourt, 1975; Schlücker *et al.*, 2003). A Raman map can then be computationally produced to construct a pseudo-colour image of the sample, with each pixel shaded according to the relative intensity of the Raman spectra at a given wavenumber or range of wavenumbers (Ling *et al.*, 2002). Currently, there is no standard approach for shading a Raman map, which has the potential to result in false-colouring and the loss or over-interpretation of the data. Better, universally-adopted approaches for shading and transparency in the shading parameters

applied are therefore required, especially in a clinical context, in order for Raman mapping to become a viable and reliable imaging technique (Ashton, Hollywood and Goodacre, 2015).

The typical set-up for a Raman microspectrometer can be seen in figure 1.4 below. The main components include: laser source, microscope objective, filters, mirrors, and CCD, which are all important for the function of the Raman spectrometer. The laser source can vary in wavelength. Stronger Raman intensities occur at shorter wavelengths because they generate a greater amount of scattered photons, but shorter wavelengths induce more autofluorescence than longer wavelengths. Autofluorescence is the natural emission of light by biological structures upon the absorption of light (Monici, 2005). As previously mentioned, as the Raman effect is usually weak, fluorescence signals can overwhelm and therefore interfere with the Raman signal (Kagan and McCreery, 1994). Shorter wavelengths are also more likely to induce photodamage and degradation of samples, which can be particularly detrimental in the study of biological material. The choice of laser is therefore an important one depending on the type of material being studied (Kann *et al.*, 2015). The microscope objective can also be altered, depending on the sample being studied. The objective determines the magnification and resolution of the image, and for cell studies a higher resolution objective, such as a x60 lens, is preferred (Thorn, 2016).

Filters are essential to remove the more intense Rayleigh scattering, and can either be notch or edge filters. There are advantages and disadvantages to both types of filters: notch filters are chosen to coincide with a specific laser wavelength and therefore different filters are required for different excitation wavelengths, whereas edge filters absorb all light up to a certain wavelength. Notch filters have a finite lifetime and degrade with time, whereas edge filters have a near infinite lifetime. Edge filters are therefore more beneficial, but they are much more expensive than notch filters (Smith and Dent, 2005). Mirrors are vital for directing

the laser photons onto the sample, and as previously discussed, the CCD detects the scattered light and constructs a Raman spectrum.

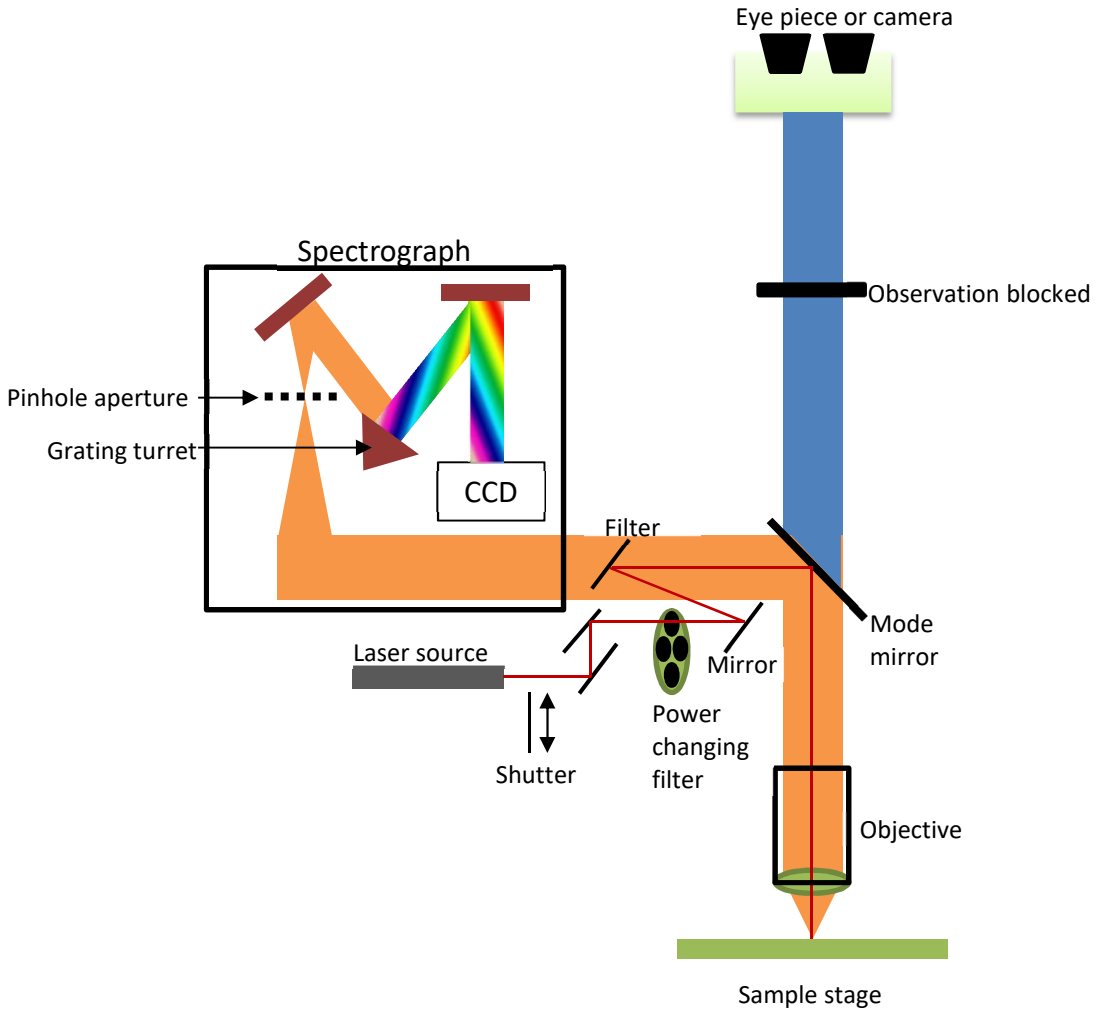

Figure 1.4: Typical set-up of a Raman spectrometer coupled to an optical microscope. Adapted from: (Smith et al., 2015).

1.3.3 Raman Imaging of Cells

Raman spectroscopy boasts several advantages over the alternative imaging techniques mentioned previously. Namely, there is no sample preparation required, and as Raman spectroscopy measures the underlying chemical composition of a sample, there is no need for the addition of labels in order to identify intracellular components (Smith and Dent, 2005). Raman spectroscopy is therefore minimally invasive. Due to the fact that water is a weak

Raman scatterer, Raman measurements can be carried out in aqueous environments, meaning that cells can be maintained in cell culture media during analysis and ensuring that conditions are as close to physiologically normal in culture as possible. Finally, the low (<1 μm) resolution that can be achieved by Raman spectroscopy (Puppels *et al.*, 1990; Schie and Huser, 2013) make it ideal for imaging both live and fixed single cells.

Since the development of Raman microscopy, numerous studies concerning the imaging and mapping of cells have been carried out. The earliest of these experiments were carried out on fixed cells, and involved seeding cells onto calcium fluoride windows (which have low background scattering and therefore a low Raman signal), fixing them with either formalin, paraformaldehyde or methanol before being imaged by a Raman microspectrometer. Most of these studies were concerned with the distribution of organelles within a cell, including the mitochondria (Matthaus *et al.*, 2007), DNA (Uzunbajakava, Lenferink, Kraan, Volokhina, *et al.*, 2003; Konorov *et al.*, 2013), and proteins (Uzunbajakava, Lenferink, Kraan, Willekens, *et al.*, 2003). Studies on fixed cells have also been used to image the response of colon cancer cell lines to the drug sorafenib (Yosef *et al.*, 2018), to monitor the interaction of actinomycin D on lung cancer cell lines (Farhane, Bonnier and Byrne, 2017), to study the effect of the drug doxorubin on lung cancer cells (Farhane, Bonnier and Byrne, 2017; Byrne, Bonnier and Farhane, 2019), and to monitor resistance to targeted cancer therapy, also in lung cancer cells (Hammoud *et al.*, 2018).

1.3.4 Live Cell Imaging

While studies on fixed cells are useful in determining cellular organisation and drug response, there is still the potential for fixing procedures to cause damage to the cells or introduce artefacts into the image, and fixed cells have been shown to have an altered Raman spectra in comparison to unfixed cells (Chan *et al.*, 2009; Chan, Taylor and Thompson, 2009; Draux *et al.*, 2010). The numerous advantages of Raman spectroscopy previously mentioned make it ideal

for studying living cells to overcome the issues associated with observing fixed cells, meaning that it can be utilised to image living cells to give valuable biochemical information that other imaging techniques are currently unable to provide.

The first studies to image live cells follow very similar preparation procedures. Cells were first seeded onto a suitable substrate before being incubated overnight to allow for attachment. They were then washed before being immersed in a petri dish containing phosphate buffered saline (PBS) before they were imaged. This technique has been used to image single living non-small cell lung cancer cells (Draux *et al.*, 2009), glioma cells (Klein *et al.*, 2012), to observe changes in morphology in different cell cycle stages (Swain, Jell and Stevens, 2008), to observe the distribution of an anti-cancer drug in live breast cancer cells (Ling *et al.*, 2002), to identify cells of the immune system without the use of labels (Chen *et al.*, 2015), and to monitor the effects of different compounds on breast cancer cells (Mignolet, Wood and Goormaghtigh, 2018). However, these studies are only studying live cells in the short-term, as they are not cultured in media but in PBS, and therefore only show immediate effects. We are interested in being able to observe cells over a longer period of time by using a Raman microscope coupled to an incubator. This is an emerging technique for live cell imaging, allowing cells to be maintained under physiological conditions (in culture media at 37 °C and 5 % CO_2) while spectral measurements and mapping occurs, and several studies have already been carried out in recent years to investigate whether it is a viable option for the imaging of live cells.

In these experiments, cells are seeded onto a suitable substrate (usually held in a sample holder or chamber) but are immersed in fresh media rather than PBS before being placed inside the microscope's incubator for mapping. This method has been used to detect changes in live cells cultured in different environments (Gargotti *et al.*, 2018)

In most studies producing Raman maps, spectra are collected by scanning single cells in a raster pattern, although the step size and integration times varies between some studies. Live

cell Raman mapping has been utilised in order to image several different cell lines over time, including breast cancer cells (Zoladek *et al.*, 2010), neural stem cells (Ghita *et al.*, 2012), and embryonic bodies (Chan *et al.*, 2009; Pascut *et al.*, 2011). These studies monitored cells over a period of several days with no loss of cell viability, suggesting that Raman spectroscopy can be used to image the same cells under normal physiological conditions over an extended period of time without any negative side effects.

All of the above live-cell studies used a 785 nm laser. There is evidence that visible lasers induce damage to biological samples even when a minimal exposure time and a low laser power is used (Puppels *et al.*, 1990; Wood *et al.*, 2005). However, at 785 nm, which is just outside the visible spectrum, this degradation does not take place even after long exposure times at a high laser power. In addition, the amount of fluorescence observed using a 785 nm laser is very low when compared to other wavelengths (Notingher *et al.*, 2002; Smith and Dent, 2005), making 785 nm an ideal wavelength for measuring the Raman spectra of living cells. However, even though this wavelength is less damaging to cells than those that have been used previously, long acquisition times are still not ideal as it increases the amount of time taken to image the entire cell, hence an acquisition time of 1 second or less is usually used.

1.3.5 Resonance Raman spectroscopy:

Resonance Raman spectroscopy is a type of Raman spectroscopy where the wavelength of the incident photon is close in energy to an electronic transition of the sample under investigation, resulting in a greater incidence of scattered photons, therefore enhancing the Raman signal (Li and Kitagawa, 2014). For example, UV resonance Raman (UVRR) spectroscopy uses UV lasers (excitation wavelength range from 180-260 nm) to create a resonance effect which enhances the Raman signal of aromatics, and therefore enhances the features of both proteins and nucleic acids (Ashton *et al.*, 2013). Previously, this technique has been primarily used in the biopharmaceutical industry, both as a tool to monitor changes in protein structure (Ashton

and Goodacre, 2011), and as a probe for cellular DNA and RNA in mammalian cell culture medium (Ashton *et al.*, 2015). However, there is also interest in using resonance Raman spectroscopy as a technique for organelle-specific labelling in cells (Kuzmin *et al.*, 2016), suggesting that it is a technique of interest in cell-based studies.

1.3.6 Raman spectroscopy and drug studies

The above single cell studies provided important structural and biological information in addition to showing that Raman spectroscopy is a valuable imaging technique. However, the fact that Raman imaging can be conducted on live cells over an extended time period provides an opportunity for time-course experiments, which is particularly useful in pharmacological studies of drug uptake and distribution.

Studies on live cells have demonstrated the ability of Raman spectroscopy to monitor cell death in response to the addition of a toxic drug into the cell culture media. Apoptosis in human breast cancer cells exposed to etoposide has been monitored over a period of several hours, with the authors showing, via Raman mapping, a build-up of lipids within the cytoplasm of these cells after treatment with the drug, in addition to changes in the intensity of Raman peaks associated with DNA (Zoladek *et al.*, 2011). Apoptosis as a result of treatment with another genotoxic agent, docetaxel, has also been studied in a different cell line by studying single cells over a period of 20 hours. This study again showed that Raman microscopy could be used to examine changes in cell structure, visualising a progressive loss of cell volume via Raman mapping, in addition to showing changes in the Raman spectra of treated cells over time in comparison to untreated cells (Bräutigam *et al.*, 2013). A more recent study showed that Raman spectroscopy was able to detect and predict the effects of the drug tamoxifen in liver cells by looking at differences between spectra of treated and untreated cells (Ali *et al.*, 2019). Live cell Raman spectroscopy has also been used to monitor glial cells response to the

drugs doxorubin and methamphetamine, and detected a number of peaks characteristic of the induction of apoptosis in these cells (D'Brant *et al.*, 2019).

These studies utilise the Raman spectra of the cellular response to the drug (e.g. changes in DNA structure), but do not detect or use the spectra of the drug itself. Drug distribution can be imaged if the drug of interest has a peak that differs or has a higher intensity than the peaks typical of the cellular components (Keating *et al.*, 2015). The movement of the drug paclitaxel into the cytoplasm of breast cancer cells has been investigated over a number of hours, using a peak at 1740 cm^{-1}, representative of the vibration of the C=O bond within the drug, to visualise its position in the cell (Hamideh Salehi *et al.*, 2013). The visualisation of drugs like these within subcellular organelles allows for a greater understanding of drug uptake, intracellular distribution and targeting, and shows that Raman spectroscopy has the potential to be a valuable development in the field of pharmokinetics.

Collectively, these studies demonstrate the usefulness of Raman spectroscopy for both monitoring and visualising the effect of toxic agents and chemicals at the single cell level. However, there is still room for improvement within this area of research, by utilising true live-cell Raman imaging, where cells are imaged within media rather than PBS. The development of live-cell imaging provides the opportunity to show the real-time response of cells to drugs under normal physiological conditions, which may allow for the development of suitable *in vitro* models for the early stages of drug testing, especially in toxicity studies.

1.3.7 Cannabinoids

Cannabinoids are pharmacologically active compounds derived from the plant *Cannabis sativa* that bind to cannabinoid receptors to produce their behavioural effects. These receptors include the CB_1 and CB_2 G-protein coupled receptors, as well as vanilloid receptors (Pertwee, 2001). There are a number of existing cannabinoids, but the two we have chosen to focus on are cannabidiol (CBD) and anandamide (AEA). CBD is a phytocannabinoid derived from the

plant, whilst AEA is an endogenous cannabinoid, a fatty acid neurotransmitter (Pertwee and Ross, 2002). The mechanism of action of both of these drugs is currently not well understood, although both CBD and AEA have been linked to the induction of apoptosis in several different cell lines, including the Caco-2 cell line (Schwarz, Blanco and Lotz, 1994; Maccarrone *et al.*, 2000; Massi *et al.*, 2004; McAllister *et al.*, 2011; Kuc, Jenkins and van Dross, 2012; Macpherson *et al.*, 2014). In addition, AEA has been said to have antiproliferative effects (De Petrocellis *et al.*, 1998).

Raman spectroscopy has previously been used to identify the presence of cannabinoids within trichomes of the *Cannabis sativa* using CARS (Ebersbach *et al.*, 2018), and surface-enhanced Raman spectroscopy (SERS) has been used for the detection of synthetic cannabinoids in forensics (Mostowtt and McCord, 2017). However, both of these studies did not detect the cannabinoids CBD or AEA, and there are no existing studies that use Raman spectroscopy to determine the effect of these drugs within cultured cells. As a result of this, and due to the fact that the mechanism of action of both drugs is currently poorly understood, Raman spectroscopy may be a suitable technique to gain more understanding of the effect of these drugs on our chosen cell line.

1.3.8 Use of metal complexes to help with Raman imaging

Whilst Raman spectroscopy is a label-free technique, it has a limited resolution and some organelles, such as the mitochondria, cannot be visualised without the use of any labels (Smith, Wright and Ashton, 2016). Therefore, in order to visualise organelles such as these, labels are required. Compounds intended to be used as biological imaging agents must have several properties to make them suitable for this use, including stability, solubility in aqueous environments, low toxicity, and they must have a good rate of uptake by cells (Fernández-Moreira, Thorp-Greenwood and Coogan, 2010). Metal complexes are ideal candidates for this and have been used in a number of Raman spectroscopy studies. An organometallic complex

has been conjugated to a drug to show the distribution of the Golgi apparatus within cells (Clède *et al.*, 2013), a metal-carbonyl complex has been shown to localise in the nuclear membrane of colon cancer cells (Meister *et al.*, 2010), and a ruthenium complex has been shown to localise to the mitochondria of cells (Burke, Byrne and Keyes, 2018). All of these studies used Raman spectroscopy as a technique to do this, indicating its potential to be used in conjunction with metal complexes in order to visualise cellular organelles.

1.4 Conclusions

To summarise, Raman spectroscopy is a technique that combines vibrational spectroscopy and light microscopy in order to allow for label free imaging of cells. It is particularly useful for cell imaging, as there is little sample preparation required, and water has a weak Raman signal, so both live and fixed cells can be studied within aqueous environments. However, at present Raman spectroscopy is not being routinely employed in cell biology due to perceived long acquisition times and a lack of consistency in data analysis. Due to its advantages over current techniques and the benefits and understanding it may bring to the field of cell biology, further research needs to be carried out to improve Raman spectroscopy for cell imaging in order to make it a viable imaging tool within laboratories.

1.5 Project Aims and Objectives

1.5.1 Research Objectives

The overall aims of the project are to develop Raman spectroscopy as a tool to study and map both live and fixed Caco-2 cells exposed to a number of different stimuli, such as a metal rhenium complex and the cannabinoid drugs CBD and AEA, and to gain a better understanding of the mechanism of action of CBD and AEA on this particular cell line.

1.5.2 Objectives

1.5.2.1 Successfully culture Caco-2 cells for Raman spectroscopy

This involved all stages of sample preparation, including the development of a suitable methodology for attaching, growing and fixing Caco-2 cells on CaF_2 windows.

1.5.2.2 Collect Raman maps of fixed single cells

In addition, once Raman maps were acquired, we determined the best pre-processing methods for these spectra.

1.5.2.3 Develop robust shading parameters

Once established, the shading parameters were then applied across all maps to ensure consistency in shading throughout the project. Once a suitable methodology was in place, we progressed onto adding substances into the cells and monitoring their response.

1.5.2.4 Collect spectra of a rhenium complex for use as an intracellular label

Once this spectrum had been collected, we carried out Raman mapping of fixed Caco-2 cells that had been treated with the complex to see if it could be used to visualise the mitochondria within cells.

1.5.2.5 Collect spectra of the cannabinoid drugs CBD and AEA

Once these spectra had been acquired, we carried out Raman mapping of fixed cells which had been treated with these drugs in order to see if Raman spectroscopy could determine the effect of these drugs on Caco-2 cells.

1.5.2.6 Establish procedures for live cell mapping

We used a cell top incubator to maintain cells under normal physiological conditions throughout analysis. Initially, we collected maps of live control cells to ensure that they were not damaged by exposure to the laser. Following this, Raman maps of live cells incubated with the rhenium complex were collected, in order to establish if its uptake by Caco-2 cells could be detected over time. Finally, we collected Raman maps of live cells incubated with the cannabinoid drugs CBD and AEA to monitor the same cells response to these drugs over time.

Chapter 2: Materials and Method Development

2.1 Introduction

Raman spectroscopy has previously been established as an imaging method, and has been used with a number of different cell lines. However, each of these studies varies in their methodology, from the fixatives used, to the wavelength of the laser, the acquisition time, and the step size used when mapping. For example, one early study mapped the DNA and protein in lymphocytes, and fixed cells in 1 % PFA, mapped with a laser wavelength of 647 nm, and had an acquisition time of 1-2 seconds (Uzunbajakava, Lenferink, Kraan, Volokhina, *et al.*, 2003). In comparison, a study to map stress-induced changes in lung fibroblasts fixed cells in formalin, used a laser wavelength of 785 nm, an acquisition time of 10 seconds and a step size of 1 µm (Krafft *et al.*, 2006). Another study used methanol to fix MCF-7 cells prior to carrying out Raman spectroscopy using a 785 nm laser (Konorov *et al.*, 2013). Finally, a 532 nm laser has been used to map cells using Raman spectroscopy, with one study using a 0.3 µm step size (Krafft *et al.*, 2005).

There are similar variations in studies using Raman spectroscopy to map live cells. As previously discussed, some of the first studies to image live cells were short-term, and cells were maintained in PBS throughout analysis (Ling *et al.*, 2002; Draux *et al.*, 2009; Klein *et al.*, 2012). However, to allow the study of healthy, living cells over longer periods of time, cells need to be maintained in cell culture medium rather than PBS, which has been implemented in more recent studies. Step size and acquisition times still vary, and some examples are a step size of 1 µm and an acquisition time of 1 second per pixel (Zoladek *et al.*, 2011), a step size of 2 µm and an acquisition time of 1 second (Pascut *et al.*, 2011), and a step size of 1 µm and an acquisition time of 0.5 seconds (Bräutigam *et al.*, 2013). Most live cell studies have been

carried out using a 785 nm laser, but some have used a laser wavelength of 532 nm (Hobro *et al.*, 2015).

Overall, this demonstrates that there are a number of considerations that need to be made when using Raman spectroscopy to map single fixed or live cells, and there is a need to develop novel methodologies to optimize the technique for specific cell lines.

The cell line used in all Raman spectroscopy experiments reported here was the colon carcinoma cell line, Caco-2. While there are some reported studies using these cells with Raman spectroscopy, these use primarily CARS (Saarinen *et al.*, 2017) or SERS (Xu *et al.*, 2016). One study has used confocal Raman spectroscopy to image Caco-2 cells, however, the authors used Raman imaging to collect only Raman spectra at the specific wavelength of 2800-3030 cm^{-1}, rather than by acquiring a full spectrum at each pixel of the image (Scalfi-Happ *et al.*, 2011). As such, suitable methodology needed to be established in order to carry out mapping of Caco-2 cells using Raman spectroscopy for all stages of sample preparation and Raman measurements, including: cell attachment, fixation, Raman setup, and data pre-processing.

2.2 Materials and Methodology

2.2.1 Cell Culture

All compounds and cell culture reagents were purchased from Fisher Scientific UK (Loughborough, UK) unless otherwise stated. The human epithelial colorectal adenocarcinoma cell line, Caco-2, was obtained from the European Collection of Cell Cultures (ECACC). Caco-2 cells were cultured in 75 cm^3 sterile cell culture flasks with complete media (MEM substituted with 10 % foetal bovine serum and 1 % non-essential amino acids) and maintained in an incubator at 37 °C and 5 % CO_2. When cells reached ~70 % confluence, flasks were washed twice with 5 mL of 1x Dulbecco's phosphate buffered saline (DPBS) and incubated with 1 mL of 0.25 % trypsin with EDTA at 37 °C for 5 min to detach cells from the flask. Cells were then

resuspended in ~4 mL of media and ~1 mL transferred to a new flask; the volume was made up to 10 mL by adding fresh complete media and flasks returned to the incubator.

2.2.2 Cell Attachment for Raman Analysis

Initially, cells were detached via trypsin as above from culture flasks and cell concentration determined using trypan blue exclusion. A concentration of ~$1x10^5$ cells were seeded onto sterile calcium fluoride (CaF_2) Raman compatible windows maintained inside 35 mm cell culture dishes. Cells were returned to the incubator and allowed to adhere for ~2 hours. After this time, 2 mL of fresh complete media was added, and dishes left in the incubator overnight for cells to continue to adhere and grow on the substrate. Cells then underwent treatment and/or fixation prior to spectral analysis (see section 2.2.6).

Early results showed that, when examined under the microscope on the Raman spectrometer, the cells had an abnormal morphology on the CaF_2 windows when compared to their morphology on cell culture flasks, suggesting that they were failing to adhere to the substrate. Cell adhesion onto the substrate that it is growing on is vital for Caco-2 cells function and normal behaviour, and failure to attach to this substrate results in cell death (Frisch and Francis, 1994). Caco-2 cells have been shown to undergo this process on a non-adhesive substrate (Kozlova *et al.*, 2001), and our results indicated that the sterile CaF_2 windows were non-adhesive to this cell line.

As CaF_2 windows are shown to be ideal for cell-based Raman studies due to their lack of background signal (Draux *et al.*, 2009; Ramoji *et al.*, 2016), instead of changing the substrate we opted to coat the windows in a substance to aid attachment. We chose poly-lysine for this as it is well established for increasing adhesion in several cell lines (Lieberman and Ove, 1958; Yavin and Yavin, 1974; Mazia, Schatten and Sale, 1975; Rainaldi, Calcabrini and Santini, 1998). In addition, it has minimal Raman signal within the biological fingerprint region (Kniggendorf, Gaul and Meinhardt-Wollweber, 2011), making it ideal for use in Raman studies. CaF_2 windows

were aseptically coated with 800 µL of poly-lysine solution (Sigma Aldrich, UK) and incubated for 5 min before the solution was removed and the surface washed with sterile cell culture water. Windows were allowed to dry for at least 2 hours prior to the introduction of cells (using the same procedure as above); cells appeared to have a normal morphology under the microscope using this method.

2.2.3 Fixation Procedure

The next step was to develop a suitable protocol for fixing cells onto the CaF_2 windows after the incubation period was complete. Media was removed from the cell culture dishes and the windows were washed twice with DPBS containing $CaCl_2$ and $MgCl_2$ in order to remove any traces of media. Different fixation methods were trialled prior to finding the optimum conditions. The first fixative used was methanol, which has previously been used to fix cells in Raman-based studies (Konorov *et al.*, 2013). After washing, cells were fixed in 2mL of ice cold (-20 $^{\circ}$C) 100 % methanol for 15 min at room temperature.

However, this method was unsuccessful. Upon examination under the microscope, cells appeared to have clumped together as a single mass, suggesting that they had not fixed correctly (figure 2.1A). Following this, ethanol, which has also been used as a fixative in previous Raman studies (Jess *et al.*, 2007) (Diem *et al.*, 2013), was used. Cells were fixed in 2 mL of 70 % ethanol at room temperature for 30 min, which gave similar results.

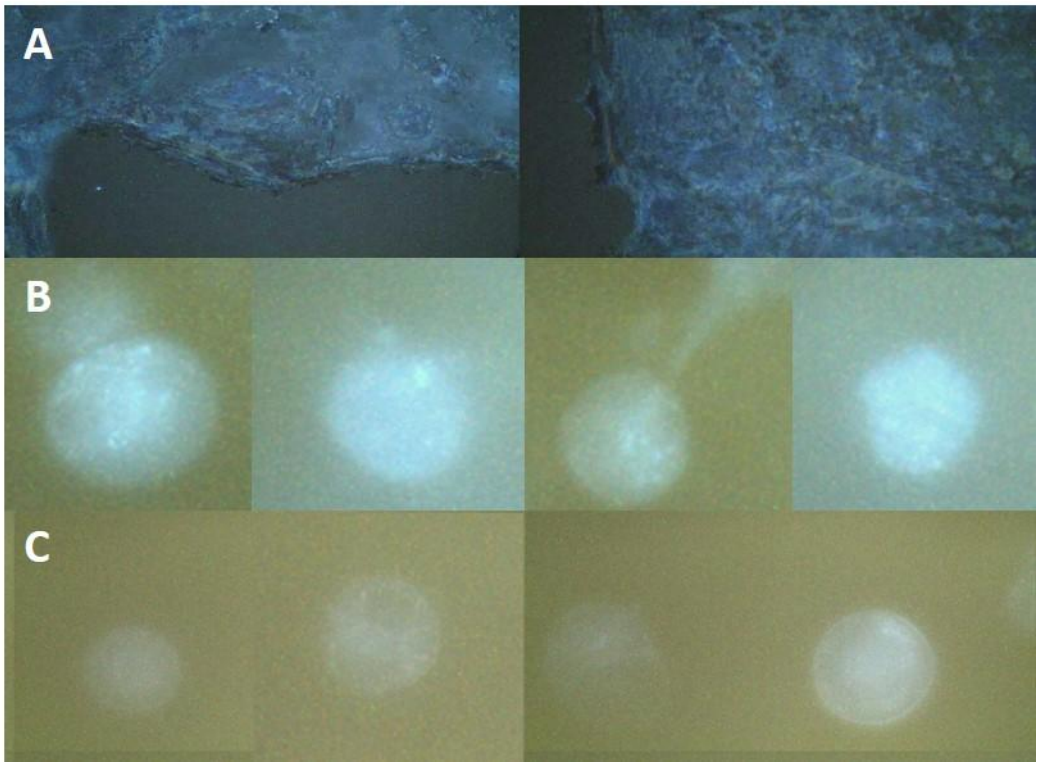

Figure 2.1: A comparison of different fixation methods on cell structure. Photographs taken beneath the Raman spectrometer microscope using a 60x water immersion objective of either cells fixed with **(A)** methanol, **(B)** PFA, or **(C)** live, unfixed cells.

As both methanol and ethanol work in a very similar way to fix cells (coagulants that denature proteins within the cell by disrupting hydrophobic and hydrogen bonding (Eltoum *et al.*, 2001)), an alternative approach was to use an aldehyde (paraformaldehyde, or PFA) as a fixative instead of an alcohol.

In this method, cells were fixed in 4 % PFA in PBS after washing and incubated for 20 min at room temperature. This was successful and allowed the visualisation of fixed single cells down the microscope for the first time (figure 2.1B). Furthermore, as PFA has been shown to induce less spectral changes in fixed versus live cells in comparison to methanol (Chan, Taylor and Thompson, 2009; Kuzmin, Pliss and Prasad, 2014; Hobro and Smith, 2017), it has an added advantage and was used as a fixative for all further Raman experiments. PFA also did not

appear to visibly alter the morphology of Caco-2 cells, as when viewed under the microscope, they appeared to have a similar morphology to live, unfixed cells (figure 2.1C).

After the incubation times mentioned above, the fixative solution was removed, and windows washed a further three times with DPBS prior to Raman analysis. Cells were maintained in DPBS throughout Raman measurements in order to prevent samples from drying out.

2.2.4 Raman Measurements

Raman spectra were collected using a confocal Raman system (inVia, Renishaw plc, Wotton-Under-Edge, UK), coupled to a 532 nm and 785 nm excitation wavelength laser. A 785 nm wavelength laser is usually preferred in live cell studies as it has been shown not to cause sample degradation (Notingher *et al.*, 2002). However, shorter wavelengths induce stronger Raman intensities (Albrecht and Hutley, 1971; Palonpon, Sodeoka and Fujita, 2013), and there was less background noise associated with the 532 nm laser observed in our experiments. It was therefore decided that the 532 nm wavelength would be used whilst cells were fixed in order to generate the best Raman signal, whilst the 785 nm laser would be better equipped for live cell studies.

StreamLineHR mapping, using a laser-spot focus, was carried out using a 60 x NA = 1.00 water immersion objective (LUMPLFLN 60XW Olympus) with a step size of 1 µm. An exposure time of 1 second was used on all samples, and the average total collection time for a complete cell varied from ~8 to ~20 min. Longer exposure times resulted in some photodamage to cells (*via* the development of a halo around the cell undergoing analysis) that has also been observed in previous studies as a result of the high laser intensity (Wood *et al.*, 2005). Shorter acquisition times have a higher level of background noise, and after trying several different acquisition times, 1 second resulted in the best trade-off for giving good quality Raman signals whilst preventing any observable photodamage or degradation of the sample.

2.2.5 Cell Treatment

2.2.5.1 Serum

All experiments were carried out under low-serum (1 %) conditions. Whilst serum is necessary for optimum cell growth, its composition is poorly defined and highly variable. Eliminating or reducing the amount of serum present therefore removes unknowns, reduces interference, and provides more reproducible experimental conditions (Pirkmajer and Chibalin, 2011). In addition, serum deprivation is thought to reduce basal cell activity (Codeluppi *et al.*, 2011), and increases homogeneity in proliferating populations of cells, as it causes them to cease the cell cycle and to enter the G_0/G_1 phase (Van Rechem *et al.*, 2010). In order to do this, after cells had been allowed to adhere to CaF_2 windows overnight, complete, 10 % serum media was removed from cells and replaced with 1 % serum media. Cells were then left overnight to allow time for synchronisation.

2.2.5.2 Cannabidiol

For experiments, cannabidiol (CBD) (Tocris Bioscience, Abingdon, UK) concentrations were made from a stock solution of 75 mM (in ethanol) and prepared in media. CBD was diluted in media, and the final concentration of CBD added to cells was either 10 or 1 µM. These concentrations were chosen as they had been used in previous studies (Shrivastava *et al.*, 2011; Macpherson *et al.*, 2014; Sultan, Marie and Sheweita, 2018).

After cells had been incubated on CaF_2 windows overnight as above, media was removed and fresh media added containing drug solutions to make final concentrations of 10 µM or 1 µM. Dishes were then returned to the incubator. After treatment with CBD, cells were returned to the incubator for a range of incubation times, from 2 to 24 hours. Following this, cells were fixed. Control dishes were also prepared using media, and ethanol used as a vehicle control (section 2.4).

2.2.5.3 Anandamide

Anandamide (AEA) (Tocris Bioscience, Abingdon, UK) concentrations were made from a stock solution of 14.4 mM (in ethanol) and prepared in media. AEA was diluted in media, and the final concentration added to cells was either 10 or 1 μM. These concentrations were chosen to be consistent with those for CBD. Cells were treated with the drug as above, for the same incubation times, and fixed prior to analysis.

2.2.5.4 Metal Complexes

For experiments, a rhenium complex (provided by Dr Mike Coogan, Lancaster University) was used at a concentration of 100 μg/mL, prepared from a stock solution of 10 mg/mL in DMSO and diluted in media. After cells had been incubated on CaF_2 windows as above, media was removed and fresh media containing the complex solution was added. Dishes were returned to the incubator for a period of either 2 or 4 hours, after which cells were fixed. Control dishes were prepared using DMSO as a vehicle control.

2.3 Spectral Analysis

2.3.1 Data Collection

Raman maps consist of many different spectra taken from across the cell. The longer the acquisition time for each individual spectrum, the less noise they contain, and they are therefore of a higher quality than spectra taken using shorter acquisition times (figure 2.2). For studies using fixed cells, this is less of an issue as longer acquisition times can be used in order to collect good-quality spectra without it having a detrimental effect on the cell (providing there is no photodamage). However, in live cell studies, measurements need to be carried out quickly as live cells are likely to move throughout analysis. Additionally, exposure time to the laser needs to be sufficiently low so as to ensure that cells are not perturbed or damaged. A 2 or 3 second acquisition time across a whole cell will result in the complete map taking upwards of two hours, which is not a realistic possibility in live cell imaging. It is

therefore vital to establish data processing techniques capable of reducing the background noise associated with shorter acquisition times in order to bring out the cellular features within the spectra.

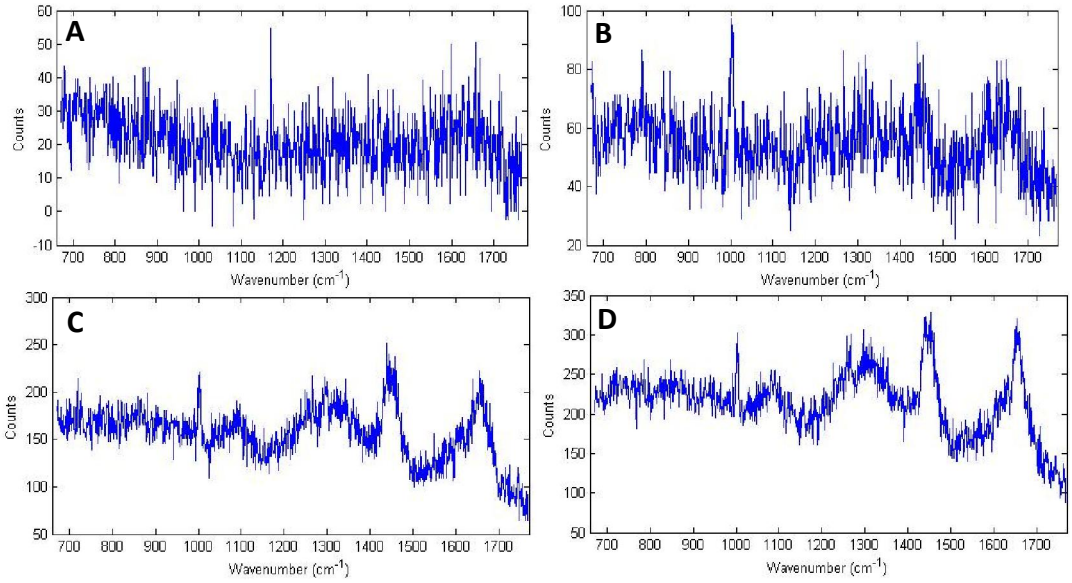

Figure 2.2: Raw Raman spectra of the cytoplasm region of fixed Caco-2 cells with varying acquisition times. Acquisition times were as follows: (A) 0.1 seconds, (B) 0.5 seconds, (C) 1 second, (D) 2 seconds. All spectra were acquired using a 532 nm wavelength excitation laser and a laser power at sample of ~30 mW.

2.3.2 Data Processing

The first step in the pre-processing of Raman data is cosmic ray removal. Cosmic rays hitting the detector in the Raman spectrometer can result in the generation of narrow spikes within the Raman spectra that cannot be attributed to features of a sample, and therefore need to be removed prior to any data analysis. This removal is straightforward due to their distinctive shape, and this process can be carried out on the instrument software (WIRE 4.2), by comparing neighbouring spectra to identify and remove any cosmic rays that occurred during data collection.

After Raman maps have undergone cosmic ray removal, there are several different types of pre-processing that can be applied to them in order to reduce the noise. For our maps, we

used the noise filter function on the instrument software (WIRE 4.2). This technique uses principal component analysis (PCA) in order to eliminate data variance that cannot be attributed to real or significant data; it will therefore remove noise from within each spectrum. It has the advantage of being included in the instrument software, and allows the user to examine each principal component in order to determine which contain all the real Raman information. Other smoothing methods such as Savitzky-Golay filtering smooth every sharp peak within a spectrum, which has the potential to reduce the spectral resolution and can remove weak spectral features completely (Mat, Clupek and Volka, 2007), which would be detrimental in later studies where we are interested in finding a peak from a drug or metal complex within a cell spectrum. The difference between a raw and noise filtered spectra can be seen in figure 2.3; it is much easier to distinguish the cellular features after data processing has been applied.

We also normalised each map, which is a process used to eliminate experimental error. As the collection of Raman maps of fixed cells can take several hours, there is the potential for variations or perturbations to occur throughout analysis that are due to factors other than the sample itself, such as a change in laser power or focus, which can influence the intensity of spectral features. Normalisation reduces these variations from the data, so differences can be attributed to sample composition rather than experimental error (Gautam *et al.*, 2015). To normalise the data we used mean variance, which transforms each spectra so that they have the same mean and variance to reduce experimental variations within the data. The inputted value for mean and variance was kept the same for all maps analysed to allow for comparison.

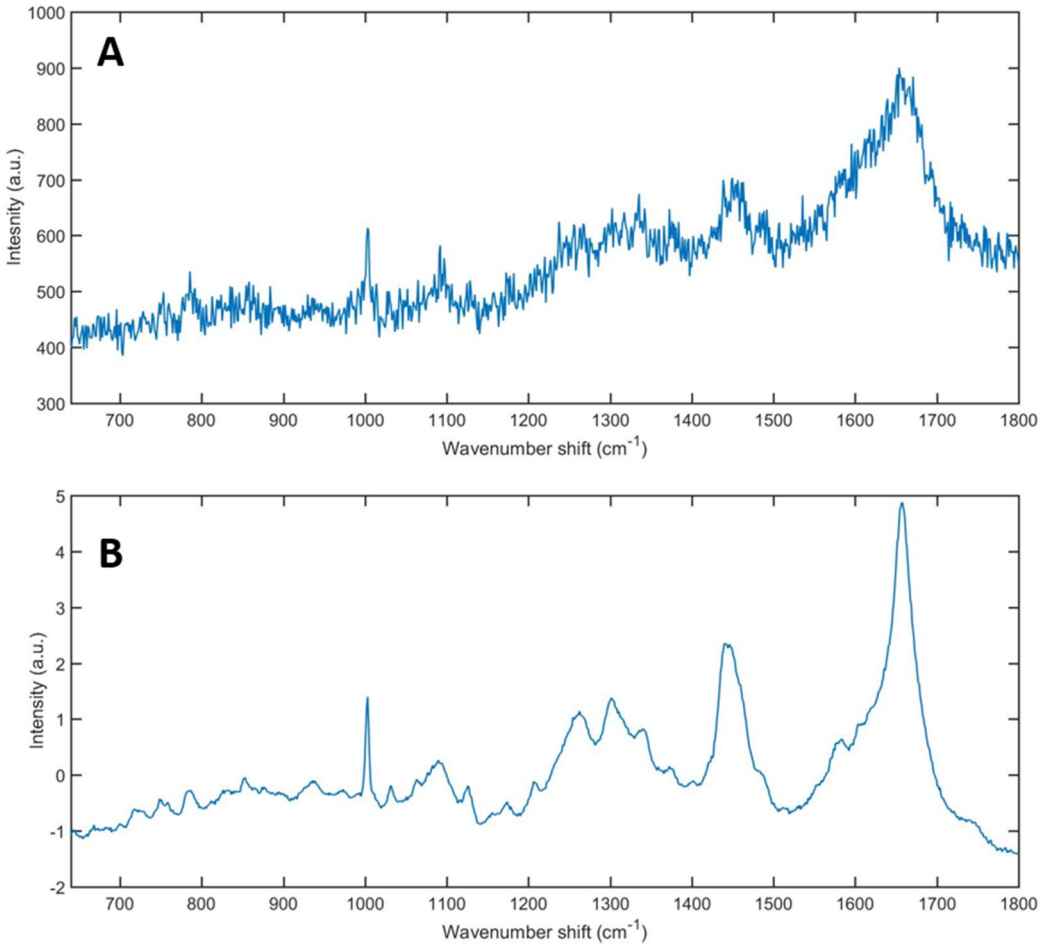

Figure 2.3: A comparison of raw and pre-processed Raman spectra taken from a fixed Caco-2 cell. (A) Typical Raman spectrum for a cell, prior to any data analysis, encompassing the spectral regions 630-1800 cm^{-1}. (B) Spectrum of the same cell after undergoing normalisation and noise filtering.

Once suitable and effective data pre-processing procedures had been established, processed spectra could be used in order to generate Raman maps of single Caco-2 cells. To do this, data was exported to MATLAB software version 2016 (The MathWorks, MA, USA) for further data analysis and the generation of distribution plots which were then used to shade images in WIRE.

2.3.3 Pseudo-Shading

All Raman maps were shaded according to the relative intensity of a specific spectral region. This allows us to distinguish between different areas of the cell, for example nucleic acid rich

regions and protein rich regions, and enables the identification of the nucleus and the cytoplasm within a specific cell. The region of 780-802 cm^{-1} was used to shade for nucleic acids (representative of bands corresponding to the nucleic acids thymine and cytosine, and the phosphate backbone (Barhoumi *et al.*, 2008; De Luca, Dholakia and Mazilu, 2015)), and the region 1630-1680 cm^{-1} to shade for proteins (representative of the amide I peak (Short *et al.*, 2005; Zhang *et al.*, 2008)).

Whilst Raman mapping is a useful technique for generated detailed chemical images based on a sample's Raman spectra, care needs to be taken when applying shading to Raman maps. As previously discussed (chapter 1, section 1.3.2), currently, there is no standard approach for shading a Raman map, which has the potential to result in false-colouring and the loss or over-interpretation of the data as the values can be arbitrarily altered in order to give the 'best' image (Ashton, Hollywood and Goodacre, 2015). To prevent this, shading needs to be carefully considered and selected, especially in circumstances where a comparison of Raman images is required.

One way to ensure that shading is consistent across all maps is to use distribution plots to aid the shading parameters chosen. These distribution plots consist of all the peak area intensity values within the Raman map. Most of the values have a very low intensity and can be attributed to background; shading at higher intensities allows us to remove this background from the image and to only examine areas of interest. Shading ranges can therefore be chosen according to the distribution plots and applied across all Raman maps to allow for more appropriate comparisons.

Figure 2.4 demonstrates the way in which the shading range used can drastically alter the end image. A shading range from minimum to maximum results in the whole image being dominated by either the protein signal, with no nucleus visible (4A), or the nucleic acid signal, with no cytoplasm of the cell visible (4D). In contrast, shading to only the highest intensity

suggests that there is very little protein, and therefore cytoplasm, within the cell (4B), or that there is no nucleic acid present within the cell (4E). For the protein content of the cell, shading to only the middle values (30-100) eliminates both the background and the highest intensity values, and shows more clearly the cytoplasm of this cell (4C). For the nucleic acid signal, shading approximately the top 60% of values (by multiplying the maximum value, ~3.3 by 0.4, and using this as our minimum value), results in a final image where the nucleus and cytoplasm of this cell are clearly visible (4F). Once a suitable range has been selected, this can then be applied to subsequent Raman maps in order to increase shading consistency.

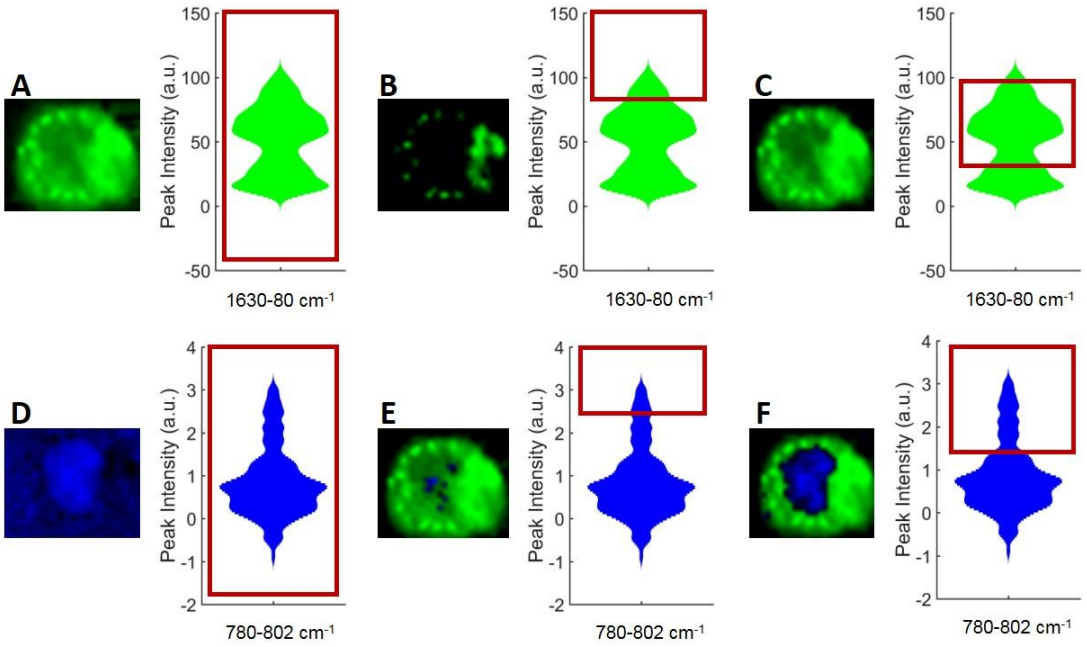

Figure 2.4: **A comparison of shading ranges.** Raman maps and distribution plots of the protein content (green, peak range 1630-80 cm^{-1}) and nucleic acid content (blue, peak range 780-802 cm^{-1}) of the same Caco-2 cell. The red box indicates the shading range applied to each map: (A) shading range of minimum too maximum, (B) top 10 % of values, and (C) middle range of values of the 1630-80 cm^{-1} peak; (D) shading range of minimum too maximum, (E) top 10 % of values, and (F) the top 60 % of values of the 780-802 cm^{-1} peak.

In addition to shading the nucleus and the cytoplasm, several studies have claimed to be able to visualise the mitochondria in cells without the use of any labels at 532 nm by using the peak

at ~750 cm^{-1} (Matthäus *et al.*, 2007; Okada *et al.*, 2012; Ichimura *et al.*, 2014), which is assigned to the pyrrole breathing mode in cytochrome c (Hamada *et al.*, 2008). The mitochondria are organelles vital for normal cellular function, and visualising these organelles within cells is valuable as they are indicators of cell health (Nunnari and Suomalainen, 2012). Using the peak range 737-767 cm^{-1}, encompassing the 750 cm^{-1} cytochrome c peak, we attempted to shade Raman maps of Caco-2 cells in order to see if we could visualise the mitochondria within cells in the same way that we could visualise the nucleus and cytoplasm. In figure 2.5, three cells, shaded to their DNA and protein content, are shown, along with the distribution plot for the cytochrome c peak, shaded to several different ranges. No matter how the shading range is adjusted, the cytochrome c peak is present around and underneath the nucleus of all three cells. As the mitochondria are present only in the cytoplasm of cells, this suggests that this peak is not suitable, in these cells, for visualising the mitochondria. As such, all cells were subsequently shaded only to their DNA and protein content.

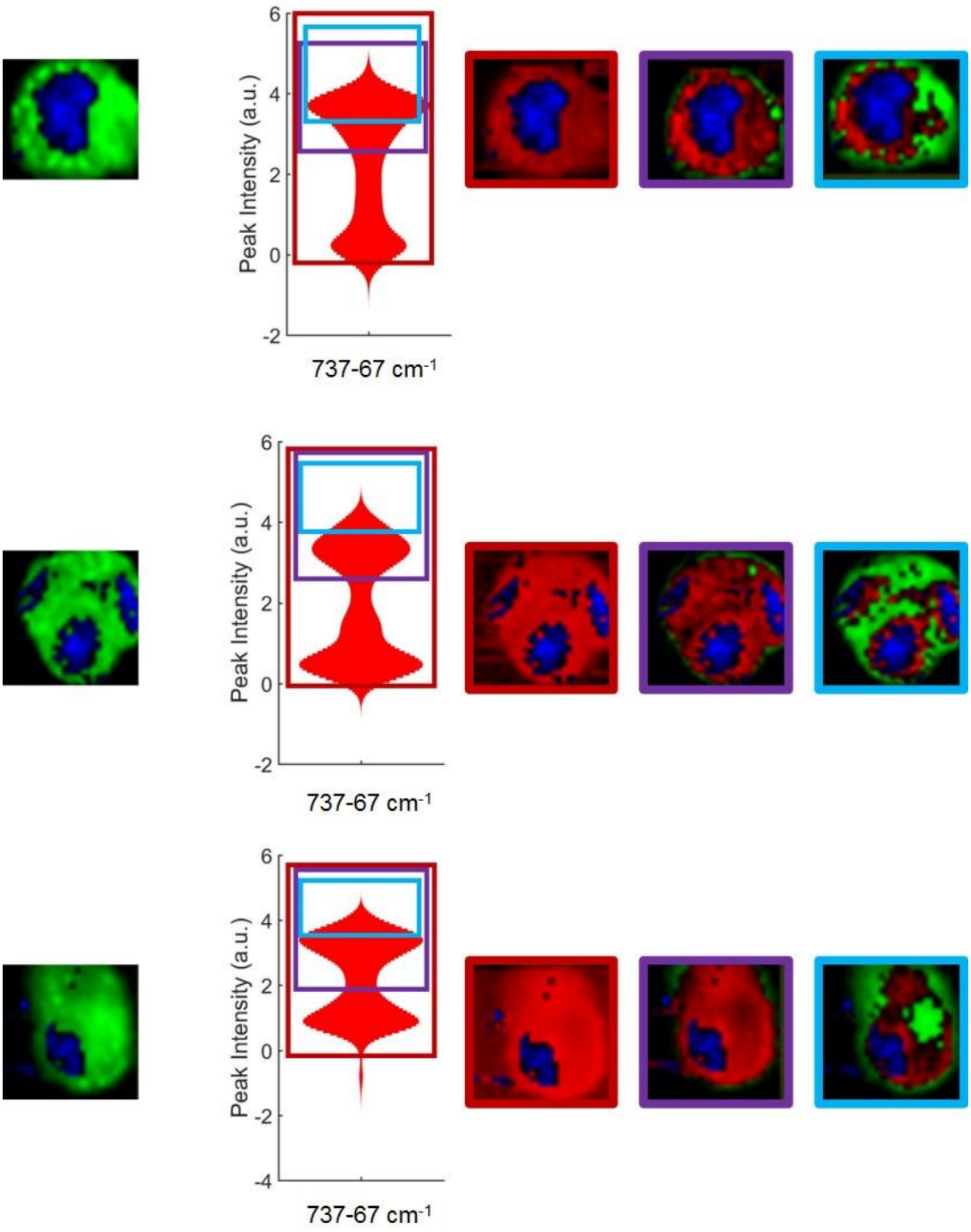

Figure 2.5: **Shading to the cytochrome c peak.** Raman maps and distribution plots of the potential cytochrome c content (red, peak range 737-767 cm^{-1}) of three different Caco-2 cells. For composite images, protein content (green, peak range 1630-80 cm^{-1}), and DNA content (blue, peak range 780-802 cm^{-1}) were shaded according to the previously established shading parameters. The boxes indicate the shading range applied to each map.

2.3.4 Principal Component Analysis

Raman spectroscopy can not only be used to gain visual information in the form of Raman maps, but also biochemical information. One way to do this is to use principal component analysis (PCA). Mathematically, PCA is defined as an orthogonal linear transformation that transforms the data to a new coordinate system, such that the greatest variance by any projection of the data comes to lie on the first coordinate (called the first principal component) the second greatest variance on the second coordinate and so on (Ringnér, 2008). It provides a method to assess how variables change with respect to each other by finding combinations of variables which describe major trends in the data.

For all PCA plots, second derivative spectra were used. This is a method that allows more specific identification of small Raman peaks, and also removes baseline errors to eliminate any variations in intensity from contributing to separation in the PCA-scores plots. The disadvantage of this technique is the loss of signal-to-noise ratio, as the signal is reduced whilst the noise is amplified (Rieppo *et al.*, 2012). Spectra therefore also had to be smoothed (using a smooth width of 25) prior to carrying out PCA. Both the calculation of second derivative spectra and subsequent smoothing were carried out in MATLAB software version 2016 (The MathWorks, MA, USA).

An example of PCA is demonstrated in figure 2.6. A total of 30 spectra were taken from either areas of high DNA content (blue) or high protein content (green) of a single Caco-2 cell, and PCA was carried out on these spectra. We would expect different areas of the cell to vary in their DNA, protein and lipid content, and there would therefore be differences in the spectra from these regions. We therefore see a clear separation in the PCA-scores plot (figure 2.6A), with spectra taken from DNA-rich areas of the cell falling on one side of the plot, and spectra from protein-rich areas on the other side of the plot. This separation occurs along the x-axis of the plot, which corresponds to PC1. If we want to investigate which peaks in the spectra

cause this separation, we can examine the PC1 loadings plot (figure 2.6B). This shows it is a mixture of DNA (780 cm^{-1}, 1090 cm^{-1}), protein (1300 cm^{-1}, 1660 cm^{-1}), and lipid (1450 cm^{-1}) peaks that are causing the separation in the PCA-scores plot.

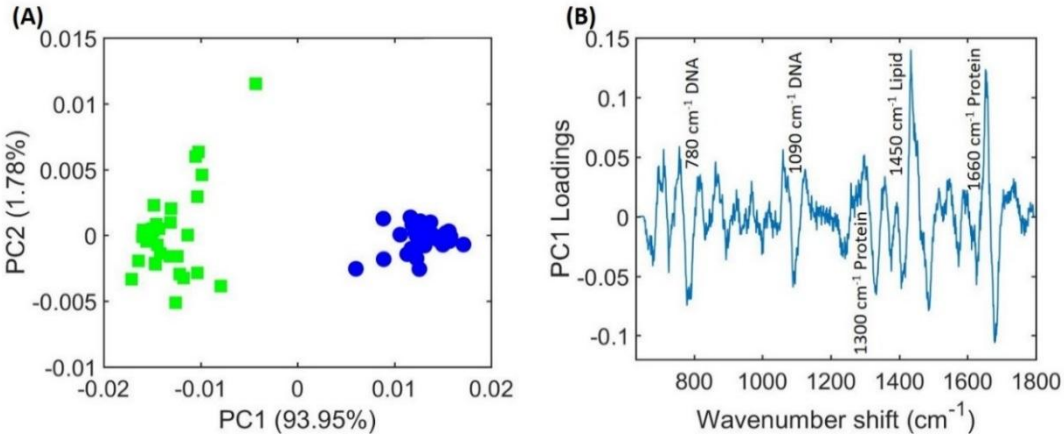

Figure 2.6: A comparison of spectra taken from DNA-rich and protein-rich areas of a single Caco-2 cell. **(A)** PCA-scores plot of PC1 against PC2 for spectra taken from either the nucleus (blue, circles) or cytoplasm (green, squares) of a Caco-2 cell. **(B)** PC1 loadings plot.

For subsequent PCA, MATLAB software version 2016 (The MathWorks, MA, USA) was used to extract spectra from collected Raman maps. These spectra were treated (cosmic rays removed, normalised and noise filtered). As the noise filter function in WIRE 4.2 uses PCA to eliminate data variance that cannot be attributed to real or significant data, we wanted to ensure that this did not have an effect when carrying out PCA, as the data would have technically undergone the process of PCA twice. To test this, we extracted the same spectra used in figure 2.6, but from a map that had undergone only cosmic ray removal and normalisation, in order to compare the PCA-plots and PC1 loadings.

Figure 2.7 shows these two plots. The separation is the same in both, with spectra taken from the cytoplasm falling on the left side of the plot, and spectra from the nucleus located on the right. The PC loadings are also very similar, showing the same peaks changing to cause the separation. The only real difference between the two plots is the percentage variance, which

is the percentage by which PC1 and PC2 contribute to the overall variance of the data. For the original PCA-scores plot, carried out on data that had been noise filtered (figure 2.7A), the percentage variance for PC1 is very high (93.95%), whereas in figure 2.7C, which used spectra that had not been noise filtered, the percentage variance for PC1 is 19.96%, which is siginificanlty lower. However, this is likely to be due to the amount of noise present in the spectra used. The plots were therefore considered to be similar enough that it was acceptable to carry out PCA on data that had been noise filtered.

As many of the individual spectra within the Raman map consist of background rather than any cellular material, in all subsequent PCA, only a small number of spectra were used as opposed to using every spectrum in the maps. Ten spectra were taken from areas identified as having a high DNA content, and ten from areas with a high protein content from Raman maps for all plots. This number was chosen as it is representative of the area chosen but isn't such a large number of spectra that it over complicates analysis when several cells are plotted together. Six principal components were calculated each time, and all PCA-scores and loadings plots were created using MATLAB.

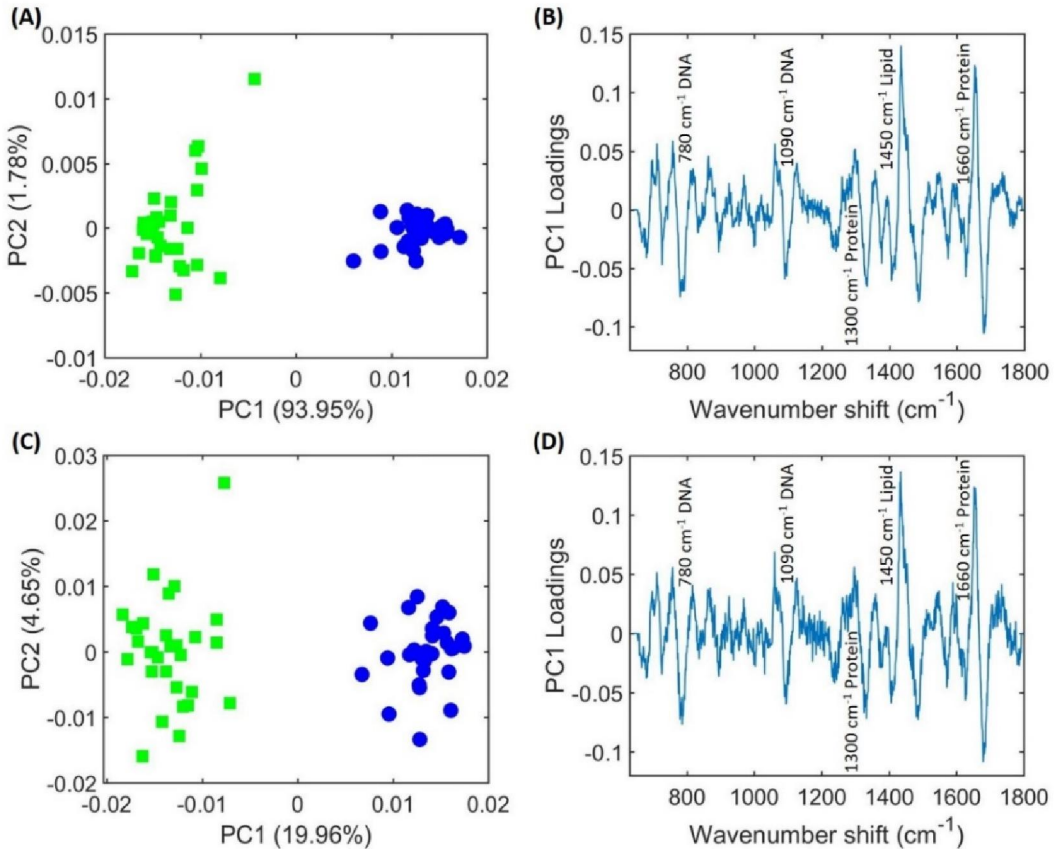

Figure 2.7: A comparison of PCA. PCA-scores plot of PC1 against PC2 for either noise filtered **(A)** or non-noise filtered **(C)** spectra taken from either the nucleus (blue, circles) or cytoplasm (green, squares) of a Caco-2 cell. **(B)** PC1 loadings plot for the PCA-scores plot in **(A)**. **(D)** PC1 loadings plot for the PCA-scores plot in **(C)**.

2.4 Vehicle Control

A vehicle control is required in studies in which a substance is used as a vehicle for a solution of the experimental compound. Using a vehicle control ensures that any effects seen are a result of the compound itself and not the vehicle it is dissolved in. The cannabinoid drugs CBD and AEA are dissolved in ethanol. Ethanol can disrupt the physical structure of cell membranes (Goldstein, 1986) and can be used as a fixative, and is therefore known to have an effect on cells. In order to ensure that the concentration of ethanol present in the final drug solutions of 1 and 10 µM used in experiments did not have a detrimental effect on cells, cells were treated with a matched concentration of ethanol or media control. Cells were treated with

either ethanol (vehicle control) or media (control) for a period of 6, 8 and 24 hours before they were mapped using Raman spectroscopy.

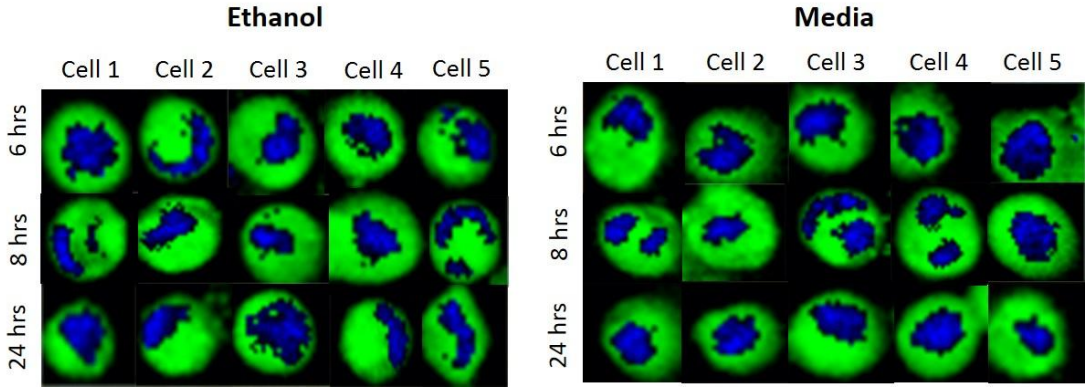

Figure 2.8: Raman maps showing the DNA and protein content of cells treated with either ethanol or media for a period of either 6, 8 or 24 hours. DNA (blue) was measured using the region 780-802 cm^{-1} and protein (green) using the region of 1630-1680 cm^{-1}.

The Raman maps (figure 2.8) showed that there was little visible difference between cells treated with ethanol and control cells, which suggested that the vehicle control has little effect on Caco-2 cells in the measured regions. To further confirm this, PCA was carried out on data taken from each of the above maps, in areas identified as the nucleus and the cytoplasm.

The PCA data shows that at all three time points, there is no clear separation between cells treated with the vehicle and control cells, as all points group together (figure 2.9). There is a larger variance in PC2 in addition to PC1 in these plots; this is likely to correspond to differences between cells rather than the effect of ethanol, as little separation can be observed. This lack of separation suggests that there is little difference in the spectra of cells treated with ethanol in comparison to control cells, suggesting that ethanol is not inducing a significant change in Caco-2 cells. It is therefore unlikely that ethanol, at the concentration present in the final drug concentrations that was used in the following experiments, has any effect on the Raman spectra of Caco-2 cells. Based on these results, we decided not to carry out both vehicle controls and controls, and just one of them was necessary.

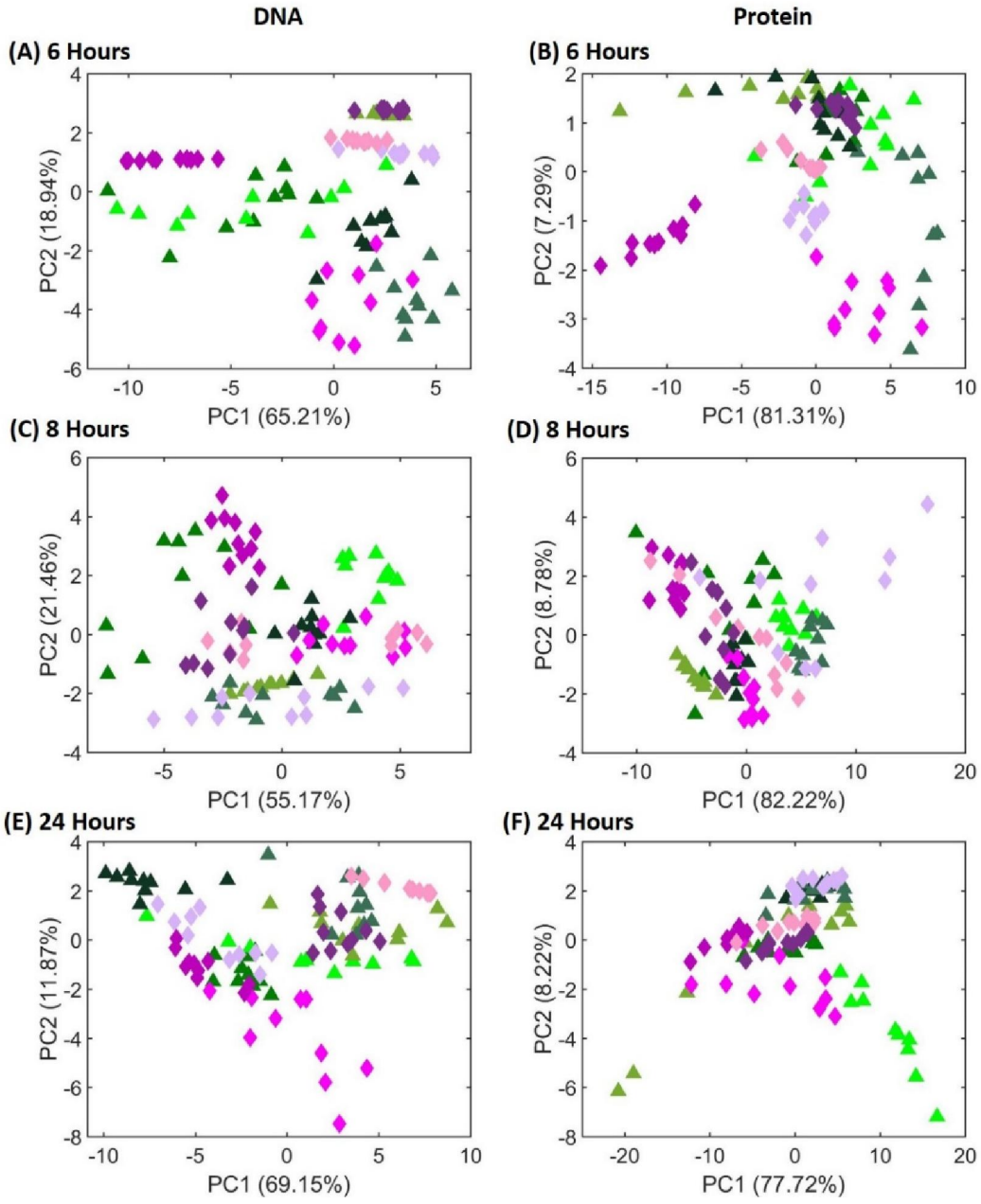

Figure 2.9: A comparison of Caco-2 cells treated with ethanol or media control after 6, 8 and 24 hours of treatment. Spectra were taken from regions of the cell identified as having a high DNA content after an incubation time of either 6 **(A)**, 8 **(C)** or 24 **(E)** hours, or from regions with a high protein content after either 6 **(B)**, 8 **(D)** or 24 **(F)** hours of incubation. Triangles represent cells treated with ethanol and diamonds cells treated with a media control. Each colour represents an individual cell.

2.5 Live Cell Raman:

To carry out live cell Raman spectroscopy, cells were seeded onto CaF_2 windows and returned to the incubator to adhere overnight. The following day, media was removed and replaced with 2.7 mL of 1 % serum media, and cells were transferred to the Raman incubator (figure 2.10) and maintained at 37 °C and 5 % CO_2. Cells were allowed to settle for ~1 hour before they were mapped. After the initial pre-treatment maps had been collected, 300 µL of a pre-warmed complex or drug solution of either CBD or AEA in media was added to the media to make a final concentration of 100 µg/mL or 10 µM, respectively. Cells were immediately mapped at the 0 hour timepoint, and over several hours following treatment before they were removed from the incubator.

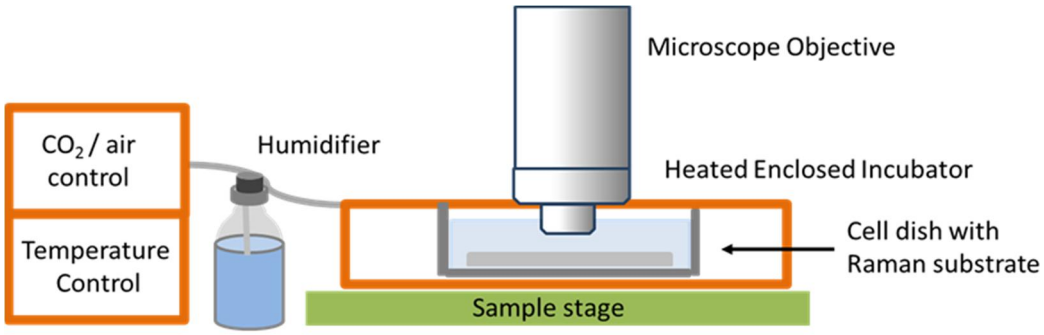

Figure 2.10: Diagram of a live-cell incubator for Raman spectroscopy (Smith, Wright and Ashton, 2016).

Control maps were taken to establish that there was no deterioration or loss of viability in cells over time in response to repeated exposure to the laser (figure 2.11). Maps were taken at regular intervals over different time periods, in order to determine that this did not influence the cells response over time. For all live cell maps, the timings are approximate, as it is not possible to map more than one cell at the same time on the same disk. Cell 1 can be mapped at '0 hours', but as maps can take 10-20 minutes, the timepoint of the second cell will reflect this and therefore is only an approximation.

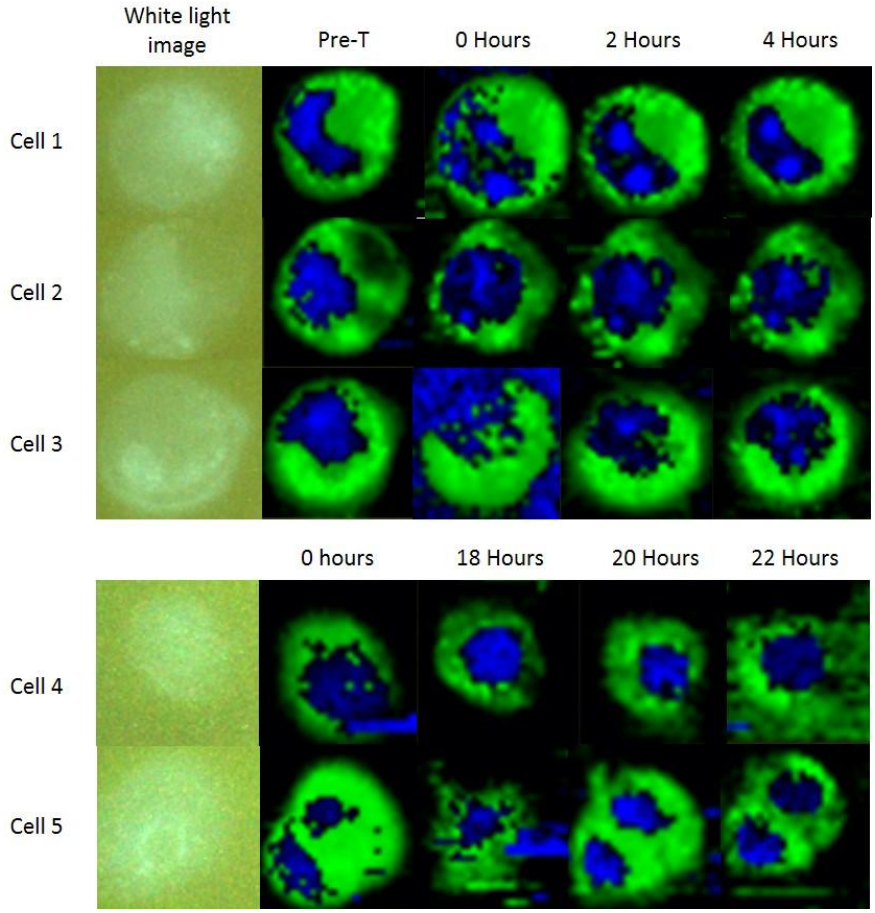

Figure 2.11: Raman maps showing the DNA (780-802 cm^{-1}, blue) and protein (1630, 1680 cm^{-1}, green) content of live control Caco-2 cells. Cells were mapped at either 0, 2 and 4 hours, or 0, 18, 20 and 22 hours. Pre-treatment (Pre-T) maps were collected in order to ensure that control cells were mapped an equal number of times as treated cells.

Control cells were mapped a total of four times, and the Raman maps do not appear to show any clear visible differences or deterioration over either time period, with maps of the same cell looking very similar in both the first and final maps. The cytoplasm of cell 5 at 18 hours appears to have degraded, but as this is not also seen at 20 hours, it is likely that this is due to the quality of the map, and not the destruction of the cell. As the cells were live, they have the potential to move whilst mapping is taking place, which can result in the end map being lower in quality than when the cell remains in place. Shorter acquisition times reduce the risk of this occurring, but it is still a possibility with each map collected. To confirm there were no biochemical changes in these cells over time, PCA was also carried out on collected data.

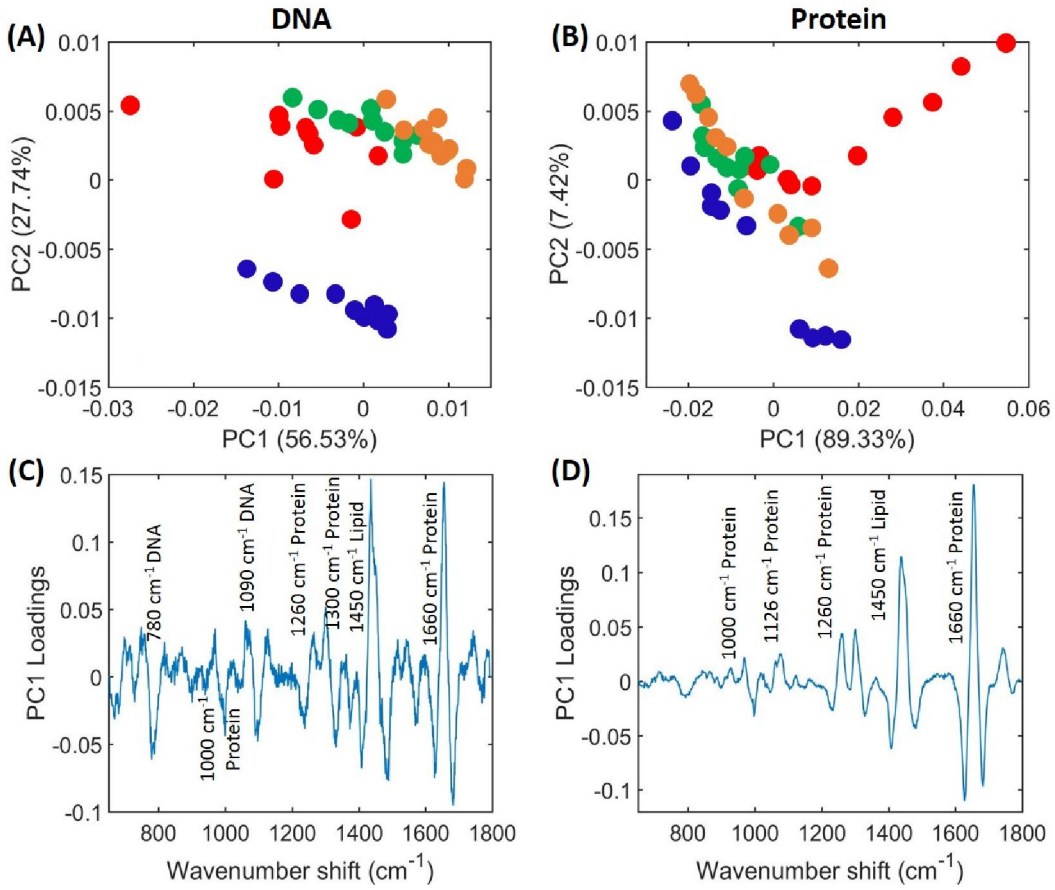

Figure 2.12: A comparison of live control cells mapped from pre-treatment to 4 hours. For PCA-scores plot of PC1 against PC2, spectra were taken from the regions of the cell identified as having a high DNA **(A)**, or protein **(B)** content. Cell spectra were taken from cell 3 (figure 2.11), which was mapped at 'pre-treatment', 0, 2 and 4 hours. Blue indicates pre-treatment cells, red 0 hours, green 2 hours and orange 4 hours. The PC loadings for each condition are shown below.

The PCA-scores plots show some separation in spectra taken from either the nucleus or the cytoplasm of cells. The spectra taken from the pre-treatment map appear to separate slightly from the other timepoints, but there is little separation at the other timepoints over 4 hours of mapping (figure 2.12A and B). Over 22 hours (figure 2.13A and B), again the pre-treatment spectra separate slightly, although this would be expected as the second map took place 18 hours later, and the cell is likely to have changed slightly in that time. There is also some separation at 22 hours. The PC loadings plots show changes mainly across lipid and protein peaks, indicating changes in the levels of these over time, which would be expected as the cell

will change throughout mapping. Overall, the PCA results suggest that there is little deterioration in live cells that have been mapped over these two time periods, indicating that live cell Raman spectroscopy is suitable for mapping the same single cell at least four times without causing any visible damage.

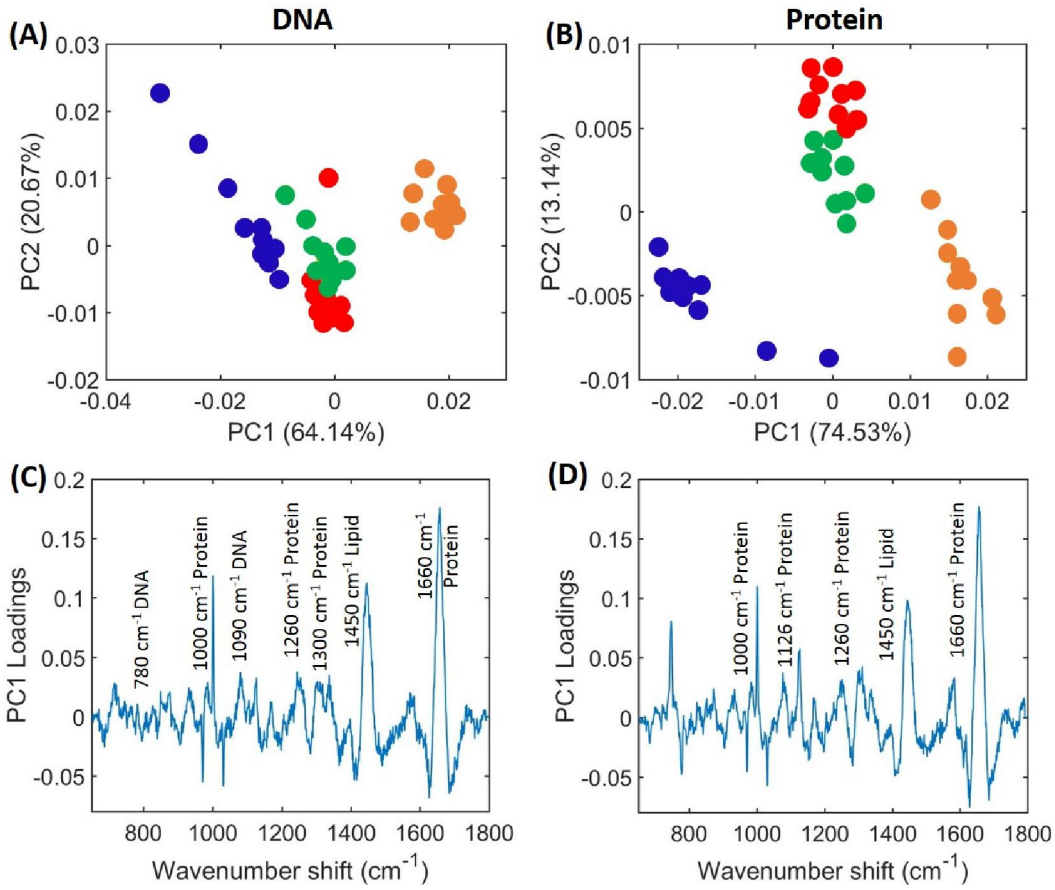

Figure 2.13: A comparison of live control cells mapped from 0 to 22 hours. For PCA-scores plot of PC1 against PC2, spectra were taken from the regions of the cell identified as having a high DNA **(A)**, or protein **(B)** content. Cell spectra were taken from cell 4 (figure 2.11), which was mapped at 0, 18, 20 and 22 hours. Each colour represents a different time point. Blue indicates the cell at 0 hours, red at 18 hours, green at 20 hours and orange at 22 hours. The PC loadings for each condition are shown below.

2.6 Conclusion

In summary, we have developed a suitable methodology for collecting Raman maps of both live and fixed Caco-2 cells. We discovered that these cells do not freely adhere and grow on

CaF_2 windows, so in order to do this we coated the windows with poly-lysine to aid cell attachment. The fixatives methanol and ethanol were not suitable for use with Caco-2 cells but treating cells with 4 % PFA for 20 min at room temperature was effective. Raman spectra were collected with an acquisition time of 1 second and a step size of 1 µm, to give the best trade-off between the quality of the resulting Raman map and the time spent mapping each single cell. Live cell Raman spectroscopy was carried out using a cell top incubator to maintain cells at 5 % CO_2 and at 37 °C; the metal complex or drug solutions were then added directly to the cell culture media and the cells response mapped over several hours. All spectra underwent the pre-processing steps of cosmic ray removal, noise filtering, and normalisation in order to reduce background noise. Once this had been carried out, Raman maps could be created by using distribution plots to shade the spectral regions of 780-802 cm^{-1} for DNA, and 1630-1680 cm^{-1} for protein. Spectra were also used to carry out PCA, which was done using second derivative spectra. Once a suitable methodology had been established, we moved on to introducing substances into cells in order to see what effect they had.

Chapter 3: Mitochondrial detection in Caco-2 cells using Raman spectroscopy and a rhenium complex

3.1 Introduction

Rhenium complexes are good candidates for biological imaging agents as they are stable, non-toxic, and have been shown to be taken up by several cell lines. They have previously been used with leukocytes (Stephenson *et al.*, 2004), pancreatic cancer cells (Raszeja *et al.*, 2017), HeLa cells (Louie *et al.*, 2011), and breast cancer cells (Amoroso *et al.*, 2008). In addition to visualising cells and components of cells such as the nucleus (Mari *et al.*, 2012), complexes can also be targeted to specific receptors (Stephenson *et al.*, 2004), making them a valuable imaging tool as cells do not need to be labelled prior to imaging.

All of the previous studies used fluorescence microscopy in order to visualise the complexes within cells, but Raman spectroscopy has also been used to image metal complexes within cells. Raman spectroscopy has been used to monitor the uptake, localisation and retention of a complex in lung adenocarcinoma cells (Feofanov *et al.*, 2000), and the intracellular localisation of metal-carbonyl complexes has also been studied in living cells (Meister *et al.*, 2010). However, little work has been done using Raman spectroscopy to visualise rhenium complexes within cells. This study therefore aims to show the potential of Raman spectroscopy to map the uptake and intracellular distribution of a rhenium complex within Caco-2 cells, and also to establish the use of Caco-2 cells as a suitable model for mapping single cells using Raman spectroscopy.

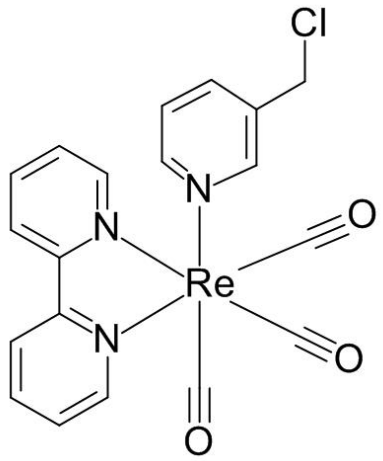

Figure 3.1: Molecular structure of the rhenium complex used in all experiments.

The specific complex used for experiments was 3-Chloromethylpyridyl bipyridine *fac*-tricarbonyl rhenium. This complex has been previously shown to accumulate within cells with a low toxicity, and target the mitochondria of cells (Amoroso *et al.*, 2007). This is because it contains a chloromethyl group, which provides thiol reactivity, and thiol reactive compounds accumulate in healthy mitochondria due to the presence of reduced thiols within these organelles (Fernández-Moreira, Thorp-Greenwood and Coogan, 2010; Lee, Leung and Lo, 2017). As previously discussed, some Raman studies have claimed to be able to visualise the mitochondria by shading to a peak corresponding to cytochrome c (Matthäus *et al.*, 2007; Okada *et al.*, 2012; Ichimura *et al.*, 2014). However, we were unable to do this by shading to the same peak as there was an overlap with the nucleus of cells, and this suggested that this peak is not suitable, in these cells, for visualising the mitochondria (chapter 2, section 2.3.3). As such, this complex was an ideal candidate for an alternative way to image the mitochondria of these cells.

3.2 Methods

3.2.1 Cell treatment

Caco-2 cells were cultured and attached to CaF_2 windows as described in the methods (chapter, section 2.2.2). Once cells had adhered to CaF_2 windows, media was removed and replaced with media containing the rhenium complex at a concentration of 100 µg/mL. After 2 or 4 hours of incubation, media was removed and cells were fixed as previously described.

3.2.2 Raman spectroscopy of fixed cells

Fixed cells were maintained in PBS throughout analysis. Raman maps were collected as described in the methods (chapter 2, section 2.2.4), using a laser wavelength of 532 nm.

3.2.3 Raman spectroscopy of live cells

Once adhered to CaF_2 windows, cells were transported to the Raman incubator and maintained at 5 % CO_2 and 37 °C. In this study, all live cells were mapped using a laser wavelength of 532 nm. Control maps were acquired by mapping the same cell over time to ensure there was no loss of viability (chapter 2, section 2.6). For the complex study, media was removed once cells were in the Raman incubator, and replaced with media containing the complex at a concentration of 100 µg/mL. Cells were then mapped at the times described.

3.2.4 Raman maps and data analysis

All Raman maps were pre-processed and shaded in WIRE 4.2 as described (chapter 2, section 2.3.3). PCA plots were created in MATLAB software version 2016 (The MathWorks, MA, USA).

3.3 Results

3.3.1 Raman maps of fixed cells

The overall aims of this study were to develop the imaging of Caco-2 cells, and to determine if Raman spectroscopy could be used to visualise the rhenium complex within Caco-2 cells. The

first stage in this process was acquiring a Raman spectrum of the complex, in order to see if there were any peaks within this spectrum that would be suitable for shading Raman maps. This spectrum is shown in figure 3.1A, alongside a typical cell spectrum (figure 3.1B), and shows several peaks of interest, most noticeably at 1035 cm^{-1}, 1317 cm^{-1}, 1493 cm^{-1} and 1604 cm^{-1}, and smaller peaks at 664 cm^{-1} and 785 cm^{-1}. The structure of the complex is shown in figure 3.2 and can be used to assign some of these peaks to the vibrational modes of the molecules within it.

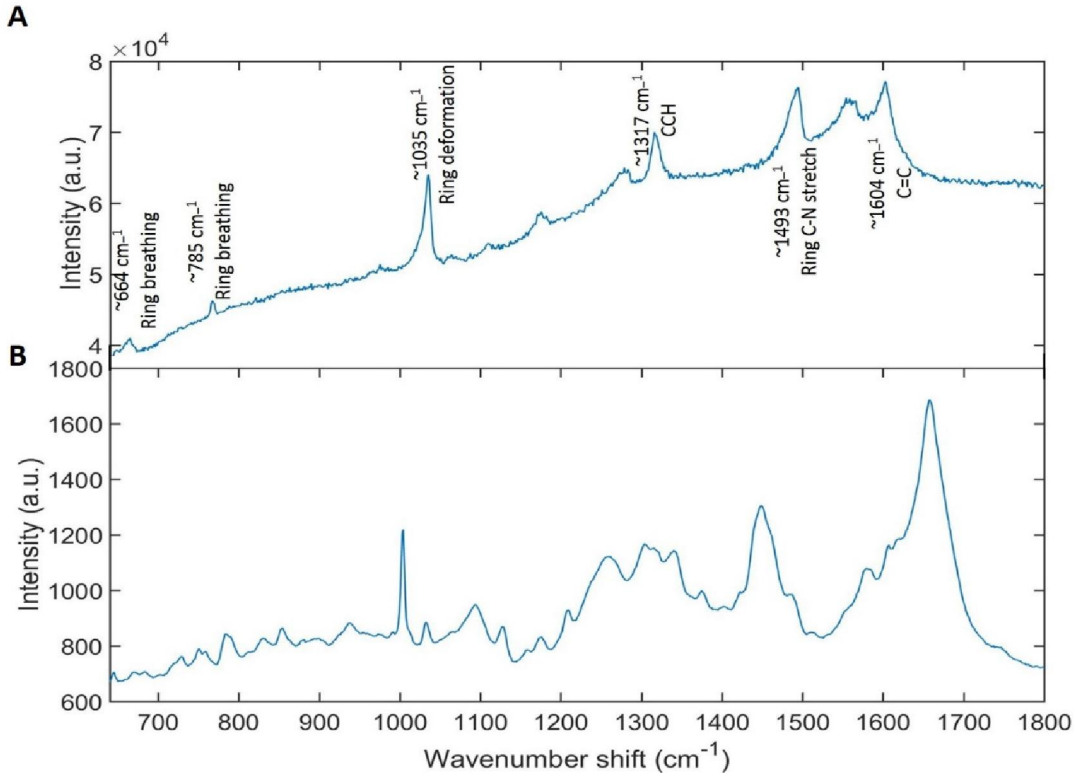

Figure 3.2: A comparison of Raman spectra of the rhenium complex and a typical cell spectrum. **(A)** Raman spectrum of the rhenium complex in a solution of DMSO, spotted and left to dry on a CaF_2 window. This spectrum was acquired using a 532 nm wavelength excitation laser, acquisition time of 4 seconds and a laser power of ~30 mW. **(B)** Raman spectrum of a fixed Caco-2 cell treated with the rhenium complex for 2 hours. This spectrum was acquired using a 532 nm wavelength excitation laser, acquisition time of 1 second and a laser power of ~30 mW. The concentration of the complex in both cases was 100 µg/mL.

Peaks at ~1035 cm^{-1} have been associated with ring deformations (Deshmukh *et al.*, 2016), at 1317 cm^{-1} with CCH in plane bending (Boyaci *et al.*, 2015), and at 1493 cm^{-1} with a ring C-N stretch (Martin, Wartell and O'Shea, 1978). A peak at ~1604 cm^{-1} has been previously attributed to C=C bonds, which are found within the ring structure (Jallapuram *et al.*, 2008). The peaks at 664 cm^{-1} and at 785 cm^{-1} are also associated with ring breathing (Benevides *et al.*, 1997) (Kann *et al.*, 2015). Aside from 664 cm^{-1}, all of these peaks fall within the range of wavenumbers used for biological studies (figure 3.1B), which could lead to complications with analysis, as they could be overshadowed by cellular components. In order to assess the potential of these peaks in determining the intracellular distribution of this complex within cells despite these difficulties, Raman maps were shaded to each of these peaks (figure 3.3). In the initial study, Raman maps were collected of fixed cells that had been incubated with the complex for a period of either 2 or 4 hours before fixation.

Prior to shading to the complex peaks, Raman maps were first shaded to show the DNA and protein distribution within the cell (figure 3.3). In order to do this, distribution plots were used to ensure that shading parameters were kept the same for each cell. The values chosen to shade each map are indicated by the red box for each distribution plot; for both regions, values under 0 were excluded because these correspond to background noise. DNA was measured from 780-802 cm^{-1}, and the first stage in shading all maps was to determine the maximum value to shade to. For some maps, e.g. figure 3.3B, they could simply be shaded to the maximum value of the map, but for others, the uppermost values had to be excluded, as they corresponded to material outside of the cell (red circles). Once this upper boundary had been determined, maps were shaded to the top 60% of values, calculated by multiplying the upper boundary value by 0.4 to determine the lower boundary for that map. For the protein region (1630-1680 cm^{-1}), this process was simpler, as maps were shaded to the middle values, after exclusion of the highest and lowest values.

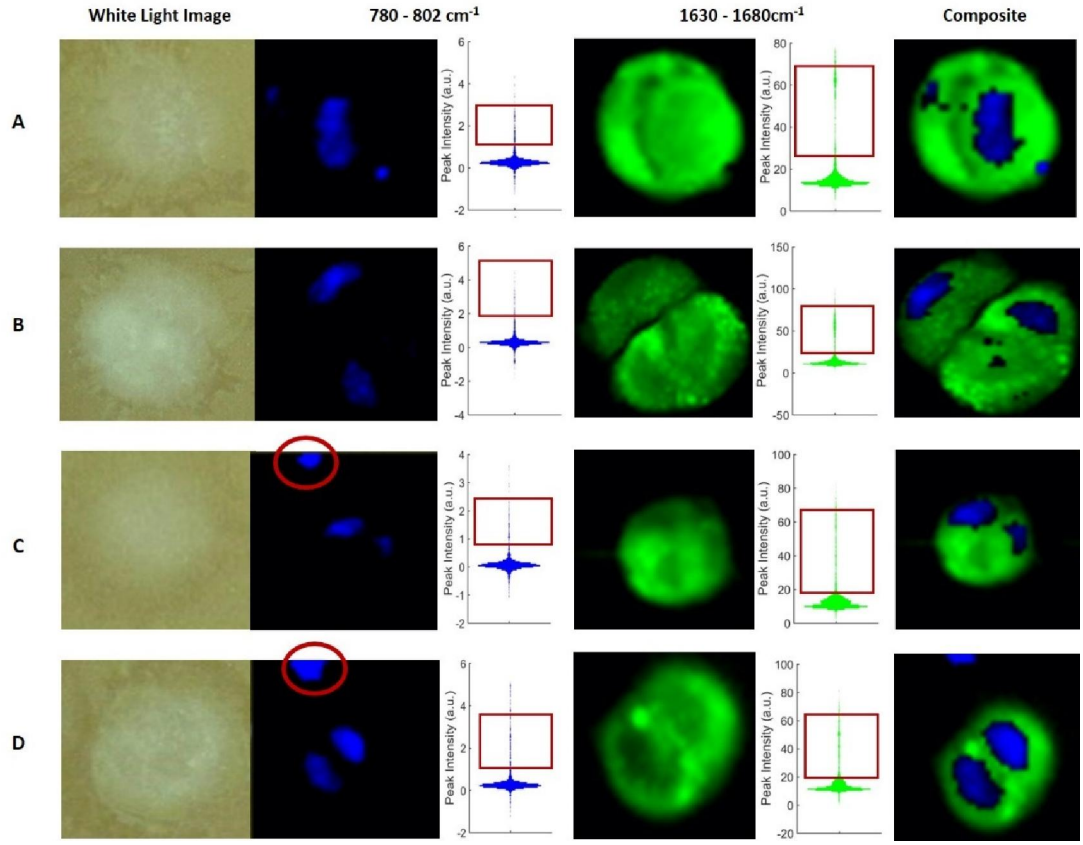

Figure 3.3: An example of shading Raman maps of single Caco-2 cells. Cells were treated with either the rhenium complex for (**A**) 2 hours or (**B**) 4 hours or DMSO control for (**C**) 2 hours or (**D**) 4 hours. DNA content was measured from 780-802 cm^{-1} and protein content from 1630-1680 cm^{-1}. The distribution plots for each area are shown, and the region shaded indicated by the red box. The red circles indicate anomalies that are discussed in the text.

Once composite maps had been created, maps could also be shaded to the peaks of interest from the rhenium complex spectrum (figure 3.4). They were also shaded to an additional peak at 1740 cm^{-1} which was from a region of background noise. All peaks were shaded using peak area, as this discounts the background noise from the axis to the peak height as spectra were not baselined before maps were created. The ranges used to shade each peak were as follows: 663-665 cm^{-1} (664 cm^{-1}), 784-786 cm^{-1} (785 cm^{-1}), 1034-1036 cm^{-1} (1035 cm^{-1}), 1316-1318 cm^{-1} (1317 cm^{-1}), 1492-1494 cm^{-1} (1493 cm^{-1}), 1603-1605 cm^{-1} (1604 cm^{-1}) and 1739-1741 cm^{-1} (1740 cm^{-1}).

The Raman maps show that, out of the six selected peaks and using these shading parameters, four of them (664 cm^{-1}, 1317 cm^{-1}, 1493 cm^{-1} and 1604 cm^{-1}) cannot be attributed to the rhenium complex, as they show an intracellular distribution in both treated and control cells. These complex peaks are therefore likely to have been overshadowed by cellular components due to the overlap mentioned previously.

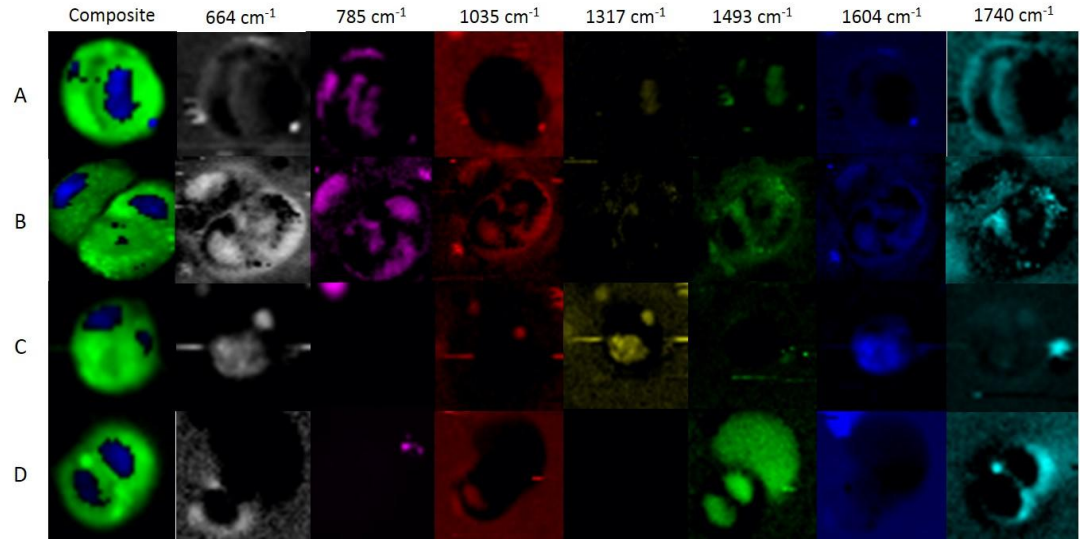

Figure 3.4: Raman maps shaded to peaks of interest from the rhenium complex spectrum. Cells were treated with either 100 µg/mL of the rhenium complex for (**A**) 2 hours or (**B**) 4 hours or DMSO control for (**C**) 2 hours or (**D**) 4 hours. The concentration of the complex added to cells was 100 µg/mL, and a 0.01% concentration of DMSO was used as a vehicle control. For the composite images, DNA content was measured from 780-802 cm^{-1} and protein content from 1630-1680 cm^{-1}. When shading to the peaks of interest from the rhenium complex spectrum, for all seven selected peaks, maps were shaded from 0 to max.

The 785 cm^{-1} and 1035 cm^{-1} peaks appear to have more potential. The peak at 785 cm^{-1} appears to show a spatial distribution within cells treated with the complex at both 2 and 4 hours, and does not seem to be found within control cells. It does appear to be seen around the edges of the cell in the two controls, so it is possible that this peak may not correspond to the complex. However, if this peak corresponded to a part of the cell such as DNA or protein, we would expect to also see it within control cells and not only around the edges. It could therefore be

attributed to something on the slide within these two maps, or could be due to background noise. The distribution plots for this peak (figure 3.5) show that the intensity is lower in the two control cells in comparison to the two treated cells.

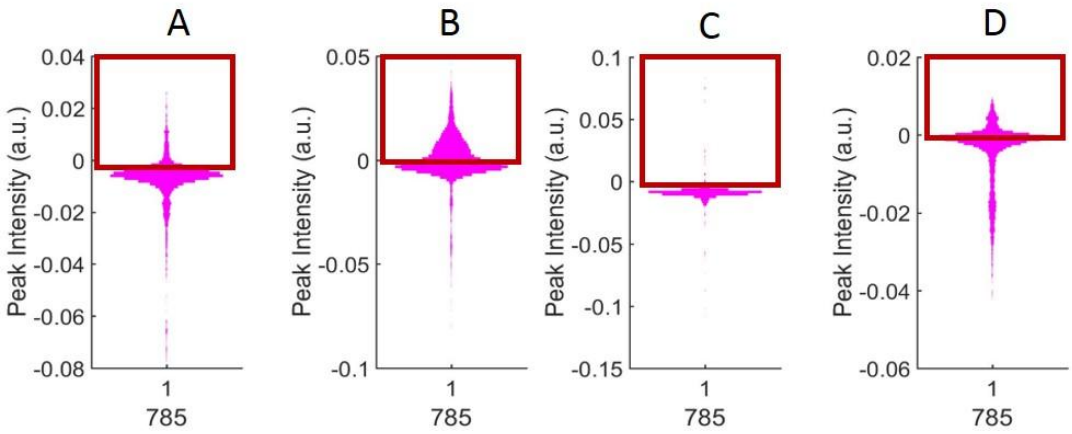

Figure 3.5: Distribution plots of the 785 cm^{-1} peak. Cells were treated with either the rhenium complex for (**A**) 2 hours or (**B**) 4 hours or DMSO control for (**C**) 2 hours or (**D**) 4 hours. The red box indicates the region shaded, which was 0 to max in all four cells.

For 1035 cm^{-1}, there is no distribution within the cell at 2 hours, but by 4 hours there does appear to be some accumulation within the cell, which may indicate the presence of the complex. In the controls, shading to this peak shows no intracellular distribution, although the map at 4 hours appears to be very similar to the map of the treated cell at 2 hours. Again, this could indicate that this peak may not correspond to the rhenium complex, but the peak does not have a high intensity within untreated cells so it is unlikely to correspond to another molecule found within the cell. Looking at the maps shaded at 1740 cm^{-1}, an area of noise with no peaks present in the Raman spectrum of either cells or the complex itself, there still appears to be some shading of the cell across all four maps. This indicates that, even when the intensity is very low and there are no spectrum peaks, maps can still show features of the cell, and this could be what is happening in the control cells or even in treated cells, as the relative intensity of each peak analysed is low, and demonstrates the complications in trying to pick out peaks representing the rhenium complex in a complicated cell spectrum.

Overall, these initial maps suggest that the peaks of 785 cm^{-1} and 1035 cm^{-1} are the most useful in trying to determine the intracellular distribution of the rhenium complex within Caco-2 cells. In figure 3.4, all of the maps were shaded from 0 to maximum for the complex peaks, which eliminates some of the background noise and begins to show some features within the cell. However, this shading range may not be the most appropriate for showing the intracellular distribution of the complex within Caco-2 cells (Ashton, Hollywood and Goodacre, 2015). In order to investigate this further, the shading range of all peaks were altered to see if a different shading range was more appropriate.

Figure 3.6 demonstrates how adjusting the shading range can affect the final Raman map. The distribution plot is shown for the 785 cm^{-1} peak for each map, with different areas highlighted to demonstrate how shading to these values can drastically change the final image of the cell. Careful consideration of shading range is particularly important when shading to try and visualise a compound within the cell, as there is the potential for overinterpretation of the results. For example, applying a shading range of minimum to maximum, containing all of the values in the map, appears to show a high distribution of the 785 cm^{-1} peak both within and outside of the cell, in all four maps; this can also be seen when shading from 5-95 % of the values.

Shading from 0 to maximum eliminates some of the background values that are likely to be noise, but this is not necessarily the best range to apply. The distribution plots show the intensity of the chosen peak throughout the whole cell, and the widest part of the plot is likely to be where all of the background is located. This is not necessarily always below 0, as the shape and intensity of the values can vary for each Raman map, so applying a different lower boundary may be more appropriate. Eliminating all but the highest values does not show any distribution within the cell, suggesting that this is also not a suitable range to use.

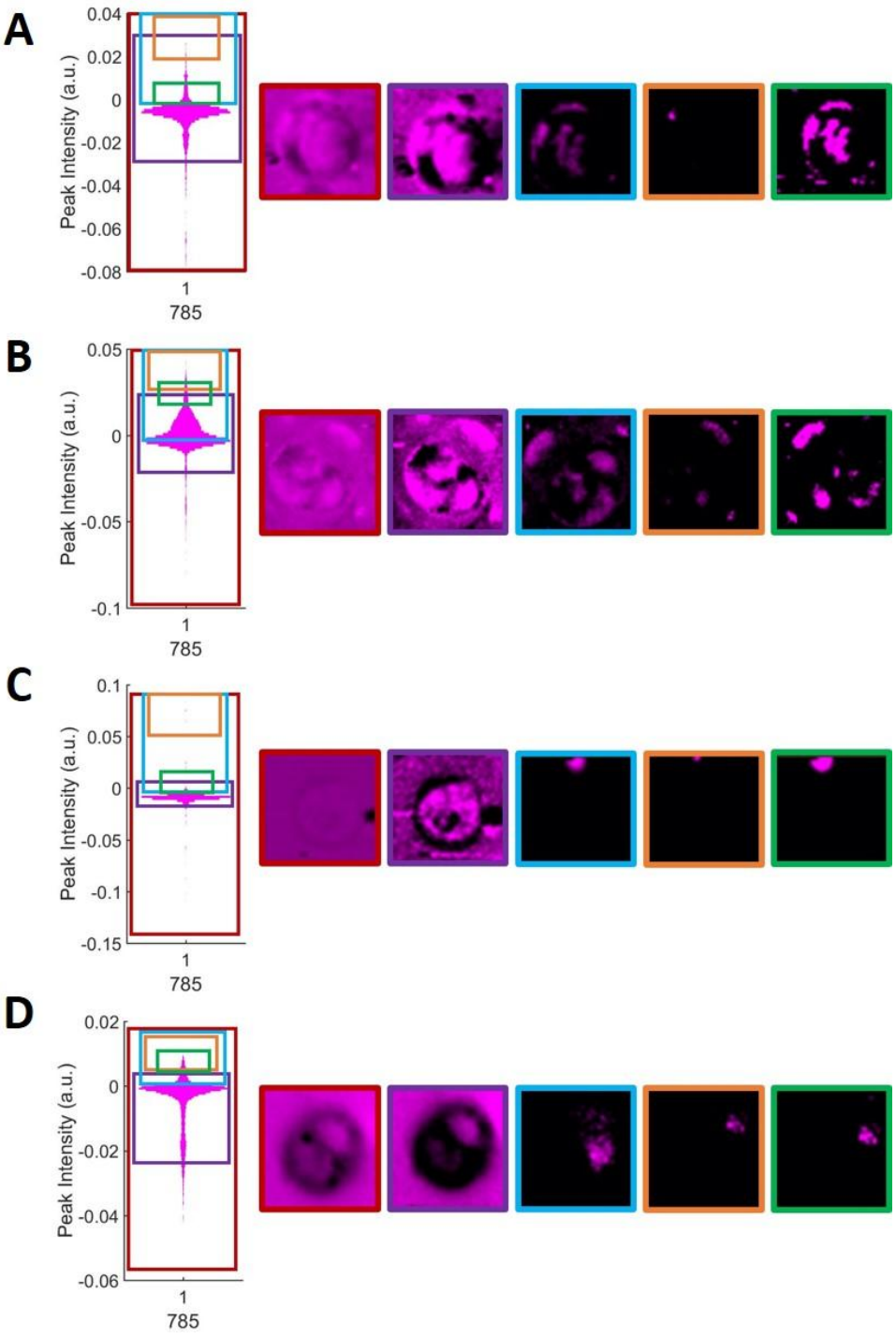

Figure 3.6: Distribution plots and Raman maps of the 785 cm^{-1} peak, demonstrating how different shading ranges can affect the map. (A) Cell incubated with the complex for 2 hours, **(B)** cell incubated with the complex for 4 hours, **(C)** cell incubated with DMSO control for 2 hours, **(D)** cell incubated with DMSO control for 4 hours. The shading ranges are as follows: minimum to maximum (red box), 5-95 % (purple), 0 to max (blue), highest values (orange) and chosen range for the final image (green). The corresponding Raman map is outlined in the same colour.

In contrast, shading to a small subset of values, eliminating both the highest and lowest values in the map, shows a clear intracellular distribution of this peak within the cell. This range can be kept consistent across all of the maps by using the shape of the distribution plot, rather than a specific value or percentage, and appears to be the most appropriate shading range for this peak when compared to the other ranges tried.

The same principle was applied to the 1035 cm^{-1} peak, in order to find the most appropriate shading range. Again, shading from minimum to maximum, 5-95 % and the highest values are not appropriate for determining the potential intracellular distribution of the complex. Shading from 0 to maximum still includes a lot of the background noise values, as the widest part of the distribution plot for most of these maps lies above 0. Eliminating this background (yellow box) provides a better representation of areas of intensity within the cell; reducing this range to eliminate the highest values and using a similar range area to the 785 cm^{-1} peak appears to show a clearer picture of this peak within cells.

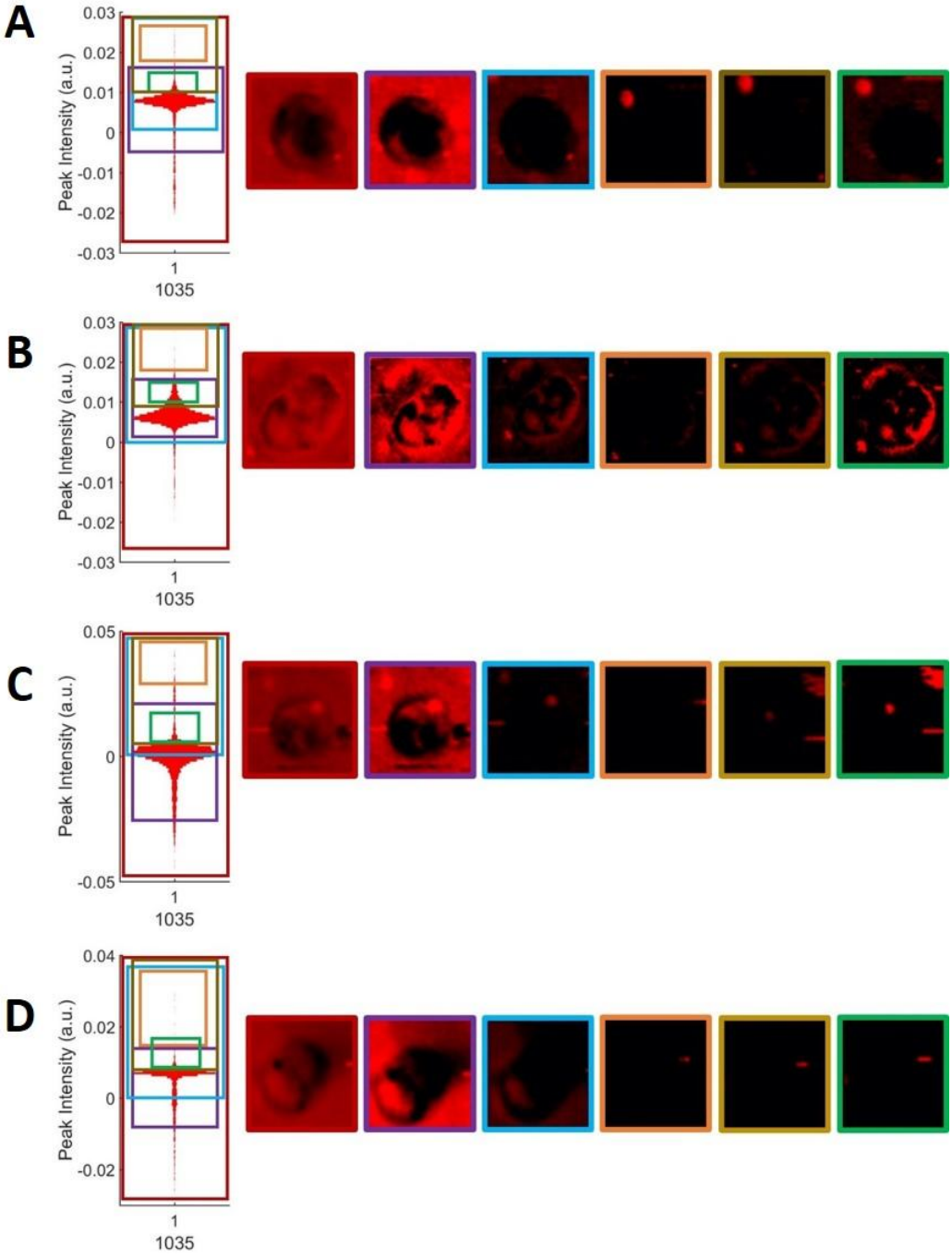

Figure 3.7: Distribution plots and Raman maps of the 1035 cm^{-1} peak, demonstrating how different shading ranges can affect the map. (A) Cell incubated with the complex for 2 hours, **(B)** cell incubated with the complex for 4 hours, **(C)** cell incubated with DMSO control for 2 hours, **(D)** cell incubated with DMSO control for 4 hours. The shading ranges are as follows: minimum to maximum (red box), 5-95% (purple), 0 to max (blue), highest values (orange), eliminating the background values in the widest part of the distribution plot and shading to max (yellow) and chosen range for the final image (green). The corresponding Raman map is outlined in the same colour.

Shading ranges were also altered for the additional complex spectrum peaks, in order to see if changing the shading range changed our earlier hypothesis that these peaks were not suitable for trying to visualise the complex within Caco-2 cells (appendix A). However, re-doing figure 3.4 with these new shading ranges still suggests that the 785 cm^{-1} and 1035 cm^{-1} peaks are the most suitable, as these are the only peaks visible within treated cells but not control cells. If these peaks both corresponded to the complex, we would expect their spatial distribution within the cell to overlap. However, the two peaks appear to localise to different parts of the cell, which may suggest that they do not both correspond to the complex. In order to investigate this further, once a suitable shading range had been chosen, four additional cells were shaded to the 785 cm^{-1} and 1035 cm^{-1} peaks in order to see if they could be used to visualise the complex within Caco-2 cells (figure 3.9).

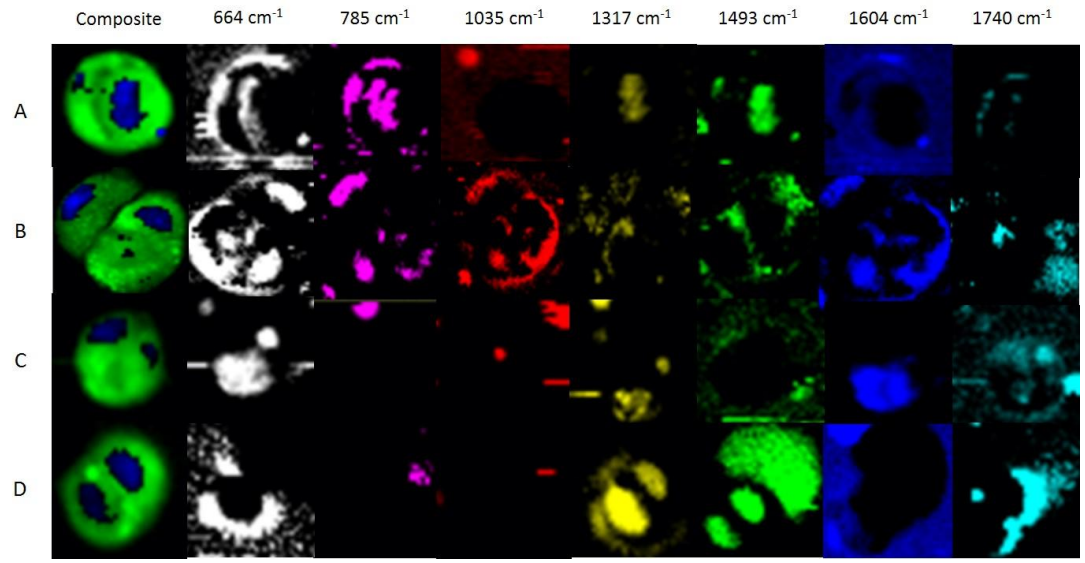

Figure 3.8: Raman maps shaded to peaks of interest from the rhenium complex spectrum, with the shading range adjusted. Cells were treated with either the rhenium complex for (**A**) 2 hours or (**B**) 4 hours or DMSO control for (**C**) 2 hours or (**D**) 4 hours. For the composite images, DNA content was measured from 780-802 cm^{-1} and protein content from 1630-1680 cm^{-1}. When shading to the peaks of interest from the rhenium complex spectrum, for all seven selected peaks, maps were shaded as specified above.

In all four maps, the peak at 785 cm^{-1} appears to correspond to something within the cell. However, for most of these maps, the distribution to this peak has some overlap with the DNA of the cell, which is unexpected if it corresponds to the complex, as it is expected to accumulate in the mitochondria of cells (Amoroso *et al.*, 2007, 2008), which are found in the cytoplasm. The peak of 785 cm^{-1} is known to be attributed to DNA (symmetric phosphodiester stretch and ring breathing modes of nucleic acids (Zhang *et al.*, 2012; De Angelis *et al.*, 2017; Farhane, Bonnier and Byrne, 2017), so it is possible that shading to this peak is picking up on the nucleic acid of the cell and not the complex. However, this peak did not shade the DNA of control cells (figure 3.4), so could pick out the presence of the complex within cells despite the overlap with DNA peaks.

In contrast, the peak at 1035 cm^{-1} does not appear to show an accumulation within cells after 2 hours of incubation, which is in line with what was seen in the previous cell. However, by 4 hours there is an intracellular distribution associated with this peak. Again, there is some overlap with the DNA regions of the cell, and this peak region can also be associated with the amino acid phenylalanine (Rehman, Movasaghi and Rehman, 2012; Zheng *et al.*, 2014; Charwat *et al.*, 2015; Gebrekidan *et al.*, 2018), which is found within cells. It is therefore difficult to determine if these maps are showing the presence of the rhenium complex within Caco-2 cells or are representative of other intracellular components. Overall, this demonstrates the difficulties of shading Raman maps, specifically in trying to shade to identify the presence of a compound within a cell when that compound's peaks fall within the wavenumber range assigned to cellular features.

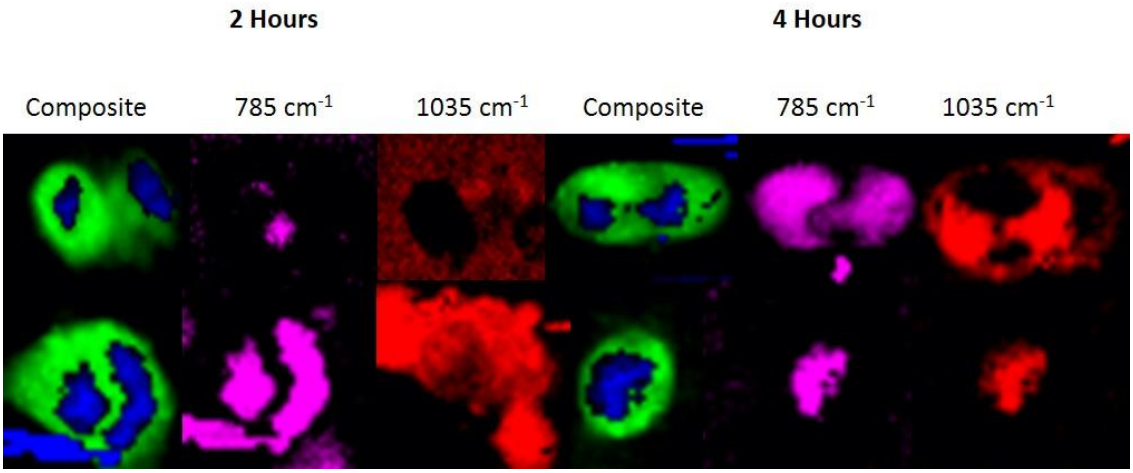

Figure 3.9: Raman maps of Caco-2 cells treated with the rhenium complex for either 2 or 4 hours, shaded to the peak at either 785 cm^{-1} or 1035 cm^{-1}. For composite images, DNA content was measured from 780-802 cm^{-1} and protein content from 1630-1680 cm^{-1}. For the selected peaks, cells were shaded as specified above.

3.3.2 Principal component analysis of fixed cells

In addition to being useful as an imaging method, Raman spectroscopy can also provide biochemical information about a sample. As previously discussed (chapter 2, section 2.3.4), PCA can be applied to distinguish trends between groups of spectra. In this study, PCA was used to compare spectra from cells treated with the complex and control cells, in order to see which peaks, if any, were changing between them. In previous studies, it has been reported that the rhenium complex was non-toxic, and that there was no loss of cell viability associated with the introduction of the complex into cells (Amoroso *et al.*, 2008). We would therefore expect to see little separation between treated and untreated cells, as if the complex was not affecting the cells, there should be no spectral differences between them.

However, complications can arise when comparing many cells in this way, as each cell is distinct from the others within a population (Altschuler and Wu, 2010), and as such can vary in response to stimuli, as well as in their DNA, lipid and protein content. The PC loadings will therefore contain a mixture of peaks corresponding to these variations between cells, and

peaks that are a result of the complex. In order to investigate which peaks are likely to correspond to cellular differences, PCA was applied to a group of control cells which showed little separation (figure 3.10). To create this plot, spectra were taken from DNA-rich and protein-rich region of control cells. The only differences are therefore due to differences between individual cells, and the PC1 loadings plot shows that several peaks show differences, including protein (1000 cm^{-1}, 1260 cm^{-1}, 1300 cm^{-1}, 1660 cm^{-1}) and lipid (1450 cm^{-1}) peaks from both regions, and additional DNA (780 cm^{-1}, 1090 cm^{-1}) peaks in regions of high nucleic acid content (figure 3.10C). Changes in these peaks reflect the fact that different cells contain different levels of DNA, protein and lipid. These loadings plots can therefore act as a benchmark, as if the same peaks are present in the PC loadings plots of cells incubated with the complex, it suggests that the complex does not have an effect on cells. In contrast, if there are different peaks present in the loadings plot, it indicates that those peaks are associated with an effect of the complex on cells. These benchmark plots were therefore plotted alongside all subsequent PC loadings plots.

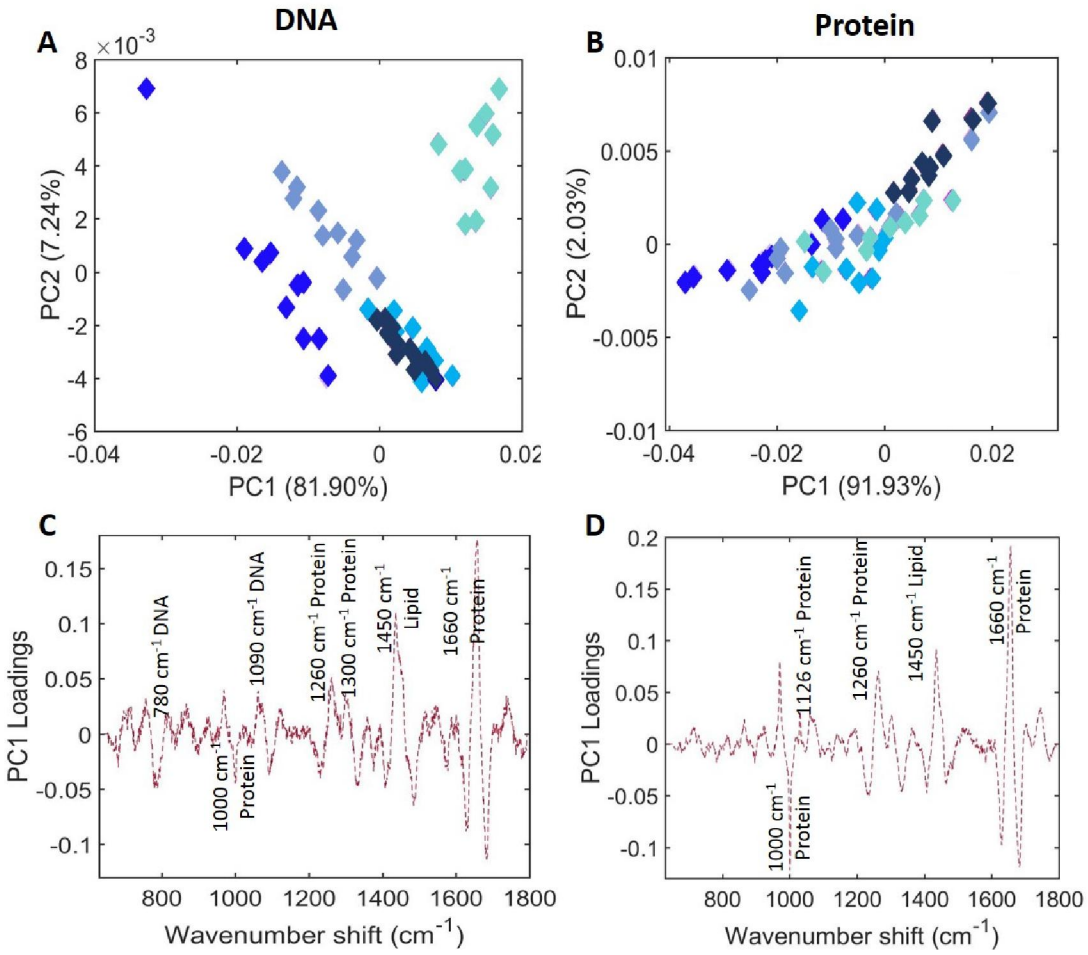

Figure 3.10: A comparison of control cells to create benchmark PC1 loadings. For PCA-scores plots of PC1 against PC2, spectra were taken from the regions of the cell identified as having a high DNA **(A)** or protein **(B)** content. The PC1 loadings for each plot are shown in **(C and D)**. Different colours indicate different cells (n=4).

The PCA scores plot in figure 3.11 shows spectra taken from areas of high DNA and protein in a mix of treated and untreated cells after 2 hours of incubation with the complex. In the protein PCA plot (figure 3.11B), there appears to be some separation along PC2, as cells incubated with the complex group towards the bottom of the plot, and control cells at the top. However, both the PC1 and PC2 loadings plots show peaks that overlap with the benchmark loadings, suggesting that any changes in these peaks are likely to be due to differences in protein and lipid content between individual cells, and not a result of the rhenium complex.

The rhenium complex therefore does not appear to have an effect on the cytoplasm of cells after 2 hours of incubation.

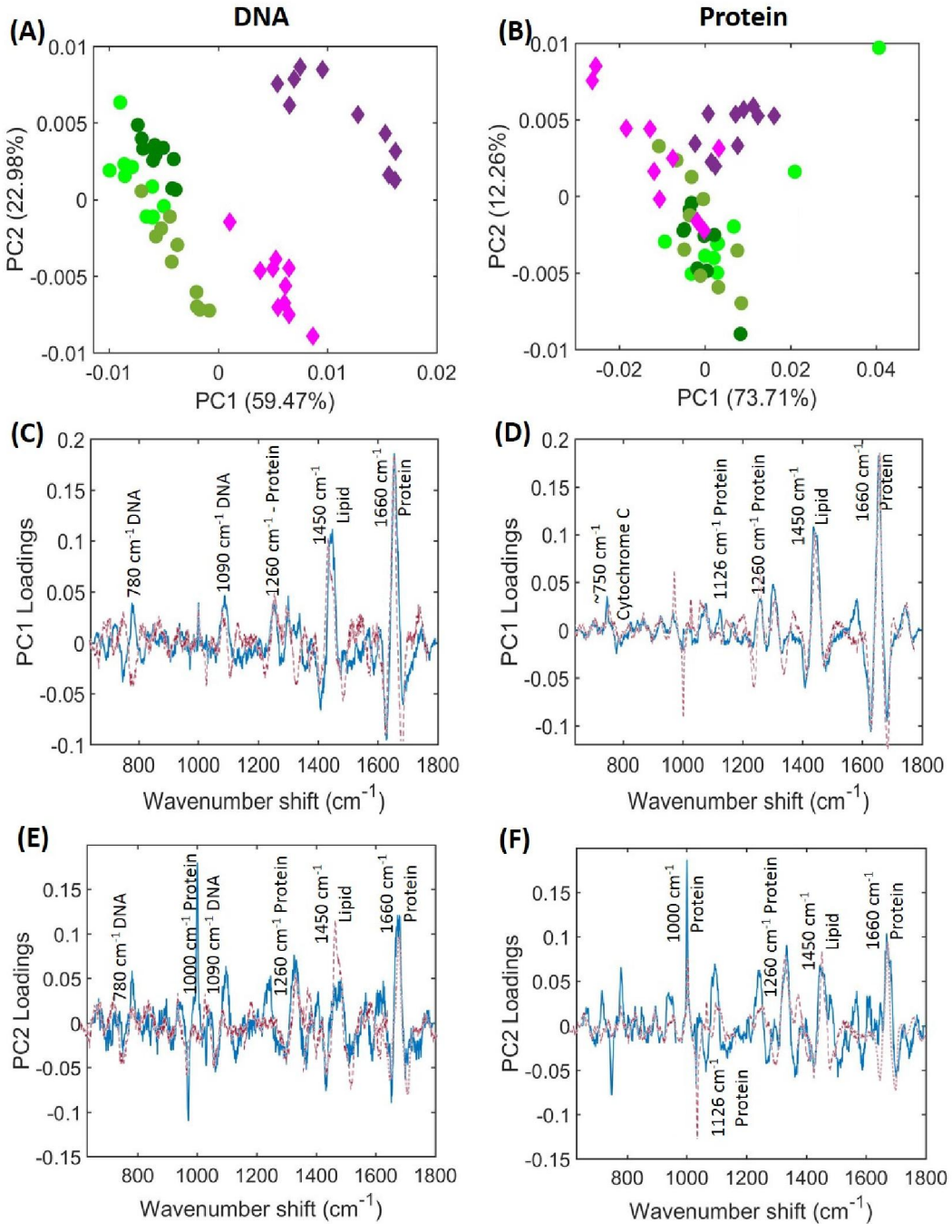

Figure 3.11: A comparison of cells treated with the rhenium complex and control cells after 2 hours of incubation. For PCA-scores plots of PC1 against PC2, spectra were taken from the regions of the cell identified as having a high DNA **(A)** or protein **(B)** content. Circles represent cells treated with the rhenium complex (n=3), and diamonds cells treated with a DMSO control (n=2). Each colour represents

an individual cell. The PC1 loadings for each PCA-scores plot are shown in **(C and D)** and the PC2 loadings are also shown **(E and F)**. The benchmark loadings are indicated by the red dotted line.

In contrast, the PCA scores plot for spectra taken from the DNA of cells shows a clear separation between treated and untreated cells (figure 3.11A), suggesting that the complex has had an effect on the DNA, or nucleus, of Caco-2 cells after 2 hours of treatment. The PC loadings for spectra taken from the DNA of cells (figure 3.11C), show that there is an overlap of some peaks with the benchmark plot, such as the 1450 cm^{-1} and 1660 cm^{-1} peaks, which are likely to be the result of differences between cells, and not the complex. However, there are some peaks that do not overlap or are different in comparison to the benchmark plot, at 780 cm^{-1}, 1090 cm^{-1} and 1300 cm^{-1}, suggesting that it is these peaks that cause the separation between control and treated cells.

The peak at ~780 cm^{-1} corresponds to DNA (Pully, Lenferink and Otto, 2011; Pascut *et al.*, 2013; Ashton, Hollywood and Goodacre, 2015), as does the peak at 1090 cm^{-1} (Pully, Lenferink and Otto, 2011; Zhang *et al.*, 2012), suggesting that the separation is caused by a change in the level of DNA within cells incubated with the complex for 2 hours. From the PC1 loadings plot it is not possible to determine whether this is an increase or a decrease in the level of DNA, but it is possible to do this by looking at the average spectra of treated and untreated cells. To do this, the ten spectra that were used for PCA were averaged for all cells and plotted on the same axis (figure 3.12). The average spectra suggest that there is an increase in the peak at 1090 cm^{-1} in cells that have been incubated with the complex, although there does not appear to be any clear differences in the 780 cm^{-1} peak between treated and control cells. Overall, this may suggest that cells incubated with the complex have an increased level of DNA in comparison to control cells.

The peak at 1300 cm^{-1} is within the amide III region, associated with proteins. Typically, this peak is broad and with two peaks at ~1260 cm^{-1} and 1300 cm^{-1} (Lo *et al.*, 2011; Rivas-Arancibia

et al., 2017), which can be seen in the PC loadings for all three PCA scores plots that do not show any separation. However, in the PC1 loadings plot that does show separation (figure 3.11C), there is a change in the peak at 1300 cm^{-1}, suggesting that the complex is causing a change in this region. Looking at the average spectra (figure 3.12), this peak appears to be increased in treated cells. Changes in this region are associated with changes in protein structure, and the 1300 cm^{-1} peak in particular is associated with α-helix structure (Lippert, Tyminski and Desmeules, 1976; Krimm and Bandekar, 1986; Herrero, 2008). The average spectra suggest that there may be an increased level of α-helices within the nucleus of cells incubated with the complex in comparison to control cells, and may be associated with changes in chromatin structure (Eberharter and Becker, 2002).

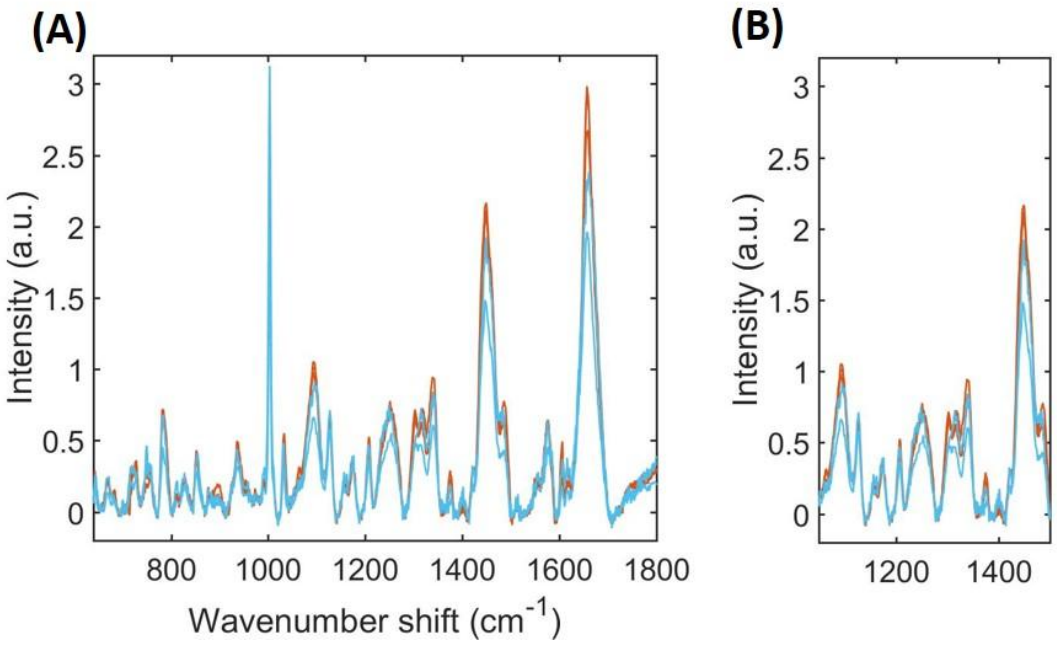

Figure 3.12: Average spectra of cells treated with the rhenium complex and control cells after 2 hours of incubation. (A) Average spectra (n=10) taken from the nucleus of cells treated with the rhenium complex (orange) and control cells (blue). Three treated and two control cells are plotted. **(B)** Insert of the region containing the peaks of interest.

Figure 3.13 shows the PCA scores plot and PC loadings of treated and untreated cells after 4 hours of incubation. The results show that there may be some separation, with one treated

cell falling within the controls but the other two cells separating from them, in both spectra taken from areas of high DNA and high protein content. However, as the PC1 loadings plot for both areas show changes across the whole cell and overlap with the benchmark plot, it is likely that this separation is due to differences between DNA, protein and lipid levels between different cells, rather than a result of the presence of the rhenium complex within cells. This suggests that, while the complex appears to have an effect on the DNA of Caco-2 cells after 2 hours of incubation, this effect is short-term and has been resolved by 4 hours of incubation.

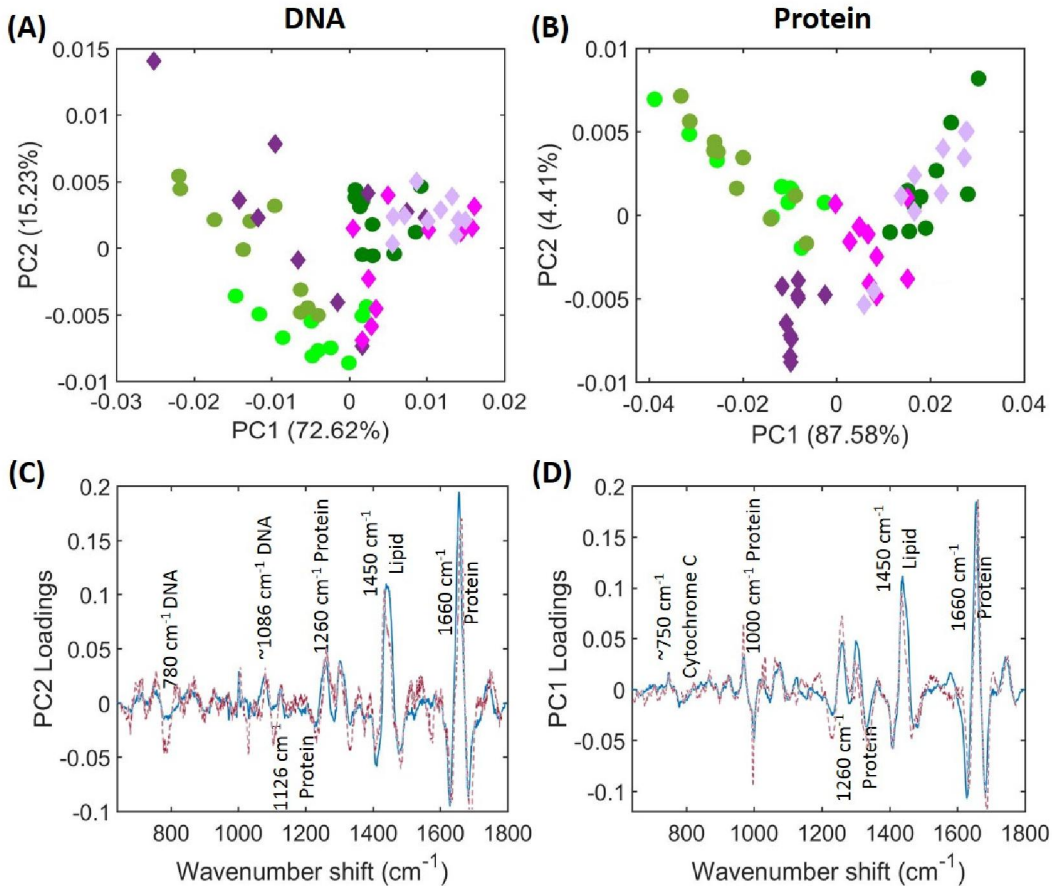

Figure 3.13: A comparison of cells treated with the rhenium complex and control cells after 4 hours of incubation. For PCA-scores plots of PC1 against PC2, spectra were taken from the regions of the cell identified as having a high DNA **(A)** or protein **(B)** content. Circles represent cells treated with the rhenium complex (n=3), and diamonds cells treated with a DMSO control (n=3). Each colour represents an individual cell. The PC1 loadings for each PCA-scores plot are shown in **(C and D)**. The benchmark loadings are indicated by the red dotted line.

3.3.3 Live cell rhenium complex maps

The previously discussed data was collected on fixed cells and, whilst valuable, can only provide a 'snapshot' of the cells state when it was fixed. There is also the risk of fixation introducing artefacts that can affect the quality of data collected (Chatterjee, 2014). One of the key advantages of Raman spectroscopy over other imaging methods is that it can be carried out on live cells maintained under normal physiological conditions. In order to further investigate the uptake of the rhenium complex by Caco-2 cells, live cells were incubated with the complex and mapped over a period of several hours. This has several advantages over studies on fixed cells, as the same cell can be monitored over time, and the uptake of the complex can also be measured in real time.

Once it had been established that repeated mapping of single live cells does not appear to damage them (chapter 2, section 2.5), Raman maps were collected of live cells incubated with the rhenium complex, to see if their uptake could be monitored over time. Cells were mapped before the complex was introduced into the medium ('pre-treatment'), and then immediately after the complex was added at 0 hours. Maps were then collected after 2, 4 and 6 hours of incubation. Raman maps were shaded to the DNA and protein content of the cell as before, and also to the peaks of 785 cm^{-1} and 1035 cm^{-1}, to determine if these peaks could be used to monitor the uptake of the complex over time (figure 3.14).

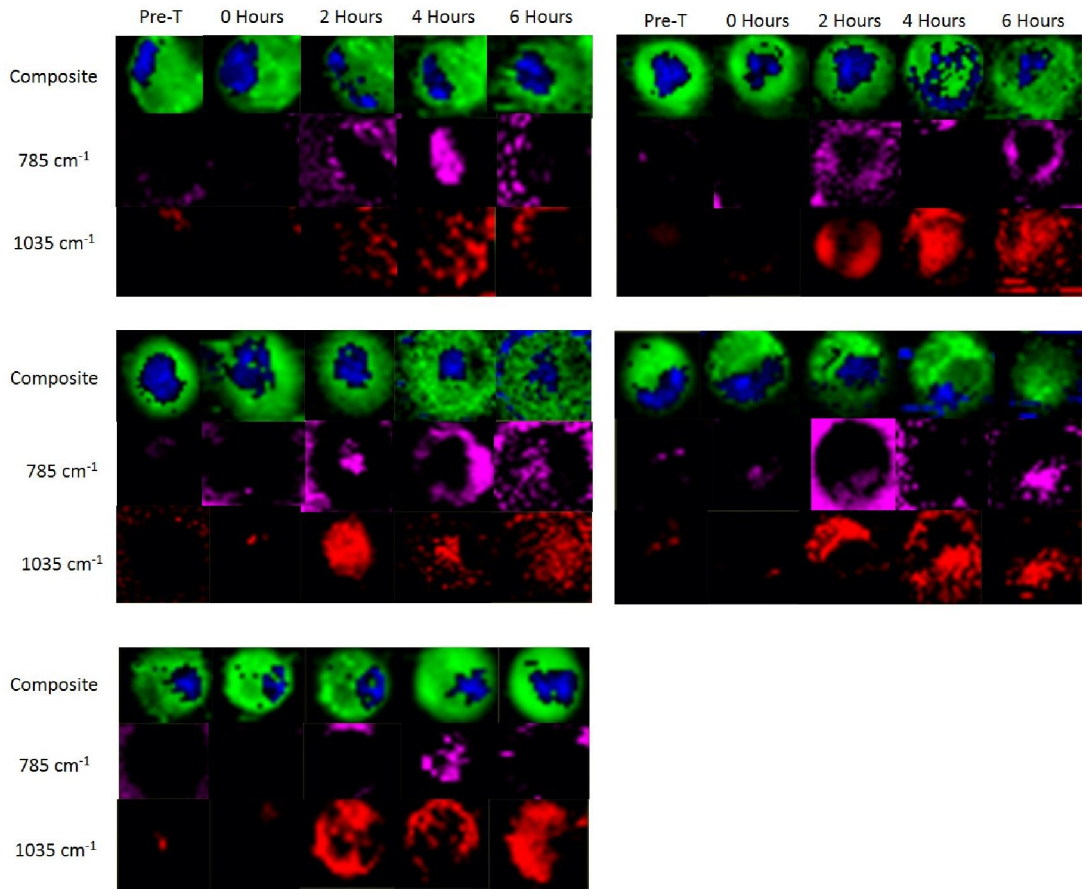

Figure 3.14: Raman maps of live Caco-2 cells treated with the rhenium complex and mapped at the timepoints listed. For composite images, DNA content was measured from 780-802 cm^{-1} and protein content from 1630-1680 cm^{-1}. Maps were also shaded to the peak at either 785 cm^{-1} or 1035 cm^{-1} using the previously established shading parameters (section 3.3.1).

The Raman maps show that for both peaks, there is very little intensity within the cell at both pre-treatment and 0 hours, suggesting that in this case, neither peak shaded with this approach corresponds to an intracellular component e.g. DNA or phenylalanine. At 2 hours, across all cells there is an increase in the intracellular intensity of the 1035 cm^{-1} peak which can be attributed to being within the cytoplasm of the cell; this intensity is also present in the cell at 4 and 6 hours. There is also an increase in the intracellular intensity of the 785 cm^{-1} peak, although this is not seen across all of the cells. There appears to be some intensity of the 785 cm^{-1} peak in the cytoplasm of several cells at 4 and 6 hours, but is not present in all of them, unlike the 1035 cm^{-1} peak. Overall, this suggests that of these two peaks,

1035 cm^{-1} appears to be the most appropriate peak to use with this complex, as it shows the most consistent shading across all five cells. The rhenium complex appears to be taken up by the cells by 2 hours of incubation and is localised to the cytoplasm; it appears to remain within cells for at least 4 hours after its initial introduction.

3.4 Discussion

The first aim of this study was to develop the imaging of Caco-2 cells. We have shown that using distribution plots, robust shading parameters can be applied across all cells to allow for consistent comparison, and that the nucleus and cytoplasm of Caco-2 cells can clearly be identified using Raman spectroscopy. The other aim was to determine if Raman spectroscopy could be used to visualise the rhenium complex, and therefore the mitochondria, within Caco-2 cells. The initial Raman maps on fixed cells (figure 3.8) suggested that two peaks, 785 cm^{-1} and 1035 cm^{-1}, may be suitable for detecting the complex within cells. However, there was an issue with both of these peaks, as 785 cm^{-1} is a well-characterised DNA peak (Zhang *et al.*, 2012; De Angelis *et al.*, 2017; Farhane, Bonnier and Byrne, 2017), and 1035 cm^{-1} can be assigned to the intracellular component phenylalanine (Rehman, Movasaghi and Rehman, 2012; Zheng *et al.*, 2014; Charwat *et al.*, 2015; Gebrekidan *et al.*, 2018). It is therefore difficult to determine if these maps are showing the presence of the rhenium complex within Caco-2 cells or are representative of other intracellular components. Shading the live cell maps to these same peaks (figure 3.16) showed some intracellular distribution for both peaks, however the 1035 cm^{-1} peak appeared to show the most consistent shading over time and in the most cells, suggesting that this was the most suitable peak to shade Raman maps to in order to visualise this rhenium complex within Caco-2 cells. However, it is difficult to determine the spatial resolution of the complex within the cell, and to definitively identify the intracellular localisation of the mitochondria. Overall, this demonstrates the difficulties of shading Raman

maps, specifically in trying to shade to identify the presence of a compound within a cell when that compound's peaks fall within the wavenumber range assigned to cellular features.

The PCA results on fixed cells suggested that the complex had an effect on the nucleus of Caco-2 cells after 2 hours of incubation (figure 3.10). This effect was not seen in the cytoplasm of cells after 2 hours of incubation, or in the nucleus or cytoplasm of cells after 4 hours of incubation with the complex, suggesting that it is a short-lived effect. The PC1 loadings plot and average spectra suggested that DNA and protein peaks were causing the separation seen in the PCA-scores plot. Specifically, the average spectra showed an increase in the 1090 cm^{-1} peak, assigned to DNA (Pully, Lenferink and Otto, 2011; Zhang *et al.*, 2012), and the 1300 cm^{-1} peak, assigned to an α-helix secondary structure in proteins (Lippert, Tyminski and Desmeules, 1976; Krimm and Bandekar, 1986; Herrero, 2008). Together, this suggests that the nucleus of cells incubated with the rhenium complex for 2 hours have an increased level of DNA, and an increased level of proteins with an α-helix structure in comparison to control cells. This could be indicative of proliferating cells, as we would expect replicating cells to have an increased level of both DNA and protein (Swain, Jell and Stevens, 2008). The increase in the 1300 cm^{-1} peak suggests that the complex induces a structural change in the proteins present in the nucleus of Caco-2 cells. Previously, post-translational modifications such as acetylation have been shown to increase the α-helical content of histone tails (Wang *et al.*, 2000). Histone acetylation alters the accessibility of chromatin and allows transcription to occur (Eberharter and Becker, 2002), so it is possible that the introduction of this particular rhenium complex into Caco-2 cells results in a cellular response that involves the induction of transcription in the nucleus, leading to an increase in the DNA content of the cell.

Overall, these results suggest that introducing an exogenous substance into the cell such as this rhenium complex can have an effect on the cell, bringing to the forefront the importance of label-free imaging techniques, and re-iterates the potential of Raman spectroscopy due to

its ability to carry this out. Raman spectroscopy has the advantage of being non-invasive, and Raman maps of the nucleus and the cytoplasm can be created without the use of any labels by shading to specific peaks. However, there is a limited resolution to which subcellular organelles Raman spectroscopy can be used to identify. As previously discussed (chapter 2, section 2.3.3), some studies have claimed to be able to visualise the mitochondria in cells without the use of any labels by using the peak at ~750 cm^{-1} (Matthäus *et al.*, 2007; Okada *et al.*, 2012; Ichimura *et al.*, 2014), which is assigned to the pyrrole breathing mode in cytochrome c (Hamada *et al.*, 2008). However, trying to replicate shading to this peak in Caco-2 cells was not successful. This leads to the issue of labels being required in order to visualise organelles other than the nucleus, but as demonstrated here, even if that label is reported to be non-toxic, it can still have an effect on cells. There is therefore a trade-off, of how much information can be revealed without risking intracellular damage by introducing a label, and the advantages and disadvantages of both should be taken into consideration during experimental design.

Chapter 4: Using Raman spectroscopy to evaluate the effect of cannabidiol on Caco-2 cells

4.1 Introduction:

Cannabidiol (CBD) is a phytocannabinoid derived from the plant *Cannabis sativa.* Its structure is shown in figure 4.1, and it is reported to have therapeutic potential in a number of different diseases. Cannabinoids are pharmacologically active compounds that bind to specific G-protein coupled receptors (Pertwee and Ross, 2002). Unlike many other cannabinoids, CBD does not appear to have a high affinity for the cannabinoid receptors CB_1 or CB_2 and appears to exert its effects via a number of different receptors independent of the endocannabinoid system (Pertwee, 2008).

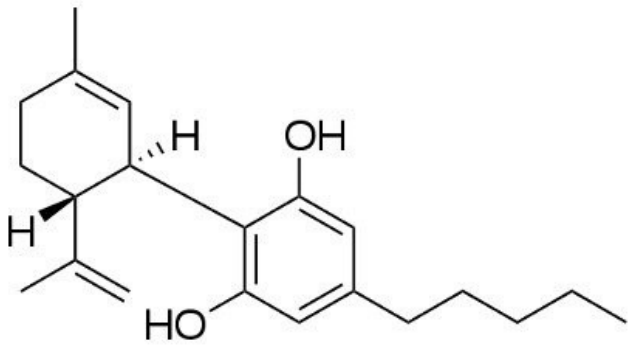

Figure 4.1: Molecular structure of cannabidiol.

The mechanism of action of CBD is currently not well understood, although it is implicated to have anti-proliferative effects in a number of different cell lines including glioma, breast cancer and intestinal Caco-2 cells (Massi *et al.*, 2004; McAllister *et al.*, 2011; Macpherson *et al.*, 2014). It is also suggested to decrease oxidative metabolism in these cells (McAllister *et al.*, 2011). However, further study is needed in order to better understand this mechanism and to

increase the therapeutic potential of this drug. Raman spectroscopy has previously been used in pharmaceutical studies to monitor drug uptake and response by cells over time (Zoladek *et al.*, 2011; Bräutigam *et al.*, 2013; H. Salehi *et al.*, 2013), and is therefore an ideal candidate for assessing the effect of CBD on both live and fixed cells.

The potential of CBD as a treatment for colon carcinogenesis (Aviello *et al.*, 2012) makes the Caco-2 cell line a particularly attractive *in vitro* model to examine the effect of CBD. These cells are a well-documented model for drug absorption and uptake (Hidalgo, Raub and Borchardt, 1989; Artursson, 1990), and to assess drug toxicity (Meunier *et al.*, 1995). As CBD has been shown previously to have an effect on Caco-2 cells (Alhamoruni *et al.*, 2010; Macpherson *et al.*, 2014), it suggests that they should act as a suitable model to use with Raman spectroscopy to evaluate the cellular response to this drug.

4.2 Methods:

4.2.1 Cell treatment

Caco-2 cells were cultured and attached to CaF_2 windows as described in the methods (chapter 2, section 2.2.2). Once cells had adhered to CaF_2 windows, media was removed and replaced with media containing CBD at a concentration of either 1 µM, 10 µM or media control. After 2, 4, 6, 8 or 24 hours of incubation, media was removed and cells were fixed as previously described (chapter 2, section 2.2.3).

4.2.2 Raman spectroscopy of fixed cells

Fixed cells were maintained in PBS throughout analysis. Raman maps were collected as described in the methods (chapter 2, section 2.2.4), using a laser wavelength of 532 nm.

4.2.3 Raman spectroscopy of live cells

Once adhered to CaF_2 windows, cells were transported to the Raman incubator and maintained at 5 % CO_2 and 37 °C. In this study, all live cells were mapped using a laser

wavelength of 785 nm. Control maps were acquired by mapping the same cell over time to ensure there was no loss of viability. For the CBD study, media was removed once cells were in the Raman incubator, and replaced with media containing CBD at a concentration of 10 µM. Cells were then mapped at the times described.

4.3 Results:

4.3.1 Raman Maps

The overall aim of this study was to determine the effect of CBD on Caco-2 cells. Initially, we wanted to investigate whether the drug could be visualised within Caco-2 cells, so the first step in this process was to acquire a spectrum of CBD. This spectrum (figure 4.2), showed several peaks of interest, at ~880 cm^{-1}, ~1090 cm^{-1} and ~1450 cm^{-1}.

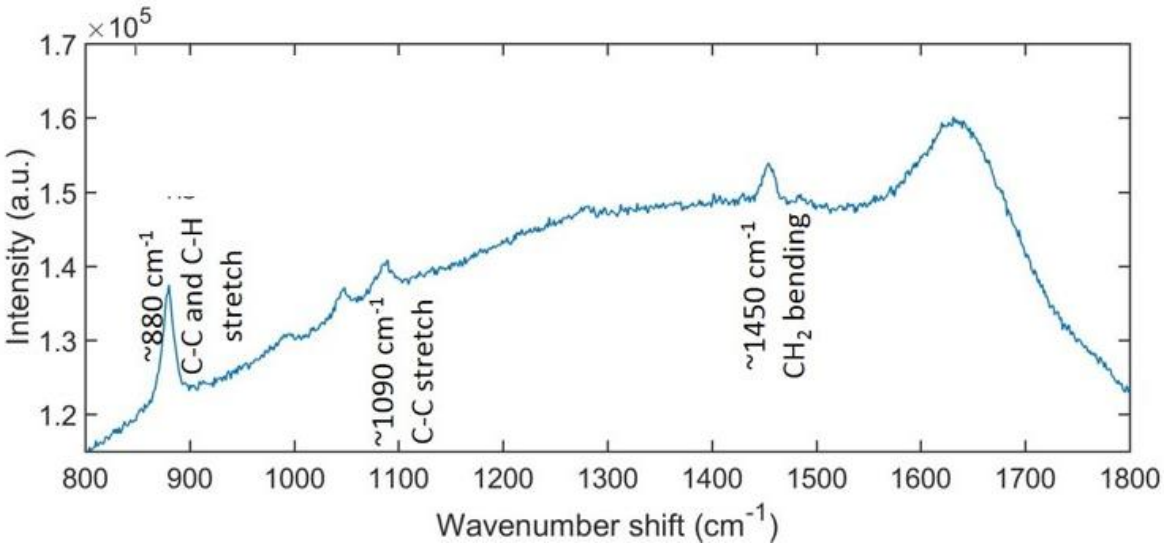

Figure 4.2: Raman spectrum of CBD, spotted and left to dry on a CaF_2 disk. The spectrum was acquired using a 532 nm wavelength excitation laser, an acquisition time of 4 seconds with 15 accumulations (total time 1 minute) and a laser power of ~30 mW.

Peaks at 880 cm^{-1} have previously been associated with both C-C (Nallasamy and Mohan, 2005) and C-H stretching (Sato and Martinho, 2018). Peaks in the region of 1090 cm^{-1} are commonly assigned to phosphate stretches, associated with DNA (Guan, Wurrey and Thomas, 1994).

However, they have also been associated with C-C stretches (Chen *et al.*, 2014), which, unlike phosphate, are bonds present within the structure of CBD. Peaks in the region of 1450 cm^{-1} are assigned to CH_2 bending, most commonly associated with lipids (Palonpon, Sodeoka and Fujita, 2013), but there are CH_2 bonds within the CBD molecule. In order to see if we could map the drug within Caco-2 cells, Raman maps were shaded to these three peaks at several timepoints (figure 4.3), using peak intensity measured from 875-890 cm^{-1}, 1080-1100 cm^{-1} and 1440-1460 cm^{-1}. However, none of these peaks showed the distribution of the drug within cells, as they could also be seen in untreated cells; this is the case even when the shading range is adjusted, as demonstrated in appendix B. The CBD peaks may therefore overlap with cellular components, particularly as the peaks at 1090 cm^{-1} and 1450 cm^{-1} are associated with DNA and lipids, respectively, or the drug itself may not enter the cell and instead exert its effect by binding to receptors at the cell membrane.

Although the drug could not be visualized within cells, the effect of the drug on cells could be investigated by shading Raman maps according to their DNA (780-802 cm^{-1}) and protein (1630-1680 cm^{-1}) content to produce composite images at each time point. These images can then be compared in order to see if any visible changes could be observed as a result of drug treatment (figure 4.4). The maps were shaded according to the previously established shading parameters (chapter 2, section 2.3.3).

A comparison of the shaded Raman maps suggests that the drug has had an effect on Caco-2 cells at the higher concentration, as after 24 hours of treatment with the drug, there is no DNA content left within cells. There do not appear to be any clear visual changes at any of the earlier timepoints in comparison to control cells, or in the Raman maps of cells treated with 1 µM of CBD. Therefore, to further examine whether CBD was having any effect on cells, PCA was carried out on selected Raman spectra.

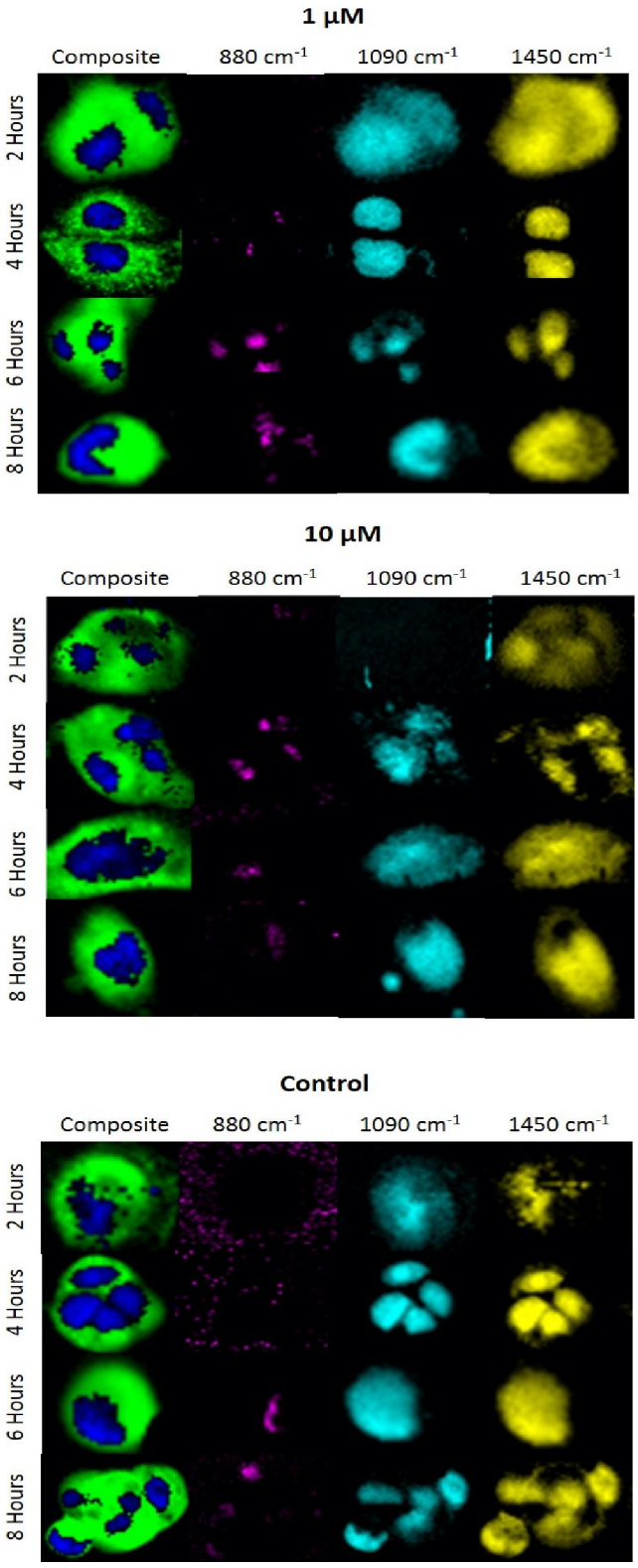

Figure 4.3: Raman maps of Caco-2 cells shaded to peaks of interest from the CBD spectrum. For the composite images, DNA was measured from 780-802 cm^{-1}, and protein from 1630-1680 cm^{-1}. When shading to peaks of interest from the CBD spectrum, all selected peaks were shaded from 0 to max.

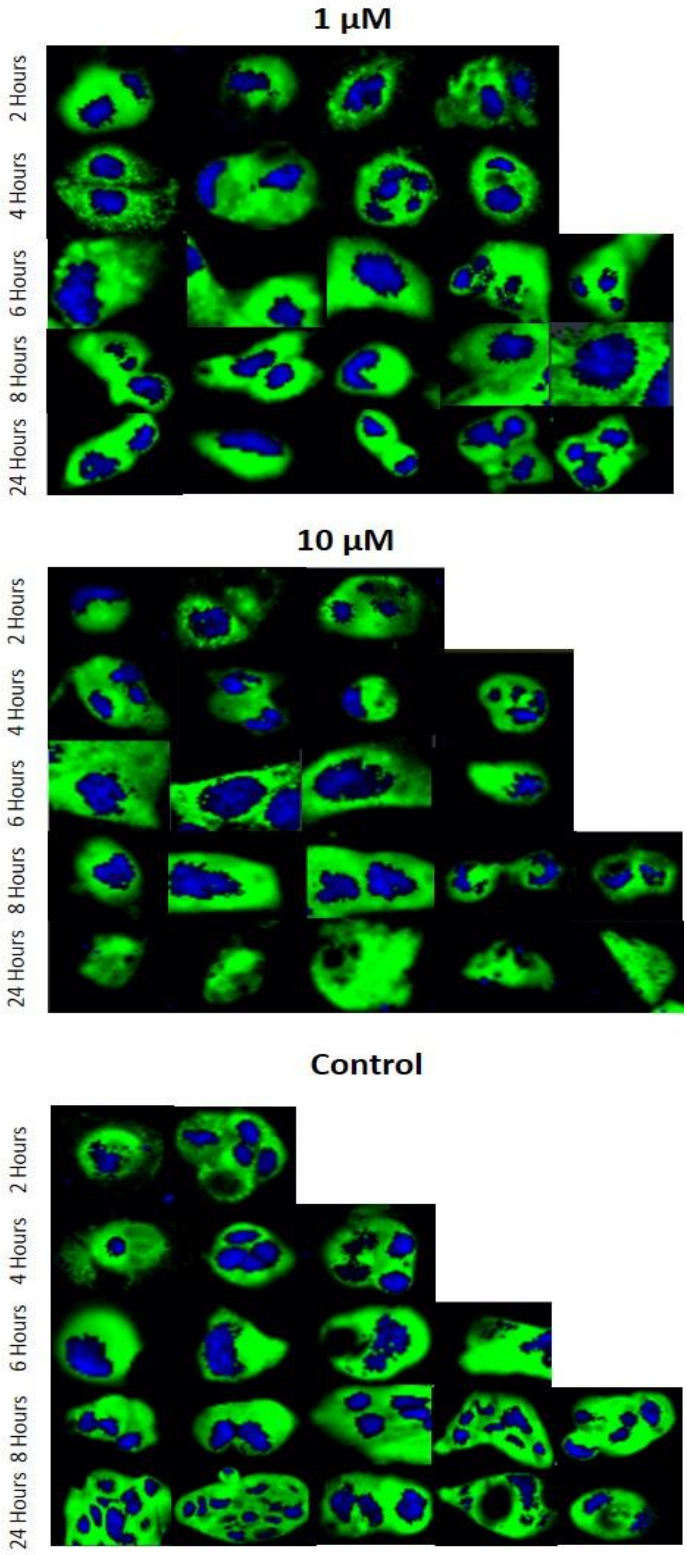

Figure 4.4: Raman maps of Caco-2 cells shaded to their DNA and protein content. Shading ranges were 780-802 cm^{-1} for DNA, blue, and 1630-1680 cm^{-1} for protein, green. Cells were treated with either 1 or 10 µM of CBD or media control for each listed time point.

4.3.2 Principal Component Analysis

The Raman maps suggested that the drug was affecting Caco-2 cells, but from the maps alone it is difficult to determine what that effect is. In order to obtain biochemical as well as visual information, PCA was carried out using ten Raman spectra selected from each of the Raman maps in figure 4.3. Ten spectra were selected from DNA rich-regions, and ten from protein-rich regions to better establish which areas of the cell the drug may be effecting. As we hypothesised that the drug would have an effect on Caco-2 cells, we expected to see separation between treated and untreated cells.

At 2 hours (figures 4.5A and 4.5B), there is a clear separation of cells treated with 1 μM of the drug from the controls, and this is seen in both the DNA and protein PCA-scores plot. This suggests that, although the Raman maps do not show any difference between cells treated with this concentration of CBD and control cells, the drug does have an effect on Caco-2 cells, and this effect is evident after 2 hours of incubation. In contrast, there is little separation seen at the 10 μM concentration of the drug, suggesting at that the two concentrations do not effect cells in the same way.

At 4 hours, separation is less clear. Cells treated with 1 μM of CBD appear to fall mostly within the controls, suggesting that the effect of the drug at this concentration may be short-lived. Some cells treated with 10 μM begin to separate from control cells at 4 hours, suggesting that, at this concentration, the effect of the drug does not occur until ~4 hours of incubation.

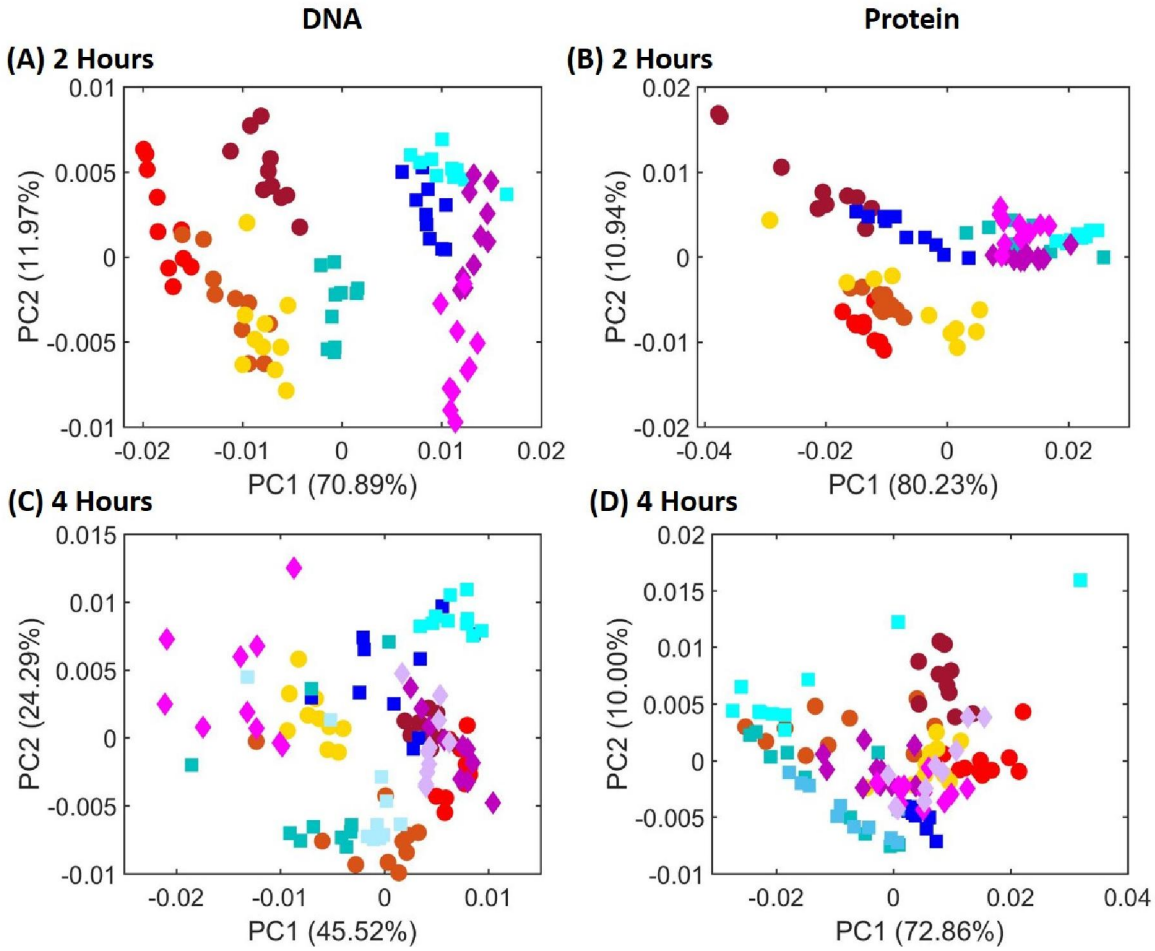

Figure 4.5: PCA-scores plots of PC1 against PC2 for spectra taken from cells treated with either CBD or media control for 2 and 4 hours. Spectra were taken from regions of the cell identified as having a high DNA content after an incubation time of either 2 **(A)** or 4 **(C)** hours, or from regions with a high protein content after either 2 **(B)** or 4 **(D)** hours of incubation. Circles represent cells treated with 1 µM of CBD (n=4), squares cells treated with 10 µM of CBD (n=3 at 2 hours, n=4 at 4 hours), and diamonds cells treated with a media control (n=2 at 2 hours, n=3 at 4 hours). Each colour represents an individual cell.

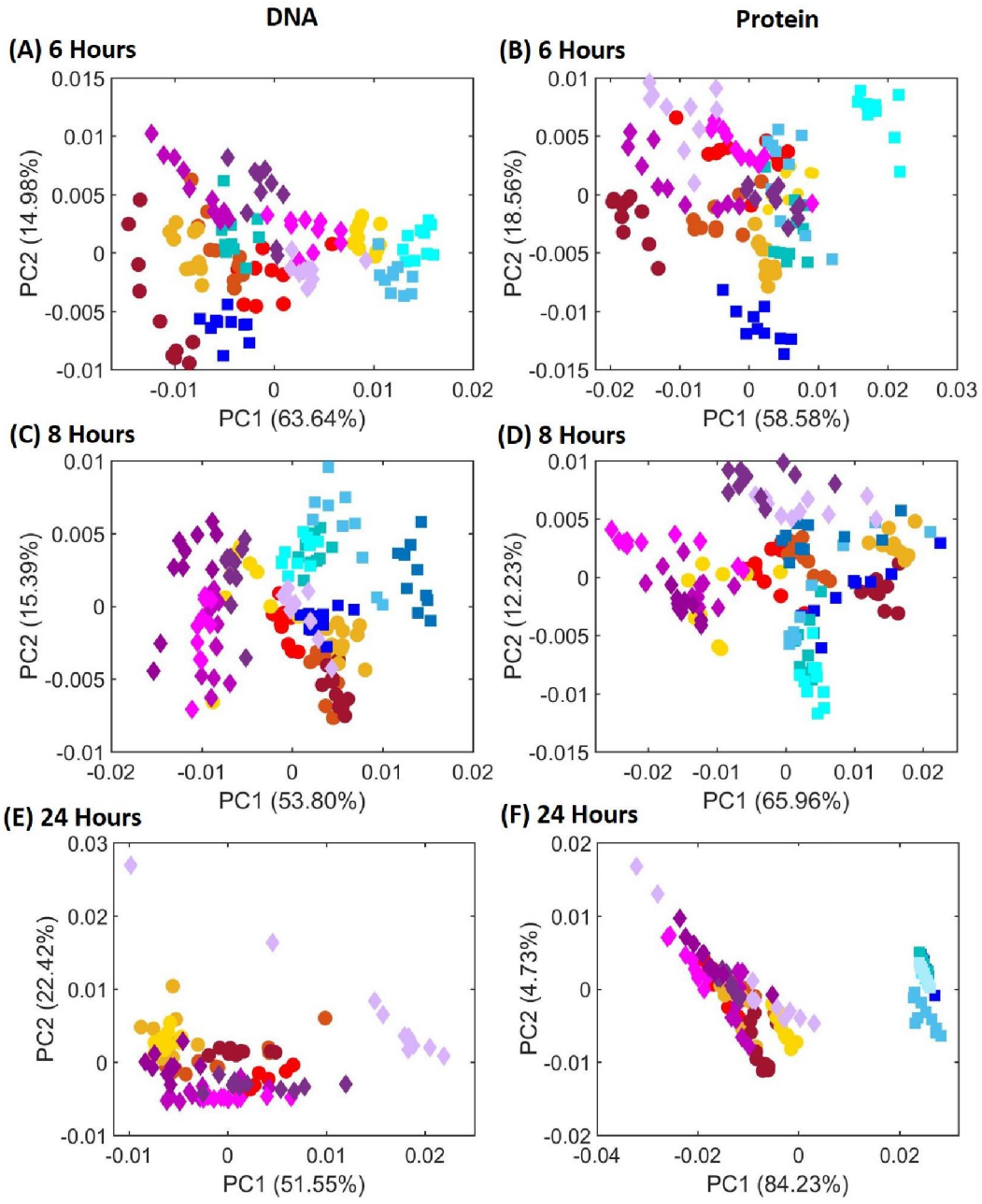

Figure 4.6: PCA-scores plots of PC1 against PC2 for spectra taken from cells treated with either CBD or media control for 6, 8 and 24 hours. Spectra were taken from regions of the cell identified as having a high DNA content after an incubation time of either 6 **(A)**, 8 **(C)** or 24 **(E)** hours, or from regions with a high protein content after either 6 **(B)**, 8 **(D)** or 24 **(F)** hours of incubation. Circles represent cells treated with 1 µM of CBD (n=5), squares cells treated with 10 µM of CBD (n=5), and diamonds cells treated with a media control (n=5). Each colour represents an individual cell.

PCA was also carried out on data collected from the maps at 6, 8 and 24 hours (figure 4.6). It can be observed in figure 4.6 that there is some separation at the 1 μM concentration of the drug. The majority of cells separate slightly in the 6 hour DNA PCA scores plot (figure 4.6A), but this is less clear in the protein plot, and there is no separation in either of the 8 hour plots, again suggesting that the effect of the 1 μM concentration of CBD occurs in the early stages of incubation, and is completed by 8 hours. At the higher concentration of the drug, some cells begin to separate from the controls at 6 hours in both the DNA and protein plots, and by 8 hours, all cells treated with 10 μM of CBD separate from control cells. A similar separation occurs after 24 hours of treatment with CBD, as all cells treated with 10 μM separate clearly from control cells and cells treated with 1 μM, which group together (figure 4.6F). As there appears to be no DNA left within cells treated with 10 μM of the drug, when looking at DNA-rich regions of the cell, only control cells and cells incubated with 1 μM could be compared (figure 4.6E), and this plot shows little separation between the two groups.

Overall, these results suggest that the effect of the lower concentration of the drug happens within 2 hours of incubation and is a short-term effect, whereas at 10 μM the effect only becomes apparent in the Raman spectra after ~4-6 hours of incubation, and the end result of this effect is the loss of DNA from within the cell.

4.3.3 PCA and Average Spectra – Initial Response

While the previous PCA scores plots are useful in determining differences between treated and untreated cells, it is difficult to determine the extent to which each peak contributes to the overall separation because so many variables are being compared. One way to reduce this variation is to reduce the number of conditions under investigation. In the initial PCA plots (figure 4.5), the greatest changes occurred in cells treated with 1 μM of CBD for 2 hours, so to look at the effect of the drug more closely, we carried out PCA to compare cells treated with this concentration of the drug and control cells (figure 4.7). As in the previous chapter, the

benchmark loadings plot was included alongside all PC loadings plots (shown in red dashed line).

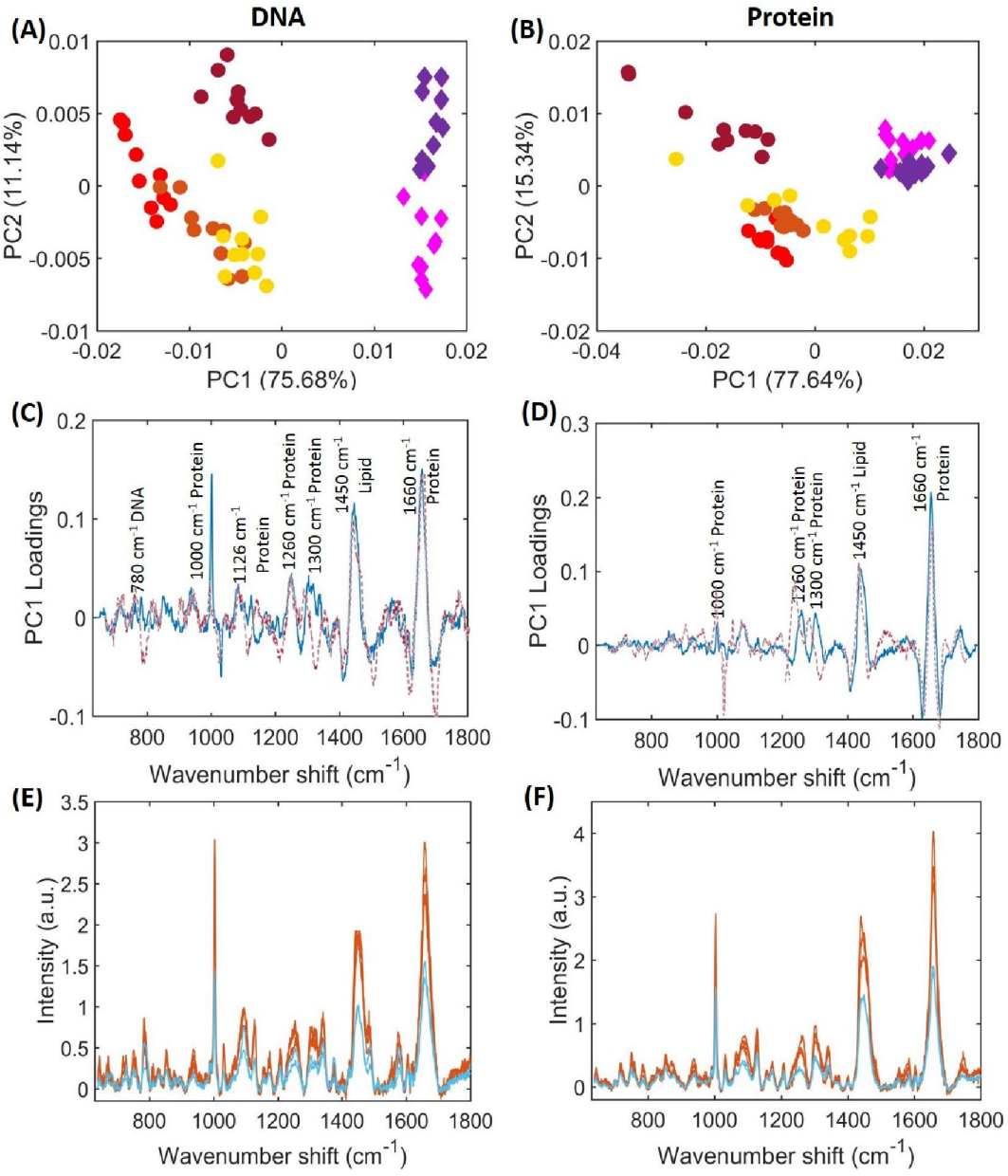

Figure 4.7: A comparison of cells treated with 1 µM of CBD and control cells after 2 hours of incubation. For PCA-scores plots of PC1 against PC2, spectra were taken from regions of the cell identified as having a high DNA **(A)** or protein **(B)** content. Circles represent cells treated with CBD (n=4), and diamonds cells treated with a media control (n=2). Each colour represents an individual cell. The PC1 loadings for each plot are shown in **(C and D)**, and the baselined spectra of treated (orange) and control (blue) cells, averaged from the 10 spectra used for PCA are shown in **(E and F)**. The benchmark loadings are indicated by the red dotted line.

These plots show the same separation as before, but as only two conditions are being compared the PC loadings are easier to analyse. The greatest changes can be observed along PC1, and the PC1 loadings plots show which peaks have changed in order to cause the separation between treated and control cells. In both the loading plots for spectra taken from the nucleus and cytoplasm of Caco-2 cells, several peaks overlap with the benchmark loadings plot, including the peaks with the greatest intensity (1450 cm^{-1} and 1660 cm^{-1}, associated with lipids and proteins, respectively). As previously discussed (chapter 3, section 3.3.2), these changes are likely to be due to differences in the level of protein and lipid between cells, and not a result of the drug. The most important peaks are the ones that differ from the benchmark loadings, and are associated with DNA (780 cm^{-1}) or protein (1300 cm^{-1}) in figure 4.6C, and protein (1260 cm^{-1}, 1300 cm^{-1}) in figure 4.6D.

In order to investigate whether the drug is causing these peaks to increase or decrease, the ten spectra that were used for PCA were averaged for treated and control cells. These spectra were then plotted on the same axis to allow for comparison (figure 4.7E). The average spectra show that the three peaks identified above (780 cm^{-1}, 1260 cm^{-1} and 1300 cm^{-1}), have all increased in cells treated with the drug.

The 780 cm^{-1} peak can be assigned to nucleic acids, and the 1260 cm^{-1} and 1300 cm^{-1} peaks to proteins. Raman spectroscopy has previously been used as a tool to study the cell cycle (Swain, Jell and Stevens, 2008), and protein levels have been shown to increase in proliferating cells (Short *et al.*, 2005). It is therefore possible that the increase in the intensity of DNA and protein peaks observed in the average spectra are indicative of cells being in different stages of the cell cycle during analysis. Previous studies have shown that some cannabinoids, including CBD, at low concentrations (1 µM or below), can enhance cell proliferation (Watanabe *et al.*, 2005; Takeda *et al.*, 2008). If this low dose of CBD induces proliferation in Caco-2 cells after 2 hours, it could be this effect that caused the separation of treated and untreated cells. These peaks

were also previously shown to be increased in Caco-2 cells treated with rhenium complexes (chapter 3, section 3.3.2) which was also linked to the induction of proliferation as a result of something being introduced to the cell.

While at lower concentrations CBD has been shown to have proliferative effect on cells, at a higher concentration it has been shown to inhibit proliferation and induce apoptosis, or programmed cell death, in a number of different cell lines (Massi *et al.*, 2004; McKallip *et al.*, 2006; Shrivastava *et al.*, 2011). In order to investigate whether we could observe this effect in Caco-2 cells, we studied the later timepoints (8 and 24 hours), in more detail.

4.3.4 PCA and Average Spectra – Later Response

The PCA-scores plots for 8 hours (figure 4.8) show that cells treated with 10 μM of CBD separate from control cells along PC1, and the peaks changing to cause this separation include DNA (780 cm^{-1}), and protein peaks (1126 cm^{-1}, 1260 cm^{-1}) in DNA-rich regions, and protein (1000 cm^{-1}, 1126 cm^{-1}) peaks in protein-rich regions, as these peaks do not overlap with the benchmark loadings. The average spectra (figure 4.8E and F) showed that some of these peaks (1126 cm^{-1}, 1260 cm^{-1}, 1300 cm^{-1}) are decreased in treated cells in comparison to control cells, suggesting that treated cells have decreased protein levels. Decreased protein levels have been seen in apoptotic cells previously (Czamara *et al.*, 2016), associated with the activation of caspases leading to the degradation of proteins (Hengartner, 2000). This suggested that CBD may be inducing apoptosis, or another pathway of cell death, in Caco-2 cells. Further evidence for this can be found in the protein loadings plot, as there was a change in a peak at 1375 cm^{-1}. This peak has been shown to increase in apoptotic cells and can potentially be used as a marker of apoptosis using Raman spectroscopy (Brauchle *et al.*, 2015), and appears to only be present in the spectra of treated cells. The PC loadings also show a change in the peak at 750 cm^{-1}, which is associated with cytochrome c (Hamada *et al.*, 2008). Changes in this peak may indicate a difference in the mitochondria of cells, as during apoptosis, cytochrome c

floods the cytoplasm of cells (Ott *et al.*, 2002), which may be what causes this peak to change.

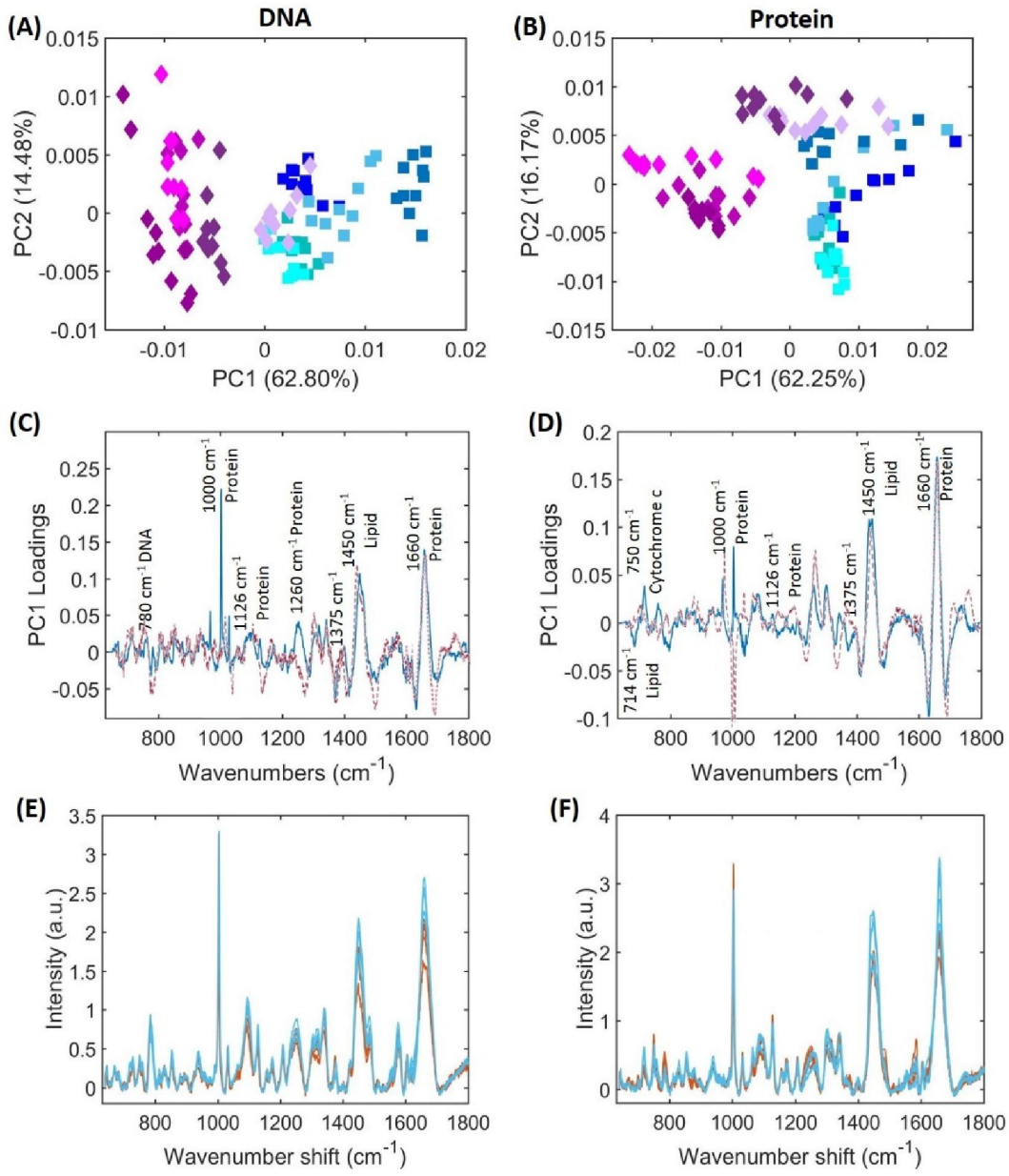

Figure 4.8: A comparison of cells treated with 10 µM of CBD and control cells after 8 hours of incubation. For PCA-scores plots of PC1 against PC2, spectra were taken from regions of the cell identified as having a high DNA **(A)** or protein **(B)** content. Squares represent cells treated with CBD (n=5), and diamonds cells treated with a media control (n=5). Each colour represents an individual cell. The PC1 loadings for each plot are shown in **(C and D)**, and the baselined spectra of treated (orange) and control (blue) cells, averaged from the 10 spectra used for PCA are shown in **(E and F)**. The benchmark loadings are indicated by the red dotted line.

Analysing the data from 24 hours appears to confirm that the effect of the 1 μM concentration of CBD is short-term, as there is no separation between treated and untreated cells (figure 4.9A). Some peaks in the PC1 loadings plot appear to be different from the benchmark plot, such as the 1260 cm^{-1} and 1450 cm^{-1} peaks, but as there is no separation in the PCA-scores plot, and there does not appear to be any differences in the average spectra between the two sets of cells, these peaks are most likely to be attributed to differences between individual cells rather than an effect of the drug.

While it is not possible to compare the DNA of cells treated with 10 μM of CBD and control cells, we can look at the drugs effect on the cytoplasm of cells in more detail. The PCA-scores plot (figure 4.9B), shows a clear separation of all treated cells from control cells. The PC loadings show several peak changes from the benchmark, associated with lipid (714 cm^{-1}, 1450 cm^{-1}, 1585 cm^{-1}) and protein (1032cm^{-1}, 1280 cm^{-1}, 1300 cm^{-1}) peaks, similar to what was observed after 8 hours of incubation. The average spectra (figure 4.9F) show that lipid and protein peaks are decreased in treated cells. Decreases in lipid levels, specifically the peak at 1450 cm^{-1}, have been seen in apoptotic cells, associated with a loss of lipid molecules due to the loss of membrane integrity (Ricci *et al.*, 2018), so these decreases in both protein and lipid content may suggest that CBD induces cell death in Caco-2 cells. In addition, there appears to be a shift from ~1266 cm^{-1} in control cells to ~1254 cm^{-1} in treated cells. This is associated with a transition in protein structure from α-helices to β-sheets, which has previously been observed in endothelial cells that had been induced to undergo apoptosis. In these cells, the change in protein structure was thought to be as a result of the activation of caspases upon the induction of cell death, which degrade peptide bonds to cause changes in secondary structure that result in protein degradation (Czamara *et al.*, 2016).

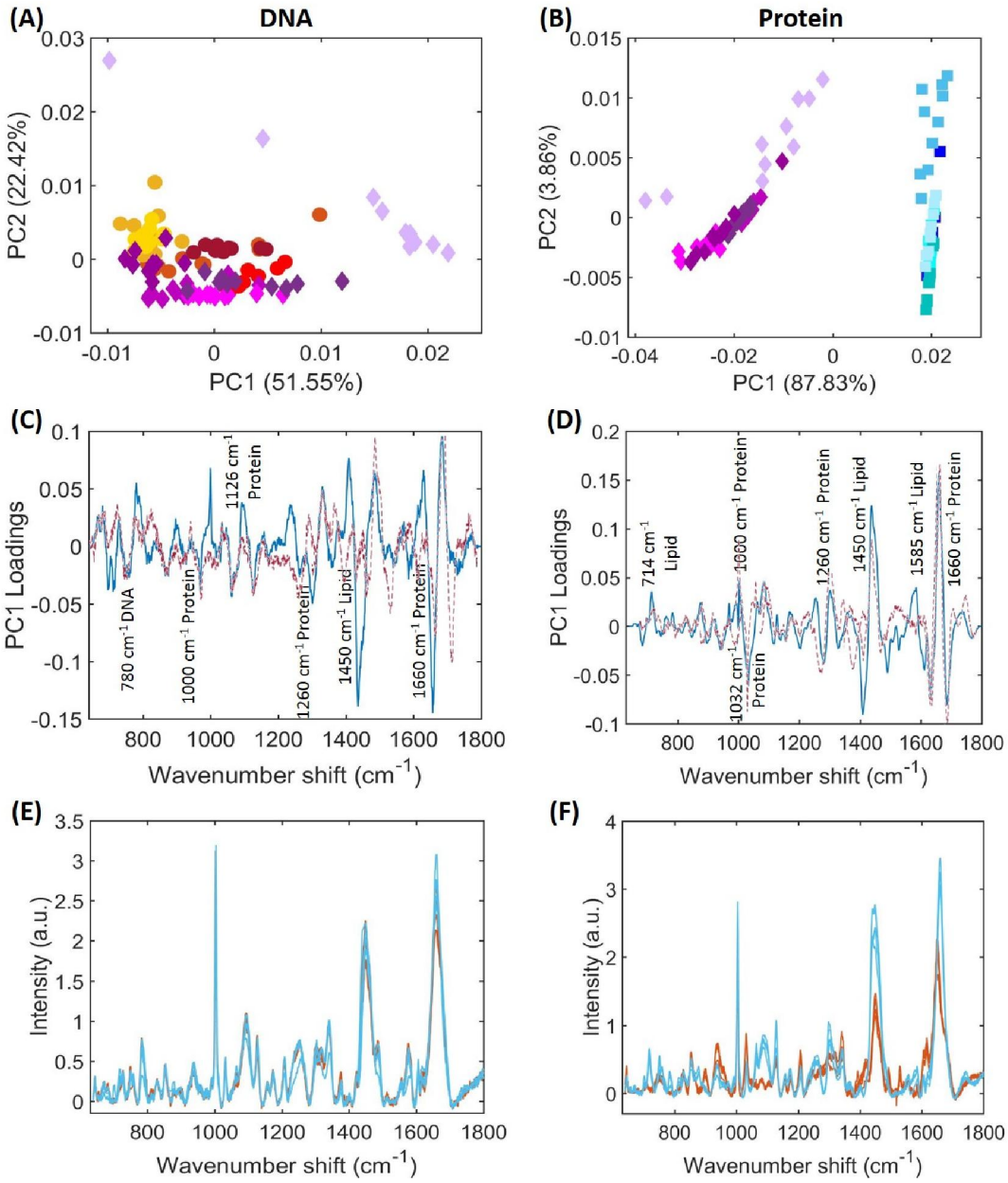

Figure 4.9: A comparison of cells treated with 10 µM of CBD and control cells after 24 hours of incubation. For PCA-scores plots of PC1 against PC2, spectra were taken from regions of the cell identified as having a high DNA **(A)** or protein **(B)** content. Circles represent cells treated with 1 µM CBD (n=5), squares cells treated with 10 µM of CBD (n=5), and diamonds cells treated with a media control (n=5). Each colour represents an individual cell. The PC1 loadings for each plot are shown in **(C and D)**, and the baselined spectra of treated (orange) and control (blue) cells, averaged from the 10 spectra used for PCA are shown in **(E and F)**. The benchmark loadings are indicated by the red dotted line.

4.3.5 Live cell Raman spectroscopy

As previously discussed, one of the key advantages of Raman spectroscopy is that it can be carried out on live cells. Therefore, in order to better understand the process of cell death CBD induces in Caco-2 cells, and the process by which the DNA of these cells is lost, Raman maps of live cells treated with the drug were collected. Figure 4.10 shows live cell maps of Caco-2 cells treated with 10 μM of CBD. In cell 1, the DNA of the cell seems to begin to break down after just 4 hours of incubation with the drug, and by 21 hours, there is no DNA remaining within the cell and the cytoplasm is beginning to break down. Whilst there appears to be no clear degradation of the DNA at 4 hours in cell 2, by 21 hours the cytoplasm again seems to be breaking down, and by 24 hours there is very little of the cell left. Cells 3 and 4 show the later stages of incubation, from 18 hours onwards. In both cells, the DNA appears to be localised on one side of the cell, towards the membrane, at 18 hours. As time increases, this DNA seems to be externalised whilst the plasma membrane is intact, and at 24 hours the cytoplasm of both cells starts to break down, and membrane integrity is lost.

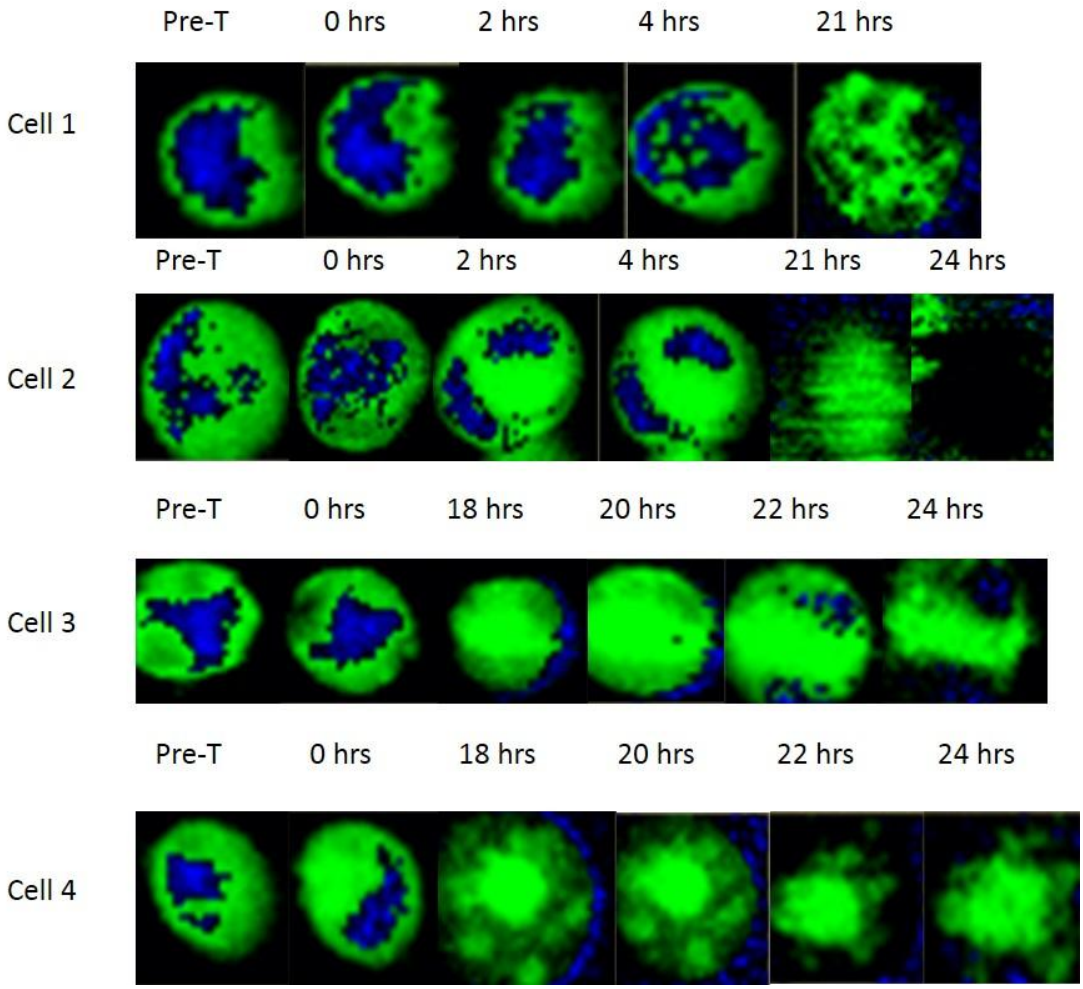

Figure 4.10: Raman maps of live Caco-2 cells treated with 10 µM of CBD, shaded to their DNA and protein content. Raman maps showing the DNA, measured from 780-802 cm^{-1} (blue) and protein, measured from 1630-680 cm^{-1} (green) content of live Caco-2 cells treated with 10 µM of CBD for each listed time point.

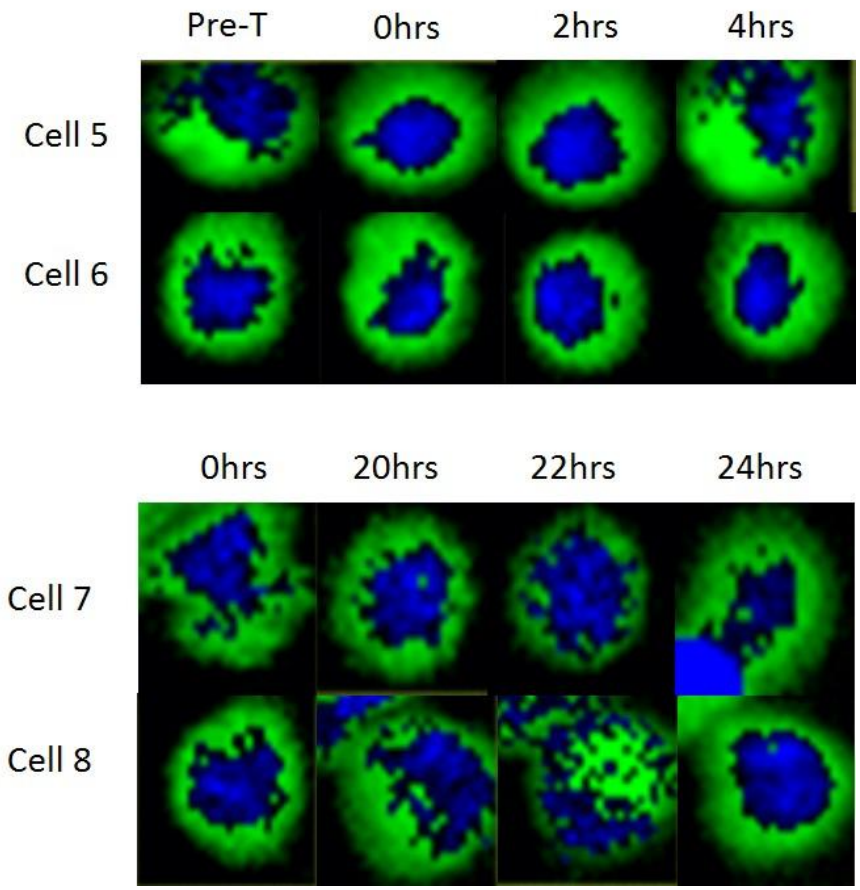

Figure 4.11: Raman maps of live control Caco-2 cells, shaded to their DNA and protein content. Raman maps showing the DNA (blue) and protein (green) content of live Caco-2 cells mapped at each listed time point.

Raman maps of control cells were also collected (figure 4.11) and mapped at similar timepoints. These cells did not show the same deterioration that could be observed in cells treated with CBD, suggesting that it is the drug causing the cell to break down, and is not a result of repeated exposure to the laser. Once control maps had been collected, PCA was carried out on spectra from both treated and untreated live cells and compared at specific timepoints. The timepoints chosen were 4 hours, as the fixed data suggested that this was the approximate timepoint at which the drug's effect on Caco-2 cells began, and 20 hours, as at this point the DNA of treated cells had broken down. As the live cell maps in this case were collected using a 785 nm laser, another benchmark PC1 loadings plot was created in the same way as before, using spectra taken from the control cells above (appendix B).

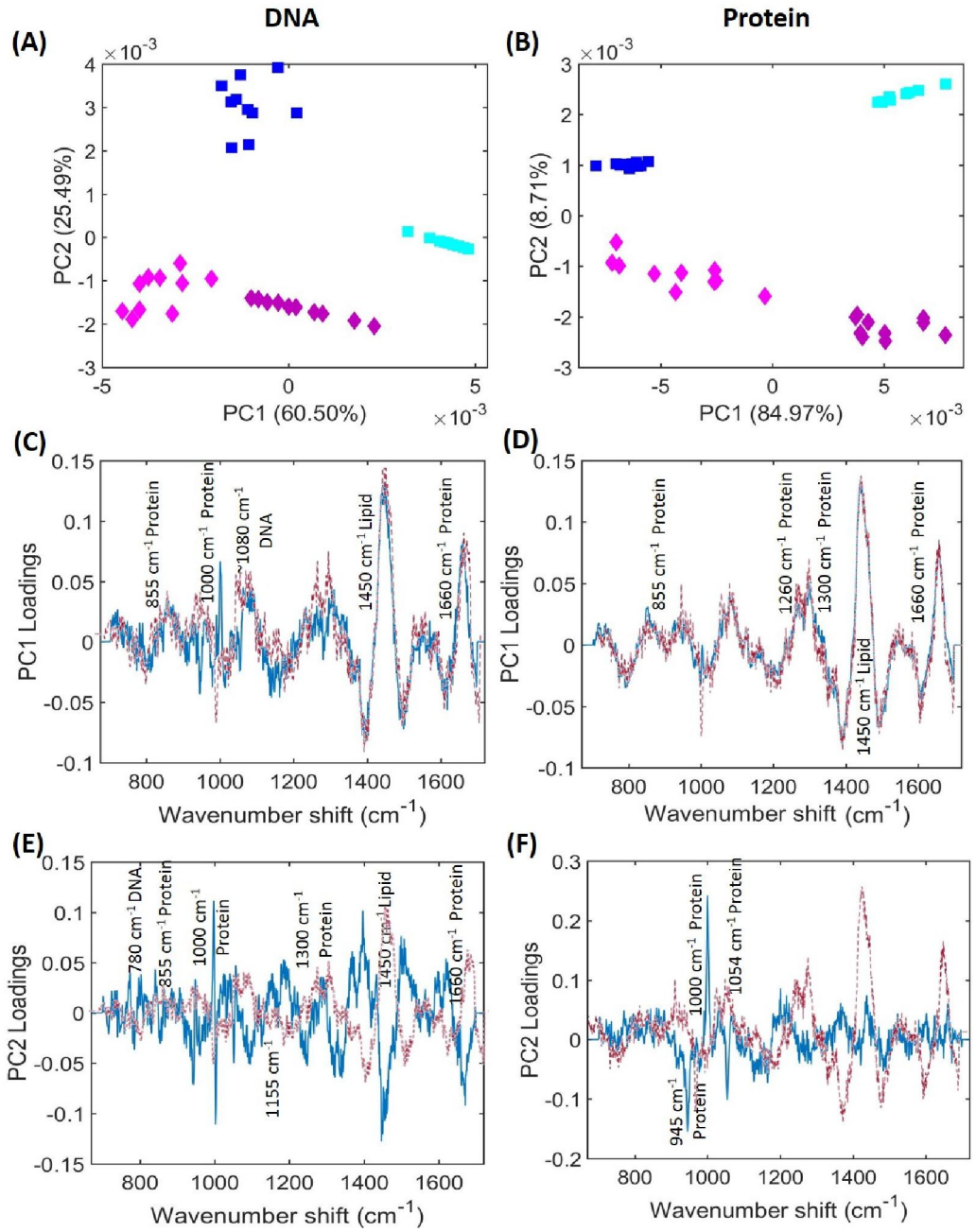

Figure 4.12: A comparison of live cells treated with 10 µM of CBD and control cells after 4 hours of incubation. For PCA-scores plots of PC1 against PC2, spectra were taken from regions of the cell identified as having a high DNA **(A)** or protein **(B)** content. Squares cells treated with 10 µM of CBD (n=2), and diamonds cells treated with a media control (n=2). Each colour represents an individual cell. The PC1 loadings for each plot are shown in **(C and D)**, and the baselined spectra of treated (orange) and control (blue) cells, averaged from the 10 spectra used for PCA are shown in **(E and F)**. The benchmark loadings are indicated by the red dotted line.

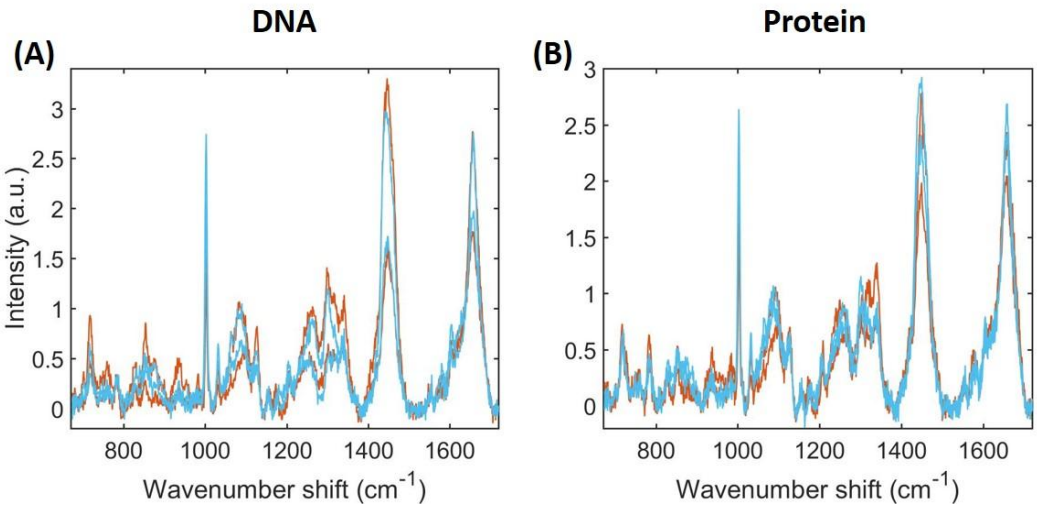

Figure 4.13: Average spectra of live cells treated with 10 µM of CBD and control cells after 4 hours of incubation. Baselined spectra of treated (orange) and control (blue) cells, averaged from the 10 spectra used for PCA are shown from **(A)** regions of high nucleic acid content, and **(B)** regions of high protein content.

Figure 4.12 shows the PCA data from 4 hours of incubation. Both PCA-scores plots show that treated and control cells separate from one another along PC2, indicating that the drug has had an effect on treated cells by 4 hours of incubation. In addition, both treated cells separate from one another along PC1, suggesting that the effect of the drug is not the same in both cells, and demonstrating how different cells can react differently to the same stimulus. The PC1 loadings overlap with the benchmark plot, and therefore reflect differences between different cells. The PC2 loadings therefore show which peaks are changing in response to the drug. Figure 4.12E shows the PC2 loadings plot for spectra taken from the nucleus of cells, and shows several peaks that are different in comparison to the benchmark plot, particularly changes in DNA (780 cm^{-1}), protein (1000 cm^{-1}, 1300 cm^{-1}, 855 cm^{-1}, and 1660 cm^{-1}) and lipid (1450 cm^{-1}) peaks. There were also changes in the peak at 1155 cm^{-1}, which has been previously been assigned to C-C stretching in carotenoids (Merlin, 2007; Ermakov and Gellermann, 2010; Addis *et al.*, 2016). In the PC2 loadings plot from spectra taken from the

cytoplasm of cells (figure 4.12F), there were changes in protein (945 cm^{-1}, 1000 cm^{-1}, 1054 cm^{-1}) peaks.

Overall, this could be indicative of differences in the level of DNA and protein in treated cells in comparison to control cells. However, the average spectra (figure 4.13A and B) show only one peak that is increased in treated cells in comparison to control cells, at ~1340 cm^{-1}; this difference appears to be present only in spectra taken from the nucleus of cells. This peak can be assigned to the nucleic acids A and G (Chan *et al.*, 2007; Su *et al.*, 2013; Casabella *et al.*, 2016), and only one treated cell appears to have an increase in this peak. It may therefore mean that this cell contains more nucleic acids than the other three cells, and the increases seen in this peak are not as a result of the drug. It is therefore difficult to determine the effect of the drug at this timepoint, as there are no clear increases or decreases in the intensity of protein peaks in treated cells in comparison to control cells.

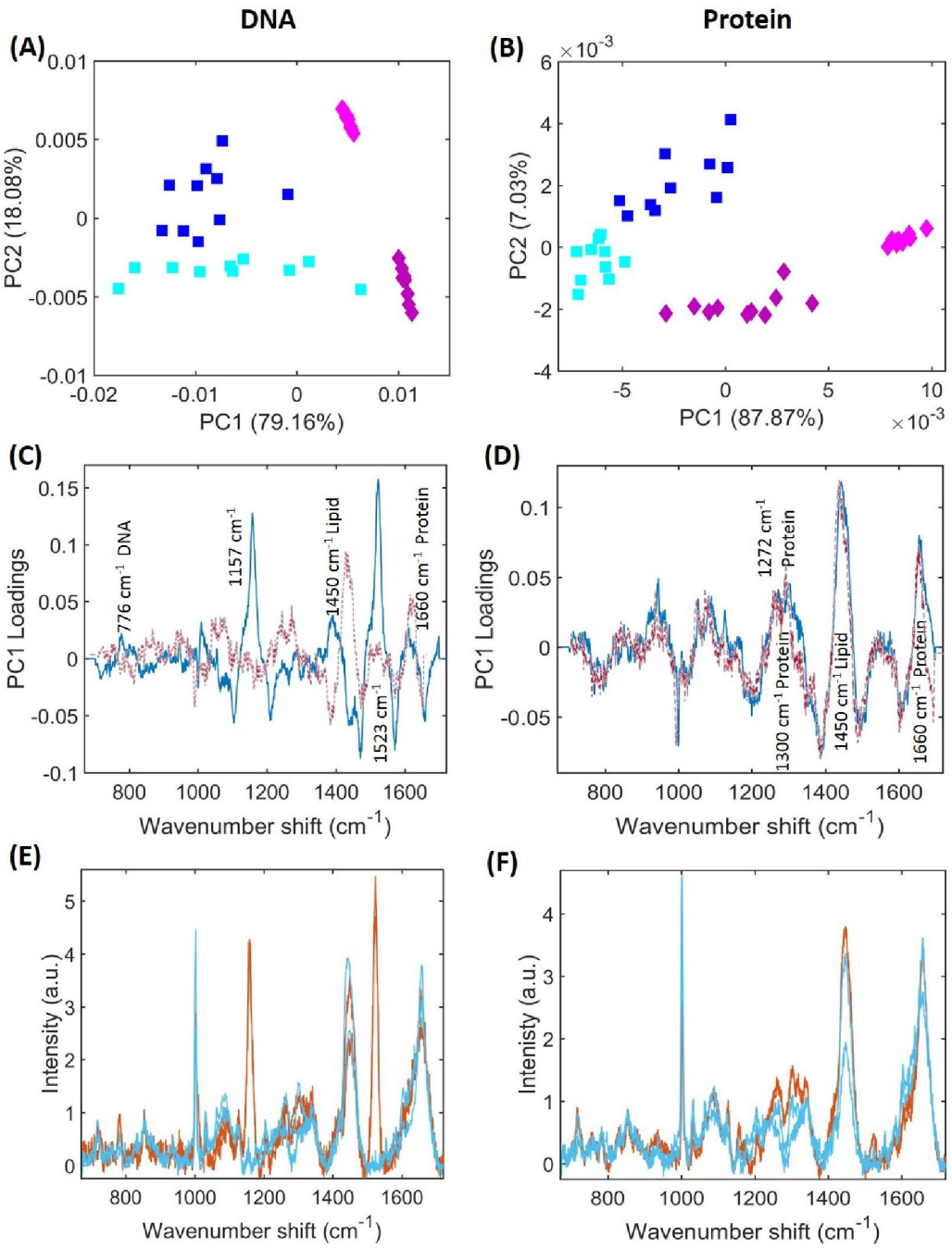

Figure 4.14: A comparison of live cells treated with 10 µM of CBD and control cells after 20 hours of incubation. For PCA-scores plots of PC1 against PC2, spectra were taken from regions of the cell identified as having a high DNA **(A)** or protein **(B)** content. Squares cells treated with 10 µM of CBD (n=2), and diamonds cells treated with a media control (n=2). Each colour represents an individual cell. The PC1 loadings for each plot are shown in **(C and D)**, and the baselined spectra of treated (orange) and control (blue) cells, averaged from the 10 spectra used for PCA are shown in **(E and F)**. The benchmark loadings are indicated by the red dotted line.

Figure 4.14 shows the PCA data from 20 hours of incubation. The nucleus of treated cells had broken down by 20 hours, but the Raman maps did appear to show some areas with a high nucleic acid concentration, so spectra from these areas were used for PCA. The PCA-scores plots show a clear separation of treated and untreated cells, and both treated cells group together. The PC loadings from spectra taken from the cytoplasm (figure 4.14D) showed that most peaks overlapped with the benchmark loadings, but there were some changes in protein (1272 cm^{-1}, 1300 cm^{-1}, 1660 cm^{-1}) peaks. The average spectra showed a change in the region 1200-1400 cm^{-1}, associated with amide III. Peaks in this region, particularly 1260 cm^{-1} and 1300 cm^{-1}, appear to be increased in treated cells, which could indicate an increased level of protein within treated cells. However, as the cytoplasm of both cells appears to begin breaking down at 22 hours of incubation with CBD, it seems unlikely that there would be an increased level of protein within the cells, as the induction of cell death would result in proteins being broken down. Changes in this region could therefore be as a result of changes in secondary structure. The amide III region comprises of a combination of N-H bending and C-N stretching of the amide group, and these vibrational modes are particularly sensitive to changes in secondary structure (Lord, 1977; Overman and Thomas, 1998; Jacob, Luber and Reiher, 2009). Both of the increased peaks (1260 cm^{-1} and 1303 cm^{-1}) have been previously associated with α-helix secondary structures (Maiti *et al.*, 2004; Esmonde-White *et al.*, 2009), suggesting that treated cells may have an increased level of proteins in an α-helix conformation in comparison to control cells. As mentioned previously (chapter 4, section 4.3.4), changes in secondary structure has been associated with the induction of cell death (Czamara *et al.*, 2016).

The PC loadings from spectra taken from areas with a high DNA content (figure 4.14C) were very different when compared to the benchmark loadings, with very few peaks overlapping. There were changes in DNA (776 cm^{-1}), lipid (1450 cm^{-1}) and protein (1660 cm^{-1}) peaks, but the greatest changes were in peaks at 1157 cm^{-1} and 1523 cm^{-1}. Both of these peaks have a high intensity in the average spectra of cells treated with CBD, but are not present in spectra from

control cells, and neither of these peaks had increased in intensity in spectra taken from the cytoplasm of cells. This suggests that these peaks are not present within the cell, as spectra corresponding to nucleic acids were taken from outside of the cell. These peaks are therefore likely to be present outside of the cell and in the medium. To confirm this, spectra were taken from areas from outside of both control and treated cells (figure 4.15). This figure shows that neither of these two peaks are present in spectra taken from control cells at any timepoint. However, when looking at the spectra from treated cells, these peaks are not present at either pre-treatment or 0 hours of treatment with CBD, but are present by 18 hours of incubation. This suggests that these peaks are likely to be a result of the drug, and not a result of repeated exposure to the laser. They are also unlikely to belong to the drug itself as we would expect them to be in the spectra at 0 hours, as the drug has been added to the medium. The 1157 cm^{-1} peak can be assigned to C-C and C-N stretching in proteins (De Gelder *et al.*, 2007; C. *et al.*, 2012; Bai *et al.*, 2015), as well as to carotenoids (Hata *et al.*, 2000), while the 1523 cm^{-1} peak has previously been assigned to both C=C stretching in carotenoids (Stone *et al.*, 2004; Yao *et al.*, 2009; Talari *et al.*, 2015), and the nucleic acid cytosine (Li *et al.*, 2013). Increases in these peaks could therefore be due to increased level of nucleic acids in the medium surrounding treated cells as they are exported from the cell as a result of the response to the drug. However, the fact that both peaks have been previously assigned to carotenoids suggests that they may be present in the media.

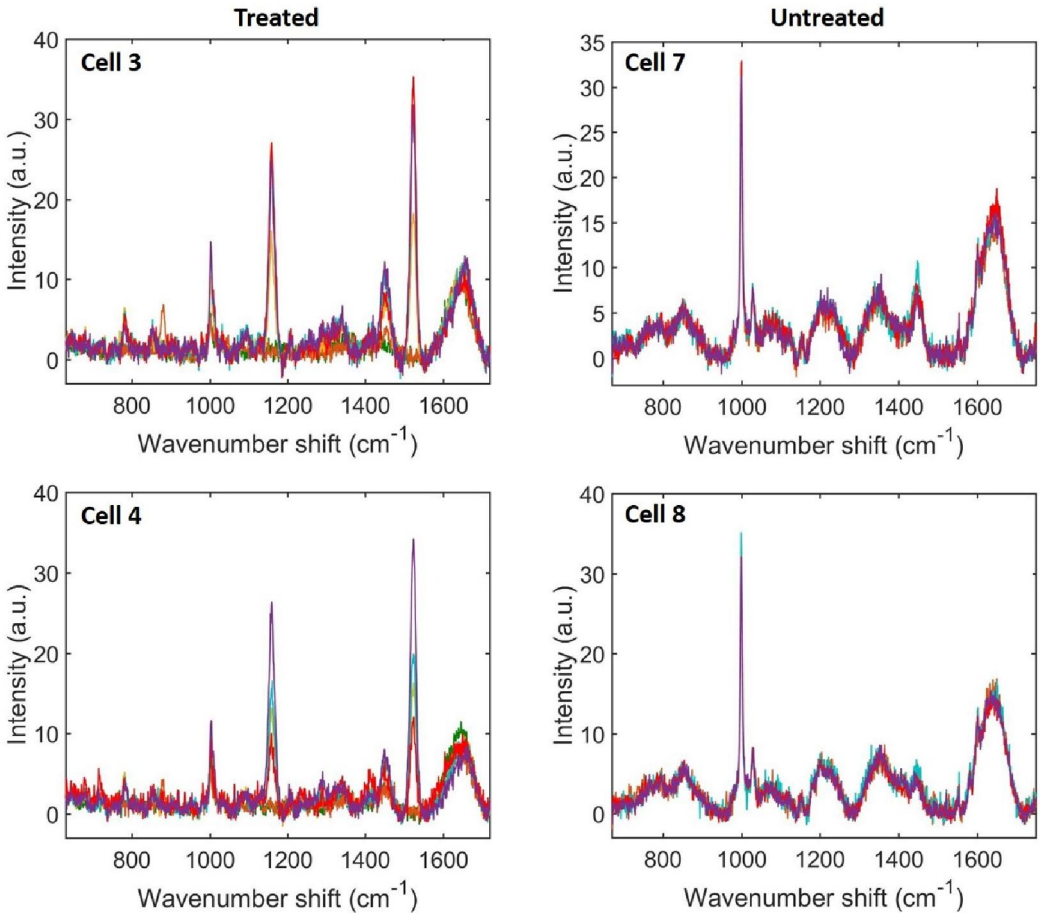

Figure 4.15: A comparison of average spectra from treated and untreated live cells. Spectra were taken from areas identified as being outside of the cell from the Raman maps, and averaged and baselined prior to being plotted. Each colour represents a different timepoint: pre-treatment (red), 0 hours (orange), 18 hours (yellow), 20 hours (dark red), 22 hours (green) and 24 hours (purple).

4.4 Discussion:

Overall, these results suggest that different concentrations of the cannabinoid drug CBD affect Caco-2 cells in different ways. A low concentration of CBD induces a change in Caco-2 cells that can be seen after just two hours of incubation with the drug. This change appears to be due to a difference in the DNA, protein and lipid content within treated cells in comparison to controls, and may induce proliferation in cells at this concentration. This effect appears to be a short-term effect, as there was little separation in any of the other PCA plots between cells treated with 1 µM of CBD and control cells.

In contrast, at a higher concentration, the drug appears to only begin to have an effect after 4-6 hours of incubation, and appears to result in cell death. The Raman maps of fixed cells showed that by 24 hours, the DNA of cells had broken down, and the cytoplasm was beginning to break down (figure 4.4). The PCA and average spectra data from both 8 (figure 4.8) and 24 (figure 4.9) hours of incubation with CBD showed several peaks associated with cell death, including decreased lipid and protein levels in treated cells in comparison to control cells, the presence of a peak at 1375 cm^{-1} that has previously been used as a marker for apoptosis, changes in cytochrome c, and a shift from ~1266 cm^{-1} to ~1254 cm^{-1}, previously associated with a transition in protein structure as a result of the activation of caspases (Czamara *et al.*, 2016), suggesting that caspases may be involved in the pathway of cell death that CBD activates in Caco-2 cells. Caspases are a family of endoproteases that have an important role in the regulation of cellular processes, but particularly in cell death. Activation of apoptotic caspases results in the generation of a signalling cascade that culminates in the induction of apoptosis (McIlwain, Berger and Mak, 2013), which may occur in cells incubated with high concentrations of CBD.

The live cell data expanded on the results collected from fixed cells, providing more detailed information on the cells response to the drug. The Raman maps suggested that CBD caused the breakdown and externalisation of DNA in Caco-2 cells at ~18 hours of incubation, followed by the degradation of the cytoplasm after 24 hours (figure 4.12). The breakdown and loss of DNA is associated with cell death, and there are considered to be three main nuclear morphological changes associated with this process. Pyknosis is nuclear condensation, and can be visualised by the shrinkage of the nucleus (Burgoyne, 1999; Hou *et al.*, 2016). Karyorrhexis is characterised by the breakdown of DNA into small fragments (Nagata, 2000). Finally, karyolysis is the breakdown and loss of DNA as a result of the action of endonucleases. Usually, upon the induction of cell death, pyknosis is the first of these changes to occur, which is followed by either karyorrhexis or karyolysis (Kroemer *et al.*, 2009; Kumar, 2012).

Karyorrhexis, or DNA fragmentation, is a hallmark of apoptosis, and occurs as a result of the activation of caspase-3 activated DNase (CAD), which cleaves chromosomal DNA into small fragments (Nagata, 2000). Earlier results suggested that caspases may be involved in the mechanism of cell death CBD induces in Caco-2 cells, however, the Raman maps do not appear to show any fragmentation, and there do not appear to be any apoptotic bodies present, which suggests that the process of cell death CBD induces in Caco-2 cells may not be apoptosis.

The PCA results from the live cell maps revealed the presence of two peaks, 1157 cm^{-1} and 1523 cm^{-1}, that are present in the medium surrounding treated cells, but not in control cells. These two peaks have been associated with proteins and nucleic acids respectively, but are also characteristic of carotenoids (Hata *et al.*, 2000). In carotenoids, the 1157 cm^{-1} peak corresponds to C-C stretch vibrations, and the 1523 cm^{-1} peak to C=C stretches (Koyama *et al.*, 1988). Carotenoids are a family of compounds, fat-soluble plant pigments that eukaryotic cells are unable to synthesise (Krinsky and Johnson, 2005). Due to this, it seems unlikely that carotenoids would be present in the medium, as they are not components of the medium itself (Sigma-Aldrich), so these peaks may be attributed to different cellular components that contain the same C-C and C=C stretches. The structure of CBD contains both C-C and C=C bonds, so it is possible that these peaks may correspond to the drug, although these peaks were not present in the spectrum of CBD (figure 4.2). They may therefore be a result of the metabolites that CBD is broken down into when metabolised by cells. There are many known metabolites of CBD, making it difficult to identify which specific ones may be present in media surrounding treated cells, and to identify their structure, although most of the major metabolites contain both types of carbon bond (Ujváry and Hanuš, 2016). As previous studies have also linked these two peaks with proteins and nucleic acids, it is possible that the medium surrounding treated cells contains nucleic acids and proteins. The Raman maps appear to support this, as the DNA of treated cells seems to be externalised, and if the cytoplasm of the cell is also breaking down, as seen in some of the maps, then proteins would also be

externalised as a result of the cellular response to CBD. Further investigation needed to be carried out in order to confirm if there were nucleic acids or proteins present in medium from treated cells, and this was done using UVRR spectroscopy (chapter 6, section 6.3.4).

In summary, we have investigated the effect of the cannabinoid drug cannabidiol on Caco-2 cells using Raman spectroscopy. CBD appears to have a dual effect on Caco-2 cells: at a low, 1 µM concentration, it may induce proliferation, but at a higher, 10 µM concentration, it appears to cause cell death. However, this data does not elucidate the mechanism of action of the drug, or how it is able to induce cell death in Caco-2 cells and the pathway by which this process occurs. Further work was therefore carried out in order to further investigate the way in which CBD induces death in Caco-2 cells (chapter 6).

Chapter 5: Using Raman spectroscopy to evaluate the effect of anandamide on Caco-2 cells

5.1 Introduction:

Anandamide (AEA) is an endocannabinoid, a fatty acid neurotransmitter derived from arachidonic acid. The structure of AEA is shown in figure 5.1. It targets the CB_1 and CB_2 receptors, as well as vanilloid receptors (Di Marzo, 1998; Pertwee, 2001). Once inside cells, AEA is broken down by the enzyme fatty acid amide hydrolase (FAAH) into arachidonic acid and ethanolamine (Maccarrone and Finazzi-Agró, 2003). Previously, AEA has been reported to have an antiproliferative effect in a breast cancer cell line (MCF-7), by arresting growth at the G_1/S transition (De Petrocellis *et al.*, 1998). It has also been associated with the induction of apoptosis in lymphocytes (Schwarz, Blanco and Lotz, 1994), keratinocytes (Kuc, Jenkins and van Dross, 2012) and neuroblastoma cells (Maccarrone *et al.*, 2000; Pasquariello *et al.*, 2009), although the mechanism of AEA-induced apoptosis is yet to be elucidated.

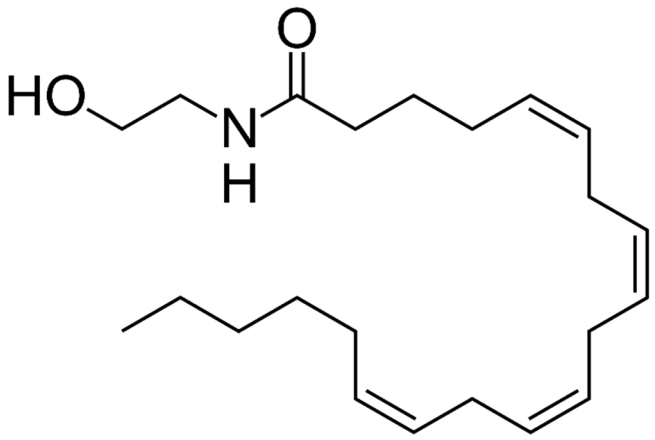

Figure 5.1: Molecular structure of anadamide.

The aim of this chapter was to investigate whether other cannabinoids would affect Caco-2 cells in the same or a different way to CBD. As AEA is known to be taken up by cells, and has previously been shown to have an effect on Caco-2 cells (Liao *et al.*, 2011), it is an ideal candidate to use with Raman spectroscopy, in order to investigate if the drug can be visualised within cells, and to determine if its effect on Caco-2 cells can be monitored using Raman spectroscopy.

5.2 Methods:

5.2.1 Cell treatment

Caco-2 cells were cultured and attached to CaF_2 windows as described in the methods (chapter 2. Section 2.2.2). Once cells had adhered to CaF_2 windows, media was removed and replaced with media containing AEA at a concentration of either 1 µM, 10 µM or media control. After 2, 4, 6, 8 or 24 hours of incubation, media was removed and cells were fixed as previously described.

5.2.2 Raman spectroscopy of fixed cells

Fixed cells were maintained in PBS throughout analysis. Raman maps were collected as described in the methods (chapter 2, section 2.2.4), using a laser wavelength of 532 nm.

5.2.3 Raman spectroscopy of live cells

Once adhered to CaF_2 windows, cells were transported to the Raman incubator and maintained at 5% CO_2 and 37°C. In this study, all live cells were mapped using a laser wavelength of 532 nm. Media was removed once cells were in the Raman incubator, and replaced with media containing AEA at a concentration of 10 µM. Cells were then mapped at the times described.

5.3 Results:

5.3.1 Raman maps

The overall aim of this study was to determine the effect of AEA on Caco-2 cells, and to see how it compares to the effect of CBD. Initially, we wanted to investigate whether the drug could be visualised within Caco-2 cells, so a spectrum of the drug was acquired (figure 5.2).

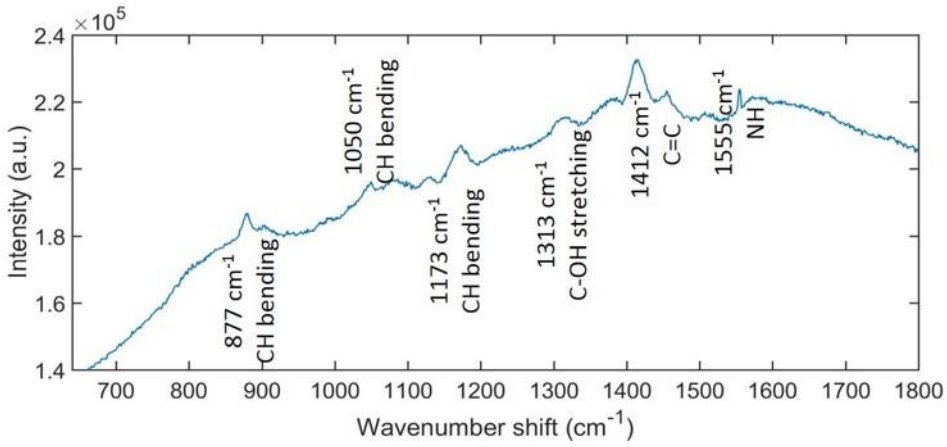

Figure 5.2: Raman spectrum of AEA, spotted and left to dry on a CaF_2 disk. The spectrum was acquired using a 532 nm excitation laser, an acquisition time of 10 seconds with 10 accumulations, and a laser power of ~30 mW. The molecular structure of AEA is also shown.

This spectrum shows several peaks of interest, at 877 cm^{-1}, 1050 cm^{-1}, 1173 cm^{-1}, 1313 cm^{-1}, 1412 cm^{-1}, and 1555 cm^{-1}, related to the structure of the drug, which is also shown. Peaks at 877 cm^{-1}, 1050 cm^{-1} and 1173 cm^{-1} are assigned to CH bending (Jones, 2009; Bai *et al.*, 2015; Boutahir *et al.*, 2016), whereas peaks in the region of 1313 cm^{-1} have previously been associated with C-OH stretching (Perna, Lasalvia and Capozzi, 2016). Peaks at around 1412 cm^{-1} have been assigned to C=C vibrations (Perna, Lasalvia and Capozzi, 2016). Finally, peaks at 1555 cm^{-1} are assigned to NH vibrations (Thomas, 2004). In order to investigate whether the drug could be visualised within cells, Raman maps were shaded to each of these peaks (figure 5.2). The shading ranges used were as follows: 874-880 cm^{-1} (877 cm^{-1}), 1047-1053 cm^{-1} (1050

cm^{-1}), 1170-1176 cm^{-1} (1173 cm^{-1}), 1310-1316 cm^{-1} (1313 cm^{-1}), 1409-1415 cm^{-1} (1412 cm^{-1}), and 1552-1558 cm^{-1}).

Figure 5.3 shows composite images of treated and control cells alongside Raman maps of them shaded to each of the drug peaks. It shows that all shaded peaks can either not be seen within either treated or control cells, or are present in both treated and control cells, suggesting that the drug cannot be visualised within cells by shading to these peaks. This was the case even when the shading parameters were altered. AEA is known to enter cells, but once inside it is rapidly broken down (Maccarrone and Finazzi-Agró, 2003), which may be why we cannot visualise the drug within cells using this method, or, as we saw with CBD, the drug peaks may be overshadowed by cellular components.

Raman maps were also shaded according to their DNA (780-802 cm^{-1}) and protein (1630-1680 cm^{-1}) content and composite images produced at each time point in order to see if any visible changes could be observed as a result of drug treatment (figure 5.4). Maps were shaded according to the previously established parameters (chapter 2, section 2.3.3).

The Raman maps do not show any clear visual differences between cells that have been treated with the drug, and control cells. Even after 24 hours of incubation, treated cells at both the 1 µM and 10 µM concentration appear to show no deterioration, and, unlike cells that have been treated with CBD, still contain DNA, and their cytoplasm appears to be intact. Therefore, to gain a better understanding of the effect of AEA on Caco-2 cells, PCA was carried out on selected spectra.

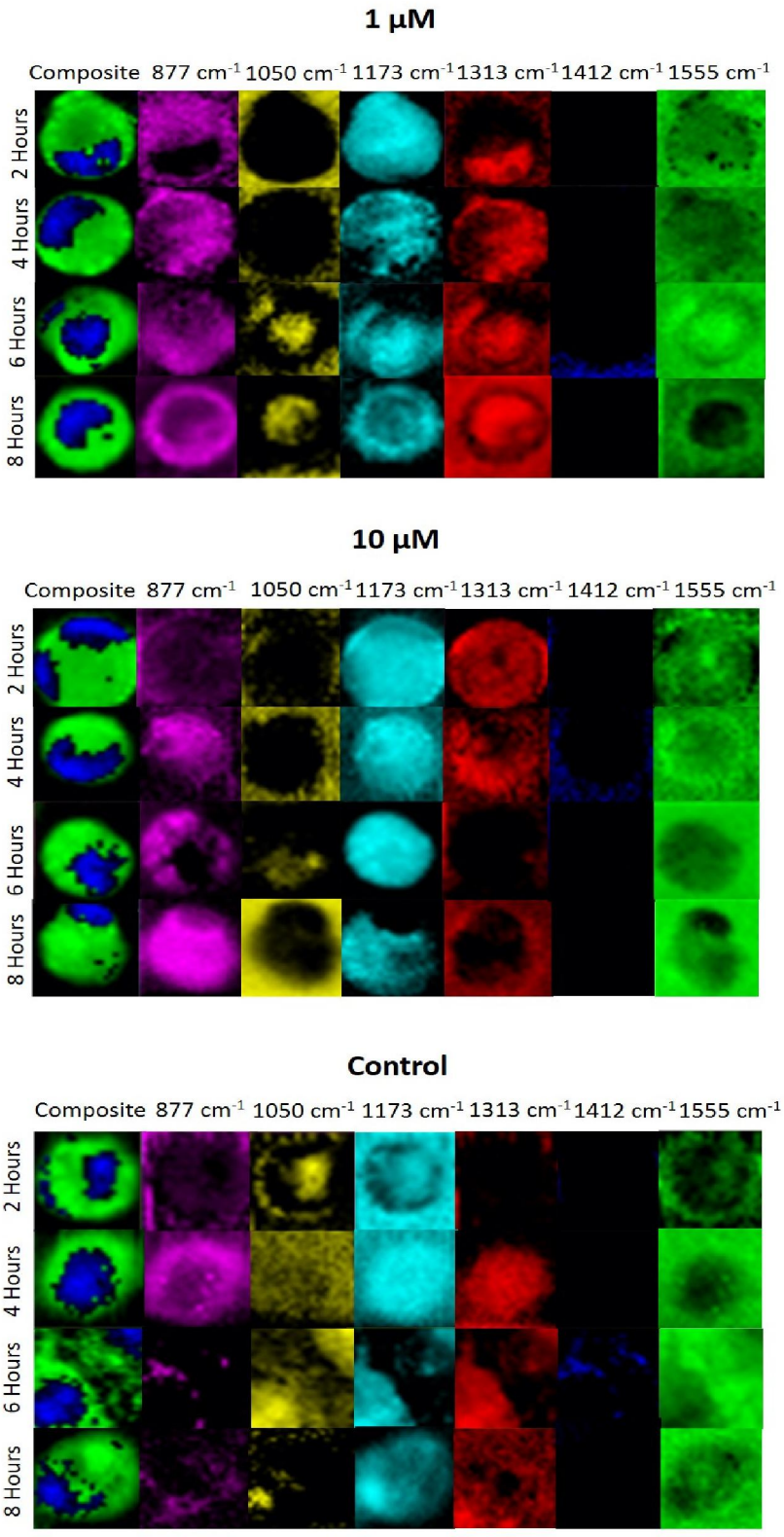

Figure 5.3: Raman maps of Caco-2 cells shaded to peaks of interest from the AEA spectrum. For the composite images, DNA was measured from 780-802 cm^{-1}, and protein from 1630-1680 cm^{-1}. When shading to peaks of interest from the AEA spectrum, all selected peaks were shaded from 0 to max.

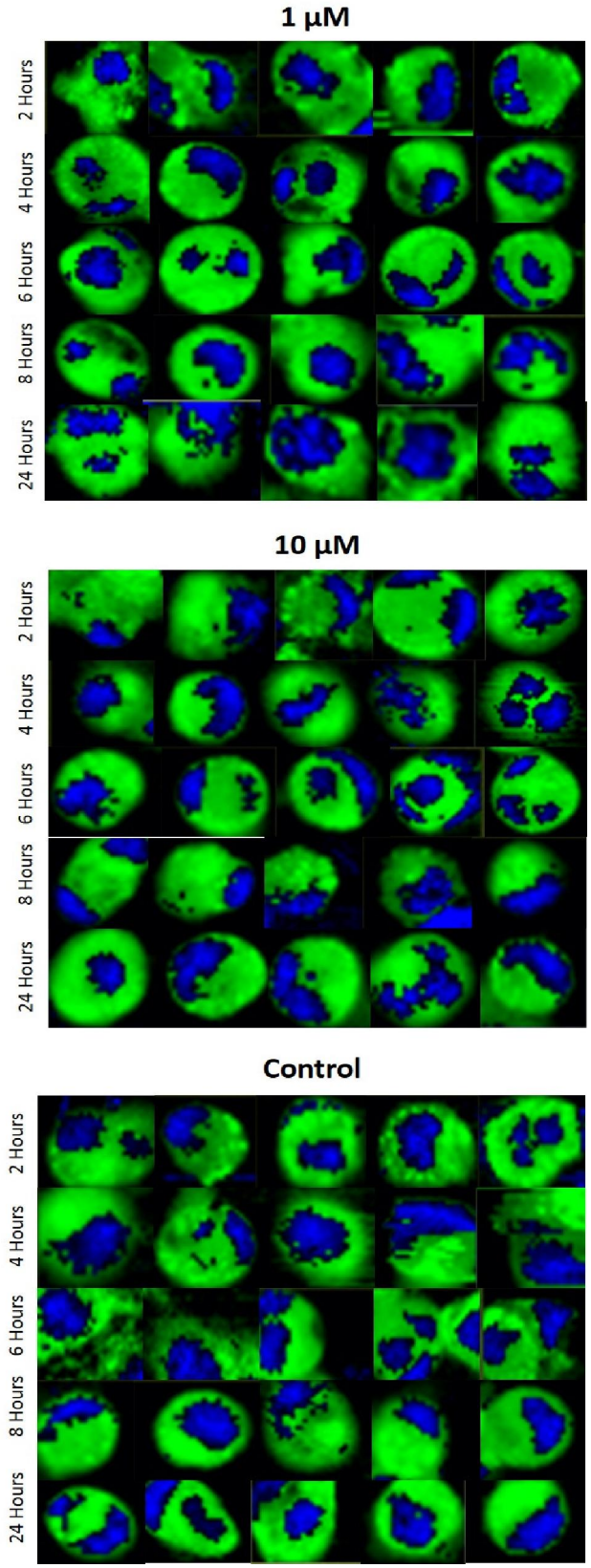

Figure 5.4: Raman maps of Caco-2 cells shaded to their DNA and protein content. Shading ranges were 780-802 cm^{-1} for DNA, blue, and 1630-1680 cm^{-1} for protein, green. Cells were treated with either 1 or 10 µM of AEA or media control for each listed time point.

5.3.2 Principal Component Analysis

As demonstrated in previous chapters, PCA was carried out using Raman spectra selected from each of the Raman maps in figure 5.4. Ten spectra were selected from DNA-rich regions, and ten from protein-rich regions in order to better establish which areas of the cell the drug may be having an effect.

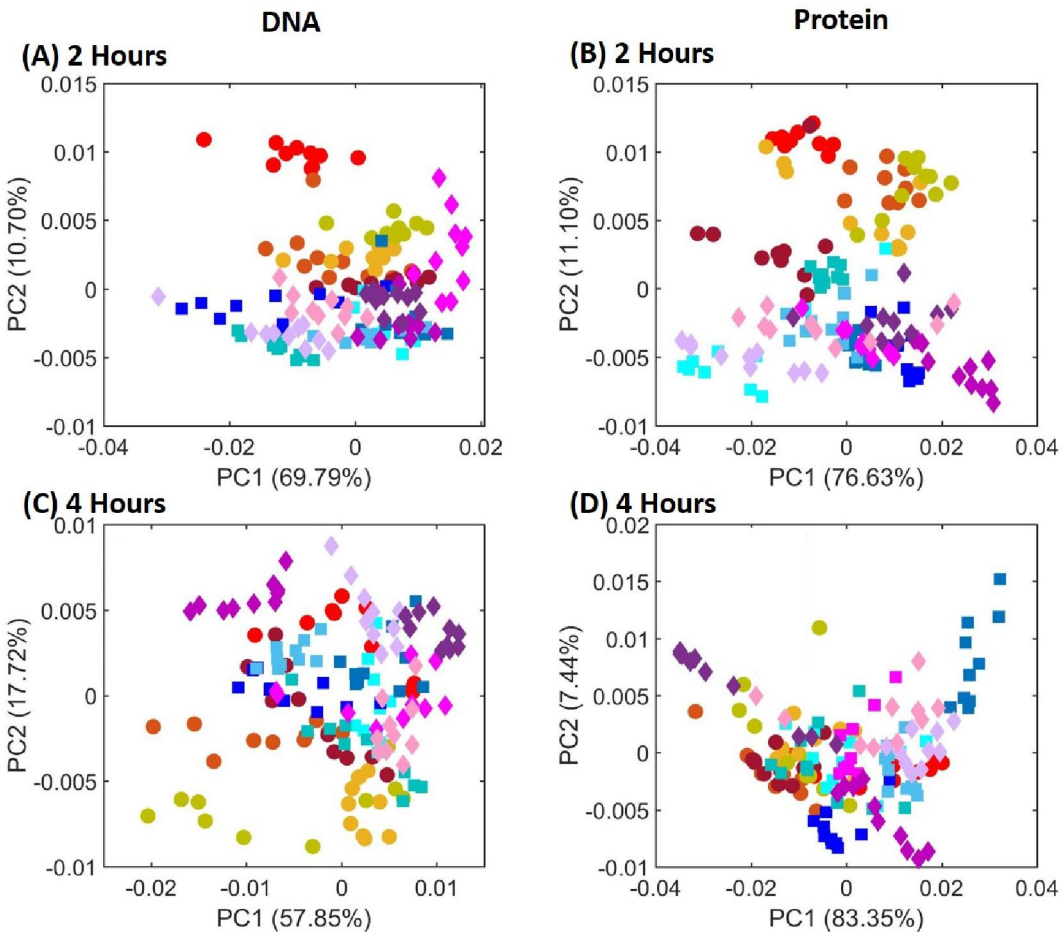

Figure 5.5: PCA-scores plots of PC1 against PC2 for spectra taken from cells treated with either AEA or media control for 2 and 4 hours. Spectra were taken from regions of the cell identified as having a high DNA content after an incubation time of either 2 **(A)** or 4 **(C)** hours, or from regions with a high protein content after either 2 **(B)** or 4 **(D)** hours of incubation. Circles represent cells treated with 1 µM of AEA (n=5), squares cells treated with 10 µM of AEA (n=5), and diamonds cells treated with a media control (n=5). Each colour represents an individual cell.

Figure 5.5 shows the PCA scores plots for 2 and 4 hours of incubation with AEA. At 2 hours, there was some separation seen at the 1 μM concentration of the drug, and this separation can be seen in both the nucleus and cytoplasm of cells, suggesting that the drug has had an effect at this concentration after just 2 hours of incubation. At 10 μM, there did not seem to be any clear separation of treated cells from control cells, suggesting that at this concentration the drug may take longer to have an effect on cells, similar to that observed with CBD at this timepoint. At 4 hours, there was little separation between treated cells and control cells in the protein PCA-scores plot, with all cells appearing to group together. This suggested that the drug had no effect on the cytoplasm of cells at either concentration after 4 hours of incubation. Several cells at 1 μM separate from control cells in figure 5.5C, suggesting that the drug may be affecting the nucleus of these cells; no separation can be seen for the 10 μM concentration of the drug.

PCA was also carried out on data collected from the maps at 6, 8 and 24 hours (figure 5.6). At 6 hours, there appeared to be little separation of treated cells at either concentration of AEA in the DNA PCA-scores plot, suggesting that the drug does not have an effect on the nucleus of cells after 6 hours of incubation. However, in the protein PCA-scores plot (figure 5.6B), some cells treated with 10 μM of AEA begin to separate from control cells; there is no separation between cells treated with 1 μM. This suggests that the initial effect of the 1 μM concentration of AEA is short-lived, and is resolved by 6 hours of incubation, whilst the effect of the 10 μM concentration only begins to occur after ~6 hours of incubation. By 8 hours of incubation, most cells treated with 10 μM of AEA separate from controls in the DNA PCA-scores plot, and all cells separate in the protein PCA-scores plot.

A similar separation can be seen after 24 hours of treatment, as cells treated with 10 μM of AEA separate from controls in both spectra taken from the nucleus and cytoplasm of cells (figure 5.6E and F). This differs from the PCA-scores plots after cells were treated with CBD, as

with those results there was a dramatic effect after 24 hours, as there was no DNA left in the cell to compare to control cells, and for protein taken from the spectra, there was a very clear separation between treated and control cells. This further demonstrates that the effects of the cannabinoids CBD and AEA, at a 10 µM concentration, are very different in Caco-2 cells. Aside from one cell in figure 5.6E, all cells treated with 1 µM of AEA group with the controls in both plots, further suggesting that the effect of this concentration of the drug is short-term, which is similar to that observed with CBD at the same concentration.

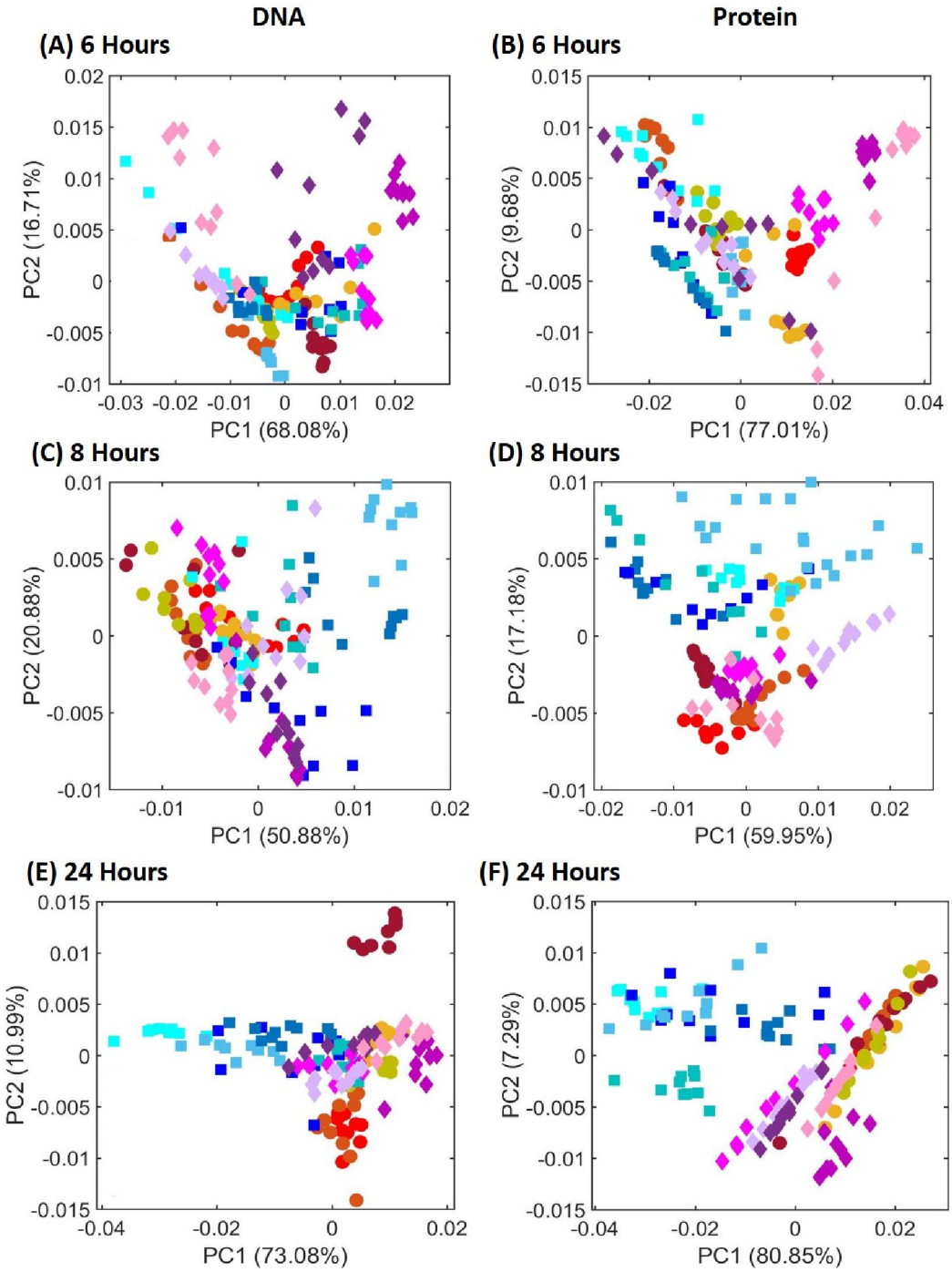

Figure 5.6: PCA-scores plots of PC1 against PC2 for spectra taken from cells treated with either AEA or media control for 6, 8 and 24 hours. Spectra were taken from regions of the cell identified as having a high DNA content after an incubation time of either 6 (**A**), 8 (**C**) or 24 (**E**) hours, or from regions with a high protein content after either 6 (**B**), 8 (**D**) or 24 (**F**) hours of incubation. Circles represent cells treated with 1 µM of AEA (n=5), squares cells treated with 10 µM of AEA (n=5), and diamonds cells treated with a media control (n=5). Each colour represents an individual cell.

5.3.3 PCA and Average Spectra – Initial Response

In order to further investigate the effect of AEA on Caco-2 cells, the number of conditions compared in the PCA-scores plots was reduced. In the initial PCA plots (figure 5.5), the greatest changes were occurring in cells treated with 1 μM of AEA for 2 hours, so PCA was carried out to compare only cells treated with this concentration of the drug and control cells (figure 5.6). As in the previous chapters, a benchmark loading plot was included alongside each PC loadings plot.

The PCA-scores plots show a clear separation between treated and control cells for spectra taken from the cytoplasm of cells (figure 5.6B), while only one treated cell separates clearly for spectra taken from the nucleus of cells. This suggests that the drug has an effect on the cytoplasm of cells after 2 hours of incubation, but not on the nucleus of all cells. The separation occurs along PC2, suggesting that the PC1 loadings show differences between cells and are not a result of the drug; this is demonstrated by the fact that they clearly overlap with the benchmark plot.

The PC2 loadings plots (figure 5.7E and F) therefore show which peaks are changing as a result of the drug. The peaks that vary from the benchmark correspond to protein (1000 cm^{-1}, 1242 cm^{-1}, 1247 cm^{-1}) and lipids (1450 cm^{-1}, 1582 cm^{-1}). The PC2 loadings plot for spectra taken from the nucleus also shows changes in DNA peaks (780 cm^{-1} and 1332 cm^{-1}). This may indicate a different level of DNA, protein and lipid between treated and untreated cells.

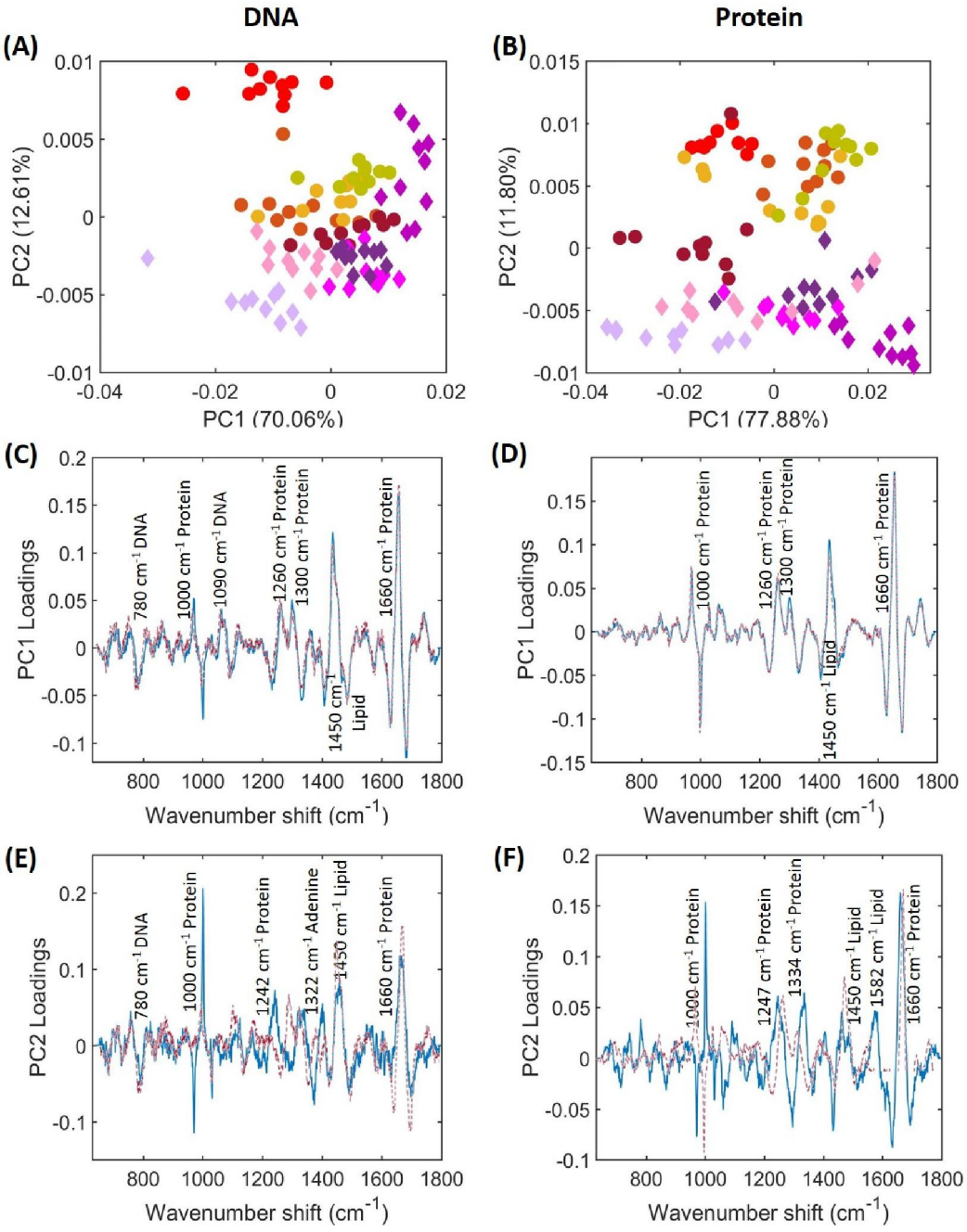

Figure 5.7: A comparison of cells treated with 1 µM of AEA and control cells after 2 hours of incubation. For PCA-scores plots of PC1 against PC2, spectra were taken from regions of the cell identified as having a high DNA **(A)** or protein **(B)** content. Circles represent cells treated with AEA (n=5), and diamonds cells treated with a media control (n=5). Each colour represents an individual cell. The PC1 loadings for each plot are shown in **(C and D)**, and the PC2 loadings are also shown **(E and F).** The red spectrum represents the benchmark loadings. The benchmark loadings are indicated by the red dotted line.

The average spectra (figure 5.8A and B) show that there may be an increase in the protein peaks at ~1260 cm^{-1} in spectra taken from the nucleus and the cytoplasm; there are also increases in the peaks at 1300 cm^{-1} and 1660 cm^{-1} in spectra taken from the cytoplasm. This suggests that AEA may cause an increase in protein level in Caco-2 cells, and as increased protein levels are associated with proliferation (Short *et al.*, 2005; Swain, Jell and Stevens, 2008)(Swain, Jell and Stevens, 2008), it may suggest that AEA, at the 1 µM concentration, induces proliferation in Caco-2 cells. The average spectra from the cytoplasm also show increases in the peaks at 717 cm^{-1} and at 1063 cm^{-1}, which are both assigned to lipids (Kunapareddy, Freyer and Mourant, 2008; Huang *et al.*, 2011; Kopec, Imiela and Abramczyk, 2019), suggesting an increased level of lipids in cells incubated with AEA.

This data gives more information on the effect of the 1 µM concentration of the drug; in order to investigate the effect of the 10 µM concentration, we examined the later timepoints (8 and 24 hours) in more detail.

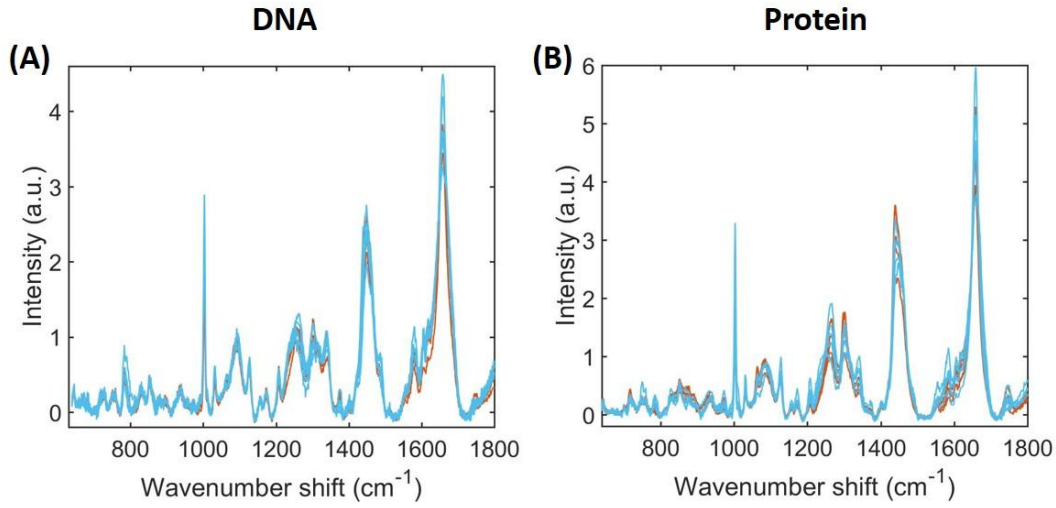

Figure 5.8: Average spectra of cells treated with 1 µM of AEA and control cells after 2 hours of incubation. Baselined spectra of treated (orange) and control (blue) cells, averaged from the 10 spectra used for PCA are shown from **(A)** regions of high nucleic acid content, and **(B)** regions of high protein content.

5.3.4 PCA and Average Spectra – Later Response

Figure 5.9 shows the PCA-scores plots from 8 hours of incubation at a 10 μM concentration of AEA. There is a clear separation between treated and untreated cells in spectra taken from protein-rich regions. In the PCA-scores plot for spectra taken from DNA-rich regions, not all cells separate from controls. Overall, this suggests that, at 10 μM, AEA has an effect on the cytoplasm of all cells after 8 hours of incubation, but only effects the nucleus of some cells.

In figure 5.9A, the separation occurs along PC1, but the loadings plot shows that most peaks overlap with the benchmark plot, so may correspond to differences between cells. The only difference appears to be in the ratio of the 1260 cm^{-1} and 1300 cm^{-1} protein peaks, with the former decreased in comparison to the benchmark, and the latter increased. The average spectra (figure 5.10A), appear to show a decrease in the intensity of some protein (1260 cm^{-1} and 1660 cm^{-1}) and lipid (1450 cm^{-1}) peaks in some treated cells in comparison to control cells, suggesting that some cells incubated with AEA may have a decreased protein and lipid content. Aside from these three peaks, it is difficult to see any clear difference in intensity in any of these peaks in treated cells in comparison to control cells.

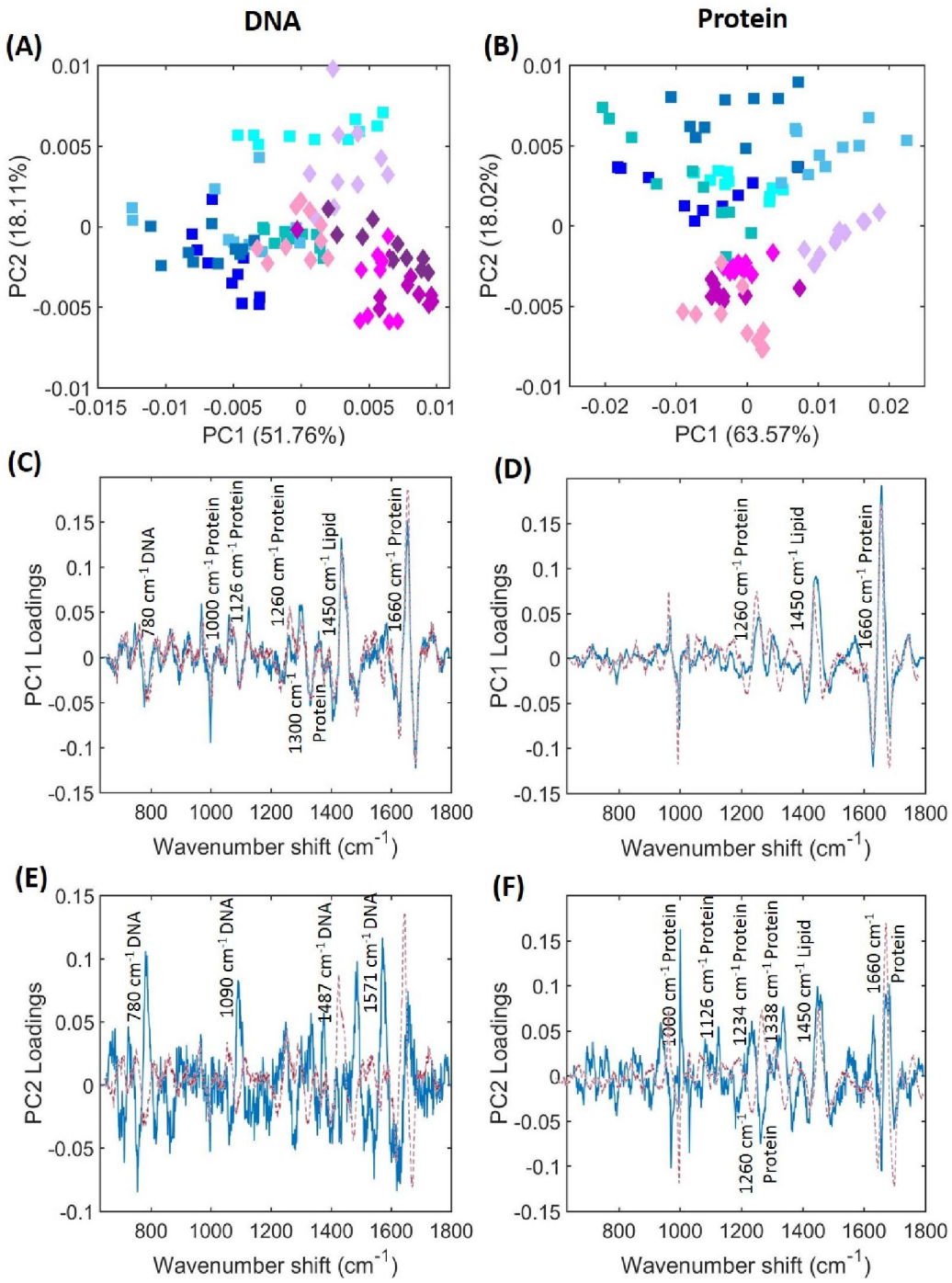

Figure 5.9: A comparison of cells treated with 10 µM of AEA and control cells after 8 hours of incubation. For PCA-scores plots of PC1 against PC2, spectra were taken from regions of the cell identified as having a high DNA **(A)** or protein **(B)** content. Squares represent cells treated with 10 µM of AEA (n=5), and diamonds cells treated with a media control (n=5). Each colour represents an individual cell. The PC1 loadings for each plot are shown in **(C and D)**, and the PC2 loadings are also shown **(E and F).** The red spectrum represents the benchmark loadings. The benchmark loadings are indicated by the red dotted line.

In figure 5.9B, taken from protein-rich areas of the cell, the separation between treated and untreated cells occurs along PC2. The PC2 loadings plot shows the peaks changing as a result of the drug are associated with protein (1000 cm^{-1}, 1126 cm^{-1}, 1234 cm^{-1}, 1260 cm^{-1}, 1338 cm^{-1}) peaks. The average spectra (figure 5.9B), appear to show an increase in intensity of the 1260 cm^{-1} and 1660 cm^{-1} peaks in treated cells in comparison to control cells, and a decrease in intensity of the 1450 cm^{-1} peak. This may indicate an increased level of protein, and a decreased level of lipid in the cytoplasm of cells that have been incubated with AEA. As previously discussed, this is characteristic of proliferating cells (Short *et al.*, 2005; Swain, Jell and Stevens, 2008), which is unexpected as AEA has previously been reported to have an anti-proliferative effect on several different cell lines (Schwarz, Blanco and Lotz, 1994; Maccarrone *et al.*, 2000; Kuc, Jenkins and van Dross, 2012). Interestingly, the average spectra taken from DNA-rich regions of the cell appear to have a decreased protein level in comparison to control cells. In addition, there is the appearance of a small peak at ~970 cm^{-1} in the average spectra of treated cells that is not present in spectra taken from control cells.

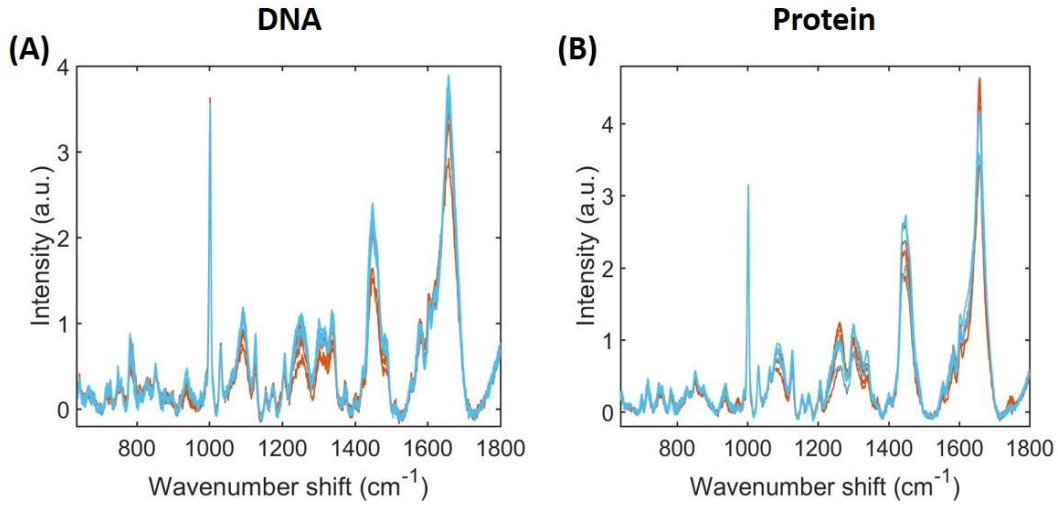

Figure 5.10: Average spectra of cells treated with 1 µM of AEA and control cells after 8 hours of incubation. Baselined spectra of treated (orange) and control (blue) cells, averaged from the 10 spectra used for PCA are shown from **(A)** regions of high nucleic acid content, and **(B)** regions of high protein content.

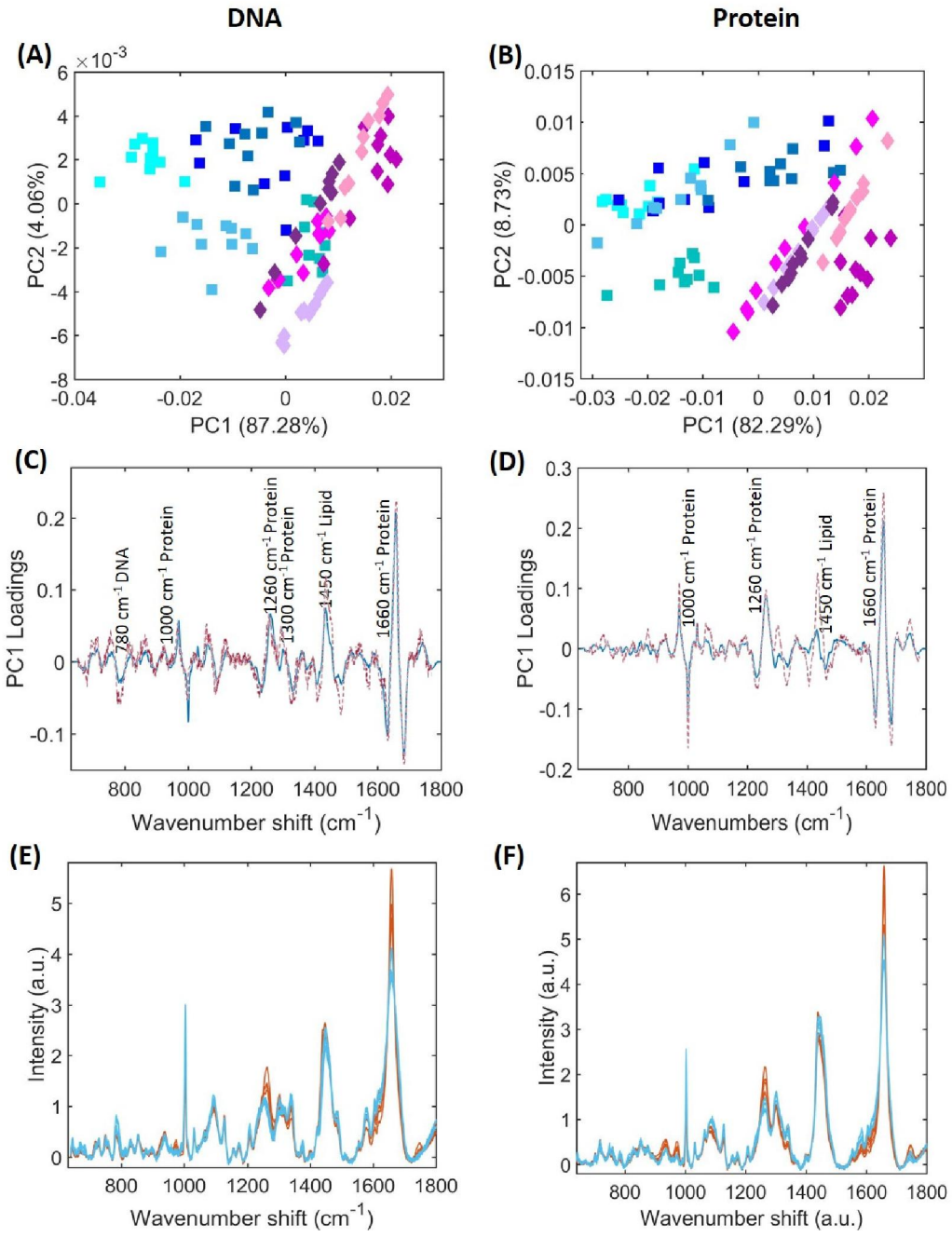

Figure 5.11: A comparison of cells treated with 10 µM of AEA and control cells after 24 hours of incubation. For PCA-scores plots of PC1 against PC2, spectra were taken from regions of the cell identified as having a high DNA **(A)** or protein **(B)** content. Squares represent cells treated with 10 µM of AEA (n=5), and diamonds cells treated with a media control (n=5). Each colour represents an individual cell. The PC1 loadings for each plot are shown in **(C and D)**, and the baselined spectra of treated (orange) and control (blue) cells, averaged from the 10 spectra used for PCA are shown in **(E and F)**. The red spectrum represents the benchmark loadings. The benchmark loadings are indicated by the red dotted line.

After 24 hours of incubation with 10 μM of AEA, aside from one cell, all treated cells separate clearly from control cells (figure 5.11), suggesting that the drug has an effect on both the cytoplasm and nucleus of cells after 24 hours of treatment. This separation occurs along PC1, and for spectra taken from the nucleus (figure 5.11C), the peaks that differ in comparison to the benchmark correspond to DNA (780 cm^{-1}), protein (1300 cm^{-1}) and lipid (1450 cm^{-1}) peaks. The 1300 cm^{-1} and 1450 cm^{-1} peaks are also changing in the loadings plot of spectra taken from the cytoplasm of cells (figure 5.11D). These changes are very subtle in comparison to the changes seen in cells incubated with 10 μM of CBD for 24 hours. The average spectra taken from the nucleus of cells (figure 5.11E) appear to show an increased level of protein in treated cells in comparison to control cells, with increases seen in the 1660 cm^{-1} peak. This is in contrast to what was observed in the average spectra from 8 hours of incubation, where decreased protein levels were observed in the nucleus of some treated cells. However, there is a decrease in the peak at 1340 cm^{-1} in treated cells, and this peak is assigned as a marker for the amino acid tryptophan (Takeuchi, 2003). There is also a shift from 1252 cm^{-1} in control cells to ~1260 cm^{-1} in treated cells, which may be associated with changes in protein structure. In addition, there may be a decreased level of DNA in treated cells, as the average spectra show that the ~780 cm^{-1} peak is increased in control cells when compared to cells incubated with AEA. However, not all control cells have an increase in this peak, so this may reflect differences in the DNA content of different cells, and not be an effect of the drug. Finally, there is the appearance of a small peak at ~970 cm^{-1}, similar to that seen in the spectra taken from 8 hours of incubation.

As observed at 8 hours, the average spectra taken from the cytoplasm of cells (figure 5.11F) show increases in the intensity of protein peaks (1265 cm^{-1} and 1660 cm^{-1}), indicative of an increased protein content in treated cells. There is also an increase in the peak at ~934 cm^{-1} in treated cells in comparison to control cells, which was not observed in any of the previous average spectra. This peak is associated with C-C backbone stretching in proteins (Bai *et al.*,

2015; Barkur *et al.*, 2015), and may also suggest an increase in protein level. However, there do not appear to be any differences in the level of lipids between treated and untreated cells, as the peak at ~1450 cm^{-1} has a similar intensity in both treated and control cells, so this effect may not be associated with proliferation. There does not appear to be a shift at ~1260 cm^{-1} in contrast to what was observed in the DNA plot and what we observed with CBD. In cells treated with CBD, this was indicative of the activation of caspases leading to protein degradation; as we do not observe the same effects with AEA, it may suggest that AEA does not activate caspases or cause changes in protein structure in the cytoplasm after 24 hours of incubation.

There is the appearance of the peak at 970 cm^{-1} in treated cells, which has also been observed in previous average spectra from 8 hours of incubation (figure 5.9B). After 8 hours, this peak was only present in spectra taken from the cytoplasm of cells, but after 24 hours of incubation with AEA, this peak could be observed in spectra taken from both the cytoplasm and nucleus of cells. As this peak is only visible in spectra from treated cells and not control cells, and is only visible in treated cells when the drug begins to effect cells (as the PCA plots only show clear separation after 8 hours of treatment), it is likely to be due to the effect of AEA. Peaks in the region of 970 cm^{-1} have previously been assigned to phosphate groups, specifically the P-O symmetric stretch (McManus *et al.*, 2011; Smith *et al.*, 2017).

Overall, the results indicate that, unlike CBD, AEA does not induce cell death in Caco-2 cells at the 10 µM concentration after 24 hours of treatment. However, AEA still has an effect on Caco-2 cells, as separation can be observed in many of the PCA plots over time, and this effect may be associated with an increase in protein level in treated cells.

5.3.5 Live Cell Raman Spectroscopy

Live cell Raman spectroscopy was also carried out, to allow a consistent comparison with the CBD study. Figure 5.12 shows live cell maps of Caco-2 cells treated with 10 µM of AEA. Cells 1,

2, 4 and 6 do not show any clear changes over time, while the only difference in cell 3 is that it appears to have begun dividing by 12 hours of incubation. In cell 5, the cytoplasm may be breaking down over time. However, there is still DNA left in this cell, and in all other cells after incubation with AEA, providing further evidence that the effect of the cannabinoids AEA and CBD in Caco-2 cells are different.

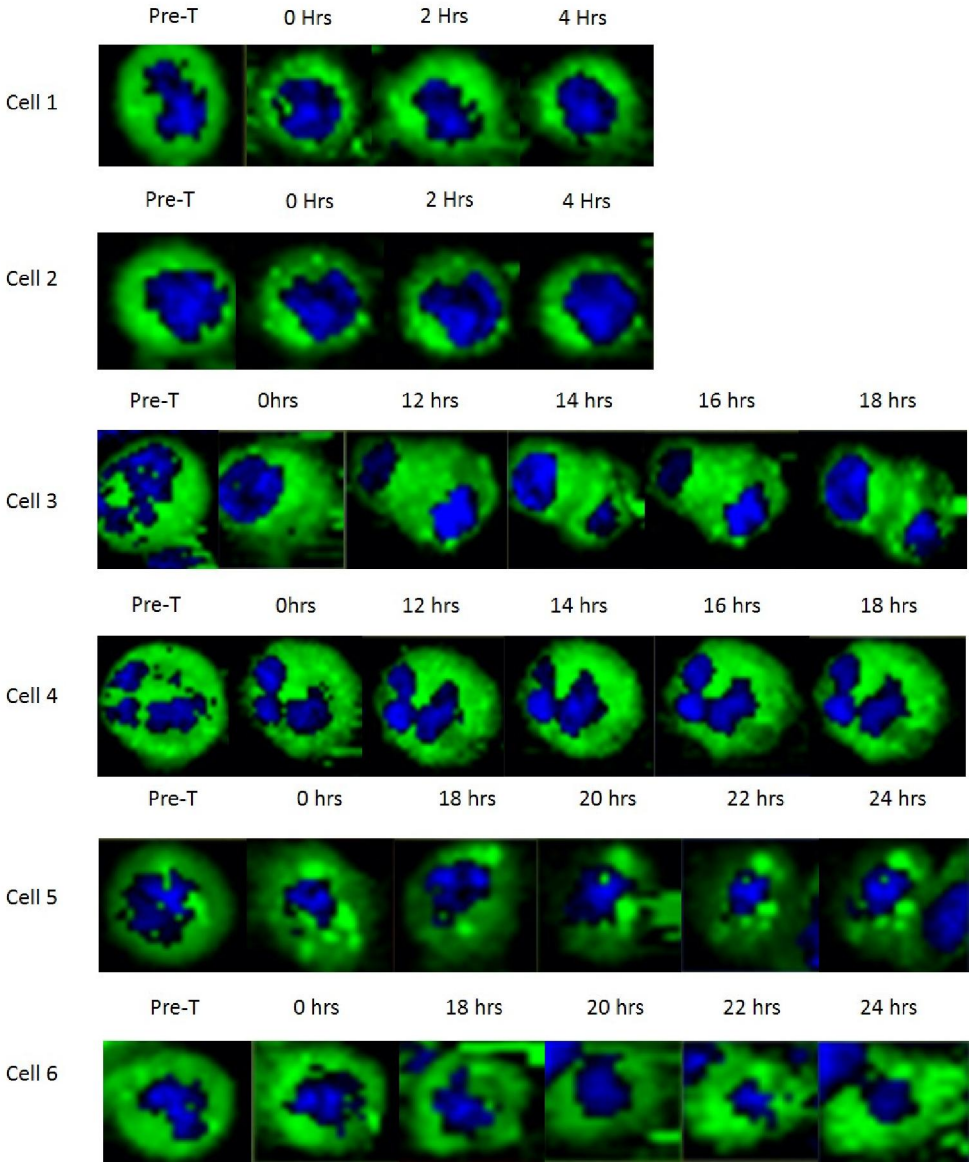

Figure 5.12: Raman maps of live Caco-2 cells treated with 10 µM of AEA, shaded to their DNA and protein content. Raman maps showing the DNA, measured from 780-802 cm^{-1} (blue) and protein, measured from 1630-680 cm^{-1} (green) content of live Caco-2 cells treated with 10 µM of AEA for each listed time point.

The previously collected control maps at 532 nm (chapter 2, section 2.5) were used to carry out PCA on the collected live cell data. The two timepoints chosen for PCA were 4 and 20 hours, as this was consistent with the timepoints used with CBD. For PCA, spectra were taken from two control and two treated cells.

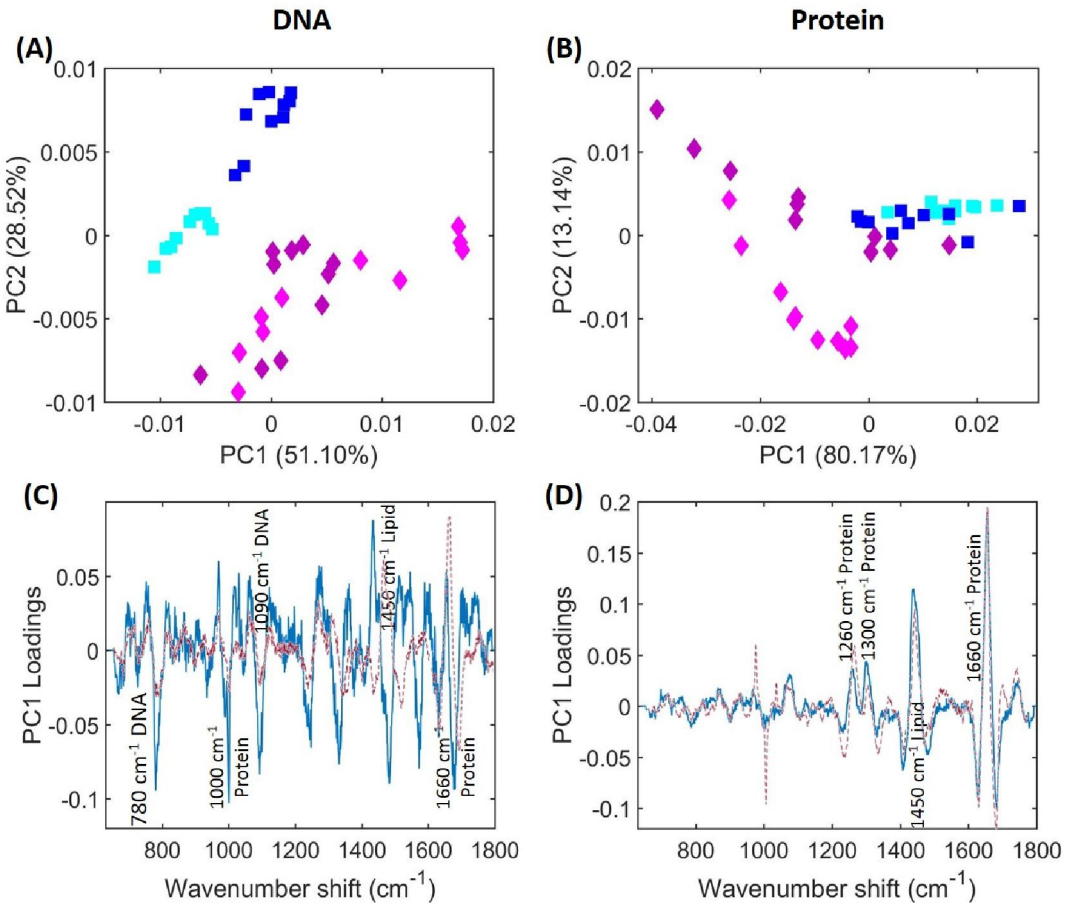

Figure 5.13: A comparison of live cells treated with 10 µM of AEA and control cells after 4 hours of incubation. For PCA-scores plots of PC1 against PC2, spectra were taken from regions of the cell identified as having a high DNA **(A)** or protein **(B)** content. Squares represent cells treated with 10 µM of AEA (n=2), and diamonds cells treated with a media control (n=2). Each colour represents an individual cell. The PC1 loadings for each plot are shown in **(C and D)**. The benchmark loadings are indicated by the red dotted line.

The PCA results for 4 hours are shown in figure 5.13. There is separation seen in both PCA-scores plots between treated and control cells. However, the loadings plot shows that most

peaks overlap with the benchmark plot, suggesting that this separation may be due to differences in cells, and not a result of the drug.

Figure 5.14 shows the PCA results for 18 hours. Again, there is separation of control and treated cells in both PCA-scores plots, suggesting that the drug is having an effect on Caco-2 cells after 18 hours of incubation. This separation occurs along PC2 in spectra taken from the nucleus of cells (figure 5.14A), and therefore only the PC2 loadings plot is shown. This consists of a lot of noise that makes it difficult to pick out individual peaks, however, two notable peaks are the one at 970 cm^{-1}, which was present in the spectra of fixed cells treated with AEA, and the peak at 1375 cm^{-1}, which has previously been assigned as an apoptotic marker (Brauchle *et al.*, 2015), and was present in the spectra of cells treated with CBD. In spectra taken from the cytoplasm of cells, separation occurs along PC1 (figure 5.14B), and the PC1 loadings plot shows that the peaks causing this separation are mostly protein (1260 cm^{-1}, 1300 cm^{-1}) and lipid (1450 cm^{-1}) peaks. Again, there is the presence of a peak at 970 cm^{-1}.

Average spectra were also plotted in order to see if there were any differences in the intensity of peaks between treated and untreated cells. In spectra taken from nucleic acid-rich regions of the cell (figure 5.14E), it is difficult to see any clear differences between treated and control cells. However, the average spectra taken from protein-rich regions (figure 5.14F), show that there is an increase in the intensity of protein peaks (1260 cm^{-1}, 1300 cm^{-1}, 1660 cm^{-1}) in treated cells in comparison to control cells, which is consistent with the results on fixed cells. There are also changes in the region 1000-1100 cm^{-1}, with increases in the intensity of peaks at ~1064 cm^{-1} and 1080 cm^{-1} in treated cells. The 1064 cm^{-1} peak is assigned to C-C stretching in lipids (Talari *et al.*, 2015; Gong *et al.*, 2017), suggesting that treated cells may have an increased level of lipid in comparison to control cells. Peaks in the region of 1080 cm^{-1} have previously been assigned to phosphate stretches (Matthäus *et al.*, 2008). This is consistent

with the results in fixed cells, which suggested increased levels of phosphate stretches, associated with an increase in the intensity of the 970 cm^{-1} peak.

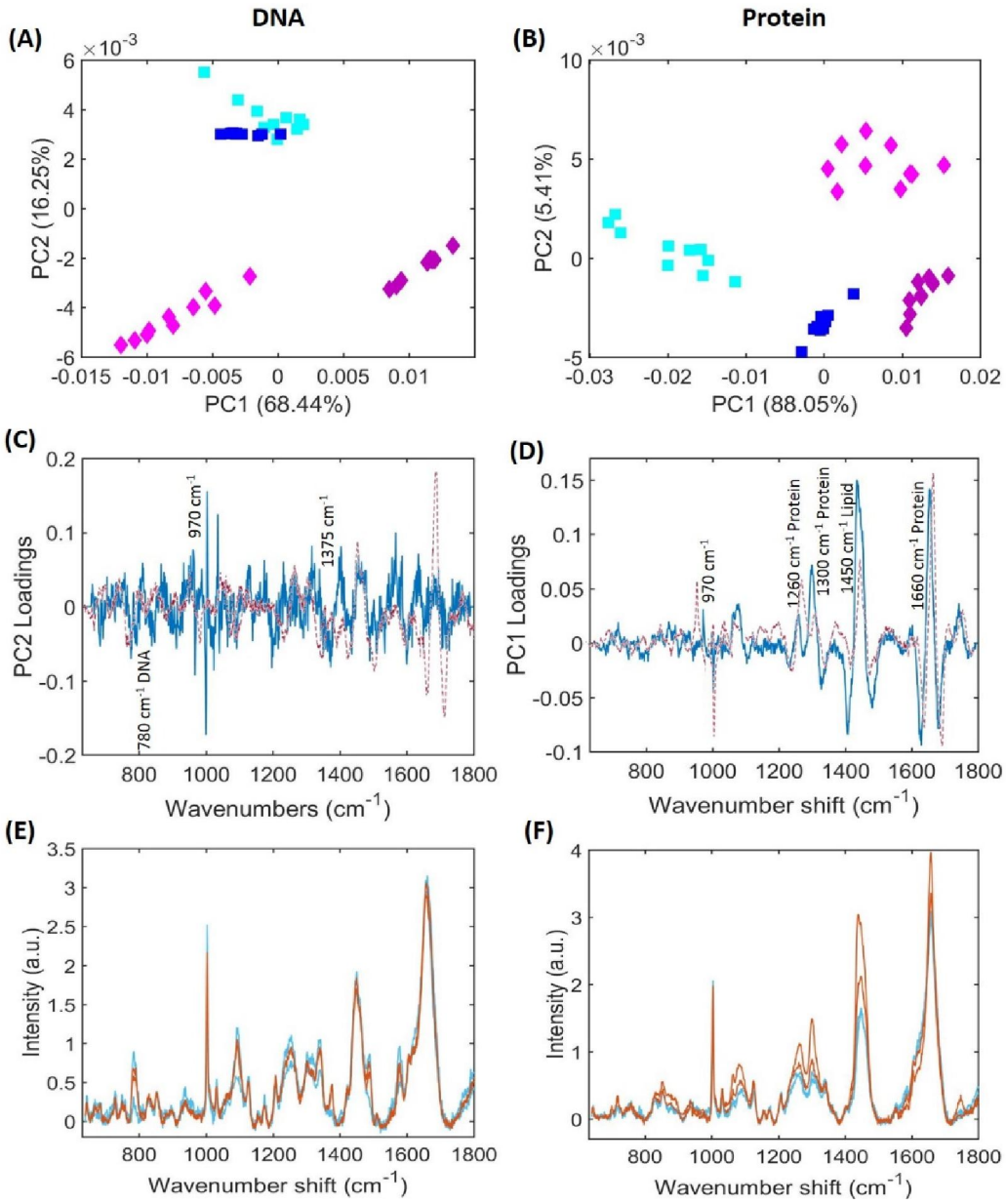

Figure 5.14: A comparison of live cells treated with 10 µM of AEA and control cells after 20 hours of incubation. For PCA-scores plots of PC1 against PC2, spectra were taken from regions of the cell identified as having a high DNA **(A)** or protein **(B)** content. Squares represent cells treated with 10 µM of AEA (n=2), and diamonds cells treated with a media control (n=2). Each colour represents an individual cell. The PC1 loadings for each plot are shown in **(C and D)**, and the baselined spectra of treated (orange) and control (blue) cells, averaged from the 10 spectra used for PCA are shown in **(E and F)**. The benchmark loadings are indicated by the red dotted line.

5.4 Discussion

The aim of this chapter was to compare the effect of the cannabinoid AEA to the results we observed with CBD, in order to see if the effect was the same or different. At a low, 1 µM concentration, the effect appears to be similar, as there is an initial response by the cell within 2 hours, that is resolved by 4 to 6 hours of incubation. This effect is associated with changes in protein and DNA peaks, and an effect of both drugs is an increase in the intensity of protein and DNA peaks in the average spectra of treated cells in comparison to control cells. As previously mentioned, increases in these components is associated with proliferation (Short *et al.*, 2005; Swain, Jell and Stevens, 2008), which low doses of CBD are known to induce. AEA has previously been shown to promote proliferation of endothelial cells at a 1 µM concentration (Hofmann *et al.*, 2014), suggesting that it may also be able to induce proliferation in Caco-2 cells at a low dose.

In contrast, cells treated with 10 µM of AEA behaved very differently to cells treated with 10 µM of CBD. The CBD results showed a clear induction of cell death by 24 hours of incubation associated with the loss of DNA from the cell, whereas with AEA, the Raman maps appeared to show healthy cells after 24 hours of incubation as the nucleus and cytoplasm of all cells was intact. The PCA results indicated that AEA was having an effect on Caco-2 cells, and the peaks contributing to this separation were protein (1000 cm^{-1}, 1126 cm^{-1}, 1234 cm^{-1}, 1260 cm^{-1}, 1338 cm^{-1}) and DNA (780 cm^{-1}) peaks. These peaks are similar to those observed with CBD, however, when looking at the average spectra we saw what appeared to be an increase in the intensity of protein peaks, and therefore protein content, in treated cells in comparison to control cells. In Caco-2 cells treated with 10 µM of CBD, we observed decreased protein content in treated cells. In addition, the PCA results from cells incubated with AEA did not reveal the presence of any cell death markers, or any peaks associated with cell death. Overall, this suggests that AEA,

at a concentration of 10 µM does not induce cell death in Caco-2 cells. This is in contrast with previous studies, which report that AEA induced apoptosis in several different cell lines (Schwarz, Blanco and Lotz, 1994; Maccarrone *et al.*, 2000; Kuc, Jenkins and van Dross, 2012).

The results suggest that AEA does not induce cell death, but that it does have an effect on Caco-2 cells. This effect is associated with the previously mentioned increased protein peak intensity, the presence of a peak at 970 cm^{-1} in the average spectra of treated cells, and a shift from 1252 cm^{-1} in control cells to ~1260 cm^{-1} in treated cells after 24 hours of incubation which may indicate a change in protein structure. Increased protein levels are associated with proliferation (Short *et al.*, 2005; Swain, Jell and Stevens, 2008), but AEA has previously been reported to have an anti-proliferative effect on several different cell lines. In some of these cells, the anti-proliferative effect of the drug was not associated with the induction of apoptosis, and instead by blocking the completion of the S phase of the cell cycle, as an increased number of cells were found to be in this stage with a subsequent reduction in the G_2/M phases that follow (De Petrocellis *et al.*, 1998; Cencioni *et al.*, 2010; Santoro, 2017). This cell cycle arrest is associated with the suppression of Cdk2 activity, which is required for cell cycle progression (Laezza *et al.*, 2006).The prior stage of the cell cycle to S phase is G_1, where cells replicate proteins that are required for DNA synthesis (Bertoli, Skotheim and De Bruin, 2013). As the protein content of cells in G_1 and S phases has been shown to increase prior to the induction of S phase (Gerner, Meyn and Humphrey, 1976), it is therefore theoretically possible that, if AEA were having an anti-proliferative effect in Caco-2 cells, there could be an increase in cellular protein content as cells prepare to divide but are unable to complete the cell cycle due to the interference of the drug.

Peaks at ~970 cm^{-1} have previously been assigned to phosphate groups, specifically the P-O symmetric stretch (McManus *et al.*, 2011; Smith *et al.*, 2017). An increase in the intensity of this peak may therefore correspond to an increased level of phosphorylation within treated

cells. Phosphorylation is a post-translation modification that involves the addition of a phosphate group (PO_4) to various amino acids, modifying the protein and allowing changes in structure important for signal transduction (Ardito *et al.*, 2017). Raman spectroscopy has previously been used to monitor the phosphorylation state of proteins using peaks in this region (Zhang *et al.*, 2005; Ashton, Johannessen and Goodacre, 2011). If this peak indicates a change in the level of phosphorylated proteins in treated cells, then this would result in a change in protein conformation that may link with the observed shift in the amide III region.

The live cell data confirmed that cells treated with 10 µM of AEA over 24 hours remain intact and appear to be healthy from the Raman maps. The PCA data also showed the presence of the 970 cm^{-1} peak, further suggesting that this peak is present as a result of treatment with the drug, and the average spectra showed an increase in protein content in treated cells. There was also the presence of a peak at 1375 cm^{-1}, which in cells treated with CBD, appeared to be an apoptotic marker. This was present in spectra taken from the nucleus of cells after 20 hours of incubation, and may suggest that the drug is inducing cell death in Caco-2 cells, and the process takes longer to complete than CBD-mediated cell death and is not finished by 24 hours of incubation. However, this peak has also been associated with highly condensed chromatin structure (Puppels, Olminkhof, *et al.*, 1991; Pully, Lenferink and Otto, 2011), so may relate to chromatin structure and not the onset of cell death.

In summary, we have investigated the effect of the cannabinoid AEA on Caco-2 cells. Like CBD, AEA appears to have a dual effect on Caco-2 cells: at a low, 1 µM concentration, it appears to induce proliferation in Caco-2 cells, but at a higher, 10 µM concentration, it appears to have an anti-proliferative effect that may be mediated by cell cycle arrest in the S phase.

Chapter 6: Investigating the mechanism of CBD-induced cell death in Caco-2 cells

6.1 Introduction:

Previous results using Raman spectroscopy indicated that the cannabinoid CBD induced cell death in Caco-2 cells, in a process that involved the breakdown and externalisation of cellular DNA, followed by cytoplasm degradation (chapter 4). However, these results did not elucidate the pathway of cell death in these cells.

There are two broad categories of cell death: regulated and unregulated (accidental). Regulated cell death is a mechanism to eliminate irreversibly damaged or harmful cells, and relies on dedicated molecular machinery, whereas accidental cell death is a result of exposure to severe insults, such as high temperatures or extreme pH changes. The most common type of regulated cell death is apoptosis, which is associated with distinct morphological changes, such as cytoplasmic shrinkage, chromatin condensation (pyknosis), nuclear fragmentation (karyorrhexis), and plasma membrane blebbing that results in the formation of apoptotic bodies. In contrast, the most common type of accidental cell death, necrosis, is characterised by rounding of the cell, the presence of dilated organelles, lack of chromatin condensation and cytoplasmic swelling. However, whereas once there were thought to be only these two types of cell death, expanding research has led to the discovery of a number of different subcategories, complicating the characterisation of cell death pathways in cells (Degterev and Yuan, 2008; Berghe *et al.*, 2010; Galluzzi *et al.*, 2018). There are currently several known pathways of cell death, which are summarised in figure 6.1, and described in table 6.1. The aim of this chapter was therefore to build on the Raman spectroscopy results, and to attempt to determine the type of cell death that CBD induces in Caco-2 cells.

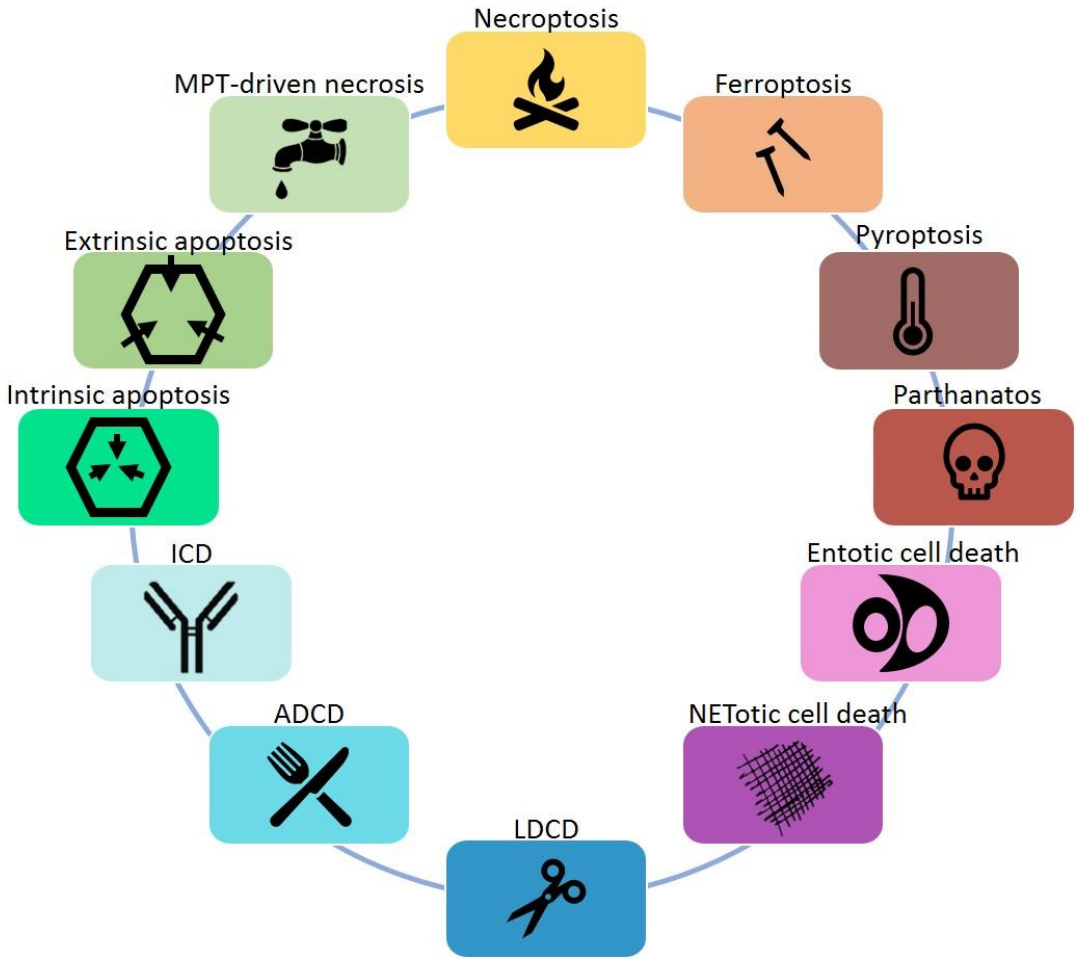

Figure 6.1: A summary of all currently accepted distinct cell death pathways. LDCD is lysosome-dependent cell death, ADCD is autophagy-dependent cell death, ICT is immunogenic cell death, and MPT-driven necrosis is mitochondrial permeability transition-driven necrosis. Adapted from (Galluzzi *et al.*, 2018).

Table 6.1: A summary of the currently accepted distinct cell death pathways, and their descriptions

Mode of cell death:	Description:
Necroptosis	A regulated form of necrosis mediated by death receptors (Berghe *et al.*, 2010)
Ferroptosis	Occurs as a result of severe lipid peroxidation (Dixon *et al.*, 2012)
Pyroptosis	An inflammatory type of cell death mediated by caspase-1 (Shi, Gao and Shao, 2017)
Parthanatos	Caused by the accumulation of PAR and translocation of apoptosis-inducing factor from the mitochondria (Fatokun, Dawson and Dawson, 2014)
Entotic cell death	Involves the engulfment and subsequent degradation of cells by non-phagocytic cells (Galluzzi *et al.*, 2018)
NETotic cell death	Restricted to cells of the hematopoietic derivation (Galluzzi *et al.*, 2018)
Lysosome-dependent cell death (LDCD)	Initiated by the permeabilization of lysosomal membranes, releasing lysosomal contents into the cytoplasm (Aits and Jaattela, 2013)
Autophagy-dependent cell death (ADCD)	A process of cell death that relies on the use of the autophagy machinery (Galluzzi *et al.*, 2018)
Immunogenic cell death (ICD)	Relies on the generation of an immune response resulting in phagocytosis (Kepp *et al.*, 2014)
Intrinsic apoptosis	Apoptosis activated by intracellular signals (Galluzzi *et al.*, 2018)
Extrinsic apoptosis	Apoptosis activated by extracellular ligands binding to cell death receptors (Galluzzi *et al.*, 2018)
Mitochondrial permeability transition-driven necrosis (MPT-driven necrosis)	Occurs when the mitochondrial membrane becomes impermeable, resulting in the loss of mitochondrial membrane potential (Izzo *et al.*, 2016)

6.2 Materials and Methods:

6.2.1 RealTime-Glo™ Annexin-V Apoptosis and Necrosis Assay

Assay components were purchased from Promega unless otherwise stated. Caco-2 cells were seeded onto clear-bottomed, black cell culture 96 well plates and left to adhere overnight.

The following morning, media was removed and replaced with 100 µL of either CBD at a 10 µM concentration or controls (ethanol as a vehicle control, media as a no treatment control, and media alone for a no-cell control). Immediately after treatments were added, 100 µL of Detection Reagent was added to each well, and the plate shaken using an orbital plate shaker

for 30 seconds at 500 rpm to mix. Luminescence and fluorescence (at 485 nm_{Ex}/520-530 nm_{Em}) were measured using a Tecan infinite 2000 pro plate reader at 0 hours. Plates were then returned to the incubator, and readings taken at further timepoints of 2, 4, 6, 8, 12, 14, 16, 18 and 24 hours.

6.2.2 Caspase-Glo® 3/7 Assay

Assay components were purchased from Promega unless otherwise stated. Caco-2 cells were seeded onto clear-bottomed, black cell culture 96 well plates and left to adhere overnight. The following morning, media was removed and replaced with 100 µL of CBD at a 10 µM concentration or controls (ethanol as a vehicle control, media as a no treatment control, and media alone for a no-cell control).

After incubation, plates were removed from the incubator and allowed to equilibrate to room temperature before 100 µL of Caspase-Glo® 3/7 Reagent to each well and mixed using an orbital plate shaker at 500 rpm for 30 seconds. Plates were then incubated at room temperature for 1 hour. Following this, luminescence was measured using a Tecan infinite 2000 pro plate reader.

6.2.3 DNA Extraction

All kit components were purchased from Fisher Scientific unless otherwise stated. Cells were seeded onto sterile 6 well culture plates and left to adhere overnight. Following this, 10 µM of CBD was added and plates incubated for a period of either 2, 4, 8, 12, 14, 16, 18 or 24 hours.

After incubation, media was removed and cells rinsed with PBS. Cells were detached from the plate by trypsinisation and transferred to a microcentrifuge tube. Cells were pelleted by centrifugation for 5 minutes at 250 x g, and the supernatant discarded. Cells were resuspended in 200 µL of PBS. Then, 200 µL of lysis solution and 20 µL of Proteinase K Solution were added to the pellet and mixed by vortexing to obtain a uniform suspension.

Samples were incubated at 56 °C using a heat block, and vortexed at regular intervals for 10 mins. Following this, 20 µL of RNase A Solution was added, mixed by vortexing, and the sample incubated for 10 mins at room temperature. 400 µL of 50 % ethanol was then added and mixed by vortexing.

The lysate was transferred to a GeneJET Genomic DNA Purification Column inserted in a collection tube. This column was centrifuged for 1 min at 8000 x g. The flow-through was discarded and the column placed into a new 2 mL collection tube.

500 µL of Wash Buffer 1 was added, and the sample centrifuged at 8000 x g for 1 min. The flow-through was discarded and the column placed back into the collection tube before 500 µL of Wash Buffer II was added. The sample was then centrifuged for 3 min at 13000 x g.

Following this, the collection tube was discarded and the column transferred to a sterile 1.5 mL microcentrifuge tube. 30 µL of elution buffer was added to the centre of the column, before it was incubated for 2 min at room temperature and centrifuged for 1 min at 8000 x g. The purification column was then discarded, and the concentration of purified DNA measured using a Nanodrop. Samples were then stored at -20 °C.

6.2.4 DNA Fragmentation Assay

0.5 mL of agarose was dissolved in 50 mL of TAE buffer to create a 1 % agarose gel. 1 µL of GelRed was added before the gel was poured into gel electrophoresis apparatus to set. Meanwhile, 10 µL of DNA samples were prepared at a concentration of 10 ng/mL in sterile water. 2 µL of sample loading buffer was then added to each sample.

When the gel was set, 12 µL of each extracted DNA sample was added to each well, in addition to 12 µL of DNA markers. The gel was then covered with TAE buffer and run at 90 volts for ~45 minutes. Following this, the gel was removed and DNA visualised using a Chemidoc.

6.2.5 UV Resonance Raman Spectroscopy

Caco-2 cells were treated with 10 µM of CBD for a period of 4, 16 or 24 hours. After this time, 1 mL of media was collected from the cells and frozen. Samples were thawed on ice before they were analysed. UVRR spectra were acquired using a Raman microscope (Renishaw, Wotton-under-edge, Gloucestershire, UK) coupled to a 244 nm Lexel Model 90 Ion Laser. 40µL of each medium sample was pipetted into a well on the lid of a 96 well microplate, with ~0.2 mW of power at sample. The laser was focused onto the sample and the focus was checked to ensure we were measuring the sample and not the plate, as this has its own spectrum. The well was continuously rotated during data collection to avoid photodegradation. Spectra were collected using an acquisition time of 30 seconds, and three spectra were acquired for each sample. Spectra were normalised using SNV (standard normal variate).

6.2.6 Mitochondrial ToxGlo™ Assay

Assay components were purchased from Promega unless otherwise stated. Caco-2 cells were seeded onto clear-bottomed, black cell culture 96 well plates and left to adhere overnight. 50 mL of galactose-containing media was prepared using glucose-free DMEM (Sigma). 0.09 g of galactose was added to 50 mL of media to give a final concentration of 10 mM of galactose, and 1.25 mL of HEPES was added to maintain pH. This solution was sterile filtered prior to use.

The following morning, media was removed and replaced with 100 µL of either CBD at a 10 µM concentration or controls (ethanol as a vehicle control, and media as a no treatment control). These compounds were made in either glucose-containing media (rows A-D), or galactose-containing media (rows E-H). Plates were then returned to the incubator for a period of 16 hours.

After incubation, 20 µL of 5 X Cytotoxicity Reagent was added to each well and mixed by orbital shaking at 500 rpm for 1 minute. Plates were then incubated at 37 °C for 30 minutes. Following this, fluorescence was measured at 485 nm_{Ex}/520-530 nm_{Em} using a Tecan infinite 2000 pro

plate reader. Plates were then equilibrated to room temperature before 100 µL of ATP Detection Reagent was added to each well and mixed by orbital shaking at 500 rpm for 3 minutes. Following this, luminescence was measured using the same plate reader.

6.2.7 Data Analysis

To determine statistical significance ($p<0.05$), t-tests were performed using Microsoft excel. This was also used to generate all graphs. UVRR spectra were averaged in Microsoft Excel before being plotted in Matlab software version 2016 (The MathWorks, MA, USA).

6.3 Results:

6.3.1 Apoptosis and Necrosis Assay

The first step in investigating the mechanism by which CBD induced cell death in Caco-2 cells was to determine whether cells exhibited characteristic features of apoptosis or necrosis, to determine whether the type of cell death fitted into the regulated or unregulated pathway. In order to do this, the RealTime-Glo™ Annexin-V Apoptosis and Necrosis Assay was carried out. This assay detects an increase in luminescence upon the induction of apoptosis as a result of phosphatidylserine exposure, and an increase in fluorescence upon the induction of necrosis as membrane integrity is lost and a membrane impermeable dye is able to enter the cell.

If CBD was inducing apoptosis in cells, we would expect to see an increase in luminescence followed by an increase in fluorescence. Conversely, if CBD was inducing necrosis in Caco-2 cells, we would expect to see an increase in fluorescence. However, the results did not appear to show any significant changes in fluorescence. Luminescence, on the other hand, increased initially from 0-8 hours before levelling off at 24 hours (figure 6.2A), and at the later timepoints increased up to 14 hours of incubation before decreasing (figure 6.2B). Overall, this data was not what would be expected if CBD was inducing either apoptosis or necrosis in Caco-2 cells,

and suggested that Caco-2 cells were following a non-apoptotic pathway of cell death in response to CBD.

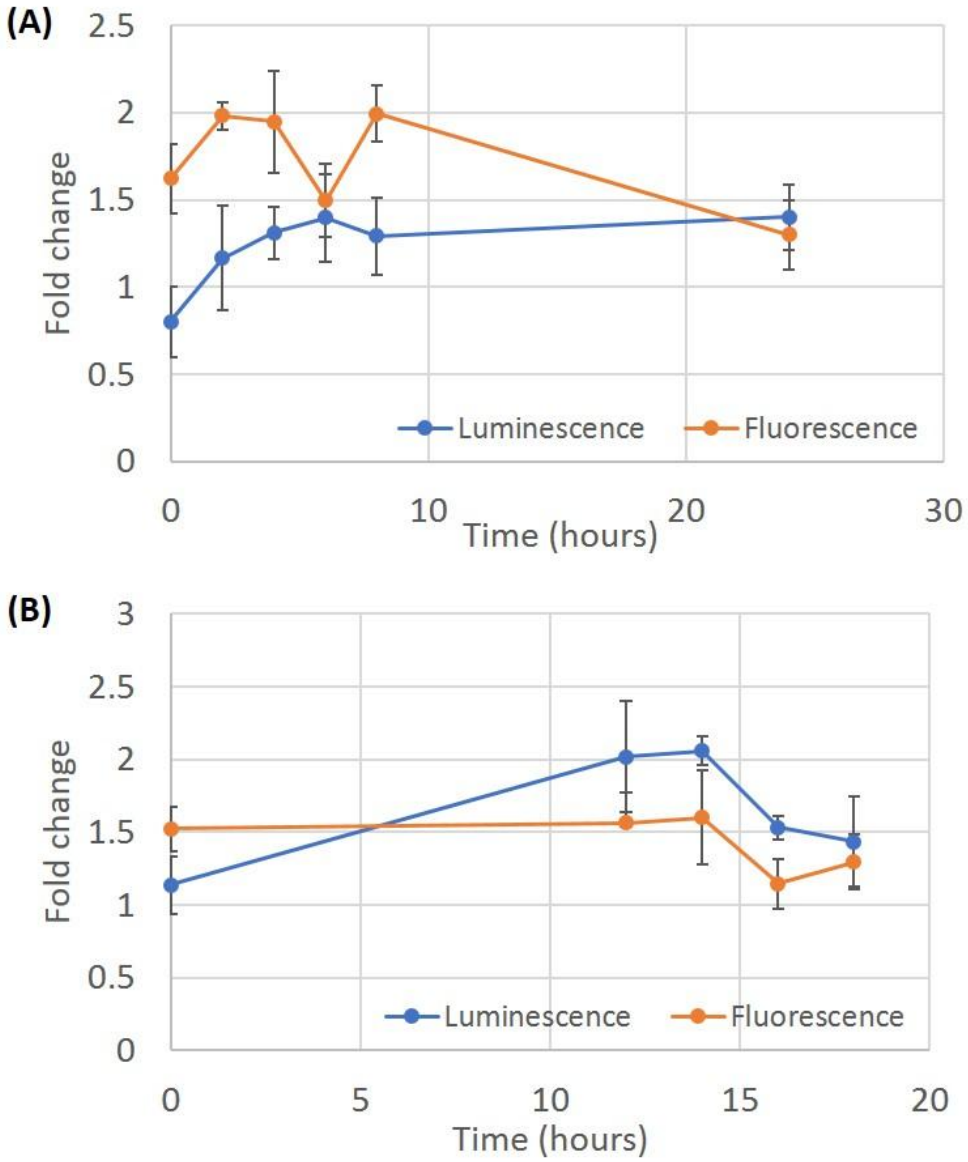

Figure 6.2: **RealTime-Glo™ Annexin-V Apoptosis and Necrosis Assay.** CBD was administered to Caco-2 cells as described in methods. Luminescence and fluorescence readings were obtained at 0, 2, 4, 6, 8 and 24 hours **(A)**, or 0, 12, 14, 16 and 18 hours **(B)**. Data was averaged and depicted as fold change over time, n=3.

6.3.2 Caspase Assay

Caspases are a family endoproteases that play an important role in regulating cell death. Caspases 3 and 7 in particular are primarily associated with apoptosis and are classified as executioner caspases (McIlwain, Berger and Mak, 2013). We therefore investigated whether CBD activated caspases 3/7 in Caco-2 cells. This assay used a luminescent dye that emits a signal when in the presence of caspases 3/7, and therefore the luminescent signal produced is proportional to the amount of caspases present.

The results show that after 12 hours of incubation with both cannabinoid drugs, there was no significant difference in the level of caspase activity when compared with controls (figure 6.3). However, after both 16 and 18 hours of incubation, significantly increased levels of luminescence, and therefore caspase activity, could be seen in cells that have been treated with CBD. As we know CBD induced cell death in Caco-2 cells at the 10 µM concentration (chapter 5, section 4.3), and we saw an increase in levels of caspase activation, it indicated that the mechanism of cell death involved the activation of caspases 3 or 7.

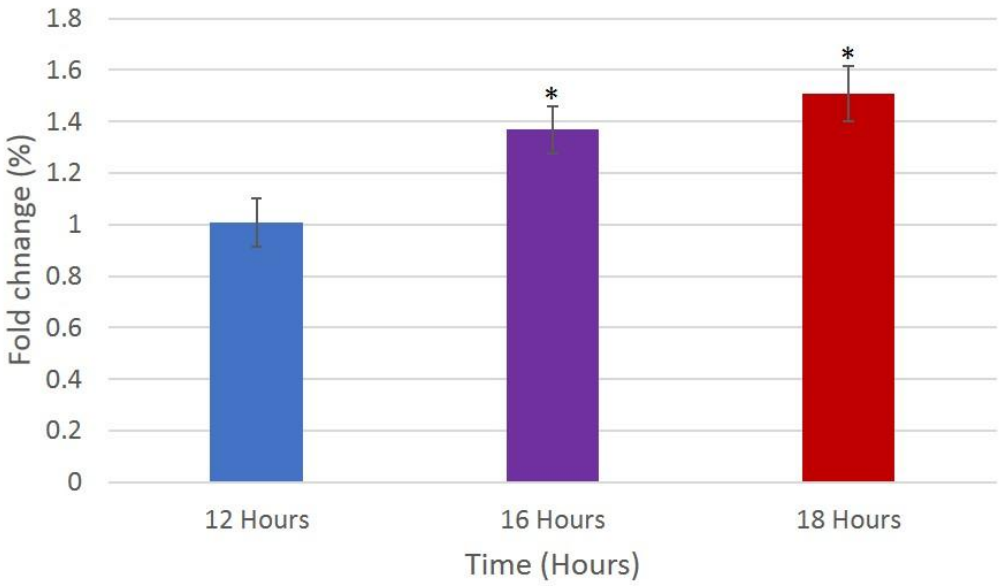

Figure 6.3: Caspase-Glo® 3/7 Assay. CBD was administered to Caco-2 cells as described in the methods. Luminescence readings were obtained after 12, 16 and 18 hours of incubation with CBD. Data was averaged and depicted as fold change in comparison to control cells on a bar chart, n=3. *p<0.05.

6.3.3 DNA fragmentation Assay

One of the key events in apoptosis is DNA fragmentation. The molecular process of this involves the activation of caspase-activated DNase (CAD) that cleaves chromosomal DNA in a caspase-dependent manner (Nagata, 2000). As the caspase assay showed that CBD caused the activation of caspases, and that CBD caused a loss of DNA in Caco-2 cells after 24 hours of incubation, we carried out a DNA fragmentation assay to determine if there was any fragmentation in the DNA of treated cells over time.

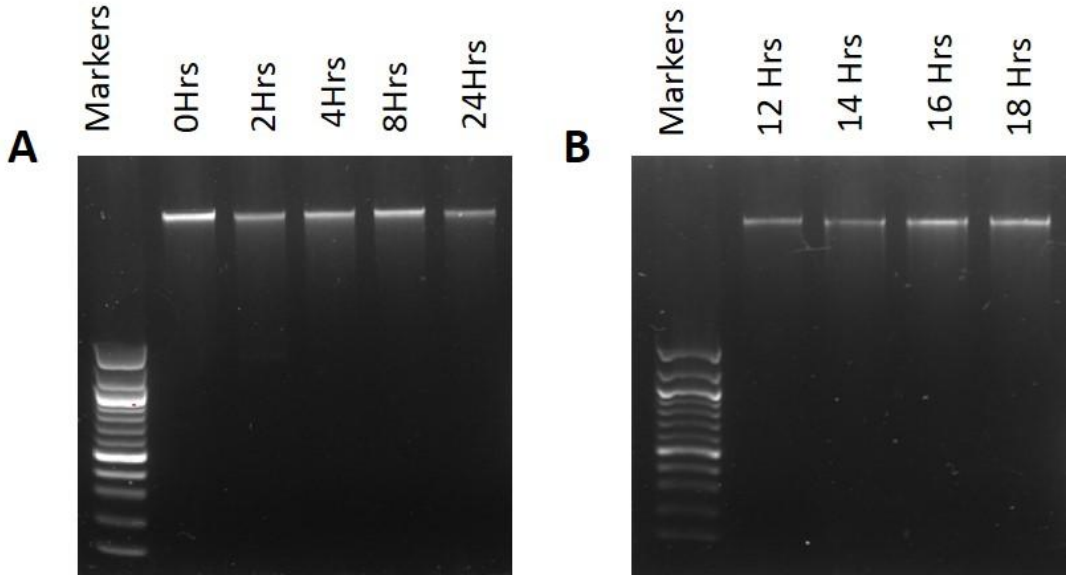

Figure 6.4: DNA Fragmentation Assay. 10 µM of CBD was administered to Caco-2 cells as described in methods. After incubation times of 0, 2, 4, 8 and 24 hours **(A)**, or 12, 14, 16 and 18 hours **(B)**, DNA was extracted from cells, and underwent gel electrophoresis prior to being imaged.

The results (figure 6.4) showed that no fragmentation of DNA can be seen at any of the timepoints tested, as the DNA appears as a single band, whereas if the DNA had fragmented we would expect to see several bands along the length of the gel. Comparing all timepoints with 0 hours suggested that there may be a decreased level of DNA in treated cells, as the bands across all other timepoints appear to be less intense than that at 0 hours, and an equal amount of DNA was added to each well. This decrease in intensity appears to be greatest after

24 hours of treatment with CBD, although we would have expected to see no band as the Raman spectroscopy results suggested that there was no DNA left within the cell at 24 hours. No fragmentation may be seen because this assay relies on the DNA being within the cell, and if it has exited the cell it may be in the culture medium, which could not be analysed using this method. UVVR spectroscopy was used to do this instead.

6.3.4 UVRR of Cell Media Samples

UV resonance Raman (UVRR) spectroscopy uses UV lasers (excitation wavelength range from 180-260 nm) to create a resonance effect, which enhances the signal by a factor of 10^3-10^5 in comparison to using lasers within the visible range. In this case, using an excitation laser of 244 nm enhances the signal of aromatics, and therefore enhances the features of both proteins and nucleic acids (Ashton *et al.*, 2013). UVRR was therefore used on media samples collected from cells treated with CBD and control cells in order to determine if nucleic acids were present in the media of treated cells, as the DNA has been shown to be exported from cells incubated with CBD for 24 hours.

Figure 6.5 shows the averaged UVRR spectra of medium samples for treated and untreated cells at 4, 16 and 24 hours. It shows a difference in the spectra of media containing the drug in comparison to controls, with increases seen in the peaks at ~1344 cm^{-1} and ~1480 cm^{-1}. Peaks in the region of 1480 cm^{-1} have been assigned to the C-N and C=N stretching in the nucleotide guanine, and to NH_2 bending in the nucleotide adenine, and therefore corresponds to DNA. The peak at 1344 cm^{-1} has previously been assigned to both C-N and C=N stretching in adenine and guanine molecules (Hobro *et al.*, 2013), and tryptophan (Chi *et al.*, 1998; Wen and Thomas, 2002), so this increase could either be due to an increase in nucleotides or proteins within the medium.

For both peaks, there was an increase in intensity over time, with the greatest intensity seen at 24 hours, which is what we expected based on the previous Raman spectroscopy results. In

control cells, both peaks showed no change in intensity over time, and showed a much lower intensity than the spectra taken from treated cells. This suggested that there is an increased level of DNA molecules within the culture medium of cells treated with CBD.

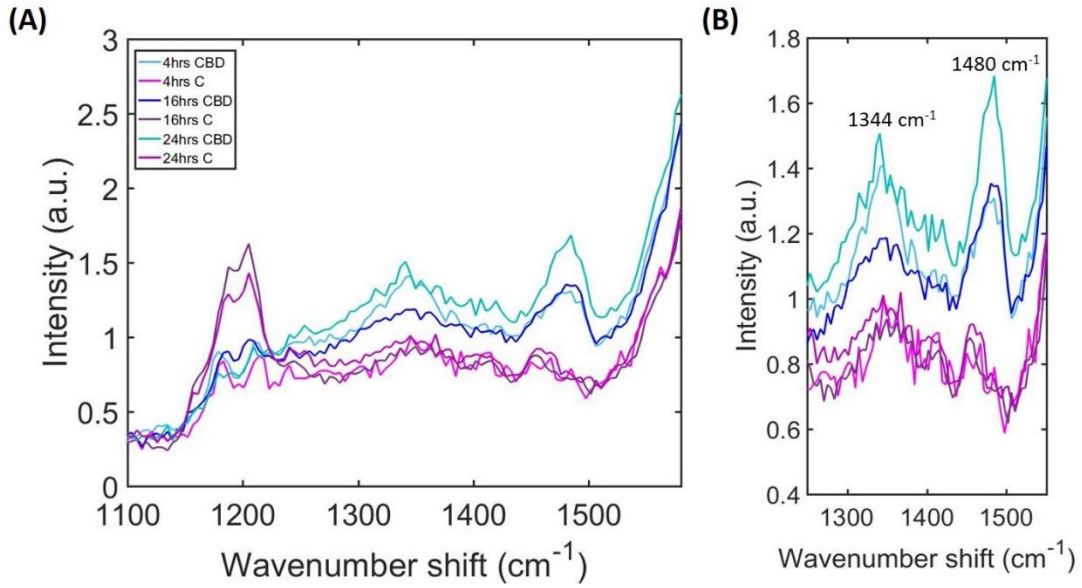

Figure 6.5: Averaged UVVR spectra of medium samples harvested at 4, 16 and 24 hours of treatment with either CBD or media control. (A) Full spectrum. **(B)** Insert of peaks of interest. Spectra were normalised using SNV prior to being plotted. (n=3).

6.6.5 Mitochondrial Toxicity Assay

Mitochondria are vital for cell function, providing cellular energy in the form of ATP and regulating a number of cellular functions, including the apoptosis pathway. Upon activation by pro-apoptotic factors, cytochrome c is released from the mitochondria, which can initiate the activation of a caspase cascade once it reaches the cytoplasm (Cai, Yang and Jones, 1998). CBD has previously been shown to reduce the oxygen consumption rate in Caco-2 cells after 2 hours of incubation (Macpherson *et al.*, 2014). This assay was used to predict mitochondrial dysfunction in response to CBD by measuring the amount of ATP present in control and treated cells; if CBD affected the mitochondria of Caco-2 cells, we would expect to see decreased levels of ATP in comparison to control cells.

Figure 6.6 showed that there was a significant decrease in the amount of ATP present within Caco-2 cells treated with CBD when compared to control cells. This decrease was present after 2 hours of incubation, but the difference can be seen more clearly after 4 hours of treatment with CBD and suggested that CBD may have a direct effect on the mitochondria.

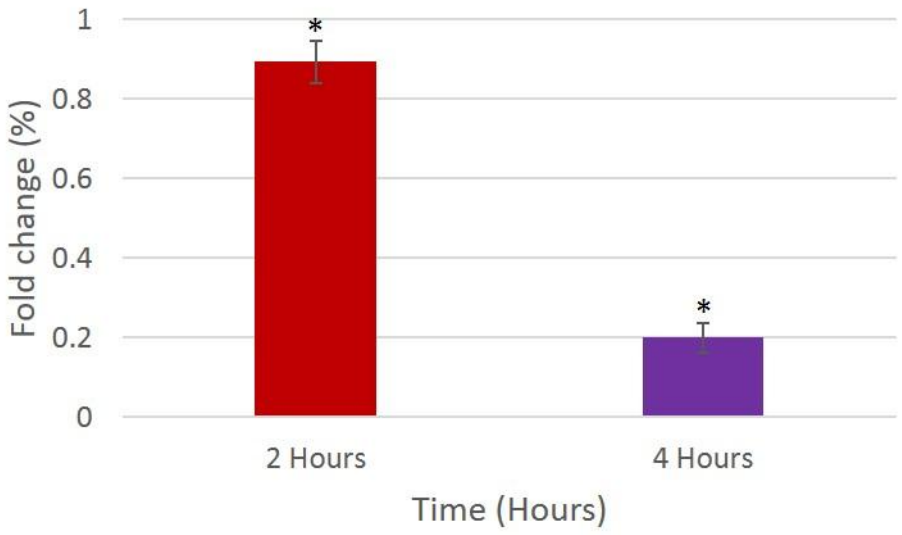

Figure 6.6: Mitochondrial ToxGlo™ Assay. CBD was administered to Caco-2 cells as described in the methods. Luminescence readings were obtained after 2 (A) and 4 (B) hours of incubation with CBD. Data was averaged and depicted as fold change in comparison to control cells on a bar chart, n=3. *p<0.05.

6.4 Discussion

The overall aim of this chapter was to better elucidate the mechanism by which CBD induced cell death in Caco-2 cells, and a number of assays were implemented in order to investigate this. Overall, the results suggested that CBD does not induce either apoptosis or necrosis in Caco-2 cells, but that it did activate caspase 3/7. The Raman spectroscopy results showed that CBD caused the loss of DNA from cells by 24 hours of incubation, but this mechanism does not occur through nuclear fragmentation. However, the nucleic acids are transported outside of the cell and are present in the medium. Finally, CBD appeared to act on the mitochondria, and reduced the amount of ATP present within cells after just 4 hours of incubation.

As previously discussed, there are two broad categories of cell death, with apoptosis and necrosis being the most common in each. CBD has previously been shown to induce apoptosis in a number of different cell lines. This includes breast cancer cells, where apoptosis was confirmed by the observation of distinct morphological changes and DNA fragmentation (Sultan, Marie and Sheweita, 2018), and colorectal cancer cells, where apoptosis was confirmed by the presence of a number of apoptotic markers (Jeong *et al.*, 2019). However, there is little research on the effect of CBD in Caco-2 cells, and our results suggested that CBD does not induce apoptosis or necrosis in Caco-2 cells, and therefore may induce another type of cell death in these cells. There are a number of other different pathways of cell death, summarised in figure 6.1, and many of these pathways overlap, sharing the same cellular machinery (Galluzzi *et al.*, 2018). Some of these pathways can be eliminated as a possible mechanism of cell death in response to CBD. For example, NETotic cell death is restricted to cells of hematopoietic derivation, such as neutrophils and eosinophils (Remijsen *et al.*, 2011). Immunogenic cell death (ICD) relies on the generation of an immune response resulting in phagocytosis (Kepp *et al.*, 2014). Similarly, entotic cell death involves the engulfment and subsequent degradation of cells by non-phagocytic cells (Krishna and Overholtzer, 2016). However, there are still several pathways that CBD could activate in Caco-2 cells, and in order to better determine this pathway, we need to consider all of the evidence we have collected.

CBD induced the activation of caspases 3 and 7 after ~16 hours of treatment, consistent with the beginning of DNA breakdown in the cell. Previously, CBD has been shown to cause an increased activation of caspases in endometrial cancer cells (Fonseca, Correia-da-Silva and Teixeira, 2018), and leukaemia cells (McKallip *et al.*, 2006), although in both cell lines this was associated with the induction of apoptosis. Caspases 3 and 7 are classified as executioner caspases, essential for apoptosis, and cause this upon their activation by cleaving structural and repair proteins. In particular, caspase 3 has been shown to be essential for several steps of apoptosis, including DNA fragmentation and nuclear collapse (Slee, Adrain and Martin,

2001). However, these caspases have also been associated with other types of cell death, including pyroptosis (Shi, Gao and Shao, 2017) and lysosomal-dependent cell death (LDCD) (Loison *et al.*, 2014). Caspase 3 has also been shown to have a role in autophagy-dependent cell death (ADCD), as it was found to be upregulated in cells that had been induced to undergo autophagic cell death (Sadasivan *et al.*, 2006). CBD has previously been shown to induce ADCD in breast cancer cells (Shrivastava *et al.*, 2011). This study suggested that CBD was able to induce both apoptosis and ADCD in these cells, and showed characteristic features of both, including increased caspase activation. This may therefore suggest that CBD induces ADCD in Caco-2 cells.

The lack of DNA fragmentation suggested that the DNA of the cell is broken down by a mechanism that does not involve the activation of CAD. Previous work in senescent cells has shown that chromatin fragments can disperse from the nucleus and into the cytoplasm in a form of nuclear blebbing. Once in the cytoplasm, these fragments were targeted and broken down by the autophagy machinery (Adams *et al.*, 2013). In autophagy, the nucleus is degraded by lysosomes, which are organelles within the cytoplasm of cells that contain enzymes able to break down nucleic acids, proteins, carbohydrates and lipids (Lodish *et al.*, 2012). In this process, a protein associated with autophagy, LC3, interacts with the nuclear protein laminin B1, and binds to laminin-associated domains on chromatin. This facilitates transport into the cytoplasm and delivery to the lysosome (Dou *et al.*, 2015). DNA has also been shown to be directly taken up by lysosomes and degraded (Fujiwara *et al.*, 2013). Lysosomes also have a central role in LDCD. This is initiated by the permeabilization of lysosomal membranes, releasing lysosomal contents into the cytoplasm, and can result in necrotic, apoptotic or apoptosis-like features (Aits and Jaattela, 2013). The extensive release of lysosomal components results in necrosis with rapid membrane permeabilization, whereas limited release can activate the intrinsic apoptosis pathway (Kagedal *et al.*, 2015) or caspase-independent cell death with apoptosis-like morphology (Kirkegaard and Jäättelä, 2009). As in

both of these mechanisms, the DNA is being broken down, there would be no fragments present in a DNA fragmentation assay, consistent with the results we observed. However, the Raman maps suggested that the DNA was being transported to the outside of the cell, and nucleic acids were present within the media of treated cells, which is inconsistent with the degradation of the nucleus by lysosomes. This suggests that the DNA may be broken down and exported by another mechanism.

The nucleus can also be broken down by other cellular machinery. Apoptosis-inducing factor (AIF) is a mitochondrial oxidoreductase that contributes to cell death programmes. Upon detrimental signals, AIF is translocated into the nucleus, where it forms a complex that causes the degradation of chromatin, leading to cell death (Bano and Prehn, 2018). AIF was originally implicated in apoptosis, and was reported to be released from the mitochondria and translocate to the nucleus in a caspase-dependent manner (Susin *et al.*, 1999; Susin, 2004). AIF has also been shown to have a role in another pathway of cell death, parthanatos (Fatokun, Dawson and Dawson, 2014), however this was shown to be caspase-independent, so it is unlikely that parthanatos is the pathway through which CBD induces cell death in Caco-2 cells.

The Raman maps of live cells treated with CBD showed a loss of the structure of the nucleus, with nucleic acids appearing to accumulate near the membrane of the cell before being exported (chapter 4, section 4.3.5). The UVRR spectroscopy results supported this, as nucleic acids were detected in the medium of cells treated with CBD but not control cells, suggesting that the nucleic acids had been broken down and then exported from the cell. This process appeared to occur before membrane integrity was lost. This is unusual, as in most pathways of cell death, nucleic acids either undergo fragmentation (intrinsic and extrinsic apoptosis), are degraded by other intracellular components (ADCD, LDCD) or the entire cell is engulfed and degraded by other cells (entotic cell death, ICD). Necrotic cell death appears to be the only reported type of death where the contents of the cell are released, but this occurs as a result

of cell membrane rupture (Zhang *et al.*, 2018), which is inconsistent with what we observed in the Raman maps.

Nucleic acids are known to be secreted from cells under normal conditions (Stroun and Anker, 1972; Anker, Stroun and Maurice, 1975; Arroyo *et al.*, 2011; Vickers *et al.*, 2011), and cells have been shown to release extracellular vesicles such as exosomes and prostasomes which contain nucleic acids (Théry, 2011; Ronquist, 2012; Thakur *et al.*, 2014). Secreted DNA is proposed to act as an intercellular messenger by entering target cells, and has been implicated in inducing tolerance against detrimental substances (Eldh *et al.*, 2010), immunomodulation (Anker *et al.*, 1980), and the development of metastasis (García-Olmo *et al.*, 2010). However, increased levels of nucleic acids were not detected in samples of media taken from control cells, suggesting that the nucleic acids secreted by treated Caco-2 cells are secreted as a result of the response to CBD. Fragmented DNA has also been detected outside of cells, thought to be the result of either apoptosis or necrosis (Bronkhorst *et al.*, 2016). It is not clear from our results whether the nucleic acids in the medium were fragmented, as the assay was carried out on DNA from within cells; attempts to isolate DNA from the medium were unsuccessful, however a number of different kits exist for extracting cell-free DNA (Diefenbach *et al.*, 2018), which may be of interest in future work.

Interestingly, recent studies have suggested that there may be a link between exosomes and autophagy. As previously mentioned, exosomes are extracellular vesicles that have been found to contain nucleic acids (Eldh *et al.*, 2010; Théry, 2011). Exosomes are nano-sized vesicles that originate from the endocytic pathway, and are released from cells when an intermediate endocytic compartment, the multivesicular body (MVB), fuses with the plasma membrane (Théry, Zitvogel and Amigorena, 2002). Some studies have reported that some of the autophagy machinery contributes to exosome formation and release (Murrow, Malhotra and Debnath, 2015; Guo *et al.*, 2017), suggesting that the activation of the autophagy

pathway, and perhaps ADCD, can result in the secretion of exosomes that may contain nucleic acids, which would explain their presence in the media of treated cells. A number of different techniques exist for both isolating (including ultracentrifugation and density-gradient separation) and detecting (including electron microscopy and flow cytometry) exosomes (summarised in (Ko, Carpenter and Issadore, 2016)), although it would be difficult to determine if the exosomes contained any DNA and whether that was a direct consequence of treatment with CBD.

Our results also suggested that CBD may act on the mitochondria. Mitochondria have been shown to play a role in apoptosis, with the loss of outer membrane potential (MOMP) leading to the release of proapoptotic factors such as cytochrome c (Galluzzi *et al.*, 2018). CBD, at a 10 µM concentration, has previously been shown to increase intracellular calcium levels, leading to changes in mitochondrial function and morphology, resulting in cell death (Rimmerman *et al.*, 2013), and demonstrating that CBD is able to effect the mitochondria of cells. In addition, impaired mitochondrial function results in increased reactive oxygen species (ROS) production (Zorov, Juhaszova and Sollott, 2014). Under normal conditions, ROS are important signalling molecules, and essential for cellular function. However, ROS can also cause DNA and protein damage (Simon, Haj-Yehia and Levi-Schaffer, 2000), and upregulated levels have been associated with apoptosis (Singh *et al.*, 2005; Zorov, Juhaszova and Sollott, 2014). CBD has been associated with increased levels of ROS, and subsequent induction of apoptosis, in several cell lines. In these studies, treatment with ROS scavengers reduced the number of cells undergoing apoptosis (Massi *et al.*, 2004; McKallip *et al.*, 2006; Shrivastava *et al.*, 2011), and therefore suggested that the generation of ROS are required to induce apoptosis in response to CBD. ROS generation was also shown to be required for the induction of autophagy-mediated cell death in breast cancer cells (Shrivastava *et al.*, 2011). CBD has been shown to generate ROS and reduce oxygen consumption rate in Caco-2 cells after 2 hours of incubation, leading to cells becoming metabolically incapable of oxygen consumption (Macpherson *et al.*,

2014). Our results showed a depletion in the level of ATP in Caco-2 cells after a similar incubation time, suggesting mitochondrial dysfunction that could lead to an increased level of ROS production that may induce cell death. ROS are also associated with other forms of cell death, and have been implicated in the induction of LDCD by damaging the lysosomal membrane and leading to membrane permeabilization (Kurz *et al.*, 2008). ROS are also thought to contribute to lysosomal membrane permeabilization by activating lysosomal calcium channels (Sumoza-Toledo and Penner, 2011). Oxidative stress has also been implicated in MPT-driven necrosis. In this type of cell death, the mitochondrial membrane becomes impermeable, resulting in the loss of mitochondrial membrane potential and leading to a necrotic phenotype (Izzo *et al.*, 2016). Our results indicated that CBD induced oxidative stress in Caco-2 cells, but we did not observe a necrotic phenotype, suggesting that MPT-driven necrosis does not occur in Caco-2 cells exposed to CBD. Similarly, ferroptosis is a form of cell death that occurs as a result of severe lipid peroxidation, which relies on the generation of ROS and iron availability (Yang and Stockwell, 2016). However, ferroptosis occurs independently of caspases and displays necrotic morphology (Dixon *et al.*, 2012), which is inconsistent with our results, and suggests that ferroptosis does not occur in Caco-2 cells as a result of incubation with CBD.

In conclusion, we have summarised the numerous pathways of cell death that are currently known, and attempted to eliminate them based on the results we have obtained whilst studying the effect of CBD on Caco-2 cells. While each cell death pathway is distinct in morphology (appearance of dying cells), mechanics (underlying molecular cascades that result in cell death) and functionality (how dying cells are perceived by the organism), there is still an overlap between different pathways and the molecular machinery that causes cell death. This leads to complications when trying to elucidate the exact pathway through which CBD causes death in Caco-2 cells. In particular, caspases and oxidative stress, which we have shown are induced in response to CBD, are linked to a variety of different pathways. In contrast, the

lack of fragmentation and externalisation of nuclear material is not reported to be associated with any of the currently accepted forms of cell death, although exosome release has been linked to the autophagy pathway. Overall, this makes it extremely difficult to confidently assign any pathway to the effect we have observed in these cells in response to CBD. Based on the gathered evidence, and by a process of elimination, it seems most likely that CBD-mediated cell death occurs through either ADCD or LDCD in Caco-2 cells (figure 6.7).

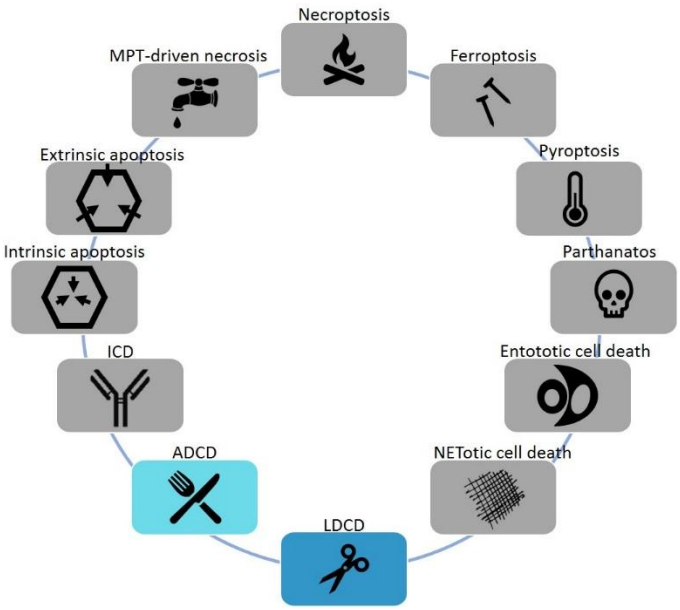

Figure 6.7: A summary of all currently accepted distinct cell death pathways, with eliminated pathways in grey, and the pathways CBD may act through in colour. LDCD is lysosome-dependent cell death, ADCD is autophagy-dependent cell death, ICT is immunogenic cell death, and MPT-driven necrosis is mitochondrial permeability transition-driven necrosis.

Chapter 7: Conclusions

7.1 Summary of work

The overall aim of the work presented in this thesis was to develop Raman microspectroscopy as a tool to study Caco-2 cells and their response to the cannabinoids CBD, AEA, and also to a metal rhenium complex. We also wanted to gain a greater understanding of the mechanism of action of the cannabinoids, as little is currently known about the cellular response and the exact mechanism of action of these drugs. Raman spectroscopy is an emerging imaging technique that is advantageous over existing techniques as it is non-invasive, label-free, and can be used to image live cells under normal physiological conditions. However, Raman spectroscopy is currently not widely used as a routine tool in cell biology due to perceived long acquisition times and complex data analysis. We have demonstrated that Raman spectroscopy can be used to study cells and give a variety of visual (via Raman mapping) and biochemical (via PCA) information about their normal state, and their response to the addition of compounds such as cannabinoid drugs and a rhenium metal complex.

7.1.1 Raman spectroscopy methodology

There are few existing studies using Raman spectroscopy to study the Caco-2 cell line; the only previously reported study in the literature to use confocal Raman spectroscopy to image Caco-2 cells used Raman imaging to collect only Raman spectra at the specific wavelength of 2800-3030 cm^{-1} (Scalfi-Happ *et al.*, 2011). As such, we needed to develop protocols to determine the best approach for mapping Caco-2 cells using Raman spectroscopy. These cells do not freely adhere and grow on CaF_2 windows, so windows were coated with poly-lysine prior to the introduction of cells. 4 % PFA was a successful fixative for these cells, but methanol and ethanol were not.

In addition to methodology for attaching and fixing cells, we also needed to develop methods for data processing, and have shown that the data pre-treatments of cosmic ray removal, normalisation and noise filtering result in good-quality Raman maps. Based on the available literature, there is currently no standard approach for shading Raman maps (Ashton, Hollywood and Goodacre, 2015), and as such we have also developed robust shading parameters using distribution plots that could be kept consistent across all maps to allow for comparison. Distribution plots consist of all the peak area intensity values within the Raman map, and can therefore be used as a guide when shading. Most of the values have a very low intensity, and can be attributed to background; shading at higher intensities allows us to remove this background from the image and to only examine areas of interest. Shading ranges were therefore chosen by looking at the distribution plots, and, once selected, these ranges were applied to all subsequent maps.

We have also developed a set of benchmark PC1 loadings that have been used across all PCA plots. These were calculated by using spectra from the nucleus and cytoplasm of control cells, and therefore account for differences between different cells which may contain different levels of cellular components. Using these benchmark loadings allowed us to immediately discount any overlapping peaks, as these are likely to contribute to separation between individual cells, and not as a result of cell treatment with either the complex or the drugs and focus only on those peaks that change as a result of cell treatment. This is a novel technique that we have not previously seen in the literature.

7.1.2 Visualisation of drugs and complexes in cells

One of the advantages of Raman spectroscopy is that it can be used in order to visualise compounds within cells by shading Raman maps to specific peaks within that compound's Raman spectrum. This is particularly useful in drug studies, as drugs can be visualised within cells without the introduction of any labels or fluorescent markers. However, we have shown

that there are difficulties when shading to specific peaks, particularly in both drug studies. While we observed a number of potential peaks in both the CBD and AEA spectra, shading to each of these was unsuccessful when trying to visualise the intracellular distribution of the drug. Cell spectra are complex and contain many different peaks; drug peaks may therefore be overshadowed by these peaks, making shading difficult. For some compounds, it may be possible to select peaks that exist outside of the cellular fingerprint region, but depending on the wavelength of those peaks, it may be difficult to identify cellular components like the nucleus as most DNA peaks exist at lower wavenumbers. The rate of drug metabolism must also be considered when trying to spatially observe drugs within cells. For example, AEA is rapidly metabolised when it is taken into cells and as such, shading to its peaks may not be successful.

While we were unable to observe the spatial distribution of cannabinoids within Caco-2 cells, we had some success with the rhenium complex. We shaded Raman maps of treated and untreated cells to each of the peaks we observed in the Raman spectrum of the complex itself, and two peaks appeared to be present in treated cells but not in untreated cells. These peaks were 785 cm^{-1} and 1035 cm^{-1}. Shading parameters had to be carefully chosen when shading to these peaks, and we demonstrated how the shading range chosen can affect the final image and needs to be carefully considered to avoid under or over interpretation of the results. When shading live cell Raman maps to these peaks, we observed that the 1035 cm^{-1} peak showed the most consistent shading across all cells and was therefore most likely to correspond to the complex. Shading appeared to be consistent with the previously observed fluorescence results using this complex (Amoroso *et al.*, 2008). However, there are potential issues with using this peak, as 1035 cm^{-1} can be assigned to phenylalanine (Rehman, Movasaghi and Rehman, 2012; Zheng *et al.*, 2014; Charwat *et al.*, 2015; Gebrekidan *et al.*, 2018). This further demonstrates the difficulties of shading Raman maps to specific peaks that fall within the fingerprint region.

7.1.3 Short-term response of Caco-2 cells to stimuli

Cells have evolved mechanisms to adjust their biochemistry in response to intracellular and extracellular signals indicating a change in their environment, which is necessary for their survival. We have observed a consistent change in Caco-2 cells in response to different stimuli that suggests that these cells may have developed a protection mechanism in response to changes in their environment. Firstly, when cells were treated with the rhenium complex, we observed a separation in the PCA scores plot at 2 hours. This was unexpected as this complex was reported to be non-toxic in previous studies (Amoroso *et al.*, 2008), and we expected that the complex would therefore not have an effect on cells. However, the observed separation was associated with changes in DNA and protein peaks. Average spectra showed an increase in the intensity of the DNA peak at 1090 cm^{-1} and also in the protein peak at 1300 cm^{-1}, suggesting an increased level of DNA and protein in cells that had been treated with the complex in comparison to control cells. We also observed similar changes in both drug studies at the lower concentration. Cells incubated with 1 µM of CBD showed an increased DNA and protein content in treated cells when compared to control cells; this also occurred in cells incubated with 1 µM of AEA. At low doses, both drugs have previously been said to induce proliferation (Watanabe *et al.*, 2005; Takeda *et al.*, 2008; Hofmann *et al.*, 2014), although this effect has not been previously reported in Caco-2 cells.

Increases in DNA and protein levels are associated with proliferation (Short *et al.*, 2005; Swain, Jell and Stevens, 2008) due to the induction of transcription. We hypothesise that the introduction of the rhenium complex, and the introduction of a 1 µM dose of the cannabinoids CBD and AEA, results in transcription. This response would result in increased DNA levels, which were observed in the average spectra, and also changes in protein structure, perhaps associated with histone acetylation, that would result in changes to the 1300 cm^{-1} peak (Wang *et al.*, 2000). By 4 hours of incubation with the complex or the drugs, this effect no longer occurs, suggesting that it is a short-term, initial effect of exogenous substances being

introduced into the medium surrounding cells. We suggest that these cells may have evolved this as a protection mechanism by increasing cell numbers in case of a negative effect of the foreign substance, e.g. the complex or cannabinoids.

7.1.4 The effect of CBD on Caco-2 cells

A key objective of this research was to investigate the effect of CBD on Caco-2 cells as very little is known about the actual cellular response. We showed that the cellular response to CBD is concentration dependent, with different responses observed at 1 and 10 µM. As previously discussed, a 1 µM concentration of CBD induces changes in DNA and protein peaks associated with the induction of proliferation. A 10 µM concentration of CBD induces cell death in Caco-2 cells. Cells that were mapped 24 hours after incubation with 10 µM of CBD were shown to undergo cell death, characterised by the lack of DNA and the degradation of the cytoplasm visible in the Raman maps. PCA data from 8 hours revealed that the observed separation between spectra acquired from treated and control cells was associated with DNA (780 cm^{-1}) and protein (1000 cm^{-1}, 1126 cm^{-1} and 1260 cm^{-1}) peaks. The average spectra showed that these peaks were decreased in treated cells, suggesting these cells had a lower DNA and protein content than control cells, consistent with the induction of cell death. We also observed the presence of a peak at 1375 cm^{-1} in the spectra of treated cells, which has previously been assigned as an apoptotic marker (Brauchle *et al.*, 2015), and a shift from ~1266 cm^{-1} to ~1254 cm^{-1} associated with a transition in protein structure as a result of the activation of caspases (Czamara *et al.*, 2016). Caspases are endoproteases that are activated during the cell death pathway and result in the degradation of cellular material such as proteins. Live cell Raman maps showed changes in the spatial distribution of the DNA within the cell. At 4 hours, the DNA of cells appeared to be undergoing a structural change; in maps taken at 18 hours, there was no clear nucleus observed in cells, only DNA content that appeared to be localised at the edges of the cells. This then appeared to be exported in later timepoints before the cytoplasm began to degrade at ~24 hours. There are no existing studies that have shown this

breakdown happening over time in these cells in response to CBD; we are also unaware of any studies that have shown the gradual breakdown and externalisation of nucleic acids using Raman spectroscopy.

A number of studies report that the pathway of cell death CBD induces in Caco-2 cells is apoptosis (Massi *et al.*, 2004; McKallip *et al.*, 2006; Shrivastava *et al.*, 2011). To investigate this, we carried out a number of biological assays. We discovered that CBD does not activate apoptosis or necrosis in Caco-2 cells, as we did not observe any phosphatidylserine exposure (associated with apoptosis) or loss of membrane integrity (associated with necrosis). CBD activated caspases 3/7, consistent with previously recorded literature (Shrivastava *et al.*, 2011; Lukhele *et al.*, 2016), although in both of these studies the activation of caspases was associated with apoptosis. However, caspases are also known to be activated during other mechanisms of cell death (Galluzzi *et al.*, 2018). We did not observe any DNA fragmentation, but UVRR spectroscopy detected the presence of nucleic acids in the media. The live cell Raman spectroscopy results showed the breakdown and externalisation of nuclear material, but the UVVR spectroscopy results confirmed that the nucleic acids had been transported out of the cell and into the culture medium. This is the first reported study to detect cell-free DNA in the culture medium of cells treated with CBD. Finally, we also observed that CBD may act on the mitochondria of Caco-2 cells, as it reduced ATP concentration within treated cells. Several distinct pathways of cell death are currently known, but the two that appear to be most consistent with our results are autophagy-dependent cell death (ADCD) and lysosomal-dependent cell death (LDCD). Both of these pathways involve the activation of caspases 3/7, are not associated with DNA fragmentation, and have been associated with mitochondrial dysfunction. We therefore hypothesise that CBD induces either ADCD or LDCD in Caco-2 cells.

7.1.5 The effect of AEA on Caco-2 cells

We have also investigated the effect of another cannabinoid drug, AEA, in order to see if it induced the same or a different response than CBD. Previous studies have investigated the effect of these two drugs together (Leweke *et al.*, 2012), but there is little existing research comparing the effect of the two separately. As previously discussed, we discovered that it has a similar effect on Caco-2 cells at a 1 μM concentration, as after 2 hours of incubation there were increases in the intensity of DNA and protein peaks, associated with proliferating cells. However, a 10 μM concentration of AEA failed to induce cell death in Caco-2 cells after 24 hours of incubation, and both live and fixed cells still contained a clear nucleus at this timepoint. The PCA results suggested that the drug was having an effect on cells, and this was associated with changes in DNA (780 cm^{-1}) and protein (1000 cm^{-1}, 1126 cm^{-1}, 1260 cm^{-1}) peaks. These peaks had an increased intensity in treated cells in comparison to control cells, suggesting an increased level of DNA and protein in treated cells. This is the opposite of the effect we observed with CBD and further suggested that AEA does not induce cell death in Caco-2 cells at a 10 μM concentration. Overall, this showed that high doses of the cannabinoids CBD and AEA have different effects in Caco-2 cells. Increases in DNA and protein intensity is associated with proliferation, but AEA has been reported to have an anti-proliferative effect on several different cell lines, caused by blocking the completion of the S phase of the cell cycle (De Petrocellis *et al.*, 1998; Cencioni *et al.*, 2010; Santoro, 2017). As in the prior stage of the cell cycle, cells replicate proteins that are required for DNA synthesis (Bertoli, Skotheim and De Bruin, 2013), we hypothesise that we observe increased levels of DNA and protein content as cells prepare to divide but are unable to complete the cell cycle due to the interference of the drug. The effect of AEA is therefore to inhibit proliferation by blocking the cell cycle, which would lead to an increased protein levels within Caco-2 cells, but would not cause cell death.

7.2 Future Directions

While we have successfully demonstrated that Raman spectroscopy can be used to collect detailed information about Caco-2 cells, we are still left with some unanswered questions, particularly in regards to the effect CBD has on these cells. We have shown that high doses of CBD induces cell death in Caco-2 cells and hypothesise that this mechanism is either ADCD or LDCD, but further work would need to be carried out in order to establish which mechanism CBD activates. ADCD could be confirmed by techniques such as fluorescence microscopy to look for the formation of autophagosomes and autolysosomes (Chan *et al.*, 2012), or assays that look for the activation of the autophagy machinery, such as the detection of LC3 proteins that play an important role in autophagosome biogenesis (Kabeya, 2000; Orhon and Reggiori, 2017). Fluorescence microscopy can also be used to detect LDCD by using dyes that accumulate in the lysosomes; a decrease in the staining with these dyes indicates lysosomal membrane permeabilization, which leads to LDCD (Wang, Gómez-Sintes and Boya, 2018).

We have shown that Raman spectroscopy has a number of different applications for the study of both live and fixed cells, including the observation of intracellular organelles, as well as monitoring and distinguishing between the cellular response to different drugs. As previously discussed, Raman spectroscopy is yet to be used as a routine tool in cell biology due to perceived long acquisition times and complex data analysis in comparison to existing techniques such as fluorescence microscopy. The advantages of Raman spectroscopy, particularly the lack of labels and the ability to collect both biochemical and visual information of both live and fixed cells, should make it the forefront of current imaging techniques, however, more still needs to be done before Raman spectroscopy can be translated into the clinic. Further reductions in acquisition time would make it a more attractive option for cell imaging, and there should be a standardised approach to the shading of Raman maps such as the use of distribution plots in order to allow for direct comparisons. Despite these challenges,

we were able to determine that metal rhenium complexes can be used in conjunction with Raman spectroscopy to image cells, and that Caco-2 cells respond differently to CBD and AEA, with CBD inducing cell death most likely due to the mechanism of ADCD or LDCD, and anandamide having an anti-proliferative effect on cells. In addition, we hypothesise that there is an initial response in Caco-2 cells to any added substance that appears to be due to an increase in transcription, and may be a potential protection mechanism.

References

Abbitt, K. B., Rainger, G. E. and Nash, G. B. (2000) 'Effects of fluorescent dyes on selectin and integrin-mediated stages of adhesion and migration of flowing leukocytes', *Journal of Immunological Methods*, 239(1–2), pp. 109–119. doi: 10.1016/S0022-1759(00)00189-7.

Adams, P. D. *et al.* (2013) 'Lysosome-mediated processing of chromatin in senescence', *Journal of Cell Biology*. doi: 10.1083/jcb.201212110.

Adar, F., Delhaye, M. and DaSilva, E. (2007) 'Evolution of Instrumentation for Detection of the Raman Effect as Driven by Available Technologies and by Developing Applications', *Journal of Chemical Education*, 84(1), p. 50. doi: 10.1021/ed084p50.

Addis, J. *et al.* (2016) 'Raman spectroscopy of endoscopic colonic biopsies from patients with ulcerative colitis to identify mucosal inflammation and healing', *Biomedical Optics Express*. doi: 10.1364/BOE.7.002022.

Aits, S. and Jaattela, M. (2013) 'Lysosomal cell death at a glance', *Journal of Cell Science*. doi: 10.1242/jcs.091181.

Albrecht, A. C. and Hutley, M. C. (1971) 'On the Dependence of Vibrational Raman Intensity on the Wavelength of Incident Light', *The Journal of Chemical Physics*, 55(9), pp. 4438–4443. doi: 10.1063/1.1676771.

Alhamoruni, A. *et al.* (2010) 'Pharmacological Effects of Cannabinoids on the Caco-2 Cell Culture Model of Intestinal Permeability', *Journal of Pharmacology and Experimental Therapeutics*. American Society for Pharmacology and Experimental Therapeutics, 335(1), pp. 92–102. doi: 10.1124/jpet.110.168237.

Ali, A. *et al.* (2019) 'Single-Cell Screening of Tamoxifen Abundance and Effect Using Mass

Spectrometry and Raman-Spectroscopy', *Analytical Chemistry*. doi: 10.1021/acs.analchem.8b04393.

Altschuler, S. J. and Wu, L. F. (2010) 'Cellular Heterogeneity: Do Differences Make a Difference?', *Cell*. doi: 10.1016/j.cell.2010.04.033.

Amer., M. (2010) 'Raman Spectroscopy, Fullerenes and Nanotechnology'. Cambridge: The Royal Society of Chemistry.

Amoroso, A. J. *et al.* (2007) 'Rhenium fac tricarbonyl bisimine complexes: Biologically useful fluorochromes for cell imaging applications', *Chemical Communications*, (29), pp. 3066–3068. doi: 10.1039/b706657k.

Amoroso, A. J. *et al.* (2008) '3-Chloromethylpyridyl bipyridine fac-tricarbonyl rhenium: A thiol-reactive luminophore for fluorescence microscopy accumulates in mitochondria', *New Journal of Chemistry*, 32(7), pp. 1097–1102. doi: 10.1039/b802215a.

De Angelis, A. *et al.* (2017) 'Combined Raman Spectroscopy and Digital Holographic Microscopy for Sperm Cell Quality Analysis', *Journal of Spectroscopy*. doi: 10.1155/2017/9876063.

Anker, P. *et al.* (1980) 'The role of extracellular DNA in the transfer of information from T to B human lymphocytes in the course of an immune response', *International Journal of Immunogenetics*. doi: 10.1111/j.1744-313X.1980.tb00742.x.

Anker, P., Stroun, M. and Maurice, P. A. (1975) 'Spontaneous Release of DNA by Human Blood Lymphocytes as Shown in an in Vitro System', *Cancer Research*.

Ardito, F. *et al.* (2017) 'The crucial role of protein phosphorylation in cell signalingand its use as targeted therapy (Review)', *International Journal of Molecular Medicine*. doi: 10.3892/ijmm.2017.3036.

Arroyo, J. D. *et al.* (2011) 'Argonaute2 complexes carry a population of circulating microRNAs independent of vesicles in human plasma', *Proceedings of the National Academy of Sciences*. doi: 10.1073/pnas.1019055108.

Artursson, P. (1990) 'Epithelial transport of drugs in cell culture. I: A model for studying the passive diffusion of drugs over intestinal absorptive (Caco-2) cells.', *Journal of Pharmacological Sciences*, 79(6), pp. 476–82.

Ashton, L. *et al.* (2013) 'The challenge of applying Raman spectroscopy to monitor recombinant antibody production', *Analyst*. doi: 10.1039/c3an01341c.

Ashton, L. *et al.* (2015) 'UV resonance Raman spectroscopy: A process analytical tool for host cell DNA and RNA dynamics in mammalian cell lines', *Journal of Chemical Technology and Biotechnology*. doi: 10.1002/jctb.4420.

Ashton, L. and Goodacre, R. (2011) 'Application of Deep Uv Resonance Raman Spectroscopy To Bioprocessing', *European Pharmaceutical Review*.

Ashton, L., Hollywood, K. a. and Goodacre, R. (2015) 'Making colourful sense of Raman images of single cells', *The Analyst*. Royal Society of Chemistry, 140(6), pp. 1852–1858. doi: 10.1039/C4AN02298J.

Ashton, L., Johannessen, C. and Goodacre, R. (2011) 'The importance of protonation in the investigation of protein phosphorylation using raman spectroscopy and raman optical activity', *Analytical Chemistry*. doi: 10.1021/ac202041f.

Aviello, G. *et al.* (2012) 'Chemopreventive effect of the non-psychotropic phytocannabinoid cannabidiol on experimental colon cancer', *Journal of Molecular Medicine*, 90(8), pp. 925–934. doi: 10.1007/s00109-011-0856-x.

Bai, H. *et al.* (2015) 'Label-free assessment of replicative senescence in mesenchymal stem cells by Raman microspectroscopy', *Biomedical Optics Express*. doi: 10.1364/boe.6.004493.

Baia, M., Astilean, S. and Iliescu, T. (2008) *Raman and SERS Investigations of Pharmaceuticals*. Berlin, Heidelberg: Springer Berlin Heidelberg. doi: 10.1007/978-3-540-78283-4.

Bano, D. and Prehn, J. H. M. (2018) 'Apoptosis-Inducing Factor (AIF) in Physiology and Disease: The Tale of a Repented Natural Born Killer', *EBioMedicine*. doi: 10.1016/j.ebiom.2018.03.016.

Barhoumi, A. *et al.* (2008) 'Surface-enhanced raman spectroscopy of DNA', *Journal of the American Chemical Society*, 130(16), pp. 5523–5529. doi: 10.1021/ja800023j.

Barkur, S. *et al.* (2015) 'Probing differentiation in cancer cell lines by single-cell micro-Raman spectroscopy', *Journal of Biomedical Optics*. doi: 10.1117/1.jbo.20.8.085001.

Benevides, J. M. *et al.* (1997) 'Polarized Raman spectroscopy of double-stranded RNA from bacteriophage ϕ6: Local Raman tensors of base and backbone vibrations', *Biophysical Journal*, 72(6), pp. 2748–2762. doi: 10.1016/S0006-3495(97)78917-3.

Berghe, T. Vanden *et al.* (2010) 'Necroptosis, necrosis and secondary necrosis converge on similar cellular disintegration features', *Cell Death and Differentiation*. doi: 10.1038/cdd.2009.184.

Bertoli, C., Skotheim, J. M. and De Bruin, R. A. M. (2013) 'Control of cell cycle transcription during G1 and S phases', *Nature Reviews Molecular Cell Biology*. doi: 10.1038/nrm3629.

Borchman, D., Tang, D. and Yappert, M. C. (1999) 'Lipid composition, membrane structure relationships in lens and muscle sarcoplasmic reticulum membranes', *Biospectroscopy*. doi: 10.1002/(SICI)1520-6343(1999)5:3<151::AID-BSPY5>3.0.CO;2-D.

Boutahir, M. *et al.* (2016) 'Vibrational properties of noncovalently oligothiophene-functionalized graphene nanomaterials', in *Journal of Physics: Conference Series*. doi: 10.1088/1742-6596/758/1/012015.

Boyaci, I. H. *et al.* (2015) 'Dispersive and FT-Raman spectroscopic methods in food analysis',

RSC Advances, pp. 56606–56624. doi: 10.1039/c4ra12463d.

Brauchle, E. *et al.* (2015) 'Cell death stages in single apoptotic and necrotic cells monitored by Raman microspectroscopy', *Scientific Reports*, 4(1), p. 4698. doi: 10.1038/srep04698.

Bräutigam, K. *et al.* (2013) 'Raman spectroscopic imaging for the real-time detection of chemical changes associated with docetaxel exposure.', *Chemphyschem : a European journal of chemical physics and physical chemistry*, 14(3), pp. 550–3. doi: 10.1002/cphc.201200800.

Bronkhorst, A. J. *et al.* (2016) 'Characterization of the cell-free DNA released by cultured cancer cells', *Biochimica et Biophysica Acta - Molecular Cell Research*. doi: 10.1016/j.bbamcr.2015.10.022.

Burgoyne, L. A. (1999) 'The mechanisms of pyknosis: Hypercondensation and death', *Experimental Cell Research*. doi: 10.1006/excr.1999.4406.

Burke, C. S., Byrne, A. and Keyes, T. E. (2018) 'Highly Selective Mitochondrial Targeting by a Ruthenium(II) Peptide Conjugate: Imaging and Photoinduced Damage of Mitochondrial DNA', *Angewandte Chemie - International Edition*. doi: 10.1002/anie.201806002.

Byrne, H. J., Bonnier, F. and Farhane, Z. (2019) 'Two-dimensional correlation analysis of Raman microspectroscopy of subcellular interactions of drugs in vitro', *Journal of Biophotonics*. doi: 10.1002/jbio.201800328.

C., Z. *et al.* (2012) 'Raman Spectroscopy for Noninvasive Monitoring of Umbilical Cord Mesenchymal Stem Cells Viability Transitions', in *Stem Cells in Clinic and Research*. doi: 10.5772/24103.

Cai, J., Yang, J. and Jones, D. P. (1998) 'Mitochondrial control of apoptosis: The role of cytochrome c', *Biochimica et Biophysica Acta - Bioenergetics*. doi: 10.1016/S0005-2728(98)00109-1.

Casabella, S. *et al.* (2016) 'Automated analysis of single cells using Laser Tweezers Raman Spectroscopy', *Analyst*. doi: 10.1039/c5an01851j.

Cebeci-Maltaş, D. *et al.* (2017) 'Photobleaching profile of Raman peaks and fluorescence background', *European Pharmaceutical Review*.

Cencioni, M. T. *et al.* (2010) 'Anandamide suppresses proliferation and cytokine release from primary human T-lymphocytes mainly via CB2 receptors', *PLoS ONE*. doi: 10.1371/journal.pone.0008688.

Chan, J., Taylor, D. and Thompson, D. (2009) 'The Effect of Cell Fixation on the Discrimination of Normal and Leukemia Cells with Laser Tweezers Raman Spectroscopy', *Biopolymers*, 91(2).

Chan, J. W. *et al.* (2007) 'Monitoring dynamic protein expression in living E. coli. Bacterial cells by laser tweezers raman spectroscopy', *Cytometry Part A*. doi: 10.1002/cyto.a.20407.

Chan, J. W. *et al.* (2009) 'Label-free separation of human embryonic stem cells and their cardiac derivatives using Raman spectroscopy', *Analytical Chemistry*, 81(4), pp. 1324–1331. doi: 10.1021/ac801665m.

Chan, L. L. Y. *et al.* (2012) 'A novel image-based cytometry method for autophagy detection in living cells', *Autophagy*. doi: 10.4161/auto.21028.

Charwat, V. *et al.* (2015) 'Potential and limitations of microscopy and Raman spectroscopy for live-cell analysis of 3D cell cultures.', *Journal of biotechnology*, 205, pp. 70–81. doi: 10.1016/j.jbiotec.2015.02.007.

Chatterjee, S. (2014) 'Artefacts in histopoathology', *J Oral Maxillofac Pathol*, 18(Suppl 1), pp. S111–S116. doi: 10.4103/0973-029X.141346.

Chen, M. *et al.* (2015) 'The use of wavelength modulated Raman spectroscopy in label-free identification of T lymphocyte subsets, natural killer cells and dendritic cells.', *PloS one*, 10(5),

p. e0125158. doi: 10.1371/journal.pone.0125158.

Chen, Y. *et al.* (2014) 'Raman spectroscopy analysis of the biochemical characteristics of molecules associated with the malignant transformation of gastric mucosa', *PLoS ONE*. doi: 10.1371/journal.pone.0093906.

Chi, Z. *et al.* (1998) 'UV resonance raman-selective amide vibrational enhancement: Quantitative methodology for determining protein secondary structure', *Biochemistry*. doi: 10.1021/bi971160z.

Clède, S. *et al.* (2013) 'Detection of an estrogen derivative in two breast cancer cell lines using a single core multimodal probe for imaging (SCoMPI) imaged by a panel of luminescent and vibrational techniques', *Analyst*. doi: 10.1039/c3an00807j.

Codeluppi, S. *et al.* (2011) 'Influence of rat substrain and growth conditions on the characteristics of primary cultures of adult rat spinal cord astrocytes', *Journal of Neuroscience Methods*. doi: 10.1016/j.jneumeth.2011.02.011.

Czamara, K. *et al.* (2016) 'Raman microscopy at the subcellular level: A study on early apoptosis in endothelial cells induced by Fas ligand and cycloheximide', *Analyst*. doi: 10.1039/c5an02202a.

D'Brant, L. Y. *et al.* (2019) 'Methamphetamine-induced apoptosis in glial cells examined under marker-free imaging modalities', *Journal of Biomedical Optics*. International Society for Optics and Photonics, 24(04), p. 1. doi: 10.1117/1.JBO.24.4.046503.

Degterev, A. and Yuan, J. (2008) 'Expansion and evolution of cell death programmes', *Nature Reviews Molecular Cell Biology*. doi: 10.1038/nrm2393.

Delhaye, M. and Dhamelincourt, P. (1975) 'Raman microprobe and microscope with laser excitation', *Journal of Raman Spectroscopy*, 3, pp. 33–43. doi: 10.1002/jrs.1250030105.

Denholm, E. M. and Stankus, G. P. (1995) 'Differential effects of two fluorescent probes on macrophage migration as assessed by manual and automated methods', *Cytometry*, 19(4), pp. 366–369. doi: 10.1002/cyto.990190412.

Derakhshandeh, K., Hochhaus, G. and Dadashzadeh, S. (2011) 'In-vitro Cellular Uptake and Transport Study of 9-Nitrocamptothecin PLGA Nanoparticles Across Caco-2 Cell Monolayer Model.', *Iranian journal of pharmaceutical research : IJPR*, 10(3), pp. 425–34. Available at: http://www.pubmedcentral.nih.gov/articlerender.fcgi?artid=3813034&tool=pmcentrez&rendertype=abstract.

Deshmukh, S. *et al.* (2016) 'Identification of Individual Components from the Manufacturing Chain of a Final Vaccine Product by Raman Spectroscopy', *American Pharmaceutical Review*.

Diefenbach, R. J. *et al.* (2018) 'Evaluation of commercial kits for purification of circulating free DNA', *Cancer Genetics*. doi: 10.1016/j.cancergen.2018.08.005.

Diem, M. *et al.* (2013) 'Applications of infrared and Raman micro-spectroscopy of cells and tissue in medical diagnostics: Present status and future promises', *Advances in Biomedical Spectroscopy*, 7, pp. 1–29. doi: 10.3233/978-1-61499-184-7-001.

Dixon, S. J. *et al.* (2012) 'Ferroptosis: An iron-dependent form of nonapoptotic cell death', *Cell*. doi: 10.1016/j.cell.2012.03.042.

Dochow, S. *et al.* (2011) 'Tumour cell identification by means of Raman spectroscopy in combination with optical traps and microfluidic environments', *Lab on a Chip*. doi: 10.1039/c0lc00612b.

Dou, Z. *et al.* (2015) 'Autophagy mediates degradation of nuclear lamina', *Nature*. doi: 10.1038/nature15548.

Draux, F. *et al.* (2009) 'Raman spectral imaging of single living cancer cells: a preliminary study.', *The Analyst*, 134(3), pp. 542–548. doi: 10.1039/b812610k.

Draux, F. *et al.* (2010) 'Raman spectral imaging of single cancer cells: probing the impact of sample fixation methods.', *Analytical and bioanalytical chemistry*, 397(7), pp. 2727–37. doi: 10.1007/s00216-010-3759-8.

Eberharter, A. and Becker, P. B. (2002) 'Histone acetylation: A switch between repressive and permissive chromatin. Second in review on chromatin dynamics', *EMBO Reports*. doi: 10.1093/embo-reports/kvf053.

Ebersbach, P. *et al.* (2018) 'Chemical fingerprinting of single glandular trichomes of Cannabis sativa by Coherent anti-Stokes Raman scattering (CARS) microscopy', *BMC Plant Biology*. doi: 10.1186/s12870-018-1481-4.

El-Diasty, F. (2011) 'Coherent anti-Stokes Raman scattering: Spectroscopy and microscopy', *Vibrational Spectroscopy*, 55(1), pp. 1–37.

Eldh, M. *et al.* (2010) 'Exosomes Communicate Protective Messages during Oxidative Stress; Possible Role of Exosomal Shuttle RNA', *PLoS ONE*. doi: 10.1371/journal.pone.0015353.

Eltoum, I. *et al.* (2001) 'Introduction to the Theory and Practice of Fixation of Tissues', *Journal of Histotechnology*, 24(3), pp. 173–190. doi: 10.1179/his.2001.24.3.173.

Ermakov, I. V. and Gellermann, W. (2010) 'Validation model for Raman based skin carotenoid detection', *Archives of Biochemistry and Biophysics*. doi: 10.1016/j.abb.2010.07.023.

Esmonde-White, K. A. *et al.* (2009) 'Raman spectroscopy of synovial fluid as a tool for diagnosing osteoarthritis', *Journal of Biomedical Optics*. doi: 10.1117/1.3130338.

Farhane, Z., Bonnier, F. and Byrne, H. J. (2017) 'Monitoring doxorubicin cellular uptake and trafficking using in vitro Raman microspectroscopy: short and long time exposure effects on lung cancer cell lines', *Analytical and Bioanalytical Chemistry*, 409(5), pp. 1333–1346. doi: 10.1007/s00216-016-0065-0.

Fatokun, A. A., Dawson, V. L. and Dawson, T. M. (2014) 'Parthanatos: Mitochondrial-linked mechanisms and therapeutic opportunities', *British Journal of Pharmacology*. doi: 10.1111/bph.12416.

Feofanov, A. V. *et al.* (2000) 'Confocal Raman microspectroscopy and imaging study of theraphthal in living cancer cells', *Biophysical Journal*. doi: 10.1016/S0006-3495(00)76612-4.

Fernández-Moreira, V., Thorp-Greenwood, F. L. and Coogan, M. P. (2010) 'Application of d6 transition metal complexes in fluorescence cell imaging', *Chemical Communications*. doi: 10.1039/b917757d.

Fonseca, B. M., Correia-da-Silva, G. and Teixeira, N. A. (2018) 'Cannabinoid-induced cell death in endometrial cancer cells: involvement of TRPV1 receptors in apoptosis', *Journal of Physiology and Biochemistry*. doi: 10.1007/s13105-018-0611-7.

Frisch, S. M. and Francis, H. (1994) 'Disruption of epithelial cell-matrix interactions induces apoptosis', *Journal of Cell Biology*, 124(4), pp. 619–626. doi: 10.1083/jcb.124.4.619.

Fujiwara, Y. *et al.* (2013) 'Direct uptake and degradation of DNA by lysosomes', *Autophagy*. doi: 10.4161/auto.24880.

Galluzzi, L. *et al.* (2018) 'Molecular mechanisms of cell death: recommendations of the Nomenclature Committee on Cell Death 2018.', *Cell death and differentiation*. doi: 10.1038/s41418-017-0012-4.

García-Olmo, D. C. *et al.* (2010) 'Cell-free nucleic acids circulating in the plasma of colorectal cancer patients induce the oncogenic transformation of susceptible cultured cells', *Cancer Research*. doi: 10.1158/0008-5472.CAN-09-3513.

Gargotti, M. *et al.* (2018) 'Raman spectroscopy detects biochemical changes due to different cell culture environments in live cells in vitro', *Analytical and Bioanalytical Chemistry*. doi: 10.1007/s00216-018-1371-5.

Gautam, R. *et al.* (2015) 'Review of multidimensional data processing approaches for Raman and infrared spectroscopy', *EPJ Techniques and Instrumentation*, 2(1), p. 8. doi: 10.1140/epjti/s40485-015-0018-6.

Gebrekidan, M. T. *et al.* (2018) 'Breast Tumor Analysis Using Shifted-Excitation Raman Difference Spectroscopy (SERDS)', *Technology in cancer research & treatment*, 17. doi: 10.1177/1533033818782532.

De Gelder, J. *et al.* (2007) 'Reference database of Raman spectra of biological molecules', *Journal of Raman Spectroscopy*. doi: 10.1002/jrs.1734.

Gerner, E. W., Meyn, R. E. and Humphrey, R. M. (1976) 'Non-histone protein synthesis during G1 phase and its relation to dna replication', *Journal of Cellular Physiology*. doi: 10.1002/jcp.1040870303.

Ghita, A. *et al.* (2012) 'Cytoplasmic RNA in undifferentiated neural stem cells: A potential label-free raman spectral marker for assessing the undifferentiated status', *Analytical Chemistry*, 84(7), pp. 3155–3162. doi: 10.1021/ac202994e.

Goldstein, D. B. (1986) 'Effect of alcohol on cellular membranes', *Annals of Emergency Medicine*, 15(9), pp. 1013–1018. doi: 10.1016/S0196-0644(86)80120-2.

Gong, Y. *et al.* (2017) 'Interpreting the biochemical specificity of mouse spinal cord by confocal raman microspectral imaging', *Journal of Innovative Optical Health Sciences*. doi: 10.1142/s1793545817430076.

Gremlich, H.-U. (2018) *Infrared and Raman Spectroscopy of Biological Materials*, *Infrared and Raman Spectroscopy of Biological Materials*. doi: 10.1201/b16936.

Guan, Y., Wurrey, C. J. and Thomas, G. J. (1994) 'Vibrational analysis of nucleic acids. I. The phosphodiester group in dimethyl phosphate model compounds: (CH3O)2PO2-, (CD3O)2PO2-, and (13CH3O)2PO2-', *Biophysical Journal*. doi: 10.1016/S0006-3495(94)80767-2.

Guo, H. *et al.* (2017) 'Atg5 Disassociates the V1V0-ATPase to Promote Exosome Production and Tumor Metastasis Independent of Canonical Macroautophagy', *Developmental Cell*. doi: 10.1016/j.devcel.2017.11.018.

Hamada, K. *et al.* (2008) 'Raman microscopy for dynamic molecular imaging of living cells', *Journal of Biomedical Optics*, 13(4), p. 044027. doi: 10.1117/1.2952192.

Hammoud, M. K. *et al.* (2018) 'Raman micro-spectroscopy monitors acquired resistance to targeted cancer therapy at the cellular level', *Scientific Reports*. doi: 10.1038/s41598-018-33682-7.

Hata, T. R. *et al.* (2000) 'Non-invasive Raman spectroscopic detection of carotenoids in human skin', *Journal of Investigative Dermatology*. doi: 10.1046/j.1523-1747.2000.00060.x.

Hengartner, M. O. (2000) 'The biochemistry of apoptosis', *Nature*, pp. 770–776. doi: 10.1038/35037710.

Herrero, A. M. (2008) 'Raman spectroscopy for monitoring protein structure in muscle food systems', *Critical Reviews in Food Science and Nutrition*. doi: 10.1080/10408390701537385.

Hidalgo, I. J., Raub, T. J. and Borchardt, R. T. (1989) 'Characterization of the human colon carcinoma cell line (Caco-2) as a model system for intestinal epithelial permeability.', *Gastroenterology*, 96(3), pp. 736–749. doi: S0016508589001009 [pii].

Hobro, A. J. *et al.* (2013) 'Deconstructing RNA: Optical measurement of composition and structure', *Physical Chemistry Chemical Physics*. doi: 10.1039/c3cp52406j.

Hobro, A. J. *et al.* (2015) 'Label-free Raman imaging of the macrophage response to the malaria pigment hemozoin', *Analyst*. doi: 10.1039/c4an01850h.

Hobro, A. J. and Smith, N. I. (2017) 'An evaluation of fixation methods: Spatial and compositional cellular changes observed by Raman imaging', *Vibrational Spectroscopy*, 91, pp.

31–45. doi: 10.1016/j.vibspec.2016.10.012.

Hofmann, N. A. *et al.* (2014) 'TRPV1 mediates cellular uptake of anandamide and thus promotes endothelial cell proliferation and network-formation', *Biology Open*. doi: 10.1242/bio.20149571.

Hou, L. *et al.* (2016) 'Necrotic pyknosis is a morphologically and biochemically distinct event from apoptotic pyknosis', *Journal of Cell Science*. doi: 10.1242/jcs.184374.

Huang, N. *et al.* (2011) 'Full range characterization of the Raman spectra of organs in a murine model', *Optics Express*. doi: 10.1364/oe.19.022892.

Ichimura, T. *et al.* (2014) 'Visualizing cell state transition using raman spectroscopy', *PLoS ONE*. doi: 10.1371/journal.pone.0084478.

Izzo, V. *et al.* (2016) 'Mitochondrial Permeability Transition: New Findings and Persisting Uncertainties', *Trends in Cell Biology*. doi: 10.1016/j.tcb.2016.04.006.

Jacob, C. R., Luber, S. and Reiher, M. (2009) 'Analysis of secondary structure effects on the IR and Raman spectra of polypeptides in terms of localized vibrations', *Journal of Physical Chemistry B*. doi: 10.1021/jp900354g.

Jallapuram, R. *et al.* (2008) 'Raman spectroscopy for the characterization of the polymerization rate in an acrylamide-based photopolymer', *Applied Optics*, 47(2), p. 206. doi: 10.1364/AO.47.000206.

Jeong, S. *et al.* (2019) 'Cannabidiol-induced apoptosis is mediated by activation of Noxa in human colorectal cancer cells', *Cancer Letters*. Elsevier, 447, pp. 12–23. doi: 10.1016/J.CANLET.2019.01.011.

Jess, P. R. T. *et al.* (2007) 'Early detection of cervical neoplasia by Raman spectroscopy', *International Journal of Cancer*, 121(12), pp. 2723–2728. doi: 10.1002/ijc.23046.

Jones, R. A. (2009) 'Volume 3. Five-membered Rings with One Heteroatom together with their Benzo and other Carbocyclic-fused Derivatives', *Comprehensive Heterocyclic Chemistry*. doi: 10.1016/B978-008096519-2.00055-2.

Kabeya, Y. (2000) 'LC3, a mammalian homologue of yeast Apg8p, is localized in autophagosome membranes after processing', *The EMBO Journal*. doi: 10.1093/emboj/19.21.5720.

Kagan, M. R. and McCreery, R. L. (1994) 'Reduction of Fluorescence Interference in Raman Spectroscopy via Analyte Adsorption on Graphitic Carbon', *Analytical Chemistry*, 66(23), pp. 4159–4165. doi: 10.1021/ac00095a008.

Kagedal, K. *et al.* (2015) 'Sphingosine-induced apoptosis is dependent on lysosomal proteases', *Biochemical Journal*. doi: 10.1042/bj3590335.

Kann, B. *et al.* (2015) 'Raman microscopy for cellular investigations - From single cell imaging to drug carrier uptake visualization', *Advanced Drug Delivery Reviews*, pp. 71–90. doi: 10.1016/j.addr.2015.02.006.

Keating, M. E. *et al.* (2015) 'Multivariate statistical methodologies applied in biomedical Raman spectroscopy: assessing the validity of partial least squares regression using simulated model datasets', *Analyst*, 140(7), pp. 2482–2492. doi: 10.1039/c4an02167c.

Kepp, O. *et al.* (2014) 'Consensus guidelines for the detection of immunogenic cell death', *OncoImmunology*. doi: 10.4161/21624011.2014.955691.

Kirkegaard, T. and Jäättelä, M. (2009) 'Lysosomal involvement in cell death and cancer', *Biochimica et Biophysica Acta - Molecular Cell Research*. doi: 10.1016/j.bbamcr.2008.09.008.

Klein, K. *et al.* (2012) 'Label-free live-cell imaging with confocal Raman microscopy', *Biophysical Journal*, 102(2), pp. 360–368. doi: 10.1016/j.bpj.2011.12.027.

Kniggendorf, A. K., Gaul, T. W. and Meinhardt-Wollweber, M. (2011) 'Effects of ethanol, formaldehyde, and gentle heat fixation in confocal resonance Raman microscopy of purple nonsulfur bacteria', *Microscopy Research and Technique*, 74(2), pp. 177–183. doi: 10.1002/jemt.20889.

Ko, J., Carpenter, E. and Issadore, D. (2016) 'Detection and isolation of circulating exosomes and microvesicles for cancer monitoring and diagnostics using micro-/nano-based devices', *Analyst*. doi: 10.1039/c5an01610j.

Kong, K. *et al.* (2013) 'Diagnosis of tumors during tissue-conserving surgery with integrated autofluorescence and Raman scattering microscopy.', *Proceedings of the National Academy of Sciences of the United States of America*, 110(38), pp. 15189–94. doi: 10.1073/pnas.1311289110.

Konorov, S. O. *et al.* (2013) 'Label-free determination of the cell cycle phase in human embryonic stem cells by raman microspectroscopy', *Analytical Chemistry*, 85(19), pp. 8996–9002. doi: 10.1021/ac400310b.

Kopec, M., Imiela, A. and Abramczyk, H. (2019) 'Monitoring glycosylation metabolism in brain and breast cancer by Raman imaging', *Scientific Reports*. doi: 10.1038/s41598-018-36622-7.

Koster, A. J. and Klumperman, J. (2003) 'Electron microscopy in cell biology: integrating structure and function.', *Nature reviews. Molecular cell biology*, Suppl(September), pp. SS6-10. doi: 10.1038/nrm1194.

Koyama, Y. *et al.* (1988) 'Raman and infrared spectra of the all-trans, 7-cis, 9-cis, 13-cis and 15-cis isomers of β-carotene: Key bands distinguishing stretched or terminal-bent configurations form central-bent configurations', *Journal of Raman Spectroscopy*. doi: 10.1002/jrs.1250190107.

Kozlova, N. I. *et al.* (2001) 'Integrin alphavbeta3 promotes anchorage-dependent apoptosis in

human intestinal carcinoma cells', *Oncogene*, 20(34), p. 4710–7. doi: 10.1038/sj.onc.1204619.

Krafft, C. *et al.* (2005) 'Identification of organelles and vesicles in single cells by Raman microspectroscopic mapping', in *Vibrational Spectroscopy*. doi: 10.1016/j.vibspec.2005.02.008.

Krafft, C. *et al.* (2006) 'Studies on stress-induced changes at the subcellular level by Raman microspectroscopic mapping', *Analytical Chemistry*, 78(13), pp. 4424–4429. doi: 10.1021/ac060205b.

Krimm, S. and Bandekar, J. (1986) 'Vibrational spectroscopy and conformation of peptides, polypeptides, and proteins', *Advances in Protein Chemistry*. doi: 10.1016/S0065-3233(08)60528-8.

Krinsky, N. I. and Johnson, E. J. (2005) 'Carotenoid actions and their relation to health and disease', *Molecular Aspects of Medicine*. doi: 10.1016/j.mam.2005.10.001.

Krishna, S. and Overholtzer, M. (2016) 'Mechanisms and consequences of entosis', *Cellular and Molecular Life Sciences*. doi: 10.1007/s00018-016-2207-0.

Kroemer, G. *et al.* (2009) 'Classification of cell death: Recommendations of the Nomenclature Committee on Cell Death 2009', *Cell Death and Differentiation*. doi: 10.1038/cdd.2008.150.

Kuc, C., Jenkins, A. and van Dross, R. T. (2012) 'Arachidonoyl ethanolamide (AEA)-induced apoptosis is mediated by J-series prostaglandins and is enhanced by fatty acid amide hydrolase (FAAH) blockade', *Molecular Carcinogenesis*. doi: 10.1002/mc.20770.

Kumar (2012) *Robbins Basic Pathology, 9th ed*, *Elsevier*. doi: 10.1007/s13398-014-0173-7.2.

Kunapareddy, N., Freyer, J. P. and Mourant, J. R. (2008) 'Raman spectroscopic characterization of necrotic cell death', *Journal of Biomedical Optics*. doi: 10.1117/1.2978061.

Kurz, T. *et al.* (2008) 'Lysosomes in iron metabolism, ageing and apoptosis', *Histochemistry and*

Cell Biology. doi: 10.1007/s00418-008-0394-y.

Kuzmin, A. N. *et al.* (2016) 'Resonance Raman Probes for Organelle-Specific Labeling in Live Cells', *Scientific Reports*. doi: 10.1038/srep28483.

Kuzmin, A. N., Pliss, A. and Prasad, P. N. (2014) 'Changes in biomolecular profile in a single nucleolus during cell fixation', *Analytical Chemistry*, p. 140929195110002. doi: 10.1021/ac503172b.

Laezza, C. *et al.* (2006) 'Anandamide inhibits Cdk2 and activates Chk1 leading to cell cycle arrest in human breast cancer cells', *FEBS Letters*. doi: 10.1016/j.febslet.2006.09.074.

Lee, L. C. C., Leung, K. K. and Lo, K. K. W. (2017) 'Recent development of luminescent rhenium(i) tricarbonyl polypyridine complexes as cellular imaging reagents, anticancer drugs, and antibacterial agents', *Dalton Transactions*. doi: 10.1039/c7dt03465b.

Leweke, F. M. *et al.* (2012) 'Cannabidiol enhances anandamide signaling and alleviates psychotic symptoms of schizophrenia', *Translational Psychiatry*. doi: 10.1038/tp.2012.15.

Li, J. and Kitagawa, T. (2014) 'Resonance Raman spectroscopy', *Methods in Molecular Biology*. doi: 10.1007/978-1-4939-0452-5_15.

Li, Y. *et al.* (2013) 'Micro-Raman spectroscopy study of cancerous and normal nasopharyngeal tissues', *Journal of Biomedical Optics*. International Society for Optics and Photonics, 18(2), p. 027003. doi: 10.1117/1.JBO.18.2.027003.

Liao, Y. S. *et al.* (2011) 'Anandamide inhibits the growth of colorectal cancer cells through CB1 and lipid rafts', *Chinese Journal of Oncology*. doi: 10.3760/cma.j.issn.0253-3766.2011.04.004.

Lieberman, I. and Ove, P. (1958) 'A protein growth factor for mammalian cells in culture.', *The Journal of biological chemistry*, 233(3), pp. 637–642. doi: 10.1084/jem.108.5.631.

Ling, J. *et al.* (2002) 'Direct Raman imaging techniques for study of the subcellular distribution

of a drug.', *Applied optics*, 41(28), pp. 6006–6017. doi: 10.1364/AO.41.006006.

Lippert, J. L., Tyminski, D. and Desmeules, P. J. (1976) 'Determination of the Secondary Structure of Proteins by Laser Raman Spectroscopy', *Journal of the American Chemical Society*. doi: 10.1021/ja00438a057.

Lo, W. L. *et al.* (2011) 'Raman spectroscopy monitoring of the cellular activities of a tissue-engineered ex vivo produced oral mucosal equivalent', *Journal of Raman Spectroscopy*, 42(2), pp. 174–178. doi: 10.1002/jrs.2688.

Lodish, H. *et al.* (2012) *Molecular Cell Biology*. 7th edn. W. H. Freeman.

Loison, F. *et al.* (2014) 'Proteinase 3-dependent caspase-3 cleavage modulates neutrophil death and inflammation', *Journal of Clinical Investigation*. doi: 10.1172/JCI76246.

Lord, R. C. (1977) 'Strategy and tactics in the Raman spectroscopy of biomolecules', *Applied Spectroscopy*. doi: 10.1366/000370277774463706.

Louie, M. W. *et al.* (2011) 'Luminescent rhenium(I) polypyridine complexes appended with an α- D -glucose moiety as novel biomolecular and cellular probes', *Chemistry - A European Journal*. doi: 10.1002/chem.201101399.

De Luca, A. C., Dholakia, K. and Mazilu, M. (2015) 'Modulated raman spectroscopy for enhanced cancer diagnosis at the cellular level', *Sensors (Switzerland)*, 15(6), pp. 13680–13704. doi: 10.3390/s150613680.

Lukhele, S. T. *et al.* (2016) 'Cannabidiol rather than Cannabis sativa extracts inhibit cell growth and induce apoptosis in cervical cancer cells', *BMC Complementary and Alternative Medicine*, 16(1), p. 335. doi: 10.1186/s12906-016-1280-0.

Maccarrone, M. *et al.* (2000) 'Anandamide induces apoptosis in human cells via vanilloid receptors. Evidence for a protective role of cannabinoid receptors', *Journal of Biological*

Chemistry. doi: 10.1074/jbc.M005722200.

Maccarrone, M. and Finazzi-Agró, A. (2003) 'The endocannabinoid system, anandamide and the regulation of mammalian cell apoptosis', *Cell Death and Differentiation*. doi: 10.1038/sj.cdd.4401284.

Macpherson, T. *et al.* (2014) 'Physiological intestinal oxygen modulates the Caco-2 cell model and increases sensitivity to the phytocannabinoid cannabidiol', *In Vitro Cellular {&} Developmental Biology - Animal*, 50(5), pp. 417–426. doi: 10.1007/s11626-013-9719-9.

Maiti, N. C. *et al.* (2004) 'Raman Spectroscopic Characterization of Secondary Structure in Natively Unfolded Proteins: α-Synuclein', *Journal of the American Chemical Society*. doi: 10.1021/ja0356176.

Mari, C. *et al.* (2012) 'Luminescent conjugates between dinuclear rhenium complexes and peptide nucleic acids (PNA): Synthesis, photophysical characterization, and cell uptake', *Organometallics*, 31(16), pp. 5918–5928. doi: 10.1021/om3004515.

Martin, J. C., Wartell, R. M. and O'Shea, D. C. (1978) 'Conformational features of distamycin-DNA and netropsin-DNA complexes by Raman spectroscopy', *Proc. Natl. Acad. Sci. USA*, 75(11), pp. 5483–5487. doi: 10.1073/pnas.75.11.5483.

Di Marzo, V. (1998) '"Endocannabinoids" and other fatty acid derivatives with cannabimimetic properties: Biochemistry and possible physiopathological relevance', *Biochimica et Biophysica Acta - Lipids and Lipid Metabolism*. doi: 10.1016/S0005-2760(98)00042-3.

Massi, P. *et al.* (2004) 'Antitumor effects of cannabidiol, a nonpsychoactive cannabinoid, on human glioma cell lines.', *The Journal of pharmacology and experimental therapeutics*, 308(3), pp. 838–845. doi: 10.1124/jpet.103.061002.

Mat, P., Clupek, M. and Volka, K. (2007) 'Noise reduction in Raman spectra: Finite impulse response filtration versus Savitzky – Golay smoothing', *Journal of Raman Spectroscopy*, 38(9),

pp. 1174–1179. doi: 10.1002/jrs.1747.

Matthaus, C. *et al.* (2007) 'Label-free detection of mitochondrial distribution in cells by nonresonant Raman microspectroscopy', *Biophysical Journal*, 93(2), pp. 668–673. doi: 10.1529/biophysj.106.102061.

Matthäus, C. *et al.* (2007) 'Label-free detection of mitochondrial distribution in cells by nonresonant Raman microspectroscopy', *Biophysical Journal*. doi: 10.1529/biophysj.106.102061.

Matthäus, C. *et al.* (2008) 'Chapter 10 Infrared and Raman Microscopy in Cell Biology', *Methods in Cell Biology*. doi: 10.1016/S0091-679X(08)00610-9.

Mazia, D., Schatten, G. and Sale, W. (1975) 'Adhesion of cells to surfaces coated with polylysine: Applications to electron microscopy', *Journal of Cell Biology*, 66(1), pp. 198–200. doi: 10.1083/jcb.66.1.198.

McAllister, S. D. *et al.* (2011) 'Pathways mediating the effects of cannabidiol on the reduction of breast cancer cell proliferation, invasion, and metastasis', *Breast Cancer Research and Treatment*, 129(1), pp. 37–47. doi: 10.1007/s10549-010-1177-4.

McIlwain, D. R., Berger, T. and Mak, T. W. (2013) 'Caspase functions in cell death and disease', *Cold Spring Harbor Perspectives in Biology*, 5(4), pp. 1–28. doi: 10.1101/cshperspect.a008656.

McKallip, R. J. *et al.* (2006) 'Cannabidiol-Induced Apoptosis in Human Leukemia Cells : A Novel Role of Cannabidiol in the Regulation of p22 phox and Nox4 Expression', *Molecular Pharmacology*, 70(3), pp. 897–908. doi: 10.1124/mol.106.023937.glioma.

McManus, L. L. *et al.* (2011) 'Raman spectroscopic monitoring of the osteogenic differentiation of human mesenchymal stem cells', *Analyst*. doi: 10.1039/c1an15167c.

Meister, K. *et al.* (2010) 'Label-free imaging of metal-carbonyl complexes in live cells by raman

microspectroscopy', *Angewandte Chemie - International Edition*. doi: 10.1002/anie.201000097.

Merlin, J. C. (2007) 'Resonance Raman spectroscopy of carotenoids and carotenoid-containing systems', *Pure and Applied Chemistry*. doi: 10.1351/pac198557050785.

Meunier, V. *et al.* (1995) 'The human intestinal epithelial cell line Caco-2; pharmacological and pharmacokinetic applications', *Cell Biology and Toxicology*, 11, pp. 187–194. doi: 10.1007/BF00756522.

Mignolet, A., Wood, B. R. and Goormaghtigh, E. (2018) 'Intracellular investigation on the differential effects of 4 polyphenols on MCF-7 breast cancer cells by Raman imaging', *Analyst*. doi: 10.1039/c7an01460k.

Monici, M. (2005) 'Cell and tissue autofluorescence research and diagnostic applications', *Biotechnology Annual Review*, pp. 227–256. doi: 10.1016/S1387-2656(05)11007-2.

Mostowtt, T. and McCord, B. (2017) 'Surface enhanced Raman spectroscopy (SERS) as a method for the toxicological analysis of synthetic cannabinoids', *Talanta*. doi: 10.1016/j.talanta.2016.11.002.

Murrow, L., Malhotra, R. and Debnath, J. (2015) 'ATG12-ATG3 interacts with Alix to promote basal autophagic flux and late endosome function', *Nature Cell Biology*. doi: 10.1038/ncb3112.

Nagata, S. (2000) 'Apoptotic DNA Fragmentation', *Experimental Cell Research*, 256(1), pp. 12–18. doi: 10.1006/excr.2000.4834.

Nallasamy, P. and Mohan, S. (2005) 'Vibrational spectroscopic characterization of form II poly(vinylidene fluoride)', *Indian Journal of Pure and Applied Physics*.

Naumann, R. *et al.* (2001) 'Early recognition of hereditary motor and sensory neuropathy type 1 can avoid life-threatening vincristine neurotoxicity', *British Journal of Haematology*. doi:

10.1046/j.1365-2141.2001.03126.x.

Neugebauer, U. *et al.* (2010) 'Towards detection and identification of circulating tumour cells using Raman spectroscopy', in *Analyst*. doi: 10.1039/c0an00608d.

Notingher, I. *et al.* (2002) 'In situ characterisation of living cells by Raman spectroscopy', *Spectroscopy*, 16(2), pp. 43–51. doi: 10.1155/2002/408381.

Nunnari, J. and Suomalainen, A. (2012) 'Mitochondria: In sickness and in health', *Cell*. doi: 10.1016/j.cell.2012.02.035.

Okada, M. *et al.* (2012) 'Label-free Raman observation of cytochrome c dynamics during apoptosis.', *Proceedings of the National Academy of Sciences of the United States of America*, 109(1), pp. 28–32. doi: 10.1073/pnas.1107524108.

Omberg, K. M. *et al.* (2002) 'Raman spectroscopy and factor analysis of tumorigenic and non-tumorigenic cells', *Applied Spectroscopy*. doi: 10.1366/000370202760171464.

Orhon, I. and Reggiori, F. (2017) 'Assays to Monitor Autophagy Progression in Cell Cultures', *Cells*. doi: 10.3390/cells6030020.

Ott, M. *et al.* (2002) 'Cytochrome c release from mitochondria proceeds by a two-step process', *Proceedings of the National Academy of Sciences*, 99(3), pp. 1259–1263. doi: 10.1073/pnas.241655498.

Overman, S. A. *et al.* (1998) 'Conformation and interactions of the packaged double-stranded DNA genome of bacteriophage T7.', *Biospectroscopy*. doi: 10.1002/(SICI)1520-6343(1998)4:5+<S47::AID-BSPY6>3.0.CO;2-7.

Overman, S. A. and Thomas, G. J. (1998) 'Amide modes of the α-helix: Raman spectroscopy of filamentous virus fd containing peptide 13C and 2H labels in coat protein subunits', *Biochemistry*. doi: 10.1021/bi972339c.

Palonpon, A. F., Sodeoka, M. and Fujita, K. (2013) 'Molecular imaging of live cells by Raman microscopy', *Current Opinion in Chemical Biology*. doi: 10.1016/j.cbpa.2013.05.021.

Pascut, F. C. *et al.* (2011) 'Noninvasive detection and imaging of molecular markers in live cardiomyocytes derived from human embryonic stem cells', *Biophysical Journal*, 100(1), pp. 251–259. doi: 10.1016/j.bpj.2010.11.043.

Pascut, F. C. *et al.* (2013) 'Non-invasive label-free monitoring the cardiac differentiation of human embryonic stem cells in-vitro by Raman spectroscopy', *Biochimica et Biophysica Acta - General Subjects*, 1830(6), pp. 3517–3524. doi: 10.1016/j.bbagen.2013.01.030.

Pasquariello, N. *et al.* (2009) 'Characterization of the endocannabinoid system in human neuronal cells and proteomic analysis of anandamide-induced apoptosis', *Journal of Biological Chemistry*. doi: 10.1074/jbc.M109.044412.

Perna, G., Lasalvia, M. and Capozzi, V. (2016) 'Vibrational spectroscopy of synthetic and natural eumelanin', *Polymer International*. doi: 10.1002/pi.5182.

Pertwee, R. G. (2001) 'Cannabinoid receptors and pain', *Progress in Neurobiology*. Pergamon, 63(5), pp. 569–611. doi: 10.1016/S0301-0082(00)00031-9.

Pertwee, R. G. (2008) 'The diverse CB1 and CB2 receptor pharmacology of three plant cannabinoids: delta9-tetrahydrocannabinol, cannabidiol and delta9-tetrahydrocannabivarin.', *British journal of pharmacology*, 153(2), pp. 199–215. doi: 10.1038/sj.bjp.0707442.

Pertwee, R. G. and Ross, R. A. (2002) 'Cannabinoid receptors and their ligands', *Prostaglandins Leukot Essent Fatty Acids*, 66(2–3), pp. 101–121. doi: 10.1054/plef.2001.0341 S0952327801903412 [pii].

De Petrocellis, L. *et al.* (1998) 'The endogenous cannabinoid anandamide inhibits human breast cancer cell proliferation.', *Proceedings of the National Academy of Sciences of the United States of America*. doi: 10.1073/pnas.95.14.8375.

Pinto, M. *et al.* (1983) 'Enterocyte-like differentiation and polarization of the human colon carcinoma cell line Caco-2 in culture', *Biology of the Cell*, 47(323), pp. 323–330.

Pirkmajer, S. and Chibalin, A. V. (2011) ' Serum starvation: caveat emptor ', *American Journal of Physiology-Cell Physiology*. doi: 10.1152/ajpcell.00091.2011.

Pully, V. V., Lenferink, A. T. M. and Otto, C. (2011) 'Time-lapse Raman imaging of single live lymphocytes', *Journal of Raman Spectroscopy*, 42(2), pp. 167–173. doi: 10.1002/jrs.2683.

Puppels, G. J. *et al.* (1990) 'Studying single living cells and chromosomes by confocal Raman microspectroscopy.', *Nature*, 347(6290), pp. 301–303. doi: 10.1038/347301a0.

Puppels, G. J., Olminkhof, J. H. F., *et al.* (1991) 'Laser irradiation and Raman spectroscopy of single living cells and chromosomes: Sample degradation occurs with 514.5 nm but not with 660 nm laser light', *Experimental Cell Research*. doi: 10.1016/0014-4827(91)90385-8.

Puppels, G. J., Garritsen, H. S., *et al.* (1991) 'Raman microspectroscopic approach to the study of human granulocytes', *Biophysical Journal*. doi: 10.1016/S0006-3495(91)82142-7.

Rainaldi, G., Calcabrini, A. and Santini, M. T. (1998) 'Positively charged polymer polylysine-induced cell adhesion molecule redistribution in K562 cells', *Journal of Materials Science: Materials in Medicine*, 9(12), pp. 755–760. doi: 10.1023/A:1008915305681.

Ramoji, A. *et al.* (2016) 'Characterization of different substrates for Raman spectroscopic imaging of eukaryotic cells', *Journal of Raman Spectroscopy*, 47(7), pp. 773–786. doi: 10.1002/jrs.4899.

Raszeja, L. J. *et al.* (2017) 'Asymmetric rhenium tricarbonyl complexes show superior luminescence properties in live cell imaging', *Chemical Communications*. doi: 10.1039/C6CC07553C.

Van Rechem, C. *et al.* (2010) 'Differential Regulation of HIC1 Target Genes by CtBP and NuRD,

via an Acetylation/SUMOylation Switch, in Quiescent versus Proliferating Cells', *Molecular and Cellular Biology*. doi: 10.1128/mcb.00582-09.

Rehman, I. ur, Movasaghi, Z. and Rehman, S. (2012) *Vibrational spectroscopy for tissue analysis*, *Vibrational Spectroscopy for Tissue Analysis*. doi: 10.1201/b12949.

Remijsen, Q. *et al.* (2011) 'Dying for a cause: NETosis, mechanisms behind an antimicrobial cell death modality', *Cell Death and Differentiation*. doi: 10.1038/cdd.2011.1.

Ricci, M. *et al.* (2018) 'Glioblastoma single-cell microRaman analysis under stress treatments', *Scientific Reports*, 8(1). doi: 10.1038/s41598-018-26356-x.

Rieppo, L. *et al.* (2012) 'Application of second derivative spectroscopy for increasing molecular specificity of fourier transform infrared spectroscopic imaging of articular cartilage', *Osteoarthritis and Cartilage*. doi: 10.1016/j.joca.2012.01.010.

Rimmerman, N. *et al.* (2013) 'Direct modulation of the outer mitochondrial membrane channel, voltage-dependent anion channel 1 (VDAC1) by cannabidiol: A novel mechanism for cannabinoid-induced cell death', *Cell Death and Disease*. doi: 10.1038/cddis.2013.471.

Ringnér, M. (2008) 'What is principal component analysis?', *Nat Biotechnol*, 26(3), pp. 303–304. doi: 10.1038/nbt0308-303.

Rivas-Arancibia, S. *et al.* (2017) 'Structural Changes of Amyloid Beta in Hippocampus of Rats Exposed to Ozone: A Raman Spectroscopy Study', *Frontiers in Molecular Neuroscience*, 10. doi: 10.3389/fnmol.2017.00137.

Ronquist, G. (2012) 'Prostasomes are mediators of intercellular communication: From basic research to clinical implications', *Journal of Internal Medicine*. doi: 10.1111/j.1365-2796.2011.02487.x.

Saarinen, J. *et al.* (2017) 'Insights into Caco-2 cell culture structure using coherent anti-Stokes

Raman scattering (CARS) microscopy', *International Journal of Pharmaceutics*. Elsevier, 523(1), pp. 270–280. doi: 10.1016/J.IJPHARM.2017.03.015.

Sadasivan, S. *et al.* (2006) 'Amino acid starvation induced autophagic cell death in PC-12 cells: Evidence for activation of caspase-3 but not calpain-1', *Apoptosis*. doi: 10.1007/s10495-006-7690-6.

Salehi, H. *et al.* (2013) 'Confocal Raman data analysis enables identifying apoptosis of MCF-7 cells caused by anticancer drug paclitaxel', *Journal of Biomedical Optics*, 18(5), p. 56010. doi: 10.1117/1.jbo.18.5.056010.

Salehi, H. *et al.* (2013) 'Label-free detection of anticancer drug paclitaxel in living cells by confocal Raman microscopy', *Applied Physics Letters*, 102(11), p. 113701. doi: 10.1063/1.4794871.

Santoro, A. et al. (2017) 'The endocannabinoid anandamide inhibits colon cancer cell growth by modulating different survival and proliferating pathways', *Italian Journal of Anatomy and Embryology*.

Sato, E. T. and Martinho, H. (2018) 'First-principles calculations of Raman vibrational modes in the fingerprint region for connective tissue', *Biomedical Optics Express*. doi: 10.1364/boe.9.001728.

Scalfi-Happ, C. *et al.* (2011) 'Investigation of lipid bodies in a colon carcinoma cell line by confocal Raman microscopy', *Medical Laser Application*. doi: 10.1016/j.mla.2011.08.002.

Schie, I. W. and Huser, T. (2013) 'Methods and applications of Raman microspectroscopy to single-cell analysis', in *Applied Spectroscopy*. doi: 10.1366/12-06971.

Schlücker, S. *et al.* (2003) 'Raman microspectroscopy: A comparison of point, line, and wide-field imaging methodologies', *Analytical Chemistry*, 75(16), pp. 4312–4318. doi: 10.1021/ac034169h.

Schrader, B. (ed.) (1995) *Infrared and Raman Spectroscopy*. Weinheim, Germany: Wiley-VCH Verlag GmbH. doi: 10.1002/9783527615438.

Schwarz, H., Blanco, F. J. and Lotz, M. (1994) 'Anadamide, an endogenous cannabinoid receptor agonist inhibits lymphocyte proliferation and induces apoptosis', *Journal of Neuroimmunology*. doi: 10.1016/0165-5728(94)90152-X.

Shappell, N. W. (2003) 'Ergovaline toxicity on Caco-2 cells as assessed by MTT, alamarBlue, and DNA assays', *In vitro cellular & developmental biology. Animal*, 39(7), pp. 329–35. doi: 10.1290/1543-706X(2003)039<0329:ETOCCA>2.0.CO;2.

Shi, J., Gao, W. and Shao, F. (2017) 'Pyroptosis: Gasdermin-Mediated Programmed Necrotic Cell Death', *Trends in Biochemical Sciences*. doi: 10.1016/j.tibs.2016.10.004.

Short, K. W. *et al.* (2005) 'Raman spectroscopy detects biochemical changes due to proliferation in mammalian cell cultures', *Biophysical Journal*, 88(6), pp. 4274–4288. doi: 10.1529/biophysj.103.038604.

Shrivastava, A. *et al.* (2011) 'Cannabidiol Induces Programmed Cell Death in Breast Cancer Cells by Coordinating the Cross-talk between Apoptosis and Autophagy', *Molecular Cancer Therapeutics*. doi: 10.1158/1535-7163.mct-10-1100.

Siebert, F. and Hildebrandt, P. (2008) *Theory of Infrared Absorption and Raman Spectroscopy*, *Vibrational Spectroscopy in Life Science*. doi: 10.1002/9783527621347.ch2.

Simon, H. U., Haj-Yehia, A. and Levi-Schaffer, F. (2000) 'Role of reactive oxygen species (ROS) in apoptosis induction', *Apoptosis*. doi: 10.1023/A:1009616228304.

Singh, S. V. *et al.* (2005) 'Sulforaphane-induced cell death in human prostate cancer cells is initiated by reactive oxygen species', *Journal of Biological Chemistry*. doi: 10.1074/jbc.M412443200.

Slee, E. A., Adrain, C. and Martin, S. J. (2001) 'Executioner Caspase-3, -6, and -7 Perform Distinct, Non-redundant Roles during the Demolition Phase of Apoptosis', *Journal of Biological Chemistry*. doi: 10.1074/jbc.M008363200.

Smith, E. and Dent, G. (2005) *Modern Raman Spectroscopy - A Practical Approach*. doi: 10.1002/0470011831.

Smith, G. P. S. *et al.* (2015) 'Raman imaging of drug delivery systems.', *Advanced drug delivery reviews*. doi: 10.1016/j.addr.2015.01.005.

Smith, R., Wright, K. L. and Ashton, L. (2016) 'Raman spectroscopy: an evolving technique for live cell studies', *The Analyst*, 141(12), pp. 3590–3600. doi: 10.1039/C6AN00152A.

Smith, S. J. *et al.* (2017) 'Detection of early osteogenic commitment in primary cells using Raman spectroscopy', *Analyst*. doi: 10.1039/c6an02469f.

Stephens, D. J. and Allan, V. J. (2003) 'Light microscopy techniques for live cell imaging', *Science (New York, N.Y.)*, 300(5616), pp. 82–86. doi: 10.1126/science.1082160.

Stephenson, K. A. *et al.* (2004) 'Bridging the gap between in vitro and in vivo imaging: Isostructural Re and99mTc complexes for correlating fluorescence and radioimaging studies', *Journal of the American Chemical Society*, 126(28), pp. 8598–8599. doi: 10.1021/ja047751b.

Stone, N. *et al.* (2004) 'Raman spectroscopy for identification of epithelial cancers', *Faraday Discussions*. doi: 10.1039/b304992b.

Stroun, M. and Anker, P. (1972) 'Nucleic acids spontaneously released by living frog auricles', *The Biochemical journal*.

Su, L. *et al.* (2013) 'In vivo and in situ monitoring of the nitric oxide stimulus response of single cancer cells by Raman spectroscopy', *Laser Physics Letters*. doi: 10.1088/1612-2011/10/4/045608.

Sultan, A. S., Marie, M. A. and Sheweita, S. A. (2018) 'Novel mechanism of cannabidiol-induced apoptosis in breast cancer cell lines', *Breast*. doi: 10.1016/j.breast.2018.06.009.

Sumoza-Toledo, A. and Penner, R. (2011) 'TRPM2: A multifunctional ion channel for calcium signalling', *Journal of Physiology*. doi: 10.1113/jphysiol.2010.201855.

Sun, S. *et al.* (2015) 'Condensing Raman spectrum for single-cell phenotype analysis', *BMC Bioinformatics*. doi: 10.1186/1471-2105-16-S18-S15.

Susin, S. A. *et al.* (1999) 'Molecular characterization of mitochodrial apoptosis-inducing factor', *Nature*. doi: 10.1038/17135.

Susin, S. A. (2004) 'Bcl-2 inhibits the mitochondrial release of an apoptogenic protease', *Journal of Experimental Medicine*. doi: 10.1084/jem.184.4.1331.

Swain, R. J., Jell, G. and Stevens, M. M. (2008) 'Non-invasive analysis of cell cycle dynamics in single living cells with Raman micro-spectroscopy', *Journal of Cellular Biochemistry*, 104(4), pp. 1427–1438. doi: 10.1002/jcb.21720.

Takeda, S. *et al.* (2008) 'Δ9-Tetrahydrocannabinol enhances MCF-7 cell proliferation via cannabinoid receptor-independent signaling', *Toxicology*, 245(1–2), pp. 141–146. doi: 10.1016/j.tox.2007.12.019.

Takeuchi, H. (2003) 'Raman structural markers of tryptophan and histidine side chains in proteins', *Biopolymers - Biospectroscopy Section*. doi: 10.1002/bip.10440.

Talari, A. C. S. *et al.* (2015) 'Raman spectroscopy of biological tissues', *Applied Spectroscopy Reviews*. doi: 10.1080/05704928.2014.923902.

Thakur, B. K. *et al.* (2014) 'Double-stranded DNA in exosomes: a novel biomarker in cancer detection', *Cell Research*. doi: 10.1038/cr.2014.44.

Théry, C. (2011) 'Exosomes: secreted vesicles and intercellular communications', *F1000*

Biology Reports. doi: 10.3410/b3-15.

Théry, C., Zitvogel, L. and Amigorena, S. (2002) 'Exosomes: Composition, biogenesis and function', *Nature Reviews Immunology*. doi: 10.1038/nri855.

Thomas, G. J. (2004) 'Applications of Infrared Spectroscopy in Biochemistry, Biology, and Medicine. Frank S. Parker', *The Quarterly Review of Biology*. doi: 10.1086/407481.

Thorn, K. (2016) 'A quick guide to light microscopy in cell biology', *Molecular Biology of the Cell*. doi: 10.1091/mbc.E15-02-0088.

Ujváry, I. and Hanuš, L. (2016) 'Human Metabolites of Cannabidiol: A Review on Their Formation, Biological Activity, and Relevance in Therapy', *Cannabis and Cannabinoid Research*. doi: 10.1089/can.2015.0012.

Uzunbajakava, N., Lenferink, A., Kraan, Y., Volokhina, E., *et al.* (2003) 'Nonresonant confocal Raman imaging of DNA and protein distribution in apoptotic cells', *Biophysical Journal*, 84(6), pp. 3968–3981.

Uzunbajakava, N., Lenferink, A., Kraan, Y., Willekens, B., *et al.* (2003) 'Nonresonant Raman imaging of protein distribution in single human cells', *Biopolymers*, 72(1), pp. 1–9. doi: 10.1002/bip.10246.

Vickers, K. C. *et al.* (2011) 'MicroRNAs are transported in plasma and delivered to recipient cells by high-density lipoproteins', *Nature Cell Biology*. doi: 10.1038/ncb2210.

Wang, F., Gómez-Sintes, R. and Boya, P. (2018) 'Lysosomal membrane permeabilization and cell death', *Traffic*. doi: 10.1111/tra.12613.

Wang, X. *et al.* (2000) 'Acetylation increases the α-helical content of the histone tails of the nucleosome', *Journal of Biological Chemistry*. doi: 10.1074/jbc.M004998200.

Watanabe, K. *et al.* (2005) 'Marijuana extracts possess the effects like the endocrine disrupting

chemicals', *Toxicology*, 206(3), pp. 471–478. doi: 10.1016/j.tox.2004.08.005.

Wen, Z. Q. and Thomas, G. J. (2002) 'UV resonance Raman spectroscopy of DNA and protein constituents of viruses: Assignments and cross sections for excitations at 257, 244, 238, and 229 nm', *Biopolymers*. doi: 10.1002/(sici)1097-0282(199803)45:3<247::aid-bip7>3.3.co;2-z.

Wilson, E. B. *et al.* (1955) 'Molecular Vibrations: The Theory of Infrared and Raman Vibrational Spectra', *Journal of The Electrochemical Society*, p. 235C. doi: 10.1149/1.2430134.

Wilson, S. M. and Bacic, A. (2012) 'Preparation of plant cells for transmission electron microscopy to optimize immunogold labeling of carbohydrate and protein epitopes', *Nature Protocols*, 7(9), pp. 1716–1727. doi: 10.1038/nprot.2012.096.

Wolthuis, R. *et al.* (1999) 'Chapter thirty-two - Raman Spectroscopic Methods for In Vitro and In Vivo Tissue Characterization', in *Biological Techniques Series*. doi: http://dx.doi.org/10.1016/B978-012447836-7/50034-8.

Wood, B. R. *et al.* (2005) 'Raman microspectroscopy and imaging provides insights into heme aggregation and denaturation within human erythrocytes.', *Journal of biomedical optics*, 10(1), p. 14005. doi: 10.1117/1.1854678.

Xu, L. *et al.* (2016) 'Multigaps Embedded Nanoassemblies Enhance in Situ Raman Spectroscopy for Intracellular Telomerase Activity Sensing', *Advanced Functional Materials*. doi: 10.1002/adfm.201504587.

Yang, W. S. and Stockwell, B. R. (2016) 'Ferroptosis: Death by Lipid Peroxidation', *Trends in Cell Biology*. doi: 10.1016/j.tcb.2015.10.014.

Yao, H. *et al.* (2009) 'Raman spectroscopic analysis of apoptosis of single human gastric cancer cells', *Vibrational Spectroscopy*. doi: 10.1016/j.vibspec.2008.11.003.

Yavin, E. and Yavin, Z. (1974) 'Attachment and culture of dissociated cells from rat embryo

cerebral hemispheres on poly lysine-coated surface', *Journal of Cell Biology*, 62(2), pp. 540–546. doi: 10.1083/jcb.62.2.540.

Yiming, X. *et al.* (1999) 'Raman spectroscopic study of microcosmic photodamage of the space structure of DNA sensitized by Yangzhou haematoporphyrin derivative and Photofrin II', *Journal of Photochemistry and Photobiology B: Biology*. doi: 10.1016/S1011-1344(99)00097-4.

Yosef, H. K. *et al.* (2018) 'Exploring the efficacy and cellular uptake of sorafenib in colon cancer cells by Raman micro-spectroscopy', *Analyst*. doi: 10.1039/c8an02029a.

Zhang, D. *et al.* (2005) 'Detection of the site of phosphorylation in a peptide using Raman spectroscopy and partial least squares discriminant analysis', *Spectrochimica Acta - Part A: Molecular and Biomolecular Spectroscopy*. doi: 10.1016/j.saa.2004.04.019.

Zhang, X. *et al.* (2008) 'Characterization of cellular chemical dynamics using combined microfluidic and Raman techniques', *Analytical and Bioanalytical Chemistry*, 390(3), pp. 833–840. doi: 10.1007/s00216-007-1564-9.

Zhang, X. *et al.* (2012) 'Label-free live-cell imaging of nucleic acids using stimulated raman scattering microscopy', *ChemPhysChem*, 13(4), pp. 1054–1059. doi: 10.1002/cphc.201100890.

Zhang, Y. *et al.* (2018) 'Plasma membrane changes during programmed cell deaths', *Cell Research*. doi: 10.1038/cr.2017.133.

Zheng, C. *et al.* (2014) 'The use of Au@SiO2shell-isolated nanoparticle-enhanced Raman spectroscopy for human breast cancer detection', *Analytical and Bioanalytical Chemistry*, 406(22), pp. 5425–5432. doi: 10.1007/s00216-014-7967-5.

Zoladek, A. *et al.* (2010) 'Development of Raman Imaging System for time-course imaging of single living cells', *Spectroscopy*, 24, pp. 131–136.

Zoladek, A. *et al.* (2011) 'Non-invasive time-course imaging of apoptotic cells by confocal

Raman micro-spectroscopy', *Journal of Raman Spectroscopy*, 42(June 2010), pp. 251–258. doi: 10.1002/jrs.2707.

Zorov, D. B., Juhaszova, M. and Sollott, S. J. (2014) 'Mitochondrial Reactive Oxygen Species (ROS) and ROS-Induced ROS Release', *Physiological Reviews*. doi: 10.1152/physrev.00026.2013.

Appendix 1

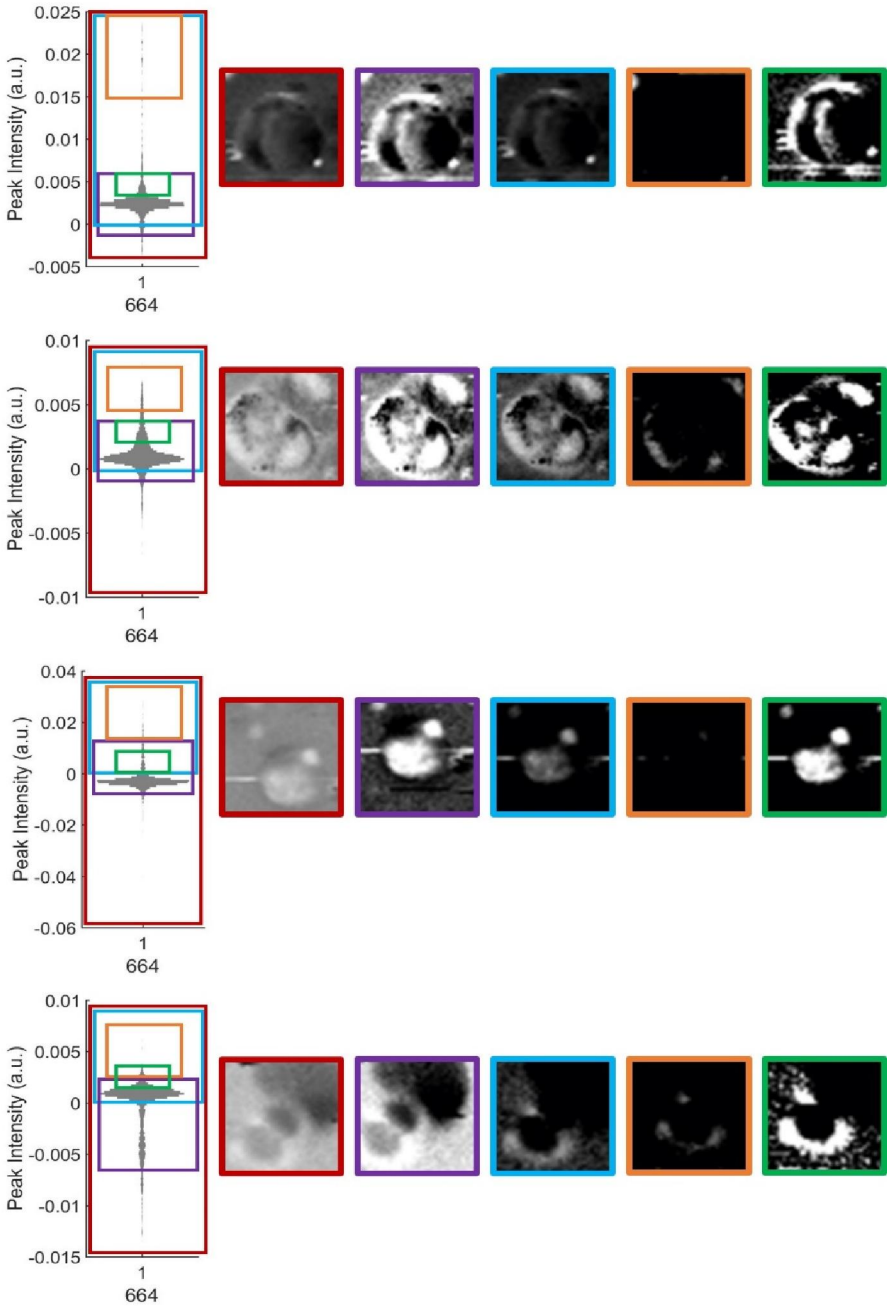

Distribution plots and Raman maps of the 664 cm^{-1} peak, demonstrating how different shading ranges can affect the map. The shading ranges are as follows: minimum to maximum (red box), 5-95% (purple), 0 to max (blue), highest values (orange) and chosen range for the final image (green). The corresponding Raman map is outlined in the same colour.

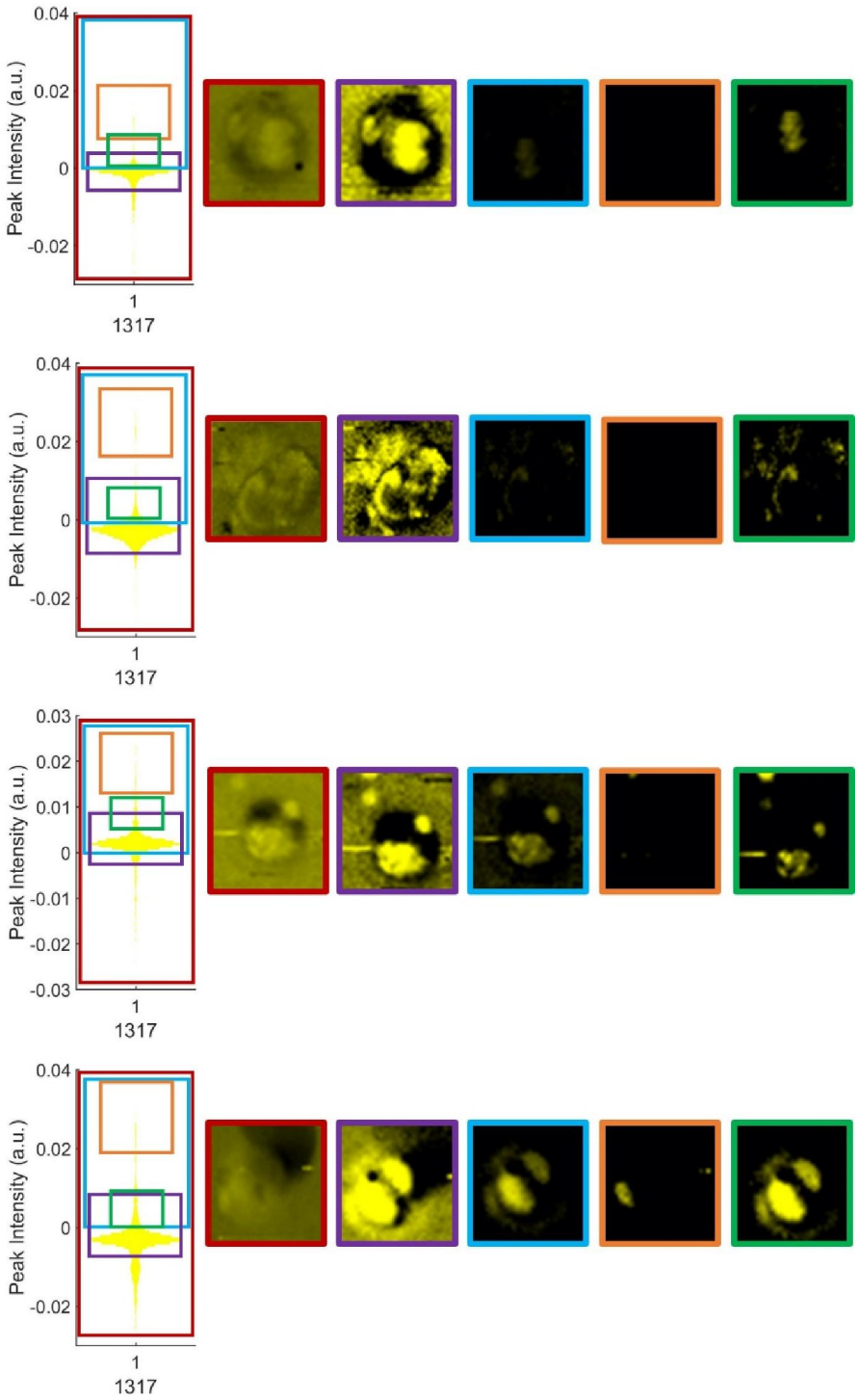

Distribution plots and Raman maps of the 1317 cm^{-1} peak, demonstrating how different shading ranges can affect the map. The shading ranges are as follows: minimum to maximum (red box), 5-95% (purple), 0 to max (blue), highest values (orange) and chosen range for the final image (green). The corresponding Raman map is outlined in the same colour.

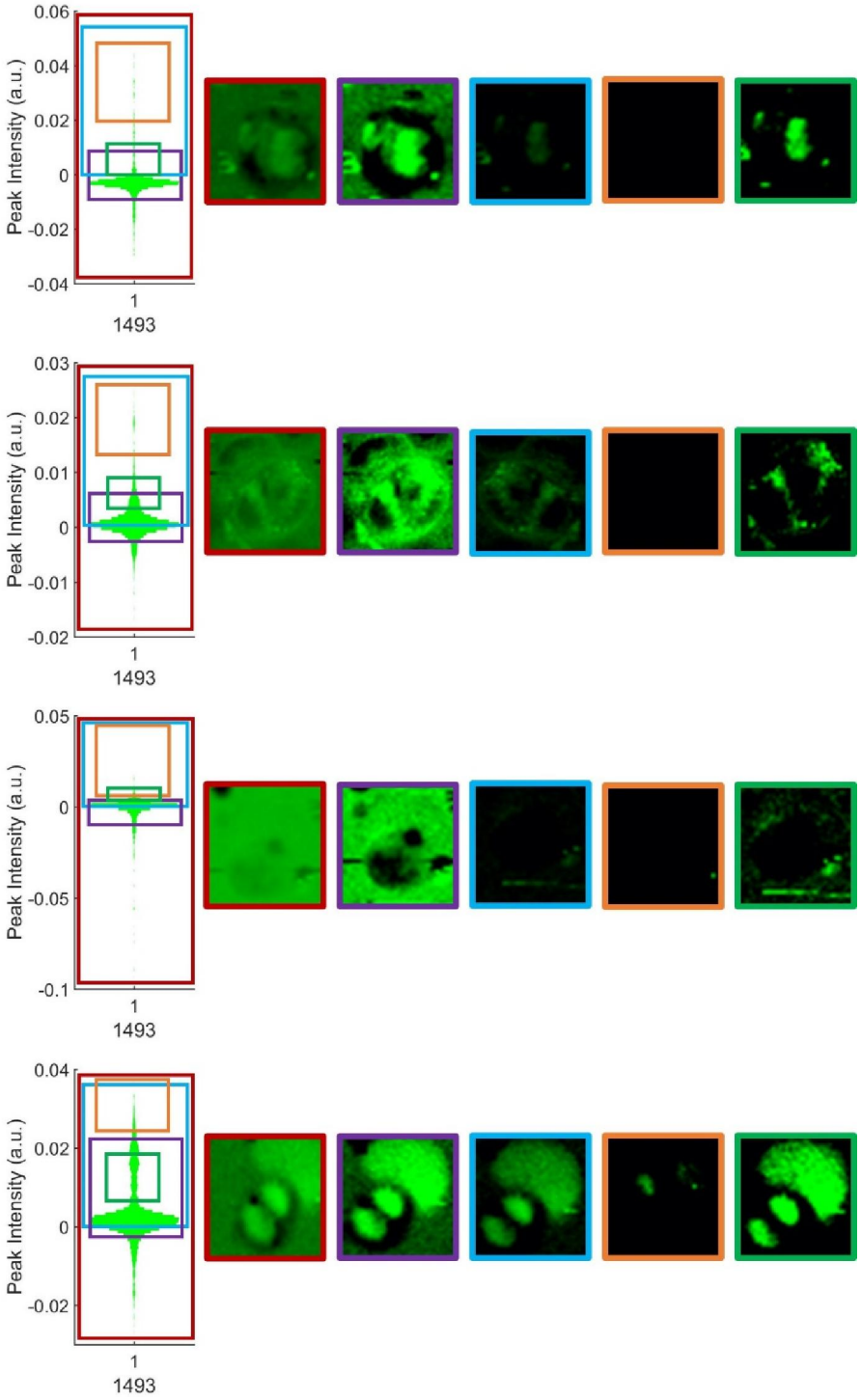

Distribution plots and Raman maps of the 1493 cm^{-1} peak, demonstrating how different shading ranges can affect the map. The shading ranges are as follows: minimum to maximum (red box), 5-95% (purple), 0 to max (blue), highest values (orange) and chosen range for the final image (green). The corresponding Raman map is outlined in the same colour.

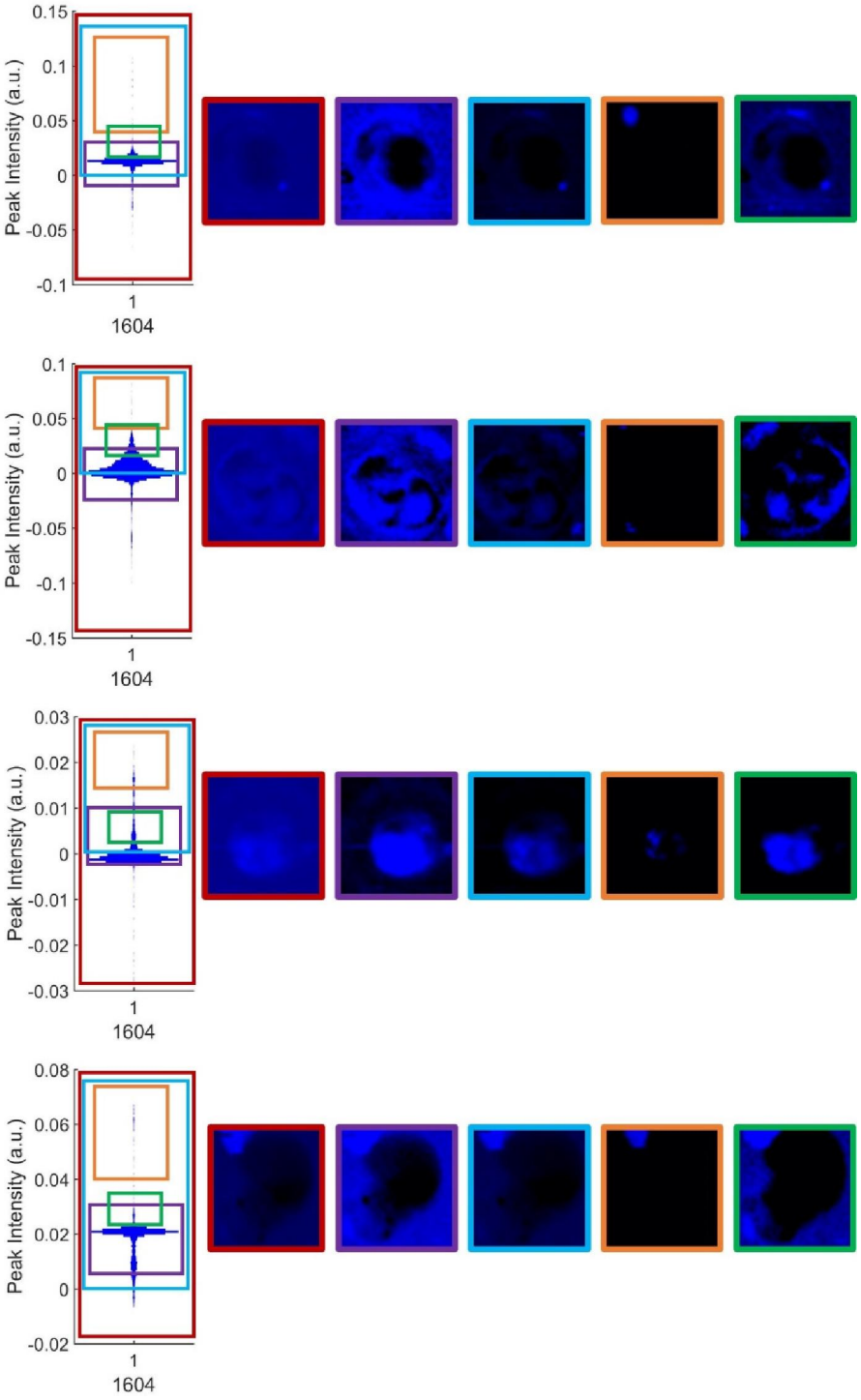

Distribution plots and Raman maps of the 1604 cm^{-1} peak, demonstrating how different shading ranges can affect the map. The shading ranges are as follows: minimum to maximum (red box), 5-95% (purple), 0 to max (blue), highest values (orange) and chosen range for the final image (green). The corresponding Raman map is outlined in the same colour.

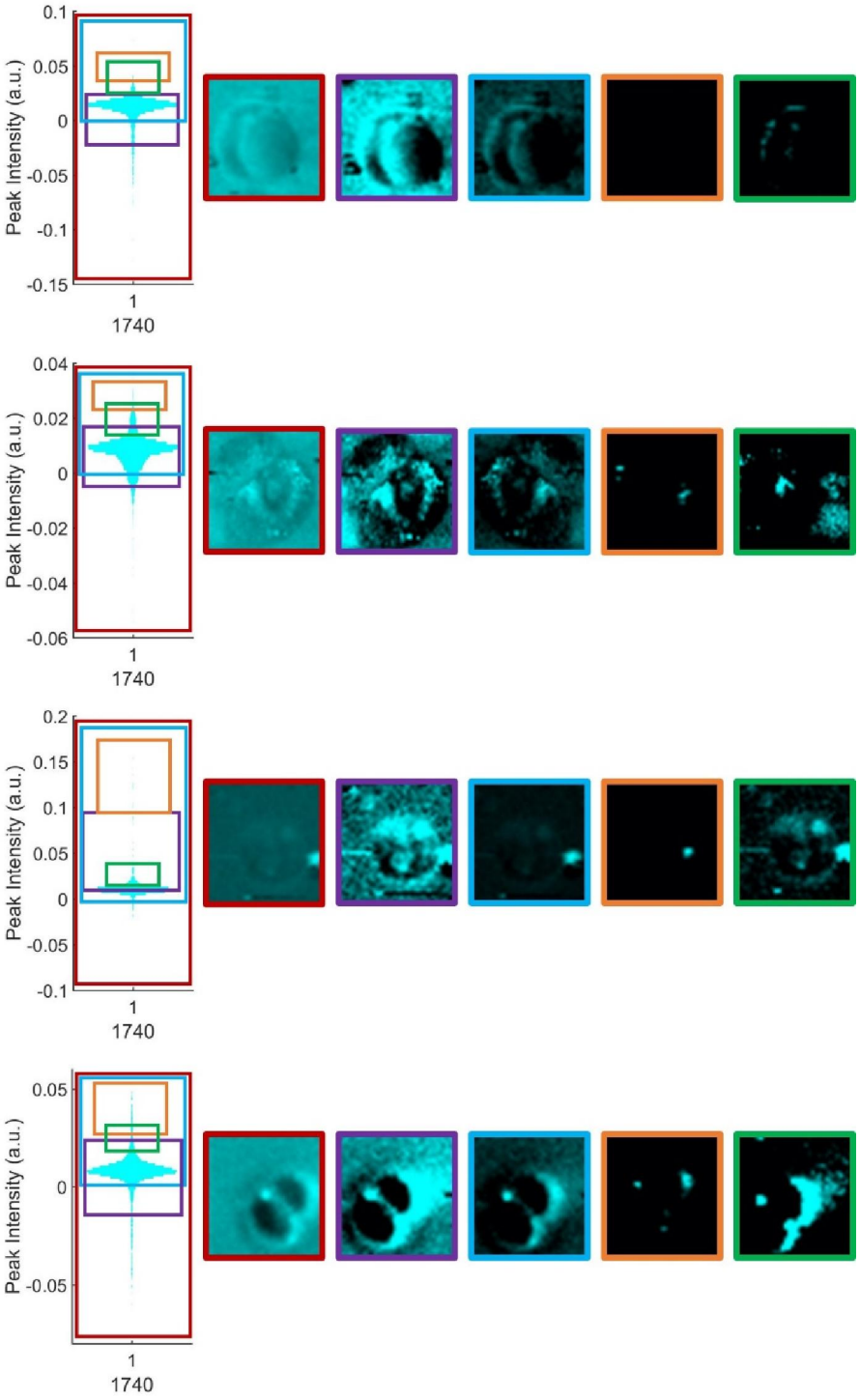

Distribution plots and Raman maps of the 1740 cm^{-1} peak, demonstrating how different shading ranges can affect the map. The shading ranges are as follows: minimum to maximum (red box), 5-95% (purple), 0 to max (blue), highest values (orange) and chosen range for the final image (green). The corresponding Raman map is outlined in the same colour.

Appendix 2

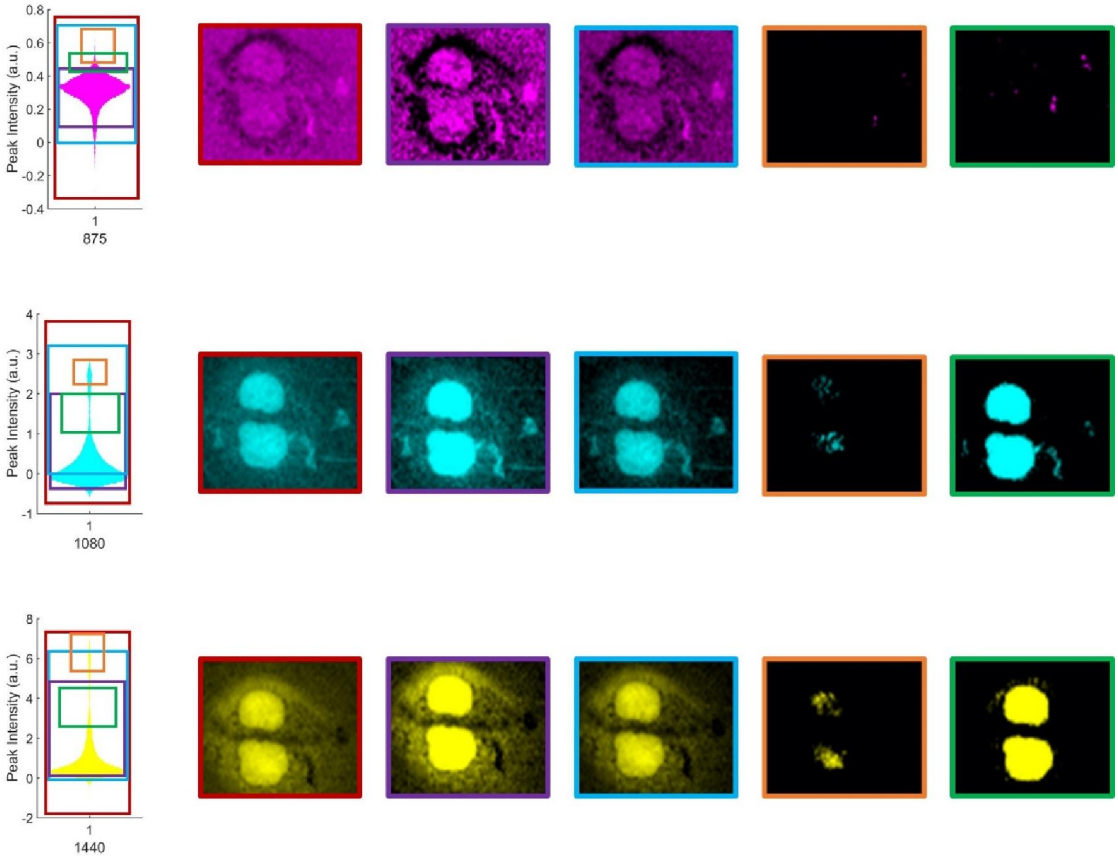

Distribution plots and Raman maps of the 875 cm^{-1}, 1080 cm^{-1} and 1440 cm^{-1} peaks, demonstrating how different shading ranges can affect the map. The shading ranges are as follows: minimum to maximum (red box), 5-95% (purple), 0 to max (blue), highest values (orange) and a narrow shading range of the central values (green). The corresponding Raman map is outlined in the same colour. This cell was treated with 1 µM of CBD for a period of 4 hours.

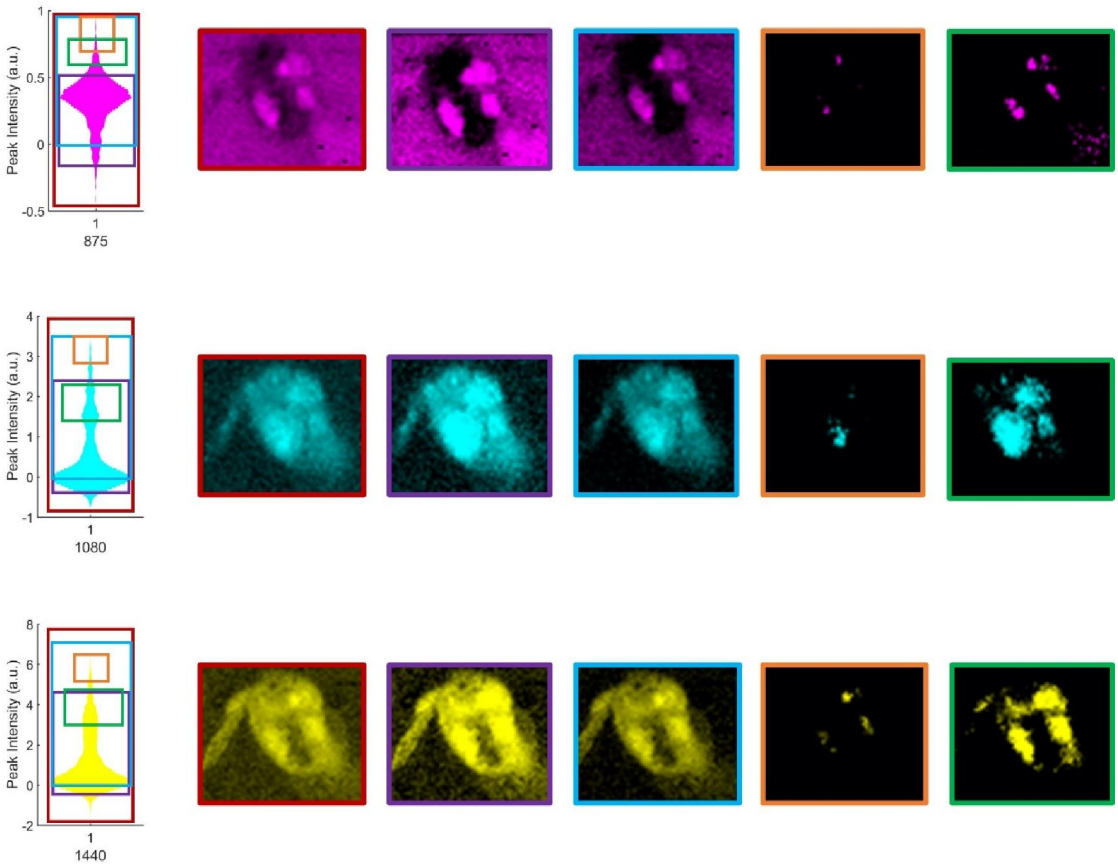

Distribution plots and Raman maps of the 875 cm^{-1}, 1080 cm^{-1} and 1440 cm^{-1} peaks, demonstrating how different shading ranges can affect the map. The shading ranges are as follows: minimum to maximum (red box), 5-95% (purple), 0 to max (blue), highest values (orange) and a narrow shading range of the central values (green). The corresponding Raman map is outlined in the same colour. This cell was treated with a 10 µM concentration of CBD for 4 hours.

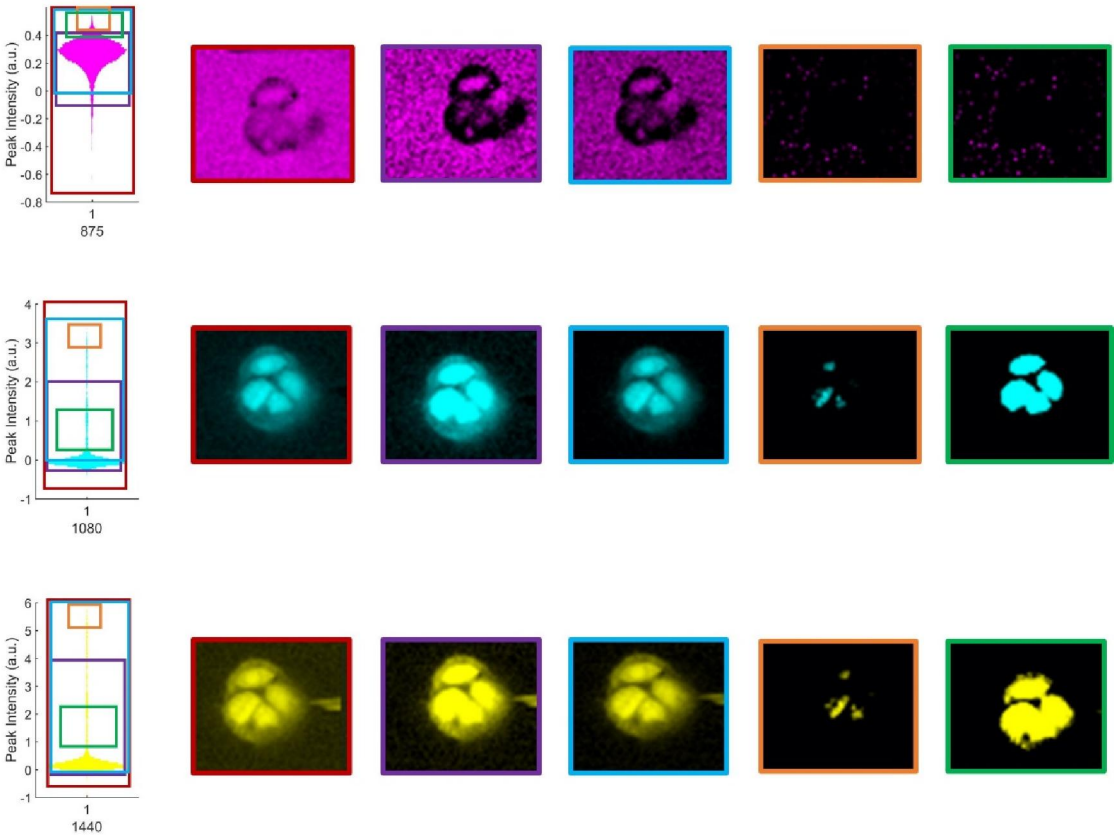

Distribution plots and Raman maps of the 875 cm^{-1}, 1080 cm^{-1} and 1440 cm^{-1} peaks, demonstrating how different shading ranges can affect the map. The shading ranges are as follows: minimum to maximum (red box), 5-95% (purple), 0 to max (blue), highest values (orange) and a narrow shading range of the central values (green). The corresponding Raman map is outlined in the same colour. This cell was treated with a media control for 4 hours.

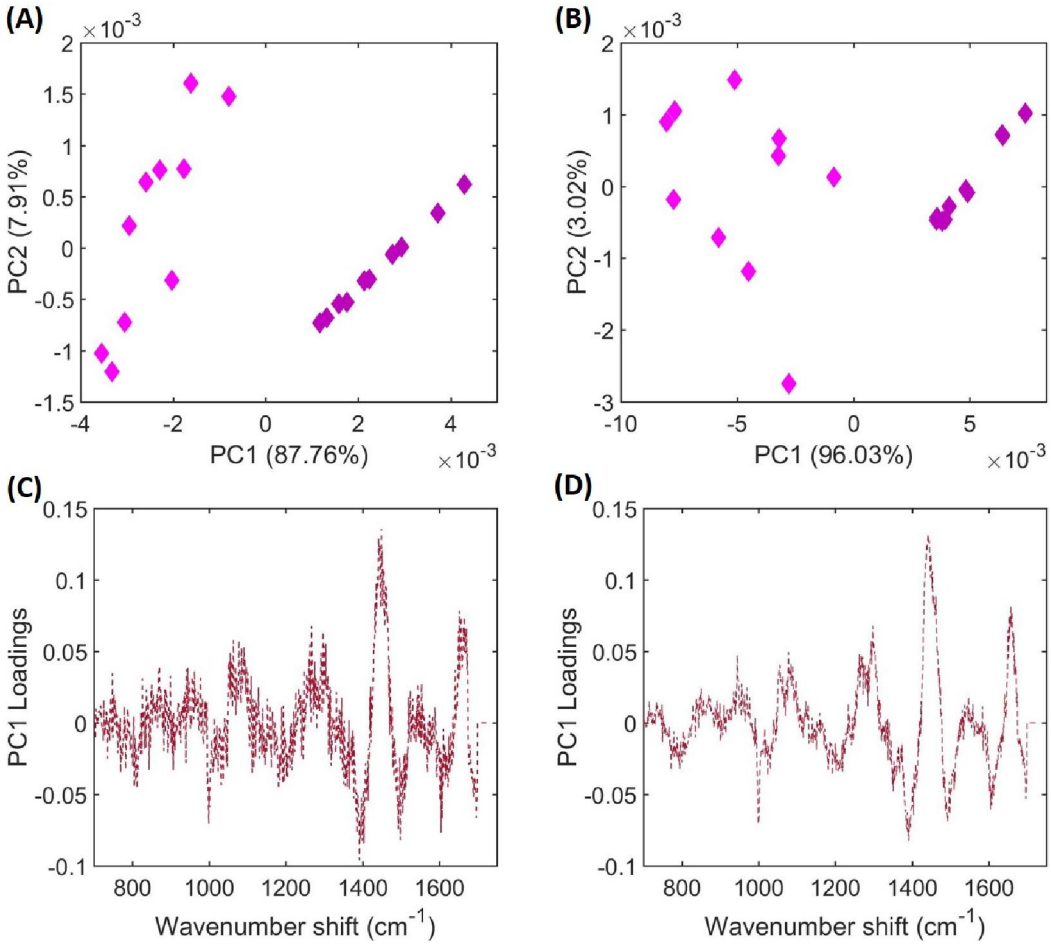

A comparison of control cells to create benchmark PC1 loadings at 785 nm. For PCA-scores plots of PC1 against PC2, spectra were taken from the regions of the cell identified as having a high DNA **(A)** or protein **(B)** content. The PC1 loadings for each plot are shown in **(C and D)**.